

Remote Sensing and Digital Image Processing

Shuanggen Jin
Estel Cardellach
Feiqin Xie



GNSS Remote Sensing

Theory, Methods and Applications



 Springer

GNSS Remote Sensing

Remote Sensing and Digital Image Processing

VOLUME 19

Series Editor:

Freek D. van der Meer
*Department of Earth Systems Analysis
International Institute for
Geo-Information Science and
Earth Observation (ITC)
Enchede, The Netherlands
&
Department of Physical Geography
Faculty of Geosciences
Utrecht University
The Netherlands*

Editorial Advisory Board:

Michael Abrams
*NASA Jet Propulsion Laboratory
Pasadena, CA, U.S.A.*

Paul Curran
*University of Bournemouth, U.K.
Finland*

Arnold Dekker
*CSIRO, Land and Water Division
Canberra, Australia*

Steven M. de Jong
*Department of Physical Geography
Faculty of Geosciences
Utrecht University, The Netherlands*

Michael Schaepman
*Department of Geography
University of Zurich, Switzerland*

EARSel Series Editor:

André Marçal
*Department of Mathematics
Faculty of Sciences
University of Porto
Porto, Portugal*

EARSel Editorial Advisory Board:

Mario A. Gomarasca
CNR - IREA Milan, Italy

Martti Hallikainen
*Helsinki University of Technology
Finland*

Håkan Olsson
*University of Zurich, Switzerland
Swedish University
of Agricultural Sciences
Sweden*

Eberhard Parlow
*University of Basel
Switzerland*

Rainer Reuter
*University of Oldenburg
Germany*

For further volumes:

<http://www.springer.com/series/6477>

Shuanggen Jin • Estel Cardellach • Feiqin Xie

GNSS Remote Sensing

Theory, Methods and Applications



Springer

Shuanggen Jin
Shanghai Astronomical Observatory
Chinese Academy of Sciences
Shanghai, China
People's Republic

Estel Cardellach
Institut d'Estudis Espacials de Catalunya
(ICE/IEEC-CSIC)
Barcelona, Spain

Feiqin Xie
Texas A&M University-Corpus Christi
Corpus Christi
TX, USA

ISSN 1567-3200
ISBN 978-94-007-7481-0 ISBN 978-94-007-7482-7 (eBook)
DOI 10.1007/978-94-007-7482-7
Springer Dordrecht Heidelberg New York London

Library of Congress Control Number: 2013950927

© Springer Science+Business Media Dordrecht 2014

This work is subject to copyright. All rights are reserved by the Publisher, whether the whole or part of the material is concerned, specifically the rights of translation, reprinting, reuse of illustrations, recitation, broadcasting, reproduction on microfilms or in any other physical way, and transmission or information storage and retrieval, electronic adaptation, computer software, or by similar or dissimilar methodology now known or hereafter developed. Exempted from this legal reservation are brief excerpts in connection with reviews or scholarly analysis or material supplied specifically for the purpose of being entered and executed on a computer system, for exclusive use by the purchaser of the work. Duplication of this publication or parts thereof is permitted only under the provisions of the Copyright Law of the Publisher's location, in its current version, and permission for use must always be obtained from Springer. Permissions for use may be obtained through RightsLink at the Copyright Clearance Center. Violations are liable to prosecution under the respective Copyright Law.

The use of general descriptive names, registered names, trademarks, service marks, etc. in this publication does not imply, even in the absence of a specific statement, that such names are exempt from the relevant protective laws and regulations and therefore free for general use.

While the advice and information in this book are believed to be true and accurate at the date of publication, neither the authors nor the editors nor the publisher can accept any legal responsibility for any errors or omissions that may be made. The publisher makes no warranty, express or implied, with respect to the material contained herein.

Printed on acid-free paper

Springer is part of Springer Science+Business Media (www.springer.com)

Preface

The Global Navigation Satellite System (GNSS) has provided an unprecedented high accuracy, flexibility and tremendous contribution to navigation, positioning, timing and scientific questions related to precise positioning on Earth's surface, since Global Positioning System (GPS) became fully operational in 1994. Since GNSS is characterized as a highly precise, continuous, all-weather and near-real-time microwave (L-band) technique, additional more applications and potentials of GNSS are being explored by scientists and engineers. When the GNSS signal propagates through the Earth's atmosphere, it is delayed by the atmospheric refractivity. GNSS radio occultation together with ground GNSS have been used to produce accurate, all-weather, global refractive index, pressure, density profiles in the troposphere, temperature with up to the lower stratosphere (35–40 km), and the ionospheric total electron content (TEC) as well as electron density profiles, to improve weather analysis and forecasting, monitor climate change, and monitor ionospheric events. Therefore, GNSS has great potentials in atmospheric sounding, meteorology, climatology and space weather.

In addition, surface multi-path is one of main error sources for GNSS navigation and positioning. It has recently been recognized, however, that the special kind of GPS multi-path delay reflected from the Earth's surface, could be used to sense the Earth's surface environments. A recent interesting result on fluctuations in near surface soil moisture has been successfully retrieved from the ground GNSS multi-path, fairly matching soil moisture fluctuations in soil measured with conventional sensors. In addition, the space-borne GNSS received delay of the GNSS reflected signal with respect to the rough surface could provide information on the differential paths between direct and reflected signals. Together with information on the receiver antenna position and the medium, the delay measurements associated with the properties of the reflecting surface can be used to produce the surface roughness parameters and to determine surface characteristics. The Bistatic radar using L-band signals transmitted by GNSS can be as an ocean altimeter and scatterometer. A number of experiments and missions using GNSS reflected signals from the ocean

and land surface have been tested and applied, such as determining ocean surface height, wind speed and wind direction of ocean surface, soil moisture, snow and ice thickness.

Therefore, the refracted, reflected and scattered GNSS signals can image the Earth's surface environments as a new, highly precise, continuous, all-weather and near-real-time remote sensing tool, which is expected to revolutionize various atmospheric sounding, ocean remote sensing and land/hydrology mapping, especially for various Earth's surfaces and the atmosphere. With the development of the next generation of multi-frequency and multi-system GNSS constellations, including the US's modernized GPS-IIIF and planned GPS-III, Russia's restored GLONASS, and the coming European Union's GALILEO system and China's Beidou/COMPASS system as well as a number of Space Based Augmentation Systems, such as Japan's Quasi-Zenith Satellite System (QZSS) and India's Regional Navigation Satellite Systems (IRNSS), more applications and opportunities will be exploited and realized using new onboard GNSS receivers on future space-borne GNSS reflectometry and refractometry missions in the near future.

GNSS Remote Sensing –Theory, Methods and Applications has been written as a monograph and textbook that guides the reader through the theory and practice of GNSS remote sensing and applications in the atmosphere, oceans, land and hydrology. This book covers Chap. 1: Introduction to GNSS, Chap. 2: GNSS Atmospheric and Multipath Delays, Chap. 3: Ground GNSS Atmospheric Sensing, Chap. 4: Ground-Based GNSS Ionospheric Sounding, Chap. 5: Theory of GNSS Radio Occultation, Chap. 6: Atmospheric Sensing using GNSS RO, Chap. 7: Ionospheric Sounding using GNSS-RO, Chap. 8: Theory of GNSS Reflectometry, Chap. 9: Ocean Remote Sensing using GNSS-R, Chap. 10: Hydrology and Vegetation Remote Sensing, Chap. 11: Cryospheric Sensing using GNSS-R and Chap. 12: Summary and Future Chances. Chapters 1, 2, 3, 4, 7, 10, 11 and 12 were contributed from Prof. Shuanggen Jin, Chaps. 5 and 6 were contributed from Dr. Feiqin Xie, Chaps. 8 and 9 and part of Chap. 11 were contributed from Dr. Estel Cardellach as well as some contributions from Rui Jin and Xuerui Wu.

This book provides the theory, methods, and applications of GNSS Remote Sensing for scientists and users who have basic GNSS background and experiences. Furthermore, it is also useful for the increasing number of next generation multi-GNSS designers, engineers and users community. We would like to thank Assistant Editor's help and Springer-Verlag for their cordial collaboration and help during the process of publishing this book.

Shanghai, People's Republic of China
Barcelona, Spain
Corpus Christi, TX, USA

Shuanggen Jin
Estel Cardellach
Feiqin Xie

Contents

Part I GNSS Theory and Delays

1	Introduction to GNSS	3
1.1	GNSS History	3
1.1.1	GPS.....	3
1.1.2	GLONASS	5
1.1.3	GALILEO	6
1.1.4	Beidou/COMPASS	7
1.1.5	Other Regional Systems	7
1.2	GNSS Systems and Signals	8
1.2.1	GNSS Segments	8
1.2.2	GNSS Signals	10
1.3	GNSS Theory and Errors	11
1.3.1	GNSS Principle	12
1.3.2	GNSS Error Sources	12
1.4	GNSS Observations and Applications	13
1.4.1	GNSS Observation Network	13
1.4.2	GNSS Applications	14
	References	16
2	GNSS Atmospheric and Multipath Delays	17
2.1	Atmospheric Refractivity	17
2.2	GNSS Atmospheric Delays	18
2.2.1	Neutral Atmospheric Delays	18
2.2.2	Empirical Tropospheric Models	19
2.3	GNSS Ionospheric Delay	20
2.3.1	The Ionosphere	20
2.3.2	GNSS Ionospheric Delay	21
2.3.3	Empirical Ionospheric Models	24

2.4	GNSS Multipath Delay	25
2.4.1	Multipath Effects	25
2.4.2	Multipath Variations	27
2.4.3	Surface Reflection Characteristics	29
	References	30

Part II GNSS Atmospheric Sensing and Applications

3	Ground GNSS Atmospheric Sensing	33
3.1	Introduction	33
3.2	Theory and Methods	34
3.2.1	Estimates of GNSS ZTD	34
3.2.2	Mapping Functions	35
3.3	ZTD Estimate and Variations	37
3.3.1	ZTD Estimates from IGS Observations	37
3.3.2	Multi-Scale ZTD Variations	40
3.4	GNSS Precipitable Water Vapor	51
3.4.1	GNSS PWV Estimate	51
3.4.2	Comparison with Independent Observations	52
3.4.3	Mean PWV Characteristics	53
3.4.4	Seasonal PWV Variations	55
3.4.5	Diurnal PWV Variations	57
3.5	3-D Water Vapor Topography	57
3.6	Summary	58
	References	58
4	Ground GNSS Ionosphere Sounding	61
4.1	History	61
4.2	GNSS Ionospheric Sounding	63
4.2.1	DCB Determination	65
4.2.2	TEC Estimate	70
4.3	2-D Ionospheric Mapping	71
4.3.1	Method of 2-D Ionospheric Mapping	71
4.3.2	Applications of 2-D GNSS TEC	74
4.4	3-D GNSS Ionospheric Mapping	79
4.4.1	3-D Ionospheric Topography	79
4.4.2	Validation of GNSS Ionospheric Tomography	81
4.4.3	Assessment of IRI-2001 Using GNSS Tomography	82
4.4.4	Ionospheric Slab Thickness	85
4.4.5	3-D ionospheric Behaviours to Storms	88
	References	90
5	Theory of GNSS Radio Occultation	93
5.1	Introduction	93
5.1.1	Radio Occultation in Planetary Sciences	93
5.1.2	GNSS Radio Occultation in Earth Sciences	94

5.2	Principle of GNSS Radio Occultation.....	98
5.2.1	Atmospheric Refraction	99
5.2.2	Geometric Optics Approximation	100
5.2.3	Spherically Symmetric Atmosphere Assumption	101
5.2.4	Bending Angle and Refractive Index	102
5.3	GNSS Radio Occultation Processing.....	104
5.3.1	Calibrating and Extracting GNSS RO Observables.....	104
5.3.2	Bending Angle Retrieval	110
5.3.3	Ionosphere Retrieval.....	113
5.3.4	Neutral Atmosphere Retrieval	115
	References.....	117
6	Atmospheric Sensing Using GNSS RO	121
6.1	GNSS RO Atmospheric Sounding.....	121
6.1.1	Parameters Retrieval from GNSS RO	121
6.1.2	Dry Atmosphere Retrieval (Density, Pressure and Temperature)	122
6.1.3	Moist Atmosphere Retrieval	123
6.1.4	1D-Var (Variational Method).....	124
6.2	Characteristics of GNSS RO Observations	124
6.2.1	Spatial Resolution (Vertical and Horizontal Resolution)	126
6.2.2	Accuracy and Precision Analysis	126
6.2.3	Measurement Errors	127
6.2.4	Calibration Errors	129
6.2.5	Retrieval Errors	130
6.2.6	Experimental Validation of RO Accuracy and Precision	135
6.3	Dynamic Processes Studies with GNSS RO	136
6.3.1	Tropopause and Stratospheric Waves	137
6.3.2	Tropical Tidal Waves	138
6.3.3	Weather Front	138
6.3.4	Tropical Cyclones (TC)	139
6.3.5	Atmospheric Boundary Layer (ABL)	140
6.4	Weather Prediction Applications	141
6.4.1	GNSS RO Data Assimilation	141
6.4.2	Operational Assimilation of GNSS RO in NWP Models	142
6.5	Climate Applications	143
6.6	Future Application of Radio Occultation	146
6.6.1	Future GNSS and GNSS RO Missions	146
6.6.2	Airborne and Mountain-Top GNSS RO	146
6.6.3	LEO-to-LEO Occultation	149
	References.....	150

7	Ionospheric Sounding Using GNSS-RO	159
7.1	Introduction	159
7.2	Ionospheric Inversion	159
7.2.1	Ionosphere Inversion Based on Doppler	161
7.2.2	Ionosphere Inversion Based on TEC	163
7.2.3	Recursive Inversion of TEC	164
7.2.4	Amplitude Inversion	165
7.3	Error Analysis	166
7.3.1	Measurement Errors	166
7.3.2	Data Processing Errors	167
7.4	Ionospheric Products	167
7.5	GNSS-RO Ionospheric Applications	168
7.5.1	Establishing Ionospheric Models	168
7.5.2	Ionospheric Tomography	168
7.5.3	Monitoring Ionospheric Anomalies	169
7.5.4	Ionospheric Scintillation	170
	References	170

Part III GNSS Reflectometry and Remote Sensing

8	Theory of GNSS Reflectometry	175
8.1	Introduction	175
8.2	Multi-static System: Geometry and Coverage	177
8.3	Specular and Diffuse Scattering	178
8.4	Delay and Doppler	184
8.5	Reflectivity Levels and Polarization Issues	188
8.6	Scattering Theories	192
8.6.1	Kirchhoff or Tangent Plane Approximation (KA)	194
8.6.2	Summary of Other Methods	198
8.6.3	Received GNSS Scattered Fields	199
8.6.4	The Bi-static Radar Equation for GNSS Modulated Signals	201
8.7	Noise and Coherence Issues	203
8.8	Systematic Errors	205
8.9	PARIS Interferometric Technique (PIT)	206
8.10	Observables	208
	References	211
9	Ocean Remote Sensing Using GNSS-R	215
9.1	Altimetry	215
9.1.1	Group Delay Altimetry	221
9.1.2	Atmospheric Corrections	224
9.1.3	GNSS-R Ocean Altimetric Performance	225
9.2	Ocean Surface Roughness	227
9.2.1	Surface Modelling	228
9.2.2	Retrieval Approaches	234
	References	236

10 Hydrology and Vegetation Remote Sensing.....	241
10.1 Introduction	241
10.2 Hydrology GNSS-Reflectometry	242
10.3 Hydrology Sensing from GNSS-R	243
10.3.1 Waveform Correlation	243
10.3.2 Interference Pattern Technique (IPT)	244
10.3.3 Hydrology Sensing from GNSS	245
10.3.4 GNSS-R Scattering Properties	246
10.3.5 GNSS-R Polarization	247
10.4 GNSS-R Forest Biomass Monitoring	248
10.5 Summary	249
References	249
11 Cryospheric Sensing Using GNSS-R	251
11.1 Dry Snow Monitoring	251
11.1.1 Dry Snow Reflection Model: Multiple-Ray Single-Reflection	252
11.1.2 Dry Snow Observable: Lag-Hologram	255
11.2 Wet Snow Monitoring	257
11.2.1 Observations from Space-Borne GNSS-R	257
11.2.2 Observations from Ground GNSS-R	258
11.3 Sounding the Sea Ice Conditions	259
References	259
12 Summary and Future Chances.....	261
12.1 Status of GNSS Remote Sensing	261
12.1.1 Atmospheric Sensing	261
12.1.2 Ocean Sensing	262
12.1.3 Hydrology Sensing	262
12.1.4 Cryosphere Mapping	263
12.2 Future Developments and Chances	263
12.2.1 More GNSS Networks and Constellations	263
12.2.2 Advanced GNSS Receivers	263
12.2.3 New Missions and Systems	265
12.2.4 New and Emerging Applications	266
12.3 Summary	267
References	268
Index.....	271

Acronyms

ABL	Atmospheric Boundary Layer
AGW	Acoustic Gravity Wave
ART	Algebraic Reconstruction Technique
AMSR-E	Advanced Microwave Scanning Radiometer for Earth Observing System
AODC	Attitude and Orbit Determination and Control
BDS	Beidou Navigation System
BOC	Binary Offset Carrier
BPSK	Binary Phase Shift Keying
C/A	Coarse/Acquisition
CAS	Chinese Academy of Sciences
CDMA	Code Division Multiple Access
CHAMP	Challenging Mini-satellite Payload
COADS	Comprehensive Ocean-Atmosphere Data Set
CL	Close-loop
CMONC	Crustal Movement Observation Network of China
CODE	Center for Orbit Determination in Europe
COSMIC	Constellation Observing System for Meteorology, Ionosphere, and Climate
CICERO	Climate Community Initiative for Continuing Earth Radio Occultation
CIT	Computerized Ionospheric Tomography
CYGNSS	CYclon GNSS
DCB	Differential Code Biases
DD	Double Difference
DDM	Delay-Doppler Map
DMC	Disaster Monitoring Constellation
DGPS	Differential GPS
DMC	Disaster Monitoring Constellation
DMSS	Directional Mean Square Slope
DNSS	Defense Navigation Satellite System

DOD	Department of Defense
DORIS	Doppler Orbitography Radio positioning Integrated by Satellite
DOT	Department of Transportation
ECMWF	European Centre for Medium-Range Weather Forecasts
EGNOS	European Geostationary Navigation Overlay Service
ESA	European Space Agency
EST	Equivalent Slab Thickness
EU	European Union
FFT	Fast Fourier Transform
FDMA	Frequency Division Multiple Access
FIO	Fourier Integral Operators
Galileo	Global Navigation Satellite System of EU
GAGAN	GPS Aided Geo Augmented Navigation
GAMIT	GPS analysis software by Massachusetts Institute of Technology
GBAS	Ground-Based Augmentation Systems
GDOP	Geometric Dilution of Precision
GEO	Geostationary Earth Orbit
GFZ	GeoForschungsZentrum Potsdam
GIPSY-OAIS	GNSS-Inferred Positioning System and Orbit Analysis
GLONASS	Global Navigation Satellite System of Russia
GMF	Global Mapping Function
GNSS	Global Navigation Satellite Systems
GO	Geometric Optics
GOLD-RTR	GPS Open-Loop Differential Real-Time Receiver
GPS	Global Positioning System
GPS/MET	GPS/Meteorology
GNSS-R	GNSS-Reflectometry
griPAU	GNSS Reflectometer Instrument for the Passive Advanced Unit
GRACE	Gravity Recovery and Climate Experiment
GTS	Global Telecommunication System
HFI	Hardy Function Interpolation
IAG	International Association of Geodesy
IEEC	Institute for Space Studies of Catalonia
IERS	International Earth Rotation Service
IEM	Integral Equation Method
IGS	International GNSS Service
IGOR	Integrated GPS and Occultation Receiver
IPT	Interference Pattern Technique
IPP	Ionosphere Pierce Point
IRNSS	India's Regional Navigation Satellite Systems
IRI	International Reference Ionospheric
ITRF	IERS Terrestrial Reference Frame
JPL	Jet Propulsion Laboratory
KA	Kirchho Approximations
KPO	KA in Physical Optics Approximation

KGO	Kirchhoff Geometrical Optics
LAAS	Local Area Augmentation System
LC	Linear Combination
LEO	Low Earth Orbit (satellite)
LHCP	Left-Hand Circular Polarization
LOS	Line-of-Sight
LS	Least Squares (adjustment)
MEO	Medium Earth Orbit
MIT	Massachusetts Institute of Technology
MSU	Microwave Sounder Unit
MSAS	Multifunction Satellite Augmentation System
MSS	Mean of the Square Slopes
NASA	National Aeronautics and Space Administration
NCAR	National Center for Atmospheric Research
NMF	Niell Mapping Function
NGS	National Geodetic Survey
NOAA	National Oceanic and Atmospheric Administration
NWP	Numerical Weather Prediction
NOC	National Oceanography Centre
OCX	Operational Control System
PARIS	PAssive Reflectometry Interferometric System
PDF	Probability Density Function
PGGA	Permanent GPS Geodetic Array
PIT	PARIS Interferometric technique
PLL	Phase-Locked Loop
PNT	Positioning, Navigation and Timing
POD	Precise Orbit Determination
PPP	Precise Point Positioning
PWV	Precipitable Water Vapor
PRN	Pseudo-Random Noise
PVT	Position, Velocity and Time
RINEX	Receiver Independent Exchange
QZSS	Quasi-Zenith Satellite System
RFI	Radio Frequency Interference
RMS	Root Mean Square
RT	Radiative Transfer
RTK	Real-Time Kinematic
RO	Radio Occultation
RHCP	Right-Hand Circular Polarization
SA	Selective Availability
SAR	Synthetic Aperture Radar
SAC-C	Satellite de Aplicaciones Cientificas-C
SBAS	Ground- and Space-Based Augmentation Systems
SGR-ReSI	Space GPS Receiver-Remote Sensing Instrument
SHAO	Shanghai Astronomical Observatory

SLM	Single Layer Model
SMEX02	Soil Moisture Experiment 2002
SMIGOL	Soil Moisture Interference-pattern GNSS Observations at L-band
SMOS	Soil Moisture and Ocean Salinity
SMAP	Soil Moisture Active and Passive mission
SNR	Signal-to-Noise Ratio
SOL	Safety-of-Life
SSC	Surrey Space Centre
SSTL	Surrey Satellite Technology Limited
SD	Single Difference
SINEX	Software Independent Exchange (format)
SLM	Single Layer Model
SLR	Satellite Laser Ranging
SNR	Signal-to-Noise Ratio
SPM	Small Perturbation Method
SSA	Small Slope Approximation
SST	Satellite-Satellite Tracking
SSTL	Surrey Satellite Technology Limited
STD	Slant Tropospheric Delay
STEC	Slant Total Electron Content
SWH	Significant Wave Height
TEC	Total Electron Content
TriG	Tri-GNSS (GPS+Galileo+GLONASS)
TOPEX	Topography Experiment
TT&C	Tracking, Telemetry and Command
URSI	International Union of Radio Science
USAF	US Air Force
UT	Universal Time
VLBI	Very Long Baseline Interferometry
VMF	Vienna Mapping Functions
WAAF	Woodward Ambiguity Function
WGS	World Geodetic System
WVR	Water Vapor Radiometry
ZTD	Zenith Tropospheric Delay
ZHD	Zenith Hydrostatic Delay
ZWD	Zenith Wet Delay
Z-V	Zavorotny and Voronovich

Part I

GNSS Theory and Delays

Chapter 1

Introduction to GNSS

The Global Navigation Satellite Systems (GNSS), including the US's Global Positioning System (GPS), Russia's GLONASS, EU's Galileo and China Beidou (also called COMPASS) as well as several regional navigation satellite systems, can be characterized as a highly precise, continuous, all-weather and near-real-time microwave (L-band) technique with signals through the Earth's atmosphere. These characteristics of GNSS imply more and wider applications and potentials (Jin et al. 2010a, b). Each GNSS satellite continuously broadcasts radio signals in two or more frequencies in L-band (1–2 GHz) with wavelength around 20 cm, the direct signals are used for navigation, positioning and timing. The refracted signals from GNSS Radio Occultation satellites together with ground GNSS observations can provide the high-resolution tropospheric water vapor, temperature and pressure, tropopause parameters and ionospheric total electron content (TEC) and electron density profile as well. The GNSS reflected signals from the ocean and land surface could determine the ocean height, wind speed and wind direction of ocean surface, soil moisture, ice and snow thickness. Therefore, the refracted and reflected GPS signals can image the Earth's surface environments as a new, highly precise, continuous, all-weather and near-real-time remote sensing tool, which will play a key role in various atmospheric sounding, ocean remote sensing and land/hydrology mapping. In the following sections, the GNSS history, system, signals, theory and applications are introduced (Fig. 1.1).

1.1 GNSS History

1.1.1 GPS

In the early 1960s, several U.S. governmental organizations were interested in developing satellite systems for position determination, e.g., the Department of Defense (DOD), the National Aeronautics and Space Administration (NASA),

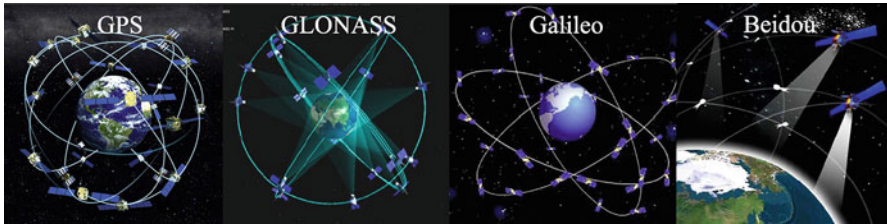


Fig. 1.1 Global Navigation Satellite Systems (GNSS)

and the Department of Transportation (DOT). The optimum system should have global coverage, continuous/all weather operation, the ability to serve high-dynamic platforms, and high accuracy. The first satellite navigation system with a constellation of five satellites, Transit, was first successfully tested in 1960, which was used by the United States Navy. The Transit could provide a navigational fix approximately once per hour (Guier and Weiffenbach 1997). In 1967, the U.S. Navy developed the Timation satellite that proved the ability to place accurate clocks in space. In the 1970s, the ground-based Omega Navigation System with phase comparison of signal transmission from pairs of stations became the first worldwide radio navigation system. In 1973, the Defense Navigation Satellite System (D NSS) was created, which was named Navstar later. With the individual satellites being associated with the name Navstar, a more fully encompassing name was used to identify the constellation of Navstar satellites, Navstar-GPS, shortly named GPS (Rip and Hasik 2002). In 1983, President Ronald Reagan issued a directive making GPS freely available for civilian use. Until the 24th satellite was launched in 1994, GPS has become operational fully.

The system originally broadcast two signals, a C/A code available to civilian uses and a more precise encrypted code reserved for military uses. In 2000 the Selective Availability (SA) – the feature where the signal available for civilian use could be intentionally degraded – was discontinued, and every user on the globe was allowed to receive a non (intentionally) degraded signal. Between 1997 and 2009, 20 satellites of blocks IIR and IIR-M were launched, and constitute now a large portion of the current GPS constellation (20 out of 31 healthy satellites, as for January 2011). The block IIR-M satellites made available to civilian users a civil encoded signal in the L2 band. An additional safety-of-life civilian-use signal (in the L5 band) will be provided with the block IIF generation of GPS satellites, which is being implemented. The first block IIF satellite was launched on 28 May, 2010, and set operative on 27 August, 2010. All GPS satellites broadcast by employing the Code Division Multiple Access (CDMA) technique as channel access method. Nowadays the official GPS space segment is composed of 24 satellites (plus three operational spares) distributed over six orbital planes, separated by 60 right ascension of the ascending node, 55 -inclined, and with an orbital radius of about 26,600 km. Each satellite orbits the Earth exactly twice each sidereal day, repeating the same ground track once a day. Therefore, the same constellation

geometry can be observed every SI (International System of Units) day with about 4 min displacement. The GPS ground-segment is composed by a primary Master Control Station at Schriever Air Force Base (Colorado, US) and ten dedicated ground antennas and monitor stations around the globe.

The GPS has been widely used for positioning, navigation and timing (PNT) globally to all users at all times since 1994. For example, the southern California Permanent GPS Geodetic Array (PGGA) was the first established in early 1990s across the Pacific-North America plate boundary to continuously monitor crustal deformation, providing the first temporal-spatial details of crustal movements before, during and after a major earthquake (Bock et al. 1997). Since GPS is highly precise, continuous, all-weather and real-time with signals that travel through the Earth's atmosphere, additional scientific applications of GPS were being explored by scientists and engineers. Notably, Ware (1992) suggested limb sounding the Earth's atmosphere and ionosphere using GPS atmospheric refracted delay signals. Following, the GPS/Meteorology Mission (GPS/MET) using the GPS radio occultation technique was launched and successfully provided accurate, all weather, global refractive index, pressure, temperature and the ionospheric total electron content (TEC) measurements and electron density profiles, which have been widely applied in the atmosphere and ionosphere (Rocken 1997; Hajj and Romans 1998).

Over the last decade, the U.S. has implemented several improvements to the GPS service, including new technology and new signals for civil use and increased accuracy and integrity for all users, all while maintaining compatibility with existing GPS equipment. GPS modernization has now become an ongoing initiative to upgrade the Global Positioning System with new capabilities to meet growing military, civil, and commercial needs. The program is being implemented through a series of satellite acquisitions, including GPS Block III and the Next Generation Operational Control System (OCX). The U.S. Government continues to improve the GPS space and ground segments to increase performance and accuracy. With the development of the new global navigation satellite systems (GNSS) constellations, including the U.S.'s GPS, Russia's GLONASS, and the coming European Union's GALILEO system and China's Beidou/COMPASS system as well as a number of Space Based Augmentation Systems, such as Japan's Quasi-Zenith Satellite System (QZSS) and India's Regional Navigation Satellite Systems (IRNSS), more applications and opportunities will be exploited and realized for multi-frequency and multi-system GNSS.

1.1.2 GLONASS

The Global Navigation Satellite System (GLONASS) by former Soviet Union was fully operational since 1995 but suspended and partially operated after collapse of USSR and now has got the latest up-gradation and is fully operational since 2010 by Russia. The GLONASS (abbreviation of GLObal'naya NAvigatsionnaya

Sputnikovaya Sistema, GLObal NAVigation Satellite System in English) is the Russian-owned constellation of positioning satellites (GLONASS-ICD, 2008). It reached full operational capability in 1995, after the efforts made by the collapsed Soviet Union were continued by the Russian Federation. Unfortunately, due to the inability to maintain the system, the constellation slowly reduced, reaching a minimum of eight operational satellites in 2002. The turning of the century saw a renewed interest in restoring the full capability by the Russian government (Dvorkin and Karutin 2006), and the system is currently (2011) formed by 20 operational satellites. The GLONASS space segment is composed of 24 satellites distributed over three orbital planes (separated by 120 right ascension of the ascending node) with radius equal to 25,500 km and 65°-inclined. GLONASS satellites broadcast signals in L1 and L2 bands, using Frequency Division Multiple Access (FDMA) technique as channel access method technique. The GLONASS ground control center in Moscow and the telemetry and tracking stations are all within the Russian Federation borders.

1.1.3 GALILEO

The Galileo navigation system, named after the Italian astronomer and physicist Galileo Galilei, was started following political reasoning that wanted European countries to be independent, in the context of satellite navigation, from the US's GPS and Russian GLONASS. GPS and GLONASS can theoretically be turned on in any moment by their respective nations, making European countries particularly vulnerable. Since its dawn, the Galileo system was intended to provide a more precise navigation service than the one provided by either GPS or GLONASS (Mendizabal et al. 2008). In March 2002, The European Union (EU) and European Space Agency (ESA) agreed to develop the Galileo positioning system, which is expected to be fully functional by 2020. Galileo is currently under development to be completed within the decade 2011–2020, which is expected to be compatible with the modernized GPS system. The receivers will be able to combine the signals from both Galileo and GPS satellites to increase accuracy significantly. Compared to US's GPS and Russian GLONASS, Galileo is designed specifically for civilian and commercial purposes. Currently, a number of countries participated in the Galileo project, e.g., China in 2003, Israel in 2004, and next 1 or 2 years the Ukraine, India, Morocco, and Saudi Arabia as well as South Korea. In 2007, the 27 members of the European Union collectively agreed to move forward with the project, with plans for bases in Germany and Italy [EU-Galileo].

Two Galileo System Test Bed satellites (Giove A and B), dedicated to take the first step of the In-Orbit Validation phase towards full deployment of Galileo, are fully operational and broadcasting on L1, E5 and E6 bands. The full constellation will consist of 30 satellites distributed over three orbital planes (56 inclinations), at an altitude of approximately 29,600 km. Each satellite will revolve around the Earth at a rate of one revolution every 14 h. The signals will be broadcast in the L1,

E5 and E6 bands, supporting 10 different navigation signals offering Open (OS), Safety-Of-Life (SOL), Commercial and Public Regulated Services. At the time of publication, the following milestones had been accomplished:

- 28 December 2005, GIOVE-A, the first GIOVE test satellite, was launched.
- 27 April 2008, GIOVE-B, with a more advanced payload than GIOVE-A, was successfully launched.
- 21 October 2011, the first two of four operational satellites were launched to validate the system.
- 12 October 2012, the other two satellites were launched.

1.1.4 Beidou/COMPASS

China is also developing its own GNSS named as Beidou Navigation System (BDS) by the year 2020 to join the GNSS community of technology and to get the market share too. The BDS is the name of the future Chinese independent GNSS, formed by a constellation of 35 satellites, of which five on Geostationary Earth Orbit (GEO) and 30 on Medium Earth Orbit (MEO). The broadcast signals will be in the E1, E2, E5 and E6 bands, possibly overlapping with Galileo frequencies. The signals will be BPSK-modulated (Bi-nary Phase-Shift Keying), and will be broadcast using CDMA techniques. Similar to Galileo and GPS, different services will be offered: a standard signal for civilian users and a more precise (encrypted) signal for reserved uses. A first experimental satellite, named COMPASS M-1, was launched in 2007 and is currently (2011) operational. Its orbit has a low eccentricity, an altitude of approximately 21.150 km and is 55° inclined. This satellite transmits two signals (I and Q, in quadrature) in three bands: B1, B2, and B3. This launch was followed by the orbit placement of three geostationary satellites, one in 2009 and two in 2010.

1.1.5 Other Regional Systems

To compete and augment the existing space-based navigation systems, several regional systems are being developed by various countries, such as the QZSS by Japan and the GAGAN/IRNSS by India.

- ***IRNSS***

The planned Indian Regional Navigational Satellite System, possibly consisting of a constellation of seven satellites (of which three geostationary) and a support ground segment.

- ***QZSS***

Quasi-Zenith Satellite System, the Japanese regional system of three satellites in Highly Elliptical Orbit, that will mainly cover the area between Japan and Australia. One satellite is in operation at the time of this publication.

In addition, there exist several Ground- and Space-Based Augmentation Systems (GBASSs and SBASSs), such as the European Geostationary Navigation Overlay Service (EGNOS), the GPS Aided Geo Augmented Navigation (GAGAN), the Joint Precision Approach and Landing System (JPALS), the Local Area Augmentation System (LAAS), the Wide Area Augmentation System (WAAS) and the Multi-functional Satellite Augmentation System (MSAS). The working principle of these systems is to make use of ground stations whose positions are precisely known. The stations gather measurements from GNSS satellites and/or other sensors to create a regional correction map that is sent back to orbiting satellites and then broadcast to the users. This enhances the quality of the computed position by mitigating the impact of certain errors (mostly atmospheric). Not less importantly, these systems have also been designed to provide and enhance integrity services.

The gurus of navigation community predict that when GPS, GLONASS, GALILEO, and Beidou/COMPASS will be fully operational and interoperable, four times more satellites as compared to present may be available for navigation, positioning, and timing, providing more types of signals broadcasted on more frequencies. This will surely result in enhancing the quality of the services and increasing the number of potential users and applications. Furthermore, a number of space-based augmentation systems and regional Navigation satellite systems will add more satellites and signals to multiple systems of satellites and, as a result, improve positioning performance in terms of accuracy, availability, reliability and integrity.

Global Positioning System (GPS) has become a clichéd terminology due to its applications in navigators and cellular technology. The modern cell phones and vehicles are equipped with GPS chipsets but the applications are far beyond these two basic concepts and have wide applications in many terrestrial, air, marine and space domains. At present, the civil applications have out marked the military applications. The wide range of applications and the promises of the prospective global navigation systems have paved the way for the development of strong market for GNSS receivers and this market is growing at an enormous rate and the prevailing market trends calls for enthusiastic contributors to participate in this development phase and reap the fruits at the end of this endeavor.

1.2 GNSS Systems and Signals

1.2.1 GNSS Segments

GNSS is consisting of a space segment having a constellation of satellites in Medium Earth Orbit (MEO) at the height of nearly 20,000 km and above, *control segment* having monitoring and control stations to monitor/control/update the constellation of satellites and the *user segment*; consisting of receivers to give position, velocity and time (PVT) of the static and mobile user all over the globe at all time using at least four satellites of the constellation in view.

The Global Navigation Satellite System (GNSS) has a well defined structure, initially designed by US and USSR and then is being followed by the systems like Galileo and Beidou. The basic segments like space, control, user and augmentation are discussed in next lines. The reference architecture is about the GPS as it is only the fully operational at this moment with maximum information too. The signal structure is also discussed briefly to understand the basic principle of navigation and finding the position and time information.

1.2.1.1 Space Segment

It consists of constellation of satellites equipped with navigational payload, precise atomic clocks, navigational antennas and other subsystems like thermal, propulsion, attitude and orbit determination and control (AODC), Tracking, Telemetry and Command (TT&C) and power subsystems. The constellation is designed considering the availability of at least four satellites at all times across the globe. The satellites are arranged in different planes to provide the best geometric dilution of precision (GDOP), a parameter of satellite geometry. Medium Earth Orbits (MEO), 20,000–30,000 km, are chosen for the constellation of satellites due to considerable launch cost and global coverage.

1.2.1.2 Control Segment

It consists of master control centre along with some monitoring stations and telemetry telecommand antennas spread all over the globe to perform the following main tasks.

- Measures the position of each satellite and controls its attitude and orbit
- Monitors the signals broadcast by satellites
- Sends information to satellites for a proper clock alignment
- Sends information to satellites for the navigation message

1.2.1.3 User Segment

User segment consists of mainly the GNSS receivers to process the signals received from the satellites and estimates the user's position. The functionalities common to any kind of receiver can be summarized as identification of the satellites in view, estimation of the user-satellite distance and Triangulation.

1.2.1.4 Augmentation Segment

It includes additional equipments like local elements, pseudolites or Geo-Satellites allowing new services or improved performance. Differential GPS (DGPS), Local

Table 1.1 GNSS signals

System	Carrier	Modulation	Multiple Address
GPS	L1/L2/L5	BPSK/BOC/MBOC/QPSK	CDMA
	L1C/L2C		
Galileo	E1/E5/E6	BOCc/CBOC	CDMA
	E5a/E5b	Alt BOC BPSK	
GLONASS	L1/L2/L3	BPSK/QPSK	FDMA/CDMA
Beidou	B1/B2/B3	MBOC/BOC	CDMA
		Alt BOC	
		QPSK	

area GPS (LGPS), Wide Area GPS (WGPS), WAAS (Wide Area Augmentation System), GDGPS (Global Differential GPS) by NASA, MSAS (Multifunction Satellite Augmentation System) by Japan and EGNOS (European Global Navigation Overlay System) by European Union are the few examples.

1.2.2 GNSS Signals

GNSS signals are summarized in Table 1.1 (Hofmann-Wellenhof et al. 2008). For example, GPS satellites continuously broadcast right-hand circularly polarized signals with both the navigation message and ranging codes modulated on two L-band microwave carrier frequencies, i.e., the L1 ($f_1 = 1.57542$ GHz, $\lambda_1 \approx 19.0$ cm) and L2 ($f_2 = 1.2276$ GHz, $\lambda_2 \approx 24.4$ cm). Starting from 2006, as part of GPS modernization effort, two new civilian-use signals L2C (L2 frequency, C denoting civilian) and L5 ($f_{L5} = 1.17645$ GHz, $\lambda_{L5} \approx 25.5$ cm) were broadcasting on the new generation GPS satellites. Also another civilian-use frequency L1C is down the road in the near future.

The navigation message includes the *ephemeris* data, used to calculate the position of the individual GPS satellite in orbit at the time of signal transmission, and the *almanac* data with the information about the time and status of the entire satellite constellation. On the other hand, the ranging code enables the user's receiver to determine the transit (or propagation) time of the signal and thereby determine the satellite-to-user range. The satellite network uses a CDMA (code division multiple access) spread-spectrum technique where the low-bit-rate message data is encoded with a high-rate “pseudo-random noise” (PRN) sequence that is unique for each GPS satellite. The PRN is a binary signal with random noise-like properties, which is generated by mathematical algorithm or “code”, and consists of repeated pattern of 1’s and 0’s.

Both L1 and L2 signals are modulated by a pseudo-random precision ranging code (P code). The L1 carrier signal is also modulated with coarse/acquisition (C/A) ranging code for civilian use. The P code can be encrypted as a so-called P(Y) code

which is only available to military equipment with a proper decryption key. The L1 and L2 signals received from each GPS satellite can be expressed as follows (Spilker 1980):

$$\begin{aligned} S_{L1}(t) &= \sqrt{2C_{C/A}} D(t) X(t) \sin(2\pi f_1 t + \theta_1) \\ &\quad + \sqrt{2C_{P1}} D(t) P(t) \cos(2\pi f_1 t + \theta_1) \end{aligned} \quad (1.1)$$

$$S_{L2}(t) = \sqrt{2C_{P2}} D(t) P(t) \cos(2\pi f_2 t + \theta_2) \quad (1.2)$$

where $C_{C/A}$ and C_{P1} are the received powers of the in-phase and quadrature components of the L1 signal, respectively, C_{P2} is the received power of L2, $D(t)$ is an amplitude modulation for L1 and L2 containing navigation data, $X(t)$ is a pseudorandom sequence of ± 1 , known as clear acquisition or C/A code-modulating the in-phase component of L1 at a rate of 1.023 MHz, and $P(t)$ is a pseudorandom sequence of ± 1 , known as P-code-modulating the quadrature component of L1 and L2 at a rate of 10.23 MHz.

The C/A-Code and the P-Code are examples of PRN codes. Each satellite transmits a unique C/A-Code and P-Code sequence (on the same L1 and L2 frequencies), and hence a satellite may be identified according to its “PRN number”, e.g. PRN2 or PRN14 are particular GPS satellites. The CDMA technique allows the receiver to recognize multiple satellites on the same frequency with different PRNs. A GPS receiver will detect amplitude, pseudo-range and phase measurements for each C/A, L1 P-code (P1) and L2 P-code (P2) signals. The C/A and P1 contained identical information, however, the C/A is preferred over P1 due to its stronger power and not being encrypted. Note that the pseudo-range is an absolute measurement of differential group delay between time of transmission and reception. It is the sum of the actual range between the transmitter and the receiver, atmospheric and ionospheric delays and transmitter and receiver clocks offsets. Note that the early GPS included a feature called Selective Availability (SA) that adds intentional, time varying errors of up to 100 m (328 ft) to the publicly available navigation signals. This was intended to deny an unauthorized use of GPS signals. The SA service was eventually terminated in year 2000.

1.3 GNSS Theory and Errors

Navigation, positioning and timing are the main outputs of any global navigation satellite system and it is achieved by the signals transmitted by the constellation of satellites. The constellation design and the choice of frequency, modulation and coding make this technology a superb master piece for applications beyond imagination. This section discusses the principle, network and applications of GNSS. The main sources of errors in getting the navigation solution are also discussed.

1.3.1 *GNSS Principle*

The basic principle to estimate PVT is the triangulation. At least four satellites are needed to compute the four unknowns, the three position coordinates and one clock error. The user segment performs two basic measurements of the GNSS signals. It compares the code that is received with a locally generated copy in order to compute the transmission delay between the satellite and the receiver. This measurement is called Pseudorange. Pseudorange use four or more satellites to determine the position of the user after the position of the GPS satellites has been obtained using the ephemerides from the navigation message. The second and more precise method is to obtain the difference in phase between the received carrier signal and a receiver-generated signal at the same frequency. This measurement is known as the carrier phase observable and it can reach millimeter precision, but it lacks the accuracy of the pseudorange because the phase when the tracking is started can only be known with an ambiguity of an unknown number of times the carrier wavelength.

1.3.2 *GNSS Error Sources*

GNSS User Equivalent Errors (USER) is defined as the errors in PVT computation due to three segments of GNSS architecture. In space segment, the source of error can be satellite clock stability, satellite perturbations or selective availability (turned off in May 2001). The control segment causes the errors like ephemeris prediction and the user segment contributes the major part due to Ionospheric delay, Tropospheric delay, receiver noise, multi-path, indoor positioning or due to urban canyons.

- Satellite and receiver clock errors
- Satellite orbit errors
- Atmospheric effects (ionosphere, troposphere)
- Multipath: signal reflected from surfaces near the receiver
- Antenna phase center
- Solar radiation pressure
- Satellite Geometry
- Relativistic Effects
- Receiver noise
- Signal Obstruction

1.4 GNSS Observations and Applications

The applications of GNSS technology are dependent on human imaginations, which are limitless. GNSS only provides the real time position, velocity and time (PVT) but the gurus of this gigantic field envisage the next millennium as the time for Positioning and Timing. The paradigm shift from the military usage to the civil applications has changed the whole scenario. At present, each new car has the built in Navigator to guide the commuter to his destination with digital maps. The talking pedestrian navigator can guide the virtually impaired people to their destination. The hikers and the mountaineers can never be lost due to their personal navigators. New cell phones are equipped with the GPS receiver and the integration between communication and navigation will produce miracles in the near future. The location-based services will enhance the mobile market with the choice of real time gamming and emergency call identification facilities. The aviation and aerospace industry is using GNSS for guidance and control. The spacecrafts get their orbit and attitude determined by the virtue of GNSS. The UAV/UMV are controlled and guided by the same technology and the guided missiles get their way by the application of this advancement. The maritime sector was the first user of GNSS. At present, GNSS is contributing in Navigation safety, Collision prevention, Vessel traceability to automate maneuvers in narrow spaces, Automatic Identification Systems (AIS), and vessel traffic management system and Search & Rescue (SAR) services. In addition to that, it has wide applications in the fields of Oceanography and Marine Engineering. In Public Transport system, GNSS is providing great features for electronic toll system, automated trains and subways, fleet management, route guidance, passenger information system, traffic management and security services like trackers. GNSS is playing a pivotal role in the fields of environment monitoring and control, agriculture and fishing, civil engineering, disaster and relief operations, Telecommunications and energy sectors. The Time information obtained by the GNSS is playing a great role in electronic banking, finance and insurance. The universal time is also maintained by the GNSS signal in space.

1.4.1 GNSS Observation Network

The International GNSS (Global Navigation Satellite Systems) Service (IGS) was formally established in 1993 by the International Association of Geodesy (IAG), and began routine operations on 1 January 1994 (Beutler et al. 1999). The IGS coordinates a worldwide network of permanent tracking stations with about 350 GPS stations (Fig. 1.2), which are financed and operated by numerous organizations, providing the high quality data products for use in GNSS related Earth science research, navigation application and educational outreach.

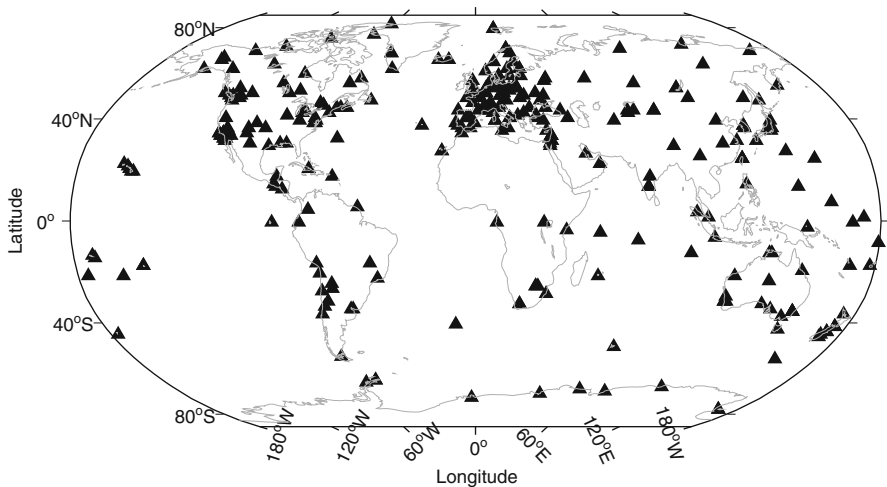


Fig. 1.2 Global IGS GNSS stations

1.4.2 GNSS Applications

1.4.2.1 Positioning, Navigation and Timing

Since GNSS has a number of advantages, such as highly precision, continuity, all-weather and near-real-time observation, it has wider applications in positioning, navigation and timing, including

- Positioning, navigation and timing
- Precise orbit determination
- Terrestrial reference frame
- Plate motion and crustal deformation
- Earthquake, volcano and geodynamics
- Glacial isostatic adjustment
- Earth rotation and variations
- Intelligent transport systems
- Precision agriculture
- Location-based services
- Electricity telecommunications
-

1.4.2.2 GNSS Remote Sensing

Due to the atmospheric refraction, GNSS signals propagate through the Earth atmosphere along a slightly curved path and with slightly retarded speeds (Fig. 1.3a).

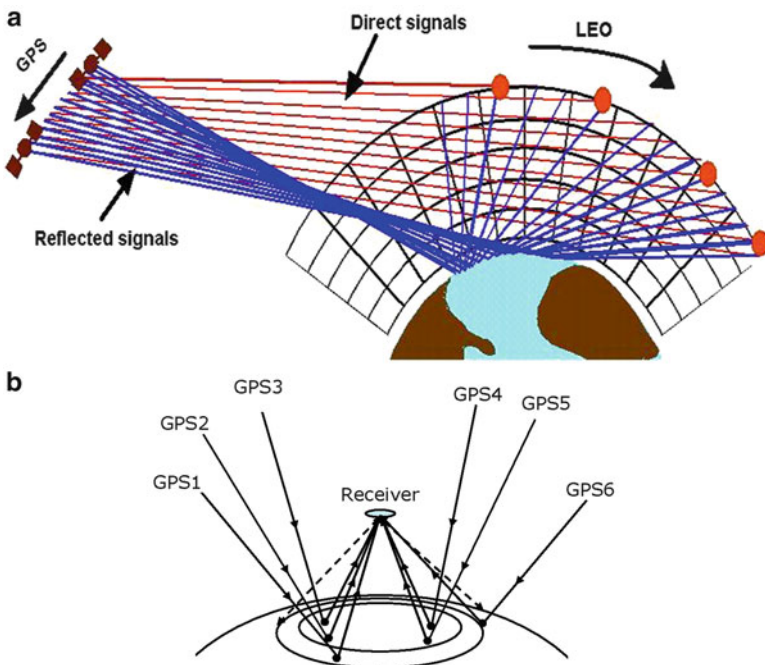


Fig. 1.3 GNSS refracted and reflected signals and geometry (Yunck 2003)

For a long time, the delay of GNSS signals in the troposphere and ionosphere was considered as a nuisance, an error source, and now it has been used to determine the useful atmospheric and ionospheric parameters. The ground GNSS observations together with GNSS Radio Occultation (RO) can provide the tropospheric water vapor, pressure, temperature, tropopause parameters, ionospheric total electron content (TEC) and electron density profiles, which were consistent with traditional instruments observations at comparable accuracies (e.g. Jin et al. 2006, 2007a; Schmidt et al. 2010).

In addition, GNSS satellites are constantly broadcasting radio signals to the Earth. However, part of the signals is reflected back from the rough Earth's surface. The delay of the GNSS reflected signal with respect to the rough surface could provide information on the differential paths between direct and reflected signals (Fig. 1.3b). Together with information on the receiver antenna position and the medium, the delay measurements associated with the properties of the reflecting surface can be used to produce the surface roughness parameters and to determine surface characteristics. Therefore, the GNSS-Reflectometry (GNSS-R) from the Earth's surface could remotely sense the land, hydrology, ocean, vegetation, snow and cryosphere.

References

- Beutler G, Rothacher M, Schaer S, Springer TA, Kouba J, Neilan RE (1999) The International GPS service (IGS): an interdisciplinary service in support of earth sciences. *Adv Space Res* 23:631–653. doi:[10.1016/S0273-1177\(99\)00160-X](https://doi.org/10.1016/S0273-1177(99)00160-X)
- Bock Y, Wdowinski S, Fang P et al (1997) Southern California Permanent GPS Geodetic Array: Continuous measurements of regional crustal deformation between the 1992 Landers and 1994 Northridge earthquakes. *J Geophys Res* 102(B8):18013–18033. doi:[10.1029/97JB01379](https://doi.org/10.1029/97JB01379)
- Dvorkin V, Karutin S (2006) GLONASS: current status and perspectives, The 3rd ALLAST open conference, Hannover
- Guier WH, Weiffenbach GC (1997) Genesis of satellite navigation. *John Hopkins APL Tech Digest* 19(1):178–181
- Hajj GA, Romans LJ (1998) Ionospheric electron density profiles obtained with the Global Positioning System: results from the GPS/MET experiment. *Radio Sci* 33(1):175–190
- Hofmann-Wellenhof B, Lichtenegger H, Wasle E (2008) GNSS - global navigation satellite systems: GPS, GLONASS, Galileo, and more. Springer, Wien/New York
- Jin SG, Park J, Wang J, Choi B, Park P (2006) Electron density profiles derived from ground-based GPS observations. *J Navig* 59(3):395–401. doi:[10.1017/S0373463306003821](https://doi.org/10.1017/S0373463306003821)
- Jin SG, Park J, Cho J, Park P (2007) Seasonal variability of GPS-derived Zenith Tropospheric Delay (1994–2006) and climate implications. *J Geophys Res* 112:D09110. doi:[10.1029/2006JD007772](https://doi.org/10.1029/2006JD007772)
- Jin SG, Luo OF, Ren C (2010a) Effects of physical correlations on long-distance GPS positioning and zenith tropospheric delay estimates. *Adv Space Res* 46(2):190–195. doi:[10.1016/j.asr.2010.01.017](https://doi.org/10.1016/j.asr.2010.01.017)
- Jin SG, Zhu WY, Afraimovich E (2010b) Co-seismic ionospheric and deformation signals on the 2008 magnitude 8.0 Wenchuan Earthquake from GPS observations. *Int J Remote Sens* 31(13):3535–3543. doi:[10.1080/01431161003727739](https://doi.org/10.1080/01431161003727739)
- Mendizabal J, Lagunilla JM, Perez RB (2008) GPS and Galileo: Dual RF front-end receiver and design, fabrication, & test. McGraw-Hill, New York, pp 208. ISBN 9780071598699
- Rip MR, Hasik JM (2002) The precision revolution: GPS and the future of aerial warfare. Naval Institute Press, Annapolis, P 65. ISBN 1-55750-973-5
- Rocken C (1997) Analysis and validation of GPS/MET data in the neutral atmosphere. *J Geophys Res* 102:29849–29866
- Schmidt T, Wickert J, Haser A (2010) Variability of the upper troposphere and lower stratosphere observed with GPS radio occultation bending angles and temperatures. *Adv Space Res* 46:150–161. doi:[10.1016/j.asr.2010.01.021](https://doi.org/10.1016/j.asr.2010.01.021)
- Spilker JJ (1980) GPS signal structure and performance characteristics. In: Janiczek PM (ed) Global Positioning System. Institute of Navigation, Washington, DC, pp 29–54
- Ware R (1992) GPS sounding of the earth atmosphere. *GPS World* 3:56–57
- Yunck TP (2003) The promise of spaceborne GPS for Earth remote sensing. Presentation at the international workshop on GPS meteorology, Tsukuba, Japan, 14–16 Jan 2003

Chapter 2

GNSS Atmospheric and Multipath Delays

2.1 Atmospheric Refractivity

The Earth's atmosphere is a kind of inhomogeneous medium. With increase of height, atmospheric mass decreases. When the electromagnetic wave propagates through the atmosphere, the deviation from a straight line occurs due to the variation of the air mass or density, which is called the atmospheric refraction. The refractive index n of a substance can be expressed as,

$$n = \frac{c}{v} \quad (2.1)$$

where c and v are the speeds of the electromagnetic waves propagating in a vacuum and in some substance, respectively. The atmospheric refractivity N is defined as,

$$N = 10^6 (n - 1) \quad (2.2)$$

The atmospheric refractivity can be further described as a function of meteorological parameters, including both hydrostatic and non-hydrostatic (dry and wet) components (Hopfield 1969) with the empirical formulas (Smith and Weintraub 1953; Hartmann and Leitinger 1984),

$$N = N_d + N_w \quad (2.3)$$

$$N_d = C_1 \frac{p}{T} \quad (2.4)$$

$$N_w = C_2 \frac{e}{T} + C_3 \frac{e}{T^2} \quad (2.5)$$

where N_d and N_w are the dry and wet component refractivity, respectively. p is the pressure of the dry gas of the atmosphere in hPa (Hectopascal), e is partial

pressure of the water vapor in hPa, T is absolute temperature in Kelvin (K), C_1 , C_2 , C_3 are empirical constants as 77.624 K/hPa, -12.92 K/hPa and $371,900$ K 2 /hPa, respectively.

2.2 GNSS Atmospheric Delays

Due to the atmospheric refraction, GNSS signals propagating through the Earth's atmosphere are slightly lengthened with retarded speeds (Fig. 2.1). The delays of GNSS signals are called the neutral atmospheric delay in the troposphere and ionospheric delay in the ionosphere. For a long time, the delays of GNSS signals in the troposphere and ionosphere were considered as a nuisance and error source, and nowadays these delays could be extracted and transformed into the useful atmospheric parameters, including tropospheric water vapor, temperature and pressure, and ionospheric total electron content (TEC) and electron density.

2.2.1 Neutral Atmospheric Delays

The atmosphere of the Earth can be divided into two major parts, i.e., ionosphere and neutral atmosphere. The ionosphere is the upper atmosphere of the Earth ionized by solar radiation with altitude from about 60 km to over 2,000 km. The neutral atmosphere, in which the atmospheric components are electrically neutral,

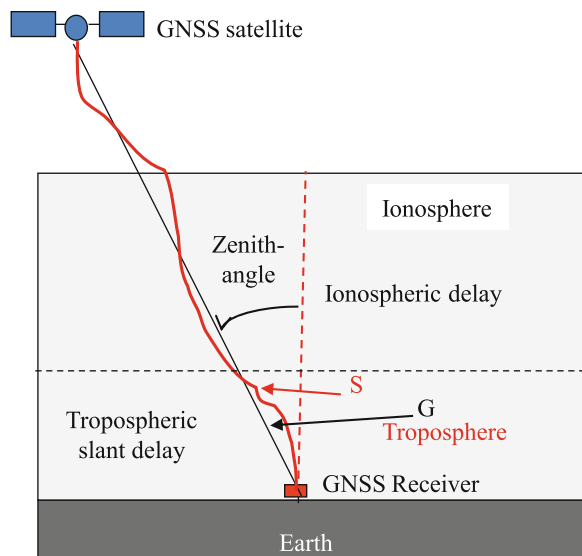


Fig. 2.1 Optic and geometric GNSS Signals

is the lower atmosphere below the ionosphere ranging from the surface to about 60 km, including the troposphere and stratosphere. The GNSS signals will be refracted when going through the neutral atmosphere, with the speed change and signal curve. The effects are called GNSS neutral atmospheric delay. Because the neutral atmospheric delay occurs mainly in the troposphere, the tropospheric delay is usually used instead of neutral atmospheric delay for the GNSS signal effects of the atmosphere below the ionosphere.

2.2.2 Empirical Tropospheric Models

Several tropospheric models have been developed to compute the atmospheric refractivity and tropospheric delay, such as Hopfield (1969) and Saastamoinen (1972, 1973) models. While surface meteorological data should be taken into account for tropospheric models.

2.2.2.1 Modified Saastamoinen Model

The modified Saastamoinen Model (Saastamoinen 1975) can be expressed as following to calculate tropospheric path delay,

$$\Delta L_{trop} = \frac{0.002277}{\cos z} W(\varphi, h_S) \left[P_S + \left(\frac{1,255}{T_S} + 0.05 \right) e_S - B \tan^2 z \right] + \Delta R \quad (2.6)$$

where ΔL_{trop} is tropospheric path delay in meters, z is the zenith angle of the satellite, T_S , P_S , and e_S are the surface temperature in Kelvin, the surface atmospheric pressure in mbar, and the partial pressure of water vapor in mbar at the station, respectively, and $W(\varphi, h_S) = 1 + 0.0026 \cos(2\varphi) + 0.00028h_S$, where h_S is the station height above sea level in km and φ is the local latitude of the station. B and ΔR are the correction terms.

2.2.2.2 Modified Hopfield Model

The modified Hopfield Model (Hopfield 1969, 1971) can be expressed as following to calculate tropospheric path delay,

$$\Delta L_{trop} = \Delta L_W + \Delta L_W \quad (2.7)$$

$$\text{and } \Delta L_i = 10^{-6} N_i \sum_{k=1}^9 \frac{f_{k,i}}{k} r_i^i, \quad (i = d, w) \quad (2.8)$$

where subscript i denotes the dry and wet components of the tropospheric path delay, N_d and N_w are the refractivity of dry and wet components of the tropospheric delay, respectively, which can be calculated from Eqs. (2.4) to (2.5), and $r_i = \sqrt{(R_E + h_i)^2 - R_E^2 \sin^2 z} - R_E \cos z$, $f_{1,i} = 1$, $f_{2,i} = 4a_i$, $f_{3,i} = 6a_i^2 + 4b_i$, $f_{4,i} = 4a_i(a_i^2 + 3b_i)$, $f_{5,i} = a_i^4 + 12a_i^2b_i + 6b_i^2$, $f_{6,i} = 4a_i b_i (a_i^2 + 3b_i)$, $f_{7,i} = b_i^2 (6a_i^2 + 4b_i)$, $f_{8,i} = 4a_i b_i^3$, $f_{9,i} = b_i^4$, where R_E is the Earth's radius, and $a_i = \frac{\cos z}{h_i}$, $b_i = \frac{\sin^2 z}{2h_i R_E}$, $h_d = 40,136 + 148.72(T_S - 273.16)$ (m), and $h_w = 11,000$ (m).

2.3 GNSS Ionospheric Delay

2.3.1 The Ionosphere

The ionospheric altitude is from 60 km to over 1,000 km (Fig. 2.2). Usually, the ionosphere is an extension of the thermosphere. Although the ionosphere represents less than 0.1 % of the total mass of Earth's atmosphere, but it has a great effect on the global electric circuit, Earth's magnetic field and electromagnetic wave propagation, which go through the Earth ionosphere due to its partially ionized gas (Kelley 2009).

Partial ionization is the most important property of Earth's ionosphere and its excitation sources mainly include the solar ultraviolet radiation with a wavelength shorter than 102.7 nm, solar X-rays, solar cosmic rays, energetic particles and

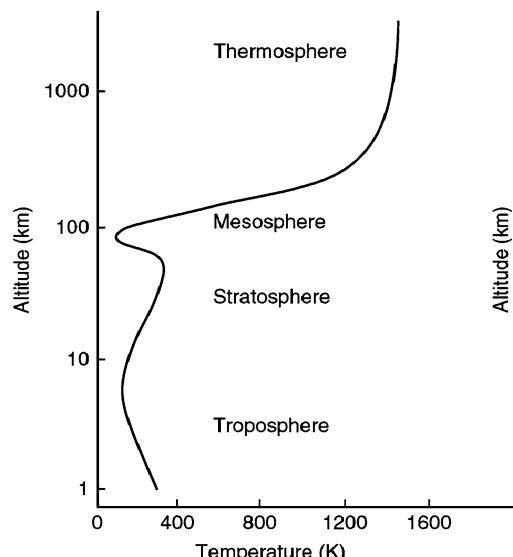
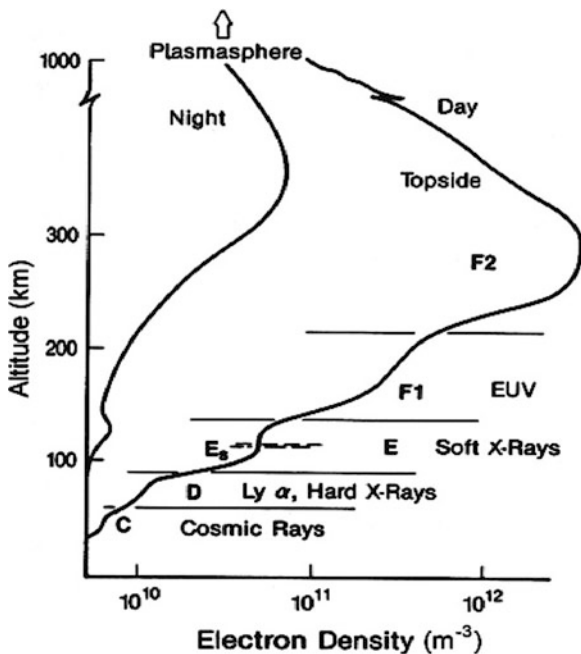


Fig. 2.2 Profile of atmospheric temperature (Kelley 2009)

Fig. 2.3 Ionospheric structures on a summer day and night in the middle latitude and the main ionization regions (Pulinets and Boyarchuk 2004)



so on. On account of the physical characteristics and chemical processes responsible for the ionosphere formation varying from the altitudes, generally, the ionosphere is divided into four different layers, i.e., D, E, F1 and F2 from the bottom to the top of the ionosphere. Figure 2.2 shows the typical midlatitude profile of neutral atmospheric temperature (Kelley 2009). Obviously, temperature of Earth's ionosphere is changing with the altitude increasing. The vertical structure and electron density of each ionospheric layer are shown in Fig. 2.3 (Pulinets and Boyarchuk 2004).

2.3.2 GNSS Ionospheric Delay

The ionosphere is a complex and changing system. As an important component of Earth space environment, the ionosphere has significant effect\ on radio science and human's space exploration and activities. With the booming development of modern communication techniques, computer science, space science, and so on, the ionosphere influence on human's life has been greatly growing since the 1950s, particularly the existence of Global Navigation Satellite Systems (GNSS). The ionospheric delay is one of the important error sources in GNSS navigation, positioning and timing. In contrast, the ionospheric delays can be extracted from dual-frequency GNSS observations, which have a wide application in space weather and space physics. As we known, Earth's ionosphere is a dispersive medium. When

GNSS electromagnetic wave signal goes through the ionosphere, the phase advance and code delay will occur, and the travel path will be changed slightly. Currently the ionospheric delay is one of main error sources in GNSS measurement, which should be considered carefully for higher accuracy GNSS applications. Here the theory and estimate of ground-based GNSS ionospheric delay are introduced.

Firstly, the refractive index for electromagnetic wave propagation in Earth's ionosphere is introduced (e.g., Bassiri and Hajj 1993). Appleton equation is shown as follow.

$$n_P^2 = 1 - \frac{X}{1 - iZ - \frac{Y_T^2}{2(1-X-iZ)} \pm \left[\frac{Y_T^4}{4(1-X-iZ)} + Y_L^2 \right]} \quad (2.9)$$

where n_P is complex phase refractive index, $i = \sqrt{-1}$, $X = \frac{\omega_0^2}{\omega^2}$, $Y = \frac{\omega_H}{\omega}$, $Z = \frac{v}{\omega}$, $\omega = 2\pi f$, $\omega_0 = 2\pi f_0 = \sqrt{\frac{Ne^2}{\epsilon_0 m}}$, and $\omega_H = 2\pi f_H = \frac{B_0|e|}{m}$, where v stands for electron collision frequency, ω is radial frequency, f is wave frequency, ω_0 is electron plasma frequency, ω_H is electron gyro frequency, ϵ_0 is permittivity of free space, B_0 is ambient magnetic field strength, e is electron charge, m is electron mass, and N is electron density. When we assume the damping term $Z = 0$, Eq. (2.9) can be written as

$$n_P^2 = 1 - \frac{X(1-X)}{1 - X - \frac{1}{2}Y^2\sin^2\theta \pm \left(\left(\frac{1}{2}Y^2\sin^2\theta \right)^2 + (1-X)^2Y^2\cos^2\theta \right)^{\frac{1}{2}}} \quad (2.10)$$

where θ is the angle between the magnetic field direction and the wave propagation direction. Usually, a Taylor expansion about the signal frequency f and a series of approximations are made for simplification. Then we could get Eq. (2.11)

$$n_P = 1 - \frac{1}{2}X - \frac{1}{2}XY|\cos\theta| - \frac{1}{8}X^2 - \frac{1}{4}XY^2\cos^2\theta - \frac{1}{4}XY^2(\cos^2\theta + \sin^2\theta) \quad (2.11)$$

With substituting X, Y and Z into Eq. (2.11), n_L can be expressed as:

$$\begin{aligned} n_P &= 1 - \frac{Ne^2}{8\pi^2\epsilon_0 mf^2} \pm \frac{B_0 Ne^3 (\cos\theta)}{16\pi^3\epsilon_0 m^2 f^3} - \frac{N^2 e^4}{128\pi^4\epsilon_0^2 m^2 f^4} \\ &\quad + \frac{1}{4}XY^2\cos^2\theta - \frac{1}{4}XY^2(\cos^2\theta + \sin^2\theta) \end{aligned} \quad (2.12)$$

And group index n_G has relationship with n_P as follow:

$$n_G = n_P + f \frac{dn_P}{dn_G} = 1 + \frac{1}{2}X + XY\cos\theta + \frac{3}{8}X^2 + \frac{3}{4}XY^2\cos^2\theta + \frac{3}{4}XY^2 \quad (2.13)$$

Usually, only the first order of the phase refractive index and group refractive index are considered during ionospheric delay estimation (Datta-Barua et al. 2008). Then, phase velocity V_P and group velocity V_G can be obtained easily as

$$V_P = \frac{c}{n_P} \approx \frac{c}{1 - 40.3 \frac{N}{f^2}} \approx c \left(1 + 40.3 \frac{N}{f^2} \right) \quad (2.14)$$

$$V_G = \frac{c}{n_G} \approx \frac{c}{1 + 40.3 \frac{N}{f^2}} \approx c \left(1 - 40.3 \frac{N}{f^2} \right) \quad (2.15)$$

As we know, GPS observation equations are expressed as:

$$P_1 = \rho + I_G(f_1) \quad (2.16)$$

$$P_2 = \rho + I_G(f_2) \quad (2.17)$$

$$L_1 = \rho + I_P(f_1) + N_1 \lambda_1 \quad (2.18)$$

$$L_2 = \rho + I_P(f_2) + N_2 \lambda_2 \quad (2.19)$$

where ρ is the sum of the true geometry range between the satellite and the receiver and frequency-independent errors, I stands for ionospheric delay, N is integer ambiguity, and λ is the wavelength of the GPS signal. If the traveling time of GPS signal is Δt , the geometry range can be written as follow:

$$\begin{aligned} \rho &= \int_{\Delta t} V_P dt \approx \int_{\Delta t} c \left(1 + 40.3 \frac{N}{f^2} \right) dt = c \Delta t + \frac{40.3}{f^2} \int_{\Delta t} c N dt = c \Delta t + \frac{40.3}{f^2} \int_s N ds \\ &= \int_{\Delta t} V_G dt \approx \int_{\Delta t} c \left(1 - 40.3 \frac{N}{f^2} \right) dt = c \Delta t - \frac{40.3}{f^2} \int_{\Delta t} c N dt = c \Delta t - \frac{40.3}{f^2} \int_s N ds \end{aligned} \quad (2.20)$$

Then, ionospheric delay I_P and I_G can be derived from Eq. (2.20).

$$\begin{aligned} I_P &= \frac{40.3}{f^2} \int_s N ds \\ I_G &= -\frac{40.3}{f^2} \int_s N ds \end{aligned} \quad (2.21)$$

The total electron content (TEC) of the ionosphere can be calculated as the integration of N along the signal path:

$$TEC = \int_s N ds \quad (2.22)$$

The ionospheric delay is related to TEC and proportional to the square of signal frequency when the first order of the refractive index is just considered.

2.3.3 Empirical Ionospheric Models

2.3.3.1 Bent Model

The Bent model is directed towards world-wide empirical ionospheric model using bottom side ionospheric sounders' data and topside sounding measurements (Bent et al. 1972), which can provide the parameters of the ionosphere from the electron density profiles, such as TEC and ionospheric delay. In this model, topside of ionosphere is expressed as three layers and one parabola layer, and the bottom of the ionosphere is expressed as double parabolic layer. Through inputting the date, time, station's location, solar flux and sunspot number into Bent model, TEC can be computed at any time and locations.

2.3.3.2 IRI Model

The first version of International Reference Ionospheric (IRI) model was released by International Union of Radio Science (URSI) and Committee on Space Research (COSPAR) in 1978, which is called IRI 1978. With the development of techniques and the accumulation of measurement data, IRI model has been updated frequently. Nowadays, the latest version is IRI 2007 (Bilitza and Reinisch 2008). Data sources of IRI model include the world-wide ionosondes, the powerful incoherent scatter radars, the ISIS and Alouette topside sounders, in situ instruments and several satellites and rockets. In this model, parameters, such as electron density, ion density, electron temperature, ion temperature, main components of positive ions et al., are expressed with mathematic formula. Ionospheric electron density profile can be derived easily after inputting date, time, location, sunspot number and some other parameters. Then the TEC and ionospheric delay can be calculated. This model has been used widely in the ionosphere research and radio science. However, the International Reference Ionospheric (IRI) model as an empirical model, which just gives the mean variation of the ionosphere and cannot give more details.

2.3.3.3 Klobuchar Model

Klobuchar model was designed by Klobuchar (1987) for single-frequency GPS users. In this model ionospheric time delay is considered as a constant in the night, which is equal to 5 ns, and a cosine function on the daytime. Time delay T_g can be mathematically expressed as follow.

$$T_g = D_c + A \cos \frac{2\pi}{B} (t - T_p) \quad (2.23)$$

where $D_c = 15\text{ns}$, $T_P = 14^h$, $A = \sum_{n=0}^3 \alpha_n \Phi_m^n$, $B = \sum_{n=0}^3 \beta_n \Phi_m^n$. Users can get parameters α_n and β_n from GPS navigation files, and Φ_m^n is the geomagnetic coordinates of the intersection of the central ionosphere layer and the signal path. This correction precision of Klobuchar model is about 50~60 % without other aided data.

In addition, there are some other ionospheric empirical models, such as Ne-Quick model. Here we will not introduce in detail one by one. All this empirical ionospheric models just reflect the average variation of the global ionosphere during a long time period. These empirical models do not precisely correct ionospheric delay, but users can get the approximate ionospheric delay without other observations.

2.4 GNSS Multipath Delay

2.4.1 Multipath Effects

The GNSS antenna can receive signals from not only the direct path, i.e. the line-of-sight (LOS) path, but also multiple indirect paths due to signal reflection or diffraction, which will result in a certain delay, phase, and amplitude difference relative to the LOS component, called GNSS multipath effects (Fig. 2.4).

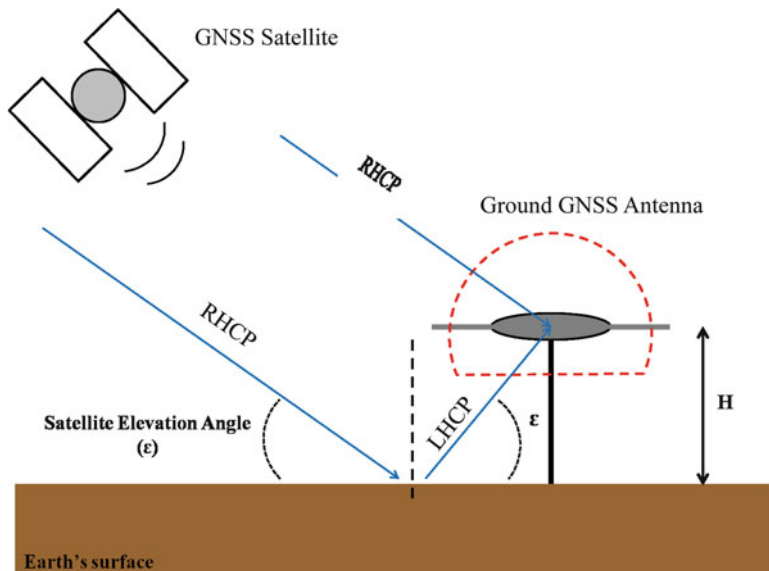


Fig. 2.4 GNSS multipath and reflected signals

Multipath propagation degrades the GNSS positioning accuracy. Since GNSS multipath effects depend on the environment near the receiver, e.g., path geometry, signal characteristics, diffraction and reflection mediums as well as their changing nature together with a complex antenna and receiver design, it is very difficult to remove or mitigate the GNSS multipath effects. Furthermore, the site-dependent characteristics of multipath decorrelate the errors caused by multipath propagation at different antenna locations and thus even differential techniques, like double differences (DD), also cannot remove or mitigate it.

GNSS multipath affects both code and phase measurements. The carrier phase multipath is the fraction of the GNSS signal's wavelength, whereas code multipath is limited by the chipping rate (Teunissen and Kleusberg 1998). The pseudorange multipath can degrade the accuracy of GNSS navigation, positioning, timing, ionospheric monitoring and RTK surveying. In particular, when the pseudorange is employed for ambiguity resolution purposes, multipath effects on the pseudorange can increase the time requirement for initialization. Pseudorange multipath on both frequencies can be investigated and evaluated using the linear combinations for both pseudorange P_1 and P_2 and carrier phase L_1 and L_2 data with eliminating the effects of receiver and satellite clocks as well as atmospheric delay. In the following, $MP1$ and $MP2$ are linear combinations using both pseudorange and carrier phase data to eliminate the effects of station clocks, satellite clocks, tropospheric delay, and ionospheric delay (Teunissen and Kleusberg 1998):

$$MP1 = P_1 - \left(1 + \frac{2}{\alpha-1}\right) L_1 + \left(\frac{2}{\alpha-1}\right) L_2 = M_1 + B_1 - \left(1 + \frac{2}{\alpha-1}\right) m_1 + \left(\frac{2}{\alpha-1}\right) m_2 \quad (2.24)$$

$$\begin{aligned} MP2 &= P_2 - \left(\frac{2\alpha}{\alpha-1}\right) L_1 + \left(\frac{2\alpha}{\alpha-1} - 1\right) L_2 \\ &= M_2 + B_2 - \left(\frac{2\alpha}{\alpha-1}\right) m_1 + \left(\frac{2\alpha}{\alpha-1} - 1\right) m_2 \end{aligned} \quad (2.25)$$

where $B_1 = -(1 + \frac{2}{\alpha-1}) n_1 \lambda_1 + (\frac{2}{\alpha-1}) n_2 \lambda_2$, $\alpha = \frac{f_1^2}{f_2^2}$, $B_2 = -(\frac{2\alpha}{\alpha-1}) n_1 \lambda_1 + (\frac{2\alpha}{\alpha-1} - 1) n_2 \lambda_2$, $\alpha = \frac{f_1^2}{f_2^2}$. P_1 and P_2 are the dual-frequency pseudorange observations, L_1 and L_2 are the dual-frequency carrier phase observations, and m_1 and m_2 are the dual-frequency carrier phase multipath. The report of TEQC (the toolkit for GPS/GLONASS/Galileo/SBAS data, UNAVCO: <http://facility.unavco.org/software/teqc/teqc.html>) is the Root Mean Square (RMS) variation of $MP1$ and $MP2$ for each satellite and a mean RMS for all satellites. Therefore the remaining in $MP1$ and $MP2$ is the effects of pseudorange noise (<25 cm), carrier phase multipath (<7 cm), and carrier phase noise (<2 mm), but these are much smaller when compared to the pseudorange multipath that can be as large as 10–15 m at low elevation angles (Hilla and Cline 2002).

2.4.2 Multipath Variations

Two types of polarized signals from GNSS satellites or the surfaces can be acquired by ground GNSS receiver, Right-Hand Circular Polarization (RHCP) and Left-Hand Circular Polarization (LHCP) (Fig. 2.4). In multipath propagation, one or multiple reflections and diffraction of the transmitted signal may occur. For different surfaces, e.g., ocean, land, snow, ice and vegetation as well as oil, the reflection processes are different. In the case of reflection of the incident field, the reflection coefficients will indicate how much the reflected field will be attenuated and how the polarization state of the incident field will be deformed.

Multipath signal depends on four parameters, the GNSS wavelength (λ), ratio of the reflected wave amplitude relative to the direct wave (α), GNSS satellite elevation angle (ε) and the GNSS antenna height (H) (See Fig. 2.4), which can be written as (Elosegui et al. 1995; Ray and Cannon 1999)

$$\delta\Phi = \tan^{-1} \left(\frac{\alpha \sin(4\pi \frac{H}{\lambda} \sin \varepsilon)}{1 + \alpha \cos(4\pi \frac{H}{\lambda} \sin \varepsilon)} \right) = \delta\Phi(\lambda, \alpha, \varepsilon, H) \quad (2.26)$$

where $\delta\Phi$ is the reflected wave phase shifted value related to the total (the reflected wave plus direct one). Here two conditions as the following are discussed.

2.4.2.1 Multipath Variations with Elevation Angle

When $M = 4\pi \frac{H}{\lambda}$, the Eq. (2.26) can be written as

$$\delta\Phi = \tan^{-1} \left(\frac{\alpha \sin(M \sin \varepsilon)}{1 + \alpha \cos(M \sin \varepsilon)} \right) = \delta\Phi(\alpha, M, \varepsilon) \quad (2.27)$$

When the GNSS antenna height (H) does not change, M would not vary during the time, so the changes in multipath during the time (velocity of multipath signal ($V\delta\Phi$)) related to the changes in the satellite elevation angle (ε) (velocity of satellite elevation angle ($V\varepsilon$)) can be defined as:

$$\frac{V_{\delta\Phi}}{V_\varepsilon} = \frac{d\delta\Phi/dt}{d\varepsilon/dt} = \frac{d\delta\Phi}{d\varepsilon} = \frac{\frac{d}{d\varepsilon} \left(\frac{\alpha \sin(M \sin \varepsilon)}{1 + \alpha \cos(M \sin \varepsilon)} \right)}{1 + \left(\frac{\alpha \sin(M \sin \varepsilon)}{1 + \alpha \cos(M \sin \varepsilon)} \right)^2} \quad (2.28)$$

and thus after simplicity of Eq. (2.28), it can be written as:

$$\frac{V_{\delta\Phi}}{V_\varepsilon} = \frac{d\delta\Phi}{d\varepsilon} = M\alpha \frac{\alpha \cos \varepsilon + \cos \varepsilon \cos(M \sin \varepsilon)}{(1 + \alpha \cos(M \sin \varepsilon))^2} \quad (2.29)$$

It can be seen that the function of multipath signal based on satellite elevation angle significantly depends on the H value since M is a function of H. When GNSS satellite elevation angle is equal to zero or $\pi/2$, it can be deduced as

$$\varepsilon = 0 \rightarrow \frac{d\delta\Phi}{d\varepsilon} = M\alpha \frac{\alpha + 1}{(1 + \alpha)^2} = \frac{M\alpha}{1 + \alpha} \quad (2.30)$$

$$\varepsilon = \frac{\pi}{2} \rightarrow \frac{d\delta\Phi}{d\varepsilon} = 0 \quad (2.31)$$

2.4.2.2 Multipath Variations with Antenna Height

The multipath signal variability with respect to the GNSS antenna height can be written as:

$$\frac{V_{\delta\Phi}}{V_H} = \frac{\frac{d\delta\Phi}{dt}}{\frac{dH}{dt}} = \frac{d\delta\Phi}{dH} = \frac{\frac{d}{dH} \left(\frac{\alpha \sin(NH)}{1 + \alpha \cos(NH)} \right)}{1 + \left(\frac{\alpha \sin(NH)}{1 + \alpha \cos(NH)} \right)^2} \quad (2.32)$$

where N is defined as a function of satellite elevation angle (ε) as the following:

$$N = \frac{4\pi}{\lambda} \sin \varepsilon \quad (2.33)$$

Similarly the following simplicity relation between multipath signal's velocity and H can be expressed as:

$$\frac{V_{\delta\Phi}}{V_H} = \frac{d\delta\Phi}{dH} = N\alpha \frac{(\cos(NH) + \alpha)}{(\alpha + \cos(NH))^2 + \sin^2(NH)} \quad (2.34)$$

Therefore, in a similar way, if the GNSS antenna height becomes zero as $H = 0$, so

$$\frac{d\delta\Phi}{dH} = N \frac{\alpha}{1 + \alpha} \quad (2.35)$$

The satellite elevation angle is important to affect the multipath signals variability when the GNSS antenna heights are changing parallel. Moreover, to understand when or where the multipath signals variability is going to be zero with respect to the changes in GNSS antenna height, it can be seen

$$\frac{d\delta\Phi}{dH} = 0 \rightarrow N\alpha (\cos(NH) + \alpha) = 0 \rightarrow \begin{cases} \varepsilon = \sin^{-1} \left(\frac{\lambda}{8H} \right) \\ \varepsilon = \sin^{-1} \left(\frac{3\lambda}{16H} \right) \end{cases} \quad (2.36)$$

2.4.3 Surface Reflection Characteristics

When the signal travels from a dense space into a less dense one, the value is more than the incidence angle known as the critical angles while thus entire signal is reflected with $R_s = R_p = 1$. This phenomenon is defined as the total internal reflection (Lakhtakia 1992). It is well-known that the reflection coefficients for horizontal and vertical polarization are simply given in the following by considering $\varepsilon = \varepsilon_r - j \frac{\sigma}{\omega \varepsilon_0}$ in Eqs. (2.37) and (2.38), respectively (van Nee 1992):

$$RC_H = \frac{\sin \theta - \sqrt{\varepsilon - (\cos \theta)^2}}{\sin \theta + \sqrt{\varepsilon - (\cos \theta)^2}} \quad (2.37)$$

$$RC_V = \frac{\varepsilon \sin \theta - \sqrt{\varepsilon - (\cos \theta)^2}}{\varepsilon \sin \theta + \sqrt{\varepsilon - (\cos \theta)^2}} \quad (2.38)$$

where θ is the grazing angle. According to GNSS receiver antenna property that can receive RHCP signals, it is necessary to assess these selected surfaces in cross-polarized and co-polarized cases (Vickerman and Gilmore 2009). According to Leroux et al. (1998), the co-polarization equation can be written as:

$$\Gamma_O = \frac{RC_H + RC_V}{2} \quad (2.39)$$

Similarly for cross-polarization:

$$\Gamma_X = \frac{RC_H - RC_V}{2} \quad (2.40)$$

where Γ_O and Γ_X is reflection coefficient for co-polarization and cross-polarization and RC_H and RC_V is reflection coefficient for horizontal and vertical linear polarization, respectively in Eqs. (2.37) and (2.38). By using GNSS scatter signals to selected surfaces, reflection coefficients for GNSS signals versus grazing angles can be computed.

Therefore, the multipath characterization of GNSS reflected signals are very complex, depending on GNSS antenna height, satellite elevation angle and ratio of the reflected wave amplitude relative to the direct wave as well as the polarization of the targeted surface in different propagation angles.

References

- Bassiri S, Hajj GA (1993) Higher-order ionospheric effect on the Global Positioning System observables and means of modeling them. *Manuscr Geodaet* 18:280–289
- Bent RB et al (1972) Description and evaluation of the Bent ionospheric model. DBA Systems, Melbourne
- Bilitz D, Reinisch BW (2008) International reference ionosphere 2007: improvements and new parameters. *Adv Space Res* 42(4):599–609
- Datta-Barua S, Walter T, Blanch J, Enge P (2008) Bounding higher-order ionosphere errors for the dual-frequency GPS user. *Radio Sci* 43:RS5010. doi:[10.1029/2007RS003772](https://doi.org/10.1029/2007RS003772)
- Elosegui P, Davis JL, Jaldehag RK, Johansson JM, Niell AE, Shapiro B (1995) Geodesy using the global positioning system: the effects of signal scattering. *J Geophys Res* 100:9921–9934
- Hartmann G, Leitinger R (1984) Range errors due to ionospheric and tropospheric effects for signal frequencies above 100 MHz. *Bull Géod* 58:109–136
- Hilla S, Cline M (2002) Evaluating pseudorange multipath effects at stations in the National CORS Network, Weikko A. Heiskanen Symposium in Geodesy, the Ohio State University Columbus, OH, 1–4 Oct 2002
- Hopfield H (1969) Two-quartic tropospheric refractivity profile for correcting satellite data. *J Geophys Res* 74(18):4487–4499
- Hopfield HS (1971) Tropospheric effect on electromagnetically measured range: prediction from surface weather data. *Radio Sci* 6:357–367
- Kelley MC (2009) The Earth's ionosphere: plasma physics & electrodynamics. Academic Press/Elsevier, San Diego
- Klobuchar JA (1987) Ionospheric time-delay algorithm for single-frequency Gps users. *IEEE Trans Aerosp Electron Syst* 23(3):325–331
- Lakhtakia A (1992) General schema for the Brewster conditions. *Optik* 90:184–186
- Leroux C, Deuze JL, Goloub P, Sergent C, Fily M (1998) Ground measurements of the polarized bidirectional reflectance of snow in the near-infrared spectral domain: comparisons with model results. *J Geophys Res* 103:19721–19731
- Pulinets SA, Boyarchuk KA (2004) Ionospheric precursors of earthquakes. Springer, Berlin, p 315
- Ray JK, Cannon ME (1999) Mitigation of static carrier-phase multipath effects using multiple closely spaced antennas. *Navigation* 46:193–201
- Saastamoinen J (1972) Atmospheric correction for the troposphere and stratosphere in radio ranging of satellites. In: The use of artificial satellites for geodesy, Geophysical monograph series 15. American Geophysical Union, Washington, pp 247–251
- Saastamoinen J (1973) Contributions to the theory of atmospheric refraction (in three parts). *Bull Geod* 105, 106, 107, 279–298, 383–397, 13–34
- Saastamoinen J (1975) Atmospheric correction for the troposphere and stratosphere in radio ranging of satellites. The use of artificial satellites for Geodesy. *Geophys Monogr* 15:247–251
- Smith EK, Weintraub S (1953) The constants in the equation for atmospheric refractive index at radio frequencies. *Proc IRE* 41:1035–1037
- Teunissen P, Kleusberg A (1998) GPS for Geodesy, 2nd edn. Springer, Berlin
- van Nee RDJ (1992) Multipath effects on GPS code phase measurements. *Navigation* 39:177–190
- Vickerman JC, Gilmore IS (2009) Surface analysis-the principal techniques, 2nd edn. Wiley, Chichester, pp 391–478

Part II

GNSS Atmospheric Sensing

and Applications

Chapter 3

Ground GNSS Atmospheric Sensing

3.1 Introduction

When GNSS signals propagate through the neutral atmosphere, the GNSS signal is delayed by the neutral atmosphere, which results in lengthening of the geometric path of the ray, usually referred to as the “tropospheric delay”. This delay is one of major error sources for GPS positioning, which contributes a bias in height of several centimeters even when simultaneously recorded meteorological data are used in tropospheric models (Tregoning et al. 1998). Nowadays, GPS has been widely used to determine the zenith tropospheric delay (ZTD) (Bevis et al. 1992, 1994; Emardson et al. 1998; Jin and Park 2005) through mapping functions (Niell 1996). The ZTD is the integrated refractivity along a vertical path through the neutral atmosphere:

$$ZTD = c\tau = 10^{-6} \int_0^{\infty} N(s)ds \quad (3.1)$$

where c is the speed of light in a vacuum, τ is the delay measured in units of time and N is the neutral atmospheric refractivity. The N is empirically related to standard meteorological variables as (Davis et al. 1985)

$$N = k_1\rho + k_2 \frac{P_w}{Z_w T} + k_3 \frac{P_w}{Z_w T^2} \quad (3.2)$$

where $k_i (i=1, 2, 3)$ is constant, ρ is the total mass density of the atmosphere, P_w is the partial pressure of water vapor, Z_w is a compressibility factor near unity accounting for the small departures of moist air from an ideal gas, and T is the temperature in degrees Kelvin. The integral of the first term of equation (3.2) is the hydrostatic component (N_h) and the integral of the remaining two terms

is the wet component (N_w). Thus, ZTD is the sum of the hydrostatic or ‘dry’ delay (ZHD) and non-hydrostatic or ‘wet’ delay (ZWD), due to the effects of dry gases and water vapor, respectively. The dry component ZHD is related to the atmospheric pressure at the surface, while the wet component ZWD can be transformed into the precipitable water vapor (PWV), which plays an important role in energy transfer and in the formation of clouds via latent heat, directly or indirectly influencing numerical weather prediction (NWP) model variables (Bevis et al. 1994; Duan et al. 1996; Tregoning et al. 1998; Manuel et al. 2001). Therefore, the Zenith Tropospheric Delay (ZTD) from GNSS is an important parameter of the atmosphere, which reflects the weather and climate processes, variations, and atmospheric vertical motions, etc.

3.2 Theory and Methods

3.2.1 Estimates of GNSS ZTD

3.2.1.1 Double Difference

With double difference for two-frequency GNSS observations, some common error sources are eliminated, e.g., satellite and receiver clock errors. For a pair of GPS observation stations and satellites (see Fig. 3.1), the ionosphere-free linear

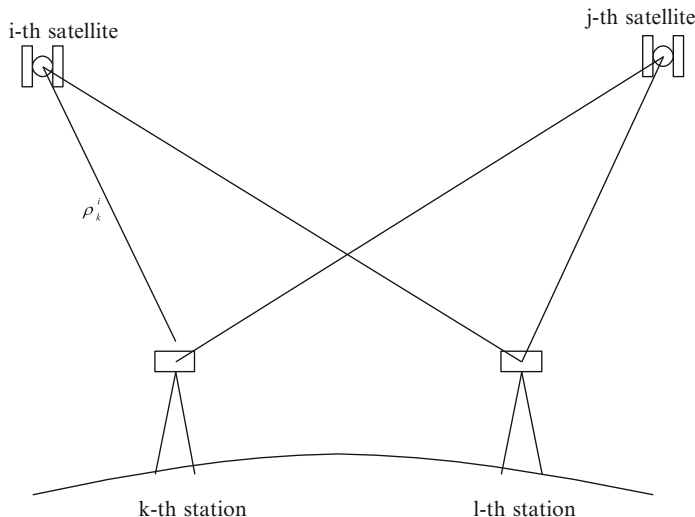


Fig. 3.1 GNSS DD observation geometry

combination (LC) equation of double-differenced (DD) phase and code observations can be expressed as:

$$\begin{aligned} LC_{kl}^{ij} &= \frac{1}{f_1^2 - f_2^2} \left(f_1^2 L1_{kl}^{ij} - f_2^2 L2_{kl}^{ij} \right) \\ &= \rho_{kl}^{ij} + Z TD_k(t) (m(z_k^i) - m(z_k^j)) - Z TD_l(t) (m(z_l^i) - m(z_l^j)) \\ &\quad + \frac{c}{f_1^2 - f_2^2} \left(f_1^2 N1_{kl}^{ij} - f_2^2 N2_{kl}^{ij} \right) + \varepsilon_{kl}^{ij} \end{aligned} \quad (3.3)$$

where ZTD is the zenith tropospheric delay, m is the mapping function, f_i is the frequency ($i = 1, 2$), L_i and N_i are the double-differenced phase and ambiguity of the frequency f_i , respectively, ρ_{kl}^{ij} is the double-differenced pseudorange, c is the velocity of light in vacuum, and ε_{kl}^{ij} is noise. Using the least square, the unknown parameters can be estimated, including ZTD, coordinate and ambiguity, etc. (Jin et al. 2010).

3.2.1.2 Non-difference Observation

With the double difference GNSS processing technique, tropospheric delays can be derived with a high accuracy, but some information are removed. Nowadays, the emerging Precise Point Positioning (PPP), high accuracy tropospheric delay can be estimated too, while the precise orbit and clock are provided by an external network such as IGS products.

3.2.2 Mapping Functions

The GNSS slant tropospheric delay (STD) is the total delay along the signal path from the satellite to the receiver throughout the neutral atmosphere. The Zenith Total Delay (ZTD) along the zenith direction can be obtained through mapping function related to the satellite zenith angle E , i.e.,

$$\begin{aligned} Z TD &= STD \cdot m(z) \\ &= ZHD \cdot m_h(z) + ZWD \cdot m_w(z) \end{aligned} \quad (3.4)$$

where STD is slant tropospheric delay, z is the corresponding elevation angle, $m(z)$ is general mapping function, $m_h(z)$ and $m_w(z)$ are dry and wet component mapping functions, respectively, ZHD and ZWD are Zenith Hydrostatic Delay and Zenith Wet Delay, respectively. Over the past 30 years or more, a number of mapping functions have been developed by geodesists and meteorologists.

3.2.2.1 Herring Mapping Function

Marini (1972) developed the mapping function with a continued fraction and Herring (1992) specified the Marini's function with three coefficients (a , b , and c) depending on the latitude and height as well as surface temperature. This is the first empirical mapping function related to the elevation angle. The wet component and dry component of this mapping function can be expressed as,

$$m_i(E) = \frac{1 + \frac{a_i}{1 + \frac{b_i}{1 + c_i}}}{\sin E + \frac{a_i}{\sin E + \frac{b_i}{\sin E + c_i}}} \quad (3.5)$$

where subscript i stands for the dry and wet components of the mapping function and the parameters a , b , and c are coefficients for the hydrostatic and wet components of the atmosphere.

3.2.2.2 Niell Mapping Function

Niell (1996) developed the mapping function following the Herring's function with the continued fraction (Eq. 3.5), i.e., Niell Mapping Function (NMF). The NMF is an empirical function that was based on 1 year of radiosonde observations mostly from the Northern Hemisphere. The coefficients of the dry component depend on the day of the year, the latitude and height above sea level of the observing site, and the coefficients of the wet component only depend on the latitude of the site (Niell 1996). The dry coefficients are defined as:

$$p_d(\varphi, t) = p_{avg}(\varphi) - p_{amp}(\varphi) \cos\left(2\pi \frac{t - T_0}{365.25}\right), \quad (p = a, b, c) \quad (3.6)$$

where p denotes the calculated coefficients of a , b , and c , φ is the latitude of the site, t is the observing time in day-of-year (DOY), and T_0 is the adopted phase, p_{avg} and p_{amp} are the mean value and the amplitude, respectively.

3.2.2.3 Vienna Mapping Functions 1 (VMF1)

The coefficients a_h and a_w were determined from a rigorous raytracing through global grids of monthly mean profiles for pressure, temperature, and humidity from the ECMWF (European Centre for Medium-Range Weather Forecasts) 40 years reanalysis data (ERA40). The coefficients b_h and c_h were derived from 1 year of ECMWF data in a least squares fit. Whereas b_h is constant, c_h depends on the day of year and the latitude. Since the coefficient a_w is sufficient to model the dependence of the wet mapping function on latitude, b_w and c_w were taken from the Niell mapping function (Niell 1996) at 45° latitude (Boehm and Schuh 2004).

3.2.2.4 Global Mapping Function

The global mapping function (GMF) is similar to NMF, whose input parameters are day of year, latitude, longitude and height. The GMF is an empirical mapping function with input arguments are only the day of year and the site location, which is consistent with VMF1. Expressions for the coefficients a_h and a_w were derived from 3 years of ECMWF data and the coefficients b and c are taken from the VMF1 (Boehm et al. 2006).

3.3 ZTD Estimate and Variations

3.3.1 ZTD Estimates from IGS Observations

The quantity observed by the GPS receiver is the interferometric phase measurement of the distance from the GPS satellites to the receiver. The processing software must resolve or model the orbital parameters of the satellites, solve for the transmitter and receiver positions, account for ionospheric delays, solve for phase cycle ambiguities and the clock drifts in addition to solving for the tropospheric delay parameters of interest. This requires the same type of GPS data processing software as that which is used for high precision geodetic measurements. We use the GAMIT software (King and Bock 1999), which solves for the ZTD and other parameters using a constrained batch least squares inversion procedure. In addition, this study uses the newly IGS recommended strategies to calculate ZTD time series with temporal resolution of 2 h from 1994 to 2006.

The GAMIT software parameterizes ZTD as a stochastic variation from the Saastamoinen model (Saastamoinen 1972), with piecewise linear interpolation in between solution epochs. GAMIT is very flexible in that it allows *a priori* constraints of varying degrees of uncertainty. The variation from the hydrostatic delay is constrained to be a Gauss-Markov process with a specified power density of $2 \text{ cm}/\sqrt{\text{hour}}$, referred to below as the “zenith tropospheric parameter constraint”. We designed a 12-h sliding window strategy in order to process the shortest data segment possible without degrading the accuracy of ZTD estimates. The Gauss-Markov process provides an implicit constraint on the ZTD estimate at a given epoch from observations at proceeding and following epochs, which means that the accuracy is expected to be lower at the beginning and end of each window. We therefore extract ZTD estimates from the middle 4 h of the window and then move the window forward by 4 h. Finally, the ZTD time series from 1994 to 2006 are obtained at globally distributed 150 IGS sites with temporal resolution of 2 h (Fig. 3.2). Figure 3.3 shows the uncertainties for the ZTD solutions at 150 sites as a histogram. It can see that the mean uncertainty of ZTD is about 3 mm.

The mean ZTD values at all GPS sites are shown in Fig. 3.4 as a color map. It has noted that lower ZTD values are found at the areas of Tibet (Asia), Andes

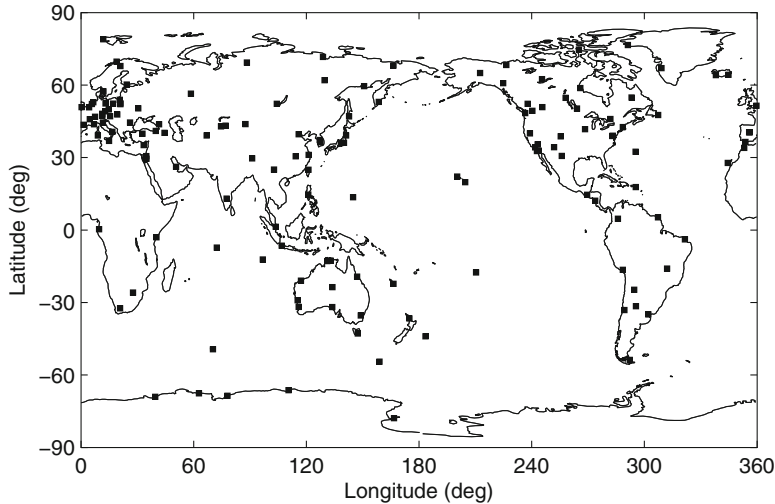


Fig. 3.2 The distribution of global IGS GPS sites

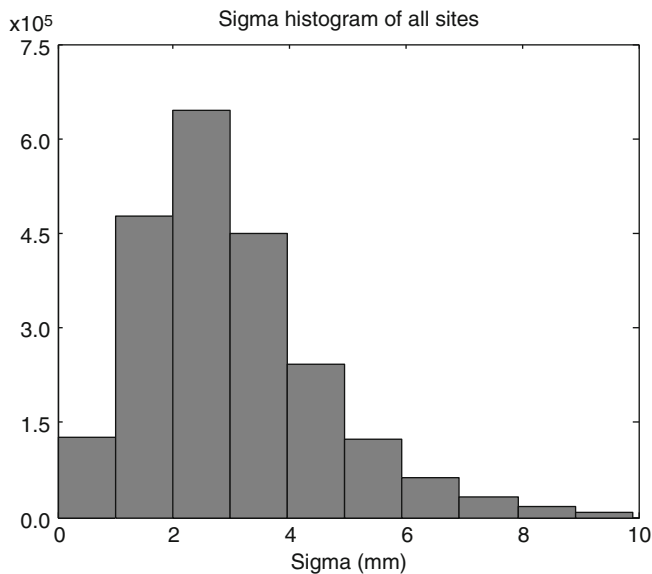


Fig. 3.3 Histogram of the uncertainty for the ZTD solutions at 150 sites

Mountain (South America), Northeast Pacific and higher latitudes (Antarctica and Arctic), and the higher ZTD values are concentrated at the areas of middle-low latitudes (also see Fig. 3.5). Figure 3.6 shows the distribution of ZTD at all IGS sites with the altitude (above the global mean sea level). It has been clearly seen that

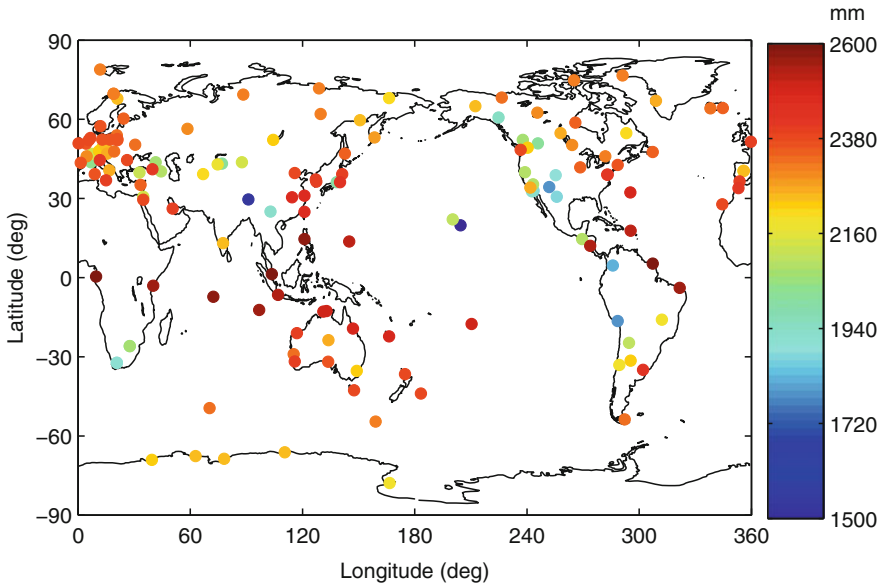
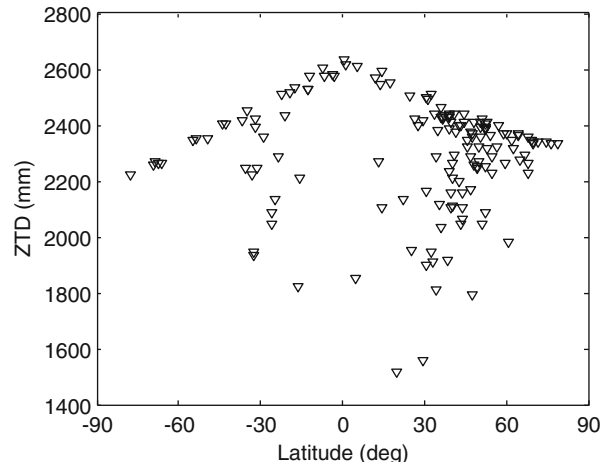


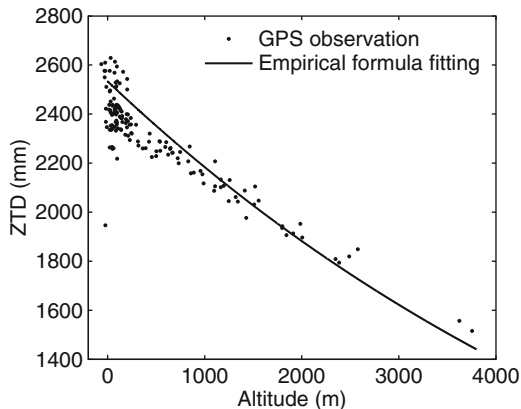
Fig. 3.4 Distribution of mean ZTD at global IGS sites

Fig. 3.5 Distribution of ZTD with the latitude



the ZTD values decrease with increasing altitude. This is due to the atmospheric pressure variations with the height increase. Atmospheric pressure is the pressure above any area in the Earth's atmosphere caused by the weight of air. Air masses are affected by the general atmospheric pressure within the mass, creating areas of high pressure (anti-cyclones) and low pressure (depressions). Low pressure areas have less atmospheric mass above their locations, whereas high pressure areas have more atmospheric mass above their locations. As elevation increases,

Fig. 3.6 Distribution of ZTD with the altitude (above the global mean sea level)



there are exponentially, fewer and fewer air molecules. Therefore, atmospheric pressure decreases with increasing altitude at a decreasing rate. The following relationship is a first-order approximation to the height (http://www.chemistrydaily.com/chemistry/Atmospheric_pressure):

$$\log_{10} P \approx 5 - \frac{h}{15.5} \quad (3.7)$$

where P is the pressure in Pascals and h is the height in km. Based on the Eq. (3.7), ZHD can be expressed as $2.28 * 10^{(5-h/15.5)}$. As the ZHD accounts for 90 % of ZTD, we can further deduce the approximate ZTD at all GPS sites as an empirical formula:

$$ZTD = 2.28 * 10^{(5-h/15.5)} / 0.9 \quad (3.8)$$

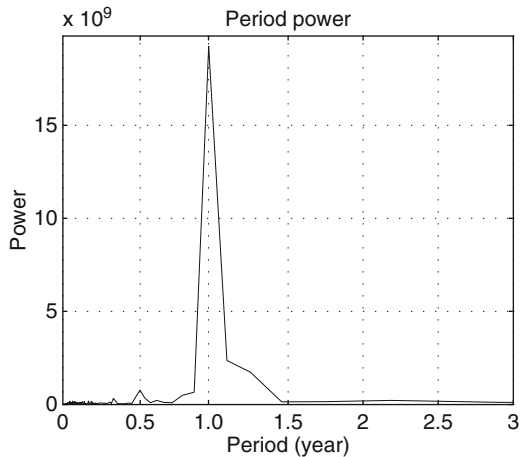
where the units of ZTD and h are in millimeters, respectively. Comparing GPS-derived ZTD with the empirical formula estimations (Fig. 3.6), it has shown a good consistency.

3.3.2 Multi-Scale ZTD Variations

To fit the time series, a model with a linear trend and a seasonal component for ZTD has been used. This model is described by the following function (Feng et al. 1978):

$$ZTD_t = a + bt + \sum_{k=1}^2 \left[c_k \sin \left(2\pi (t - t_0) / p_k + \varphi_k \right) \right] + \varepsilon_t \quad (3.9)$$

Fig. 3.7 Power chart of ZTD time series at Wuhan site



Where a and b are the constant and linear terms, c_k, p_k and φ_k are the amplitude, period and phase at period k , respectively, and ε_t is the residual. We analyzed all the ZTD time series at GPS stations with Fast Fourier transform and found that the most obvious periods of all GPS stations' ZTD time series are about 359.5 days and 180.1 days. For example, Fig. 3.7 shows the period power chart of ZTD time series at Wuhan (China) GPS site. It has shown clear annual and semiannual variations. No other periods stand out, so we here analyze the ZTD time series using $p_1 = 1$ year and $p_2 = 0.5$ year in Eq. (3.9). Through the method of least squares we can determine the unknown parameters in Eq. (3.9) with the original series of 2-h ZTD, and then we further analyze the characteristics of annual and semi-annual variations and those of the constant and linear terms.

The ZTD consists of the hydrostatic delay (ZHD) and wet delay (ZWD). The ZHD can be well calculated from surface meteorological data, ranging 1.5–2.6 m, which accounts for 90 % ZTD. It derives from the relationship with hydrostatic equilibrium approximation for the atmosphere. Under hydrostatic equilibrium, the change in pressure with height is related to total density at the height h above the mean sea level by

$$dp = -\rho(h)g(h)dh \quad (3.10)$$

where $\rho(h)$ and $g(h)$ are the density and gravity at the height h . It can be further deduced as

$$ZHD = kp_0 \quad (3.11)$$

where k is constant (2.28 mm/hPa) and p_0 is the pressure at height h_0 (Davis et al. 1985). It shows that the ZHD is proportional to the atmospheric pressure at the site. The ZWD is highly variable due possibly to varying climate, relating

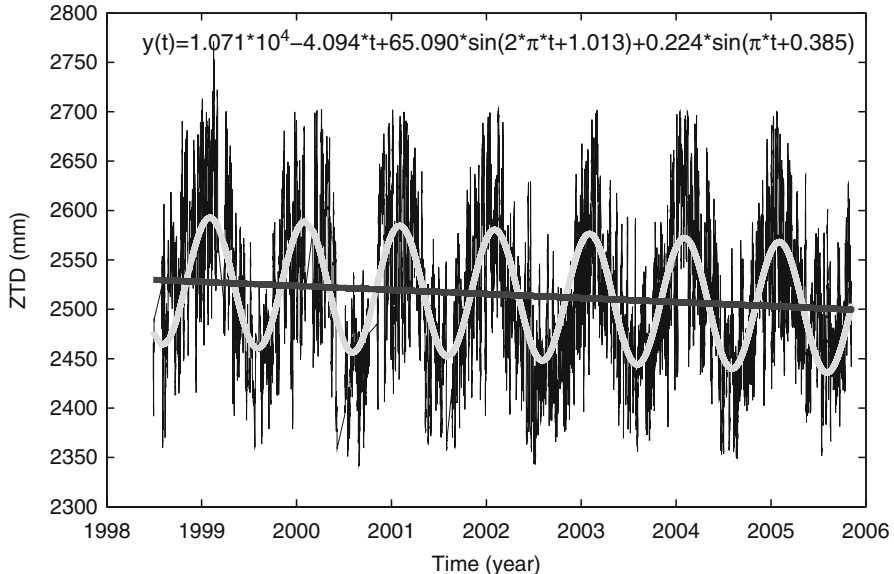


Fig. 3.8 ZTD time series at TOW2 station, Australia. The *solid line* is the fitting results, consisting of a linear decrease and seasonal components

to the temperature and water vapor. Unfortunately, only fewer IGS sites have meteorological instruments which can directly obtain the real ZWD or PWV. If one calculated the ZWD or PWV using the meteorological data from the European Centre for Medium-Range Weather Forecasts (ECMWF), it has some differences relative to the real observation results with meteorological instrument data (Hagemann et al. 2003). Therefore, we here analyze the variation and relationship between atmospheric parameters at GPS stations equipped the meteorological instruments. For example, the GPS station Wettzell (WETT), Germany has equipped the meteorological instruments. The positions of humidity and temperature sensors are the same as the GPS antenna, and the pressure sensor is 10.5 m below the GPS antenna. The data frequencies of relative humidity, temperature and pressure are all 15 min, and their accuracies are 1.5 % (relative to height), 0.3 °C and 0.1 mbar, respectively. The seasonal variations in ZTD are due primarily to the wet component (ZWD), even though the wet delay is only 10 % of the total delay (ZTD). In addition, the ZHD is proportional to the atmospheric pressure (Eq. 3.11) while the pressure is mainly related to height, and therefore, the ZHD is almost constant, again showing that the seasonal variations of ZTD are due primarily to the ZWD.

3.3.2.1 Secular ZTD Variations

The GPS ZTD time series have been analyzed for 4–12 years at globally distributed 150 GPS sites. Figure 3.8 shows an example of an original ZTD time series and the

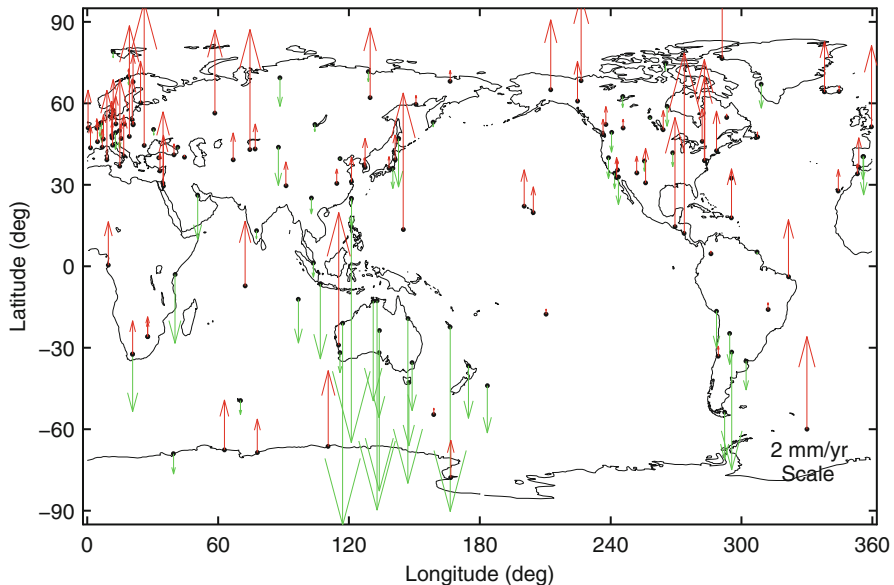
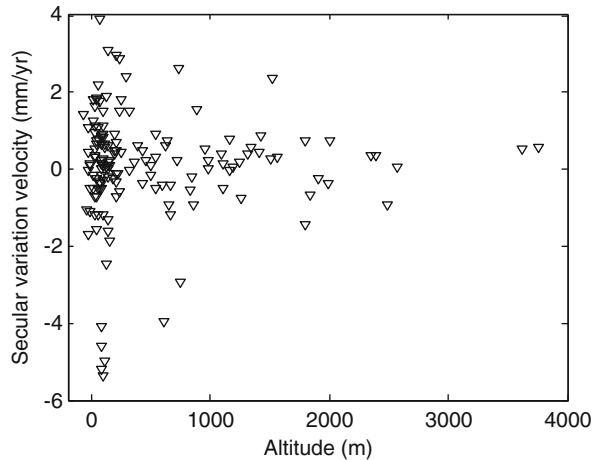


Fig. 3.9 Secular variation trend of ZTD at global IGS sites. The *red upwards arrows* represent the increase of secular ZTD variations and the *green downwards arrows* stand for the decrease of secular ZTD variations

fitting lines at TOW2 station, Australia. The solid line is the fitting results, consisting of a linear decrease and seasonal components (annual and semiannual terms). It has shown a clear trend and seasonal variations of ZTD time series at the TOW2 in Australia with lower values in the winter and higher values in the summer. Using the model from Eq. (3.9), the fitting parameters of all GPS site are obtained, including trend and seasonal variation terms. The mean secular ZTD variation trend is about 1.5 ± 0.001 mm/year. Figure 3.9 shows the distribution of the secular ZTD variation trends at all GPS sites as the yearly increase or decrease. It can be seen that the trends are positive in most parts of the Northern Hemisphere and negative in most parts of the Southern Hemisphere (excluding positive in Antarctic), corresponding to a systematic increase or decrease of ZTD. It is interesting to note that the downtrend in Australia is larger than other regions. This downtrend of ZTD is probably due to the highly deserted in Australia. In addition, Fig. 3.10 shows the relationship of secular ZTD variation trend with the altitude. It has been seen that the ZTD variation trend decreases with increasing altitude, and furthermore, the ZTD trends are almost symmetrical with altitude. This indicates that the secular ZTD variations are larger at the lower altitude and at the higher altitude the secular ZTD variations hardly increase or decrease. In addition, the sum of downward and upward trends at globally distributed GPS sites is almost zero, which possibly indicates that the secular variation is in balance at a global scale, but subjecting to unevenly distributed GPS stations, etc. It need further be confirmed with much denser GPS network in

Fig. 3.10 Distribution of ZTD secular variation velocities (trend) with the altitude of all IGS sites



the future. These secular ZTD variation characteristics reflect the total variations of surface atmospheric pressure, temperature and relative humidity, atmospheric vertical motions, etc.

3.3.2.2 Seasonal ZTD Variations

Meanwhile, the seasonal components are also obtained using Eq. (3.9), which can be used to study the seasonal cycle, including amplitude and phase shift. The fitted phase shift is used to determine in which month the seasonal maximum takes place. The annual variation of ZTD ranges from 25 to 75 mm depending on the site, and the average amplitude is about 50 mm at most sites (Fig. 3.11). The annual variation amplitudes of ZTD at the IGS sites near Oceanic coasts are generally larger than in the continental inland. In addition, larger amplitudes of annual ZTD variation are mostly found at middle-low latitudes (near 20S° and 40N°), and the amplitudes of annual ZTD variation are especially smaller at higher latitudes (e.g. Antarctic and Arctic) and the equator areas (see Fig. 3.12). Sites on the eastern Atlantic and northeast Pacific coasts have lower annual variations, probably because of the moderating effect of the ocean on climate. Sites on the lee side of the Alps have higher annual variation, possibly due to the combined effects of a rain shadow in the winter and high moisture from the Mediterranean in the summer (Haase et al. 2003; Deblonde et al. 2005). Figure 3.13 shows the annual phase distribution with the latitude, where phase values are counted as clockwise from the north. It can be seen that the phase of annual ZTD variation is almost found at about 60° (about February, summer) in the Southern Hemisphere and at about 240° (about August, summer) in the Northern Hemisphere, which is just a half-year difference.

The mean amplitude of semiannual ZTD variations is much smaller than annual variations with about 10 mm. The amplitudes of the semiannual oscillations are much smaller on the Southern Hemisphere than on the Northern Hemisphere.

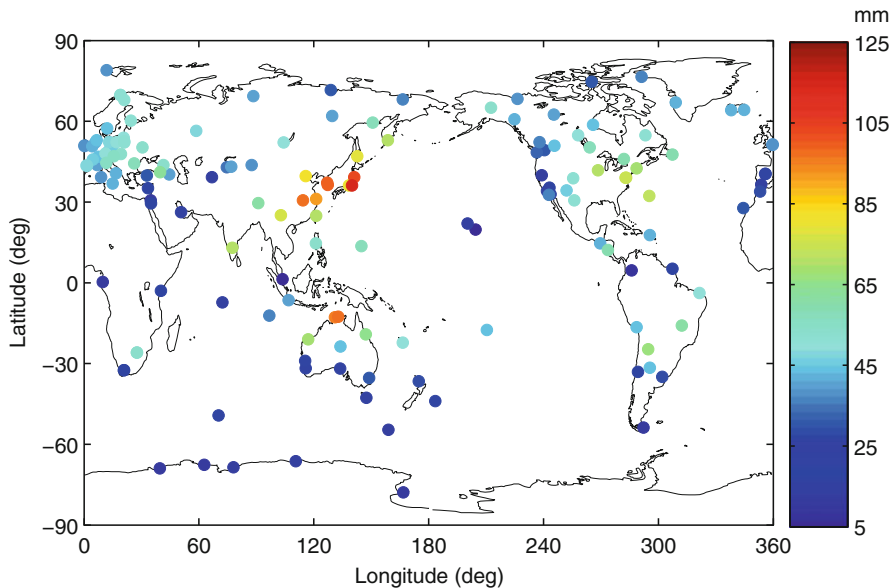


Fig. 3.11 Annual variation amplitude of ZTD at globally distributed 150 GPS sites

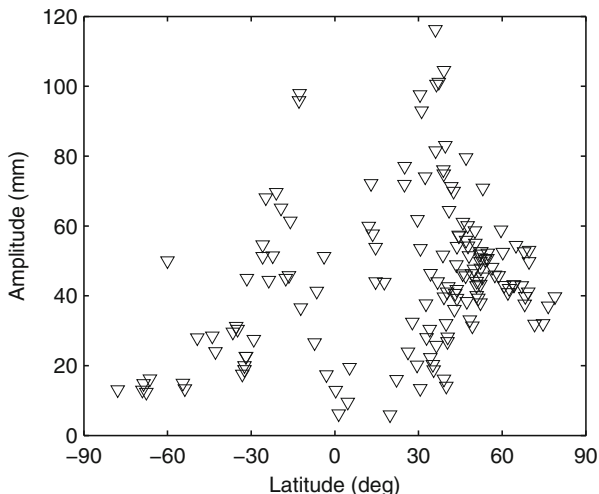


Fig. 3.12 Distribution of annual ZTD variation amplitude with the latitude

The distribution of the semiannual variation phase with the latitude has no clear symmetry (Fig. 3.14). For example, at the latitudes of 40°N–50°N in the Northern Hemisphere, the semiannual phase is about 30° (about January), while at the latitudes of 40°S–50°S in the Southern Hemisphere, the semiannual phase is about 330° (November).

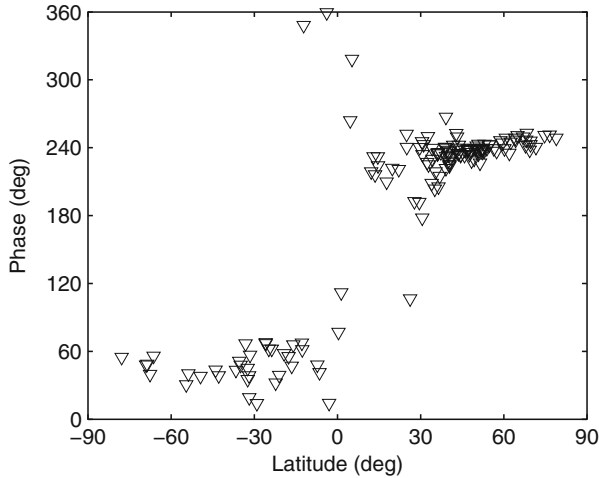


Fig. 3.13 Distribution of annual variation phase with the latitude. The phases are counted as clockwise from the north

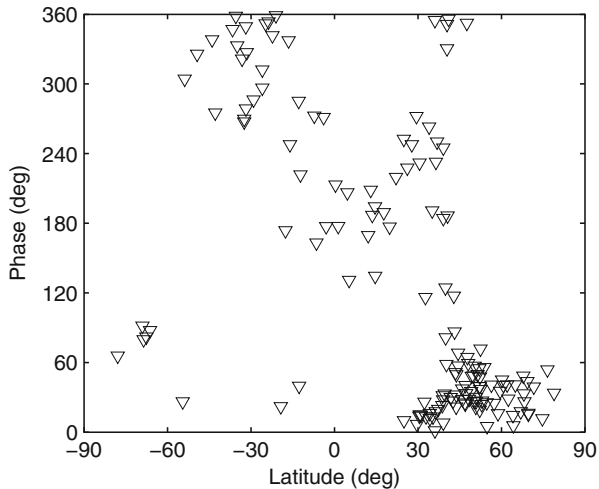


Fig. 3.14 Distribution of semiannual variation phase with the latitude. The phase values are counted as clockwise from the north

3.3.2.3 Diurnal and Semidiurnal ZTD Cycles

The non-seasonal ZTD residuals have significant diurnal and semidiurnal variations. Figure 3.15 shows a case of the 10-year ZTD time series (upper), power spectrum (middle) and the mean diurnal ZTD values (bottom) at local times (LT) in two hour increments ($LT = 1, 3, 5, \dots, 23$) at Wuhan (WUHN), China, where the mean diurnal ZTD values are calculated from the 2-h ZTD time series over

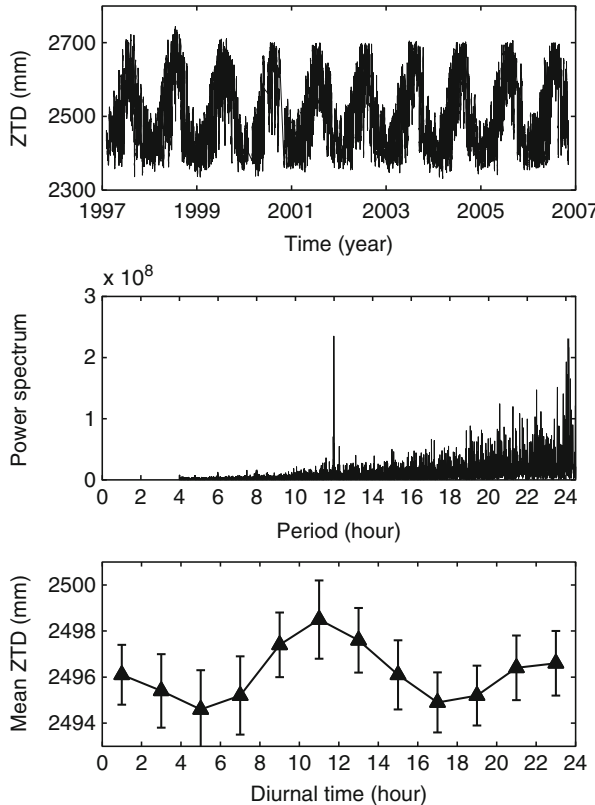


Fig. 3.15 Times series of zenith total delay (ZTD) (upper), power spectrum (middle) and mean diurnal ZTD values at each of local time ($LT = 1, 3, 5, \dots, 23$) over the entire period with error bars (bottom) at Wuhan (WUHN), China

10 years. Significant annual variations (upper panel) and subdiurnal variations with obvious 12 and 24 h periods are observed. To better demonstrate the short time scale variation, the diurnal component (24 h period, S_1) and semidiurnal component (12 h period, S_2) of the 10-year GPS-derived ZTD time series are further analyzed.

Figure 3.16 shows a colour coded map of diurnal ZTD amplitudes derived from the GPS data. The diurnal cycle (S_1) has amplitudes between 0.2 and 10.9 mm with an uncertainty of about 0.5 mm. The diurnal ZTD amplitudes reduce with increasing latitude with the largest amplitudes appearing in the low-latitude equatorial areas, in particular in tropical Asia and the Gulf of Mexico. At these low latitudes, amplitudes of up to 10.9 mm are observed, while the high latitude areas reveal generally lower diurnal ZTD amplitudes. The peak values of the diurnal cycles occur spreading over the whole day (Fig. 3.17). For the European stations there appears to be a preference for the second half of the day. At the semidiurnal cycle (S_2), amplitudes between

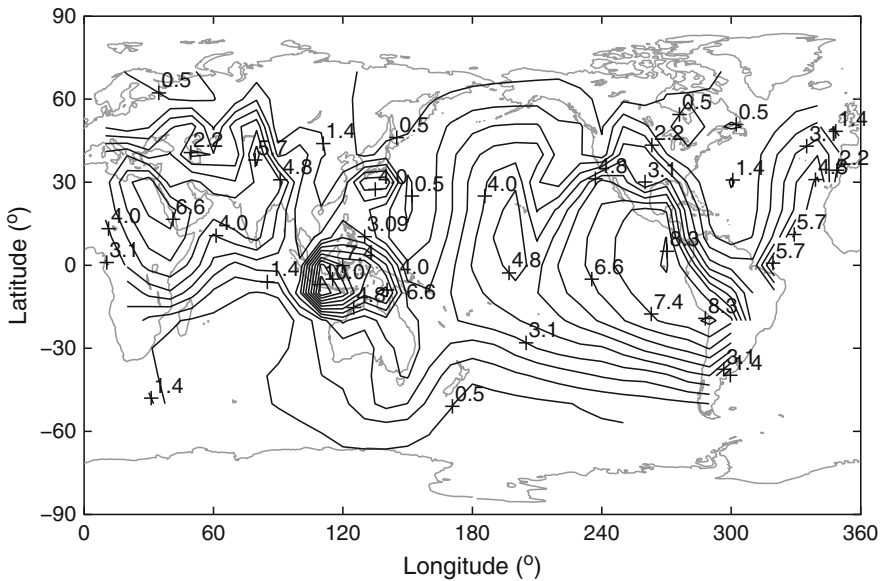


Fig. 3.16 Diurnal variation amplitudes (mm) from GPS-derived ZTD

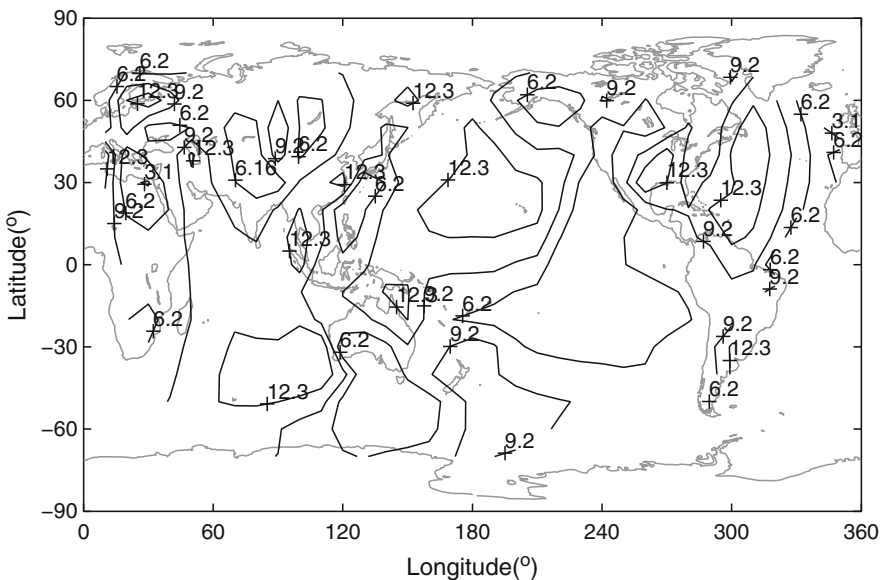


Fig. 3.17 Time of diurnal peak values at local time (LT: hour) at each GPS sites longitude where the Sun is at its highest elevation at 12:00 LT from global IGS GPS observations

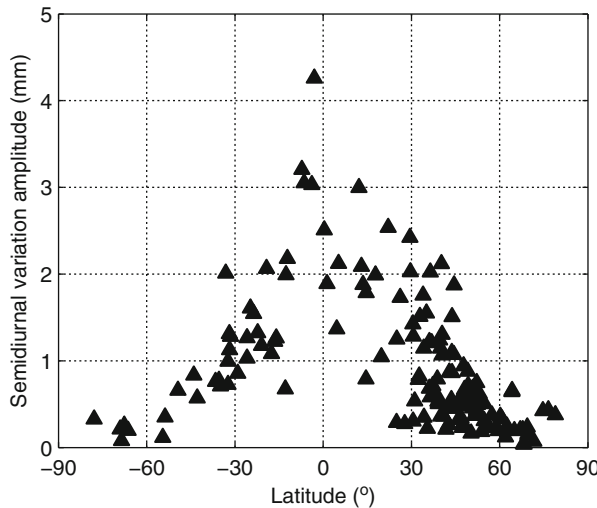


Fig. 3.18 Semidiurnal ZTD amplitudes as a function of station latitude

0.1 and 4.3 mm with an uncertainty of about 0.2 mm are observed. Similar to the diurnal results mentioned above, the largest semidiurnal amplitudes are also found in low-latitude equatorial areas (see Fig. 3.18). The first peak of the semidiurnal cycle occurs typically around local noon. These diurnal and semidiurnal cycles of ZTD may be due to certain short time scale physical processes such as diurnal convection, atmospheric tides, general circulation and the coupling between the lower and the middle and upper atmosphere.

The atmospheric density changes the refractive index of the zenith column of air under the influence of the atmospheric tides, which causes oscillations in the ZTD at tidal frequencies. Thus, the oscillations in ZTD within periods of a solar day (diurnal) and half a solar day (semidiurnal) may reflect the diurnal and semidiurnal tides induced on the atmosphere by thermal and gravitational excitation from the Sun. Under the assumption of hydrostatic equilibrium, the change in pressure with height is related to total density at altitude h through the approximate relationship with hydrostatic equilibrium approximation. Based on Eq. (3.11), the zenith hydrostatic delay (ZHD) can be expressed as $ZHD = 2.28 p_0$. As the hydrostatic component ZHD accounts for approximately 90 % of ZTD, ZTD is strongly correlated with surface pressure p_0 at the site. It can be seen that if subdiurnal surface pressure varies by 1 hPa, the scale factor predicts a subdiurnal ZTD variation with amplitude of 2.28 mm.

The GPS-derived S_1 and S_2 signals in ZTD are compared with 3-h surface synoptic pressure observations from 1997 to 2007 that are archived at the National Center for Atmospheric Research (NCAR) (DS464.0; <http://rda.ucar.edu/datasets/ds464.0>).

Notably, these results are adjusted by a scale factor 2.28 mm/hPa, which are accounted for in the comparison. These pressure data origin from more than 8,000 land and ocean weather stations including the Global Telecommunication System (GTS) and marine reports from the Comprehensive Ocean-Atmosphere Data Set (COADS) (Dai and Wang 1999). The plots of diurnal ZTD cycles (Figs. 3.20 and 3.21) and semidiurnal ZTD cycles (Figs. 3.22 and 3.24) show general similarities, indicating that the diurnal and semidiurnal atmospheric tides are probably the main driver of the diurnal and semidiurnal ZTD variations derived from GPS. However, there are also some discrepancies with the global surface pressure estimates, particularly in the S_1 . The larger discrepancies occur in the Pacific Ocean area and tropical regions, e.g. tropical south-east Asia, but also in North America and Western Europe. These discrepancies probably can be related to observation errors, different locations of the weather and GPS observation sites, the underlying geophysical signals and other processes.

On the one hand, reasons for differences in S_1 and S_2 between the GPS-derived results and those calculated from surface pressure data are suspected to lie in the applied mapping functions and the loading of the earth's crust, as these have unique diurnal and semidiurnal characteristics that are different from the S_1 and S_2 pressure tides. However, a recent simulation study by Humphreys et al. (2005) showed that the impact of the mapping functions of Niell (1996) is less than 11 % on the amplitude of the subdiurnal oscillations in ZTD, assuming an average distribution of elevation angles and an elevation cutoff of 7°. The effect of atmospheric pressure loading was found to be less than 11 % of the amplitude of the subdiurnal oscillations in ZTD (Humphreys et al. 2005). Also the estimated errors due to the solid Earth tide (Watson et al. 2006) and the ocean loadings (Dach and Dietrich 2000) on the amplitude of the subdiurnal oscillations in ZTD are found to be as high as 17 %. However, these effects are mitigated by applying corrections based on the solid Earth tide model IERS03 and ocean tide model FES2004, respectively. In addition, the water vapor diurnal variations will affect surface and atmospheric longwave radiation and atmospheric absorption of solar radiation (Dai et al. 2002; Pramualsakdikul et al. 2007) and possible atmospheric tides. However, this is difficult to verify as IGS stations have few co-located meteorological observations which would allow us to determine the amount of water vapor at the IGS stations independently. Further work is needed to investigate the importance of diurnal and semidiurnal variations in water vapor on ZTD. On the other hand, the differences in subdiurnal variations (particularly S_1) may be due to other processes, such as the diurnal cycle of convection and atmospheric large-scale vertical motion. Actually the classic tidal theory predicts that the diurnal tide S_1 is very complex and irregularly distributed (Chapman and Lindzen 1970). It needs to further investigate the complex subdiurnal variations and mechanism with more data in the future.

3.4 GNSS Precipitable Water Vapor

3.4.1 GNSS PWV Estimate

ZTD is the sum of the hydrostatic or dry delay (ZHD) and non-hydrostatic or wet delay (ZWD), due to the effects of dry gases and water vapor, respectively. The ZHD is related to the atmospheric pressure at the surface, i.e.

$$ZHD = 2.2779 \times 10^3 \frac{P_s}{f(\lambda, H)} \quad (3.12)$$

where P_s is the total surface pressure in millibars and $f(\lambda, H)$ is a factor for correcting the local gravity as $f(\lambda, H) = 1 - 0.00266 \cos(2\lambda) - 0.28H$, where λ is the latitude and H is the height above the ellipsoid in meters. The wet component ZWD can be obtained by subtracting ZHD from ZTD, which can be transformed into the precipitable water vapor (PWV) via the following function (Bevis et al. 1994):

$$PWV = \prod .ZWD \quad (3.13)$$

where $\prod = (10^{-6} \rho R_v [(k_3/T_m) + k_2'])^{-1}$, ρ is the density of liquid water, R_v is the specific gas constant for water vapor, T_m is a weighted mean temperature of the atmosphere, $k_2' = k_2 - mk_1$ and m is M_w/M_d , the ratio of the molar masses of water vapor and dry air (Davis et al. 1985). Therefore, if the pressure and temperate data are available, the water vapor can be derived from GPS-derived ZTD.

Due to the absence of local surface temperature and pressure data, the surface synoptic observations and numerical weather models' reanalysis products are used to calculate the P_s and T_m . The P_s is interpolated from global 3-h surface synoptic observations of all land and ocean surface weather stations with more than 15,000 including in the Global Telecommunication System (GTS) and marine reports from the Comprehensive Ocean-Atmosphere Data Set (COADS) (Dai and Wang 1999) (<http://dss.ucar.edu/datasets/ds464.0>). The T_m should be the best estimated from the 6-hourly re-analysis products ERA-40 (European Centre for medium range weather forecast 40 year reanalysis), but currently ERA-40 data are only available from 1948 to 2002, and the data after 2002 are not available. While the NCEP/NCAR reanalysis products are available from 1948 to present, and furthermore the interpolated T_m results are almost similar with a small difference between ERA-40 and NCEP/NCAR reanalysis (Wang et al. 2007). Therefore, in this study the 2-h T_m is estimated from the 6-hourly NCEP/NCAR reanalysis products (<ftp://ftp.cdc.noaa.gov/Datasets/ncep.reanalysis/>) with an interpolation technique (Wang et al. 2007). Thus, 2-h PWV time series for 1994–2007 over all global IGS sites can

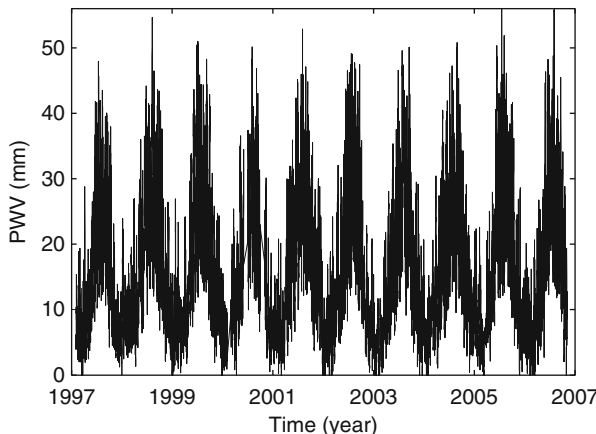


Fig. 3.19 PWV time series at ALGO, Canada

be derived from GPS-observed ZTD, surface synoptic observation-estimated P_s and NCEP/NCAR reanalysis-estimated T_m with errors of about 1.0–1.5 mm due to errors in ZTD, P_s and T_m . Also our GPS-derived PWV data are consistent with PWV estimates from IGS-provided combined ZTD (1997–2007) with a RMS of less 0.2 mm. For example, Fig. 3.19 shows the PWV time series at ALGO station (Canada).

3.4.2 Comparison with Independent Observations

The IGS GPS-derived PWV data are compared with another co-located independent technique-Very Long Baseline Interferometry (VLBI). Here VLBI-PWV was derived from co-located meteorological observations data. Snajdrova et al. (2005) analyzed 15 continuous days of VLBI data during the Continuous VLBI 2002 (CONT02) campaign and found that the ZTD from VLBI and GPS were in good agreement at the 3–10 mm level as well as with the Doppler Orbitography Radio positioning Integrated by Satellite (DORIS). Meanwhile, VLBI and GPS observed ZTDs are also quite good agreements with those from the European Centre for Medium-Range Weather Forecasts (ECMWF) and WVR. Niell et al. (2001) compared the results of a 2-week VLBI campaign in August 1995 (CONT95) at Westford (USA) with GPS, Water Vapor Radiometry (WVR) and radiosondes and found the VLBI technique was the most accurate for the determination of ZTD. These show that the VLBI can obtain a high accuracy reliable ZTD estimation. The Analysis Centers (Acs) of the International VLBI Service (IVS) process all available VLBI observation data and corresponding products (e.g. ZTD) are transferred to the IGG AC (Institute of Geodesy and Geophysics, Vienna University of Technology, Austria), for combination. The combined ZTD time series are available from

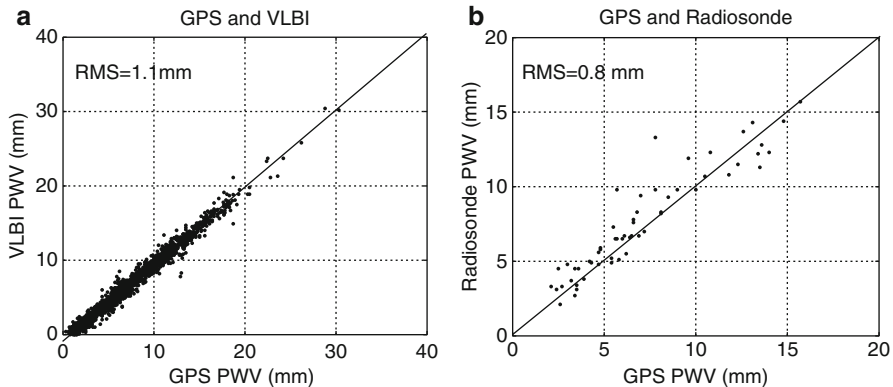


Fig. 3.20 Comparison of GPS-derived PWV with VLBI (upper panel) and radiosonde (bottom panel) at co-located station NYA1

IVS Data Centers (<ftp://cddis.gsfc.nasa.gov/vlbi/ivsproducts/trop>). Figure 3.20a is comparison of 3-year GPS and VLBI PWV data (2004–2007) at co-located station NYN1 (Norway). In total, the GPS-derived PWV agrees well with the co-located VLBI observations with a RMS of less than 1.1 mm. Also the GPS-derived PWV data are almost consistent with the radiosonde at NYA1 (Norway) with a RMS less than 0.8 mm (Fig. 3.20b).

3.4.3 Mean PWV Characteristics

Precipitable water vapor is a key parameter of the atmosphere and varies with a high degree of spatial and temporal variability, depending upon the season, topography and other local and regional climatic conditions. The global high spatial-temporal resolution IGS observations provide an important water vapor source to describe precipitable water vapor distribution features and to understand its variability and change. The mean PWV at each IGS site was calculated from the 2-h PWV time series for whole 13 years and their distributions are shown in Fig. 3.21. The mean water vapors are ranging from 5.0 ± 1.2 mm. The water vapor has a significant latitudinal distribution feature on a global scale. The larger water vapor concentrations are located in low latitudes, particularly in tropical areas with about 30–60 mm and generally decrease to the high latitude with less than 15 mm north of 60°N and south of 60°S . Water vapor contents over high elevations are generally lower (Fig. 3.22), decreasing with the increase of the elevation. In addition, the denser PWV distributions are shown a regionally-distributed feature. For example, the high PWV in Southeast Asia-North Australia may due to the influence of the Asian and west Pacific monsoons. Higher PWV in southeast of the Tibet are due to water vapor transportation from the Bay of Bengal and adjacent areas. At the same

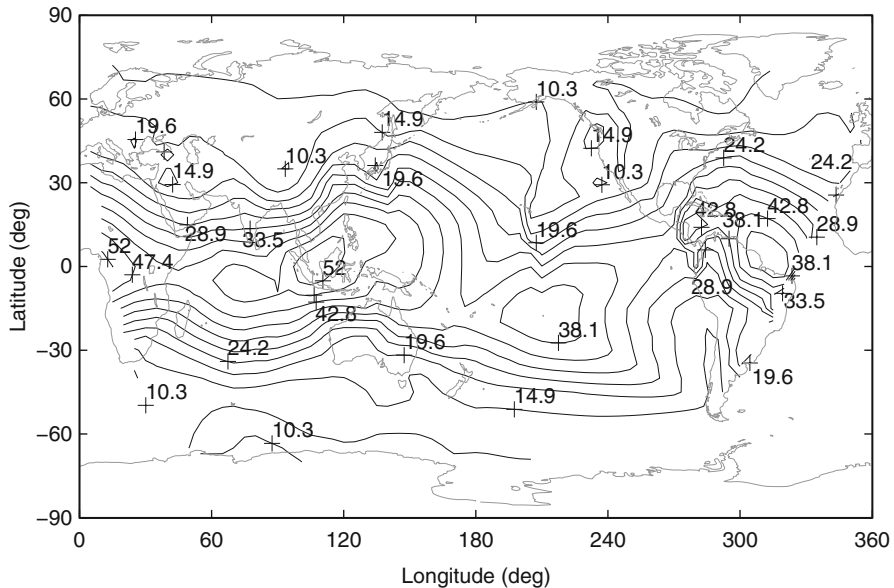


Fig. 3.21 Distribution of mean PWV (in mm) from global IGS observations for 1994–2007. The mean PWV at each site was calculated from the 2-h PWV time series for 13 years

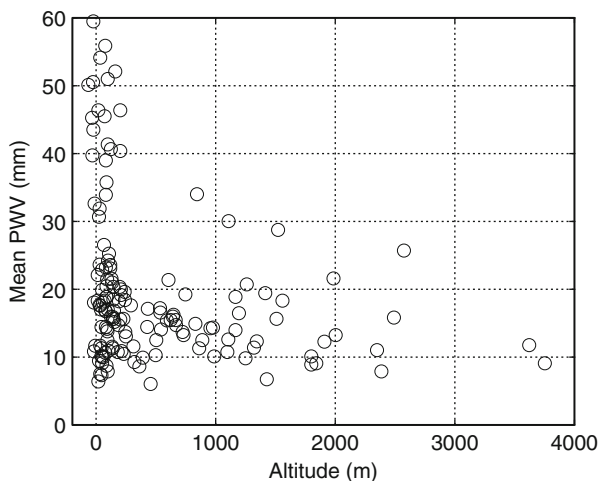


Fig. 3.22 Distribution of mean PWV with the elevation. The *circle* represents the mean PWV at each site

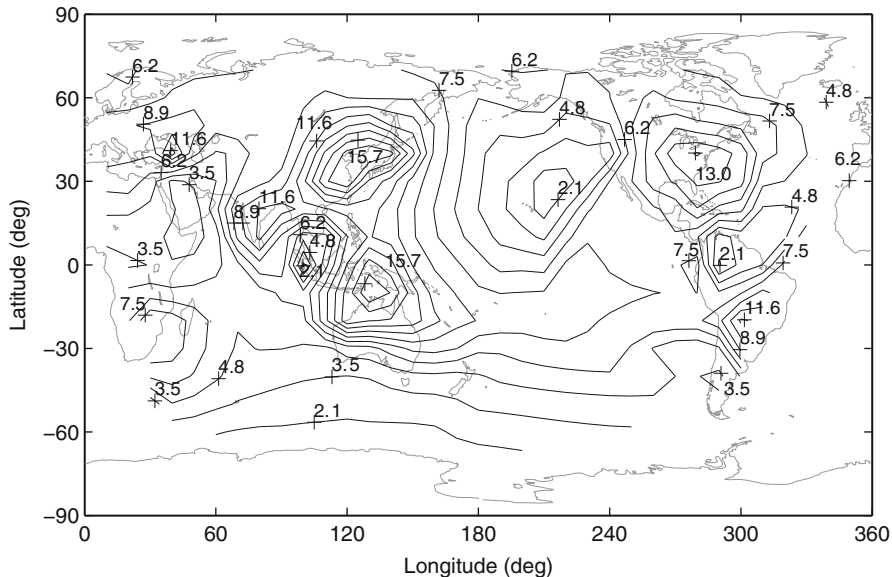


Fig. 3.23 Amplitude (in mm) of annual PWV variations from global IGS observations

latitude, the water vapor in western China is lower than in eastern China, which may be caused by a colder atmosphere over the high, snow-covered surface over the western areas, i.e. Tibet (Jin et al. 2008). Therefore, the distribution of atmospheric water vapor in the globe is mainly dominated by the latitude, topographical features, and climatic conditions.

3.4.4 Seasonal PWV Variations

The annual cycle of water vapor reflects the atmospheric process and circulation patterns. Figure 3.23 shows the amplitude (in units of mm) of annual PWV variations from global IGS observations. The higher amplitudes are found in mid-latitudes with about $10\text{--}20 \pm 0.5$ mm and the lower amplitudes with about 5 ± 0.5 mm are located in high latitudes and equatorial areas (Fig. 3.24). The peak of maximum water vapor concentration is in summer, i.e. July–August for the Northern Hemisphere and January–February for the Southern Hemisphere (Fig. 3.25). In contrast, the minimum water vapor content is in winter. The strong seasonal cycles in summer with a maximum water vapor are due to the influence of a moist summer

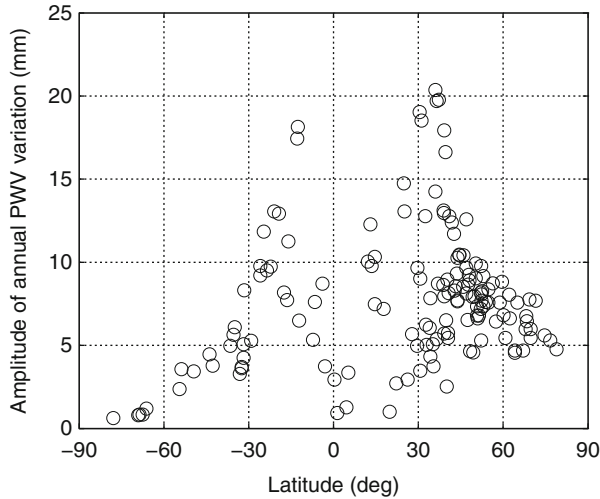


Fig. 3.24 Distribution of annual PWV variation amplitude with the latitude

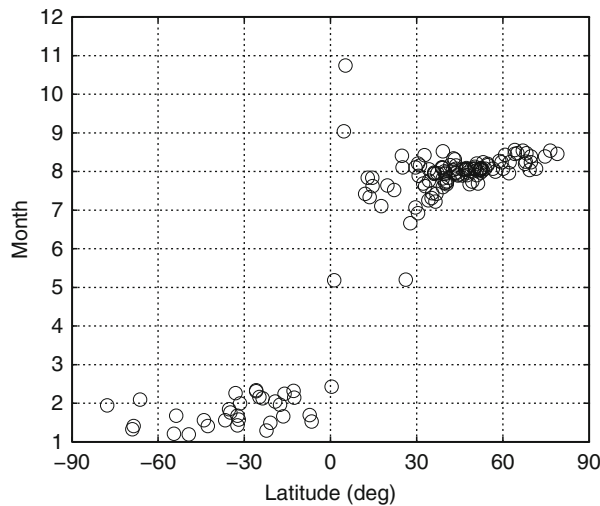


Fig. 3.25 Distributions of annual peak PWV phases with the latitude

monsoon and minimum water vapors in winter are due to a cold temperature. The semi-annual variation amplitudes are weak with about 0.5 ± 0.2 mm. The peak time of maximum semi-annual PWV variations are about in February–April and August–October.

3.4.5 Diurnal PWV Variations

The significant diurnal variations of the water vapors are also found over all GPS stations. The amplitudes of diurnal PWV variations are ranging from 0.2 to 1.2 \pm 0.1 mm. The diurnal PWV cycles are stronger in summer than in winter. The diurnal PWV cycles are closely related to the temperature. The peak times of diurnal PWV variations are from the noon to mid-night. The semidiurnal (12 h) PWV variations (S_2) are much weaker than the diurnal variations with amplitudes of less than 0.3 mm in difference seasons. The phase of the S_2 is noisier than that of the S_1 . In general, the S_2 peaks occur in early morning and afternoon (for the second cycle), or around midnight and noon. The diurnal PWV cycles are mainly controlled by atmospheric large-scale vertical motion, atmospheric low-level moisture convergence and precipitation, surface evapotranspiration and other factors (Dai et al. 2002).

3.5 3-D Water Vapor Topography

The Slant water vapor is defined as the line integral of the water density as expressed by:

$$SWV = \int W_e(\lambda, \phi, h) ds \quad (3.14)$$

where $W_e(\lambda, \phi, h)$ is the water density, λ , ϕ and h are the longitude, latitude and height, respectively. To obtain W_e , the troposphere is divided into grid pixels with a small cell where the water density is assumed to be constant, so that the SWV in Eq. (3.14) along the ray path can be approximately written as a finite sum over the pixels (i, j, k) as follows:

$$SWV = \sum_{i=1}^{N_i} \sum_{j=1}^{N_j} \sum_{k=1}^{N_k} a_{i,j,k} x_{i,j,k} \quad (3.15)$$

where $a_{i,j,k}$ is the length of the path-pixel intersections in the pixel (i, j, k) along the ray path, and $x_{i,j,k}$ is the water density for the pixel (i, j, k) . Each set of SWV measurements along the ray paths from all observable satellites at consecutive epochs are combined with the ray path geometry into a linear expression. The unknown water densities x can be estimated by the water tomographic technique. Due to the poor satellite-receiver geometry, Eq. (3.15) is ill conditioned, which needs additional constraints to resolve the ill-equation, e.g., with a covariance matrix for the correlation between the two voxels obtained from empirical water-field models or radiosonde observations.

3.6 Summary

The ground IGS observation data can provide high temporal resolution zenith tropospheric delay (ZTD). Together with global 3-hourly surface weather observations and 6-hourly NCEP/NCAR reanalysis products, water vapor can be obtained, which can be used to investigate the water vapor climatology and variability. It has been shown that the stronger water vapors are located in low latitudes, while high latitudes have lower water vapor contents. The distinct season cycles are found over all IGS stations. The marked seasonal cycles are in summer with a maximum water vapor and in winter with a minimum water vapor. The higher amplitudes are located in mid-latitudes with about $10\text{--}20 \pm 0.5$ mm and the lower amplitudes are located in high latitudes and equatorial areas with about 5 ± 0.5 mm. The semi-annual variation amplitudes are relatively weak with about 0.5 mm. The peak time of semi-annual PWV variations are about in February–April and August–October. In addition, significant diurnal variations of PWV are found over most IGS stations. The diurnal (24 h) cycle has amplitude of $0.2\text{--}1.2 \pm 0.1$ mm, which is closely related to the temperature, and the peak time is about from the noon to mid-night. The semidiurnal (12 h) cycle is weaker, with amplitude of less than 0.3 mm.

With the development and increase of existing IGS stations and regional permanent GPS network, such as national Crustal Movement Observation Network of China (CMONC) with about 30 continuous GPS sites, GPS Earth Observation Network (GEONET) of Japan with about 1,000 continuous GPS sites, and Korean GPS Network with about 80 continuous GPS sites, etc. it will provide denser GPS observations. Meanwhile, recent GPS radio occultation missions (e.g. CHAMP/GRACE, Formosat-3/COSMIC, and TerraSAR-X) also provide high spatial global 3-D water vapor estimations. In the near future, denser and near-real time atmospheric delay and water vapor data can be achieved from all available continuous GPS and radio occultation observations as well as other satellite observations, which provide new chances for meteorology and atmospheric research.

References

- Bevis M, Businger S, Herring TA, Rocken C, Anilis RA, Ware RH (1992) GPS meteorology: remote sensing of atmospheric water vapor using the Global Positioning System. *J Geophys Res* 97:15787–15801
- Bevis M, Businger S, Chiswell S et al (1994) GPS meteorology: mapping Zenith Wet Delays onto precipitable water. *J Appl Meteorol* 33:379–386
- Boehm J, Schuh H (2004) Vienna mapping functions in VLBI analyses. *Geophys Res Lett* 31:L01603. doi:[10.1029/2003GL018984](https://doi.org/10.1029/2003GL018984)
- Boehm J, Niell A, Tregoning P, Schuh H (2006) Global Mapping Function (GMF): a new empirical mapping function based on numerical weather model data. *Geophys Res Lett* 33:L07304. doi:[10.1029/2005GL025546](https://doi.org/10.1029/2005GL025546)
- Chapman S, Lindzen RS (1970) Atmospheric tides: thermal and gravitational. Gordon and Breach, New York, 200 pp
- Dach R, Dietrich R (2000) Influence of the ocean loading effect on GPS derived precipitable water vapor. *Geophys Res Lett* 27(18):2953–2956

- Dai A, Wang J (1999) Diurnal and semidiurnal tides in global surface pressure fields. *J Atmos Sci* 56:3874–3891
- Dai A, Wang J, Ware RH, Van Hove T (2002) Diurnal variation in water vapor over North America and its implications for sampling errors in radiosonde humidity. *J Geophys Res* 107(D10):4090. doi:[10.1029/2001JD000642](https://doi.org/10.1029/2001JD000642)
- Davis JL, Herring TA, Shapiro I, Rogers A, Elgered G (1985) Geodesy by radio interferometry: effects of atmospheric modeling errors on estimates of baseline length. *Radio Sci* 20(6):1593–1607
- Deblonde G, Macpherson S, Mireault Y et al (2005) Evaluation of GPS precipitable water over Canada and the IGS network. *J Appl Meteorol* 44(1):153–166
- Duan J, Bevis M, Fang P et al (1996) GPS meteorology: direct estimation of the absolute value of precipitable water. *J Appl Meteorol* 35:830–838
- Emardson TR, Elgered G, Johansson JM (1998) Three months of continuous monitoring of atmospheric water vapor with a network of GPS receivers. *J Geophys Res* 103:1807–1820
- Feng K, Zhang J, Zhang Y, Yang Z, Chao W (1978) The numerical calculation method. National Defense Industry Press, Beijing, 311 pp
- Haase J, Ge M, Vedel H, Calais E (2003) Accuracy and variability of GPS tropospheric delay measurements of water vapor in the western Mediterranean. *J Appl Meteorol* 42(11):1547–1568
- Hagemann S, Bengtsson L, Gendt G (2003) On the determination of atmospheric water vapor from GPS measurements. *J Geophys Res* 108(D21):4678. doi:[10.1029/2002JD003235](https://doi.org/10.1029/2002JD003235)
- Herring TA (1992) Modeling atmospheric delays in the analysis of space geodetic data. In: De Munck JC, Spoelstra TATH (eds) Refraction of transatmospheric signals in Geodesy. Netherland Geodetic Commission Publications in Geodesy, 36, pp 157–164
- Humphreys TE, Kelley MC, Huber N, Kintner PM Jr (2005) The semidiurnal variation in GPS-derived zenith neutral delay. *Geophys Res Lett* 32:L24801. doi:[10.1029/2005GL024207](https://doi.org/10.1029/2005GL024207)
- Jin SG, Park PH (2005) A new precision improvement of zenith tropospheric delay estimates by GPS. *Curr Sci* 89(6):997–1000
- Jin SG, Li Z, Cho J (2008) Integrated water vapor field and multi-scale variations over China from GPS measurements. *J Appl Meteorol Clim* 47:3008–3015. doi:[10.1175/2008JAMC1920.1](https://doi.org/10.1175/2008JAMC1920.1)
- Jin SG, Luo OF, Ren C (2010) Effects of physical correlations on long-distance GPS positioning and zenith tropospheric delay estimates. *Adv Space Res* 46(2):190–195. doi:[10.1016/j.asr.2010.01.017](https://doi.org/10.1016/j.asr.2010.01.017)
- King RW, Bock Y (1999) Documentation for the GAMIT GPS analysis software. Massachusetts Institute of Technology, Cambridge, MA
- Manuel H, Juan J, Sanz J et al (2001) A new strategy for real-time integrated water vapor determination in WADGPS networks. *Geophys Res Lett* 28(17):3267–3270
- Marini JW (1972) Correction of satellite tracking data for an arbitrary tropospheric profile. *Radio Sci* 7(2):223–231
- Niell AE (1996) Global mapping functions for the atmospheric delay at radio wavelengths. *J Geophys Res* 101(B2):3227–3246
- Niell AE, Coster AJ, Solheim FS, Mendes VB, Toor PC, Langley RB, Upham CA (2001) Comparison of measurements of atmospheric wet delay by radiosonde, water vapor radiometer, GPS, and VLBI. *J Atmos Ocean Technol* 18:830–850
- Pramualsakdikul S, Haas R, Elgered G, Scherneck HG (2007) Sensing of diurnal and semi-diurnal variability in the water vapor content in the tropics using GPS measurements. *Meteorol Appl* 14:403–412. doi:[10.1002/met.39](https://doi.org/10.1002/met.39)
- Saastamoinen J (1972) Atmospheric correction for the troposphere and stratosphere in radio ranging of satellites. In: The use of artificial satellites for geodesy, Geophysical monograph series 15. American Geophysical Union, Washington, pp 247–251
- Snajdrova K, Boehm J, Willis P, Haas R, Schuh H (2005) Multi-technique comparison of tropospheric zenith delays derived during the CONT02 campaign. *J Geod* 79(10–11):613–623. doi:[10.1007/s00190-005-0010-z](https://doi.org/10.1007/s00190-005-0010-z)
- Tregoning P, Boers R, O'Brien D (1998) Accuracy of absolute precipitable water vapor estimates from GPS observations. *J Geophys Res* 103(28):701–710

- Wang J, Zhang LY, Dai A, Van Hove T, Van Baelen J (2007) A near-global, 2-hourly data set of atmospheric precipitable water from ground-based GPS measurements. *J Geophys Res* 112:D11107. doi:[10.1029/2006JD007529](https://doi.org/10.1029/2006JD007529)
- Watson C, Tregoning P, Coleman R (2006) Impact of solid Earth tide models on GPS coordinate and tropospheric time series. *Geophys Res Lett* 33:L08306. doi:[10.1029/2005GL025538](https://doi.org/10.1029/2005GL025538)

Chapter 4

Ground GNSS Ionosphere Sounding

4.1 History

The ionosphere is about 60–1,000 km above the earth’s surface, which is actually plasma of ionized gas of the upper atmosphere by solar radiation and high energy particles from the Sun. The ionized electrons concentrations vary with the height above earth’s surface, location, time of the day, season, and amount of solar activity. In the past decades, different observing instruments have been developed and used to gather information on the ionosphere and plasmasphere, such as ionosonde, scatter radars (Tsunoda 1988), topside sounders onboard satellites (Reinisch et al. 2001), in situ rocket and satellite observations (Klobuchar 1991). But most instruments are restricted to either the bottomside ionosphere (ionosondes) or the lower part of the topside ionosphere (usually lower than 800 km), such as ground based radar measurements. The Global Positioning System (GPS) has provided an unprecedented high accuracy, flexibility and tremendous contribution to navigation, positioning, timing and scientific questions related to precise positioning on Earth’s surface, since it became fully operational in 1994. The Global Positioning System (GPS) is a satellite microwave technique whose signals are transmitted on microwave (L-band) carriers through the Earth’s atmosphere, and it inevitably suffers the ionospheric effect. When the GPS signal propagates through the Earth’s ionosphere, it is delayed by the ionospheric refractivity, which results in lengthening of the geometric path of the ray, i.e., ionospheric delay. Ionospheric delay will bring errors for GPS navigation and positioning as the electromagnetic wave signal goes through the earth’s ionosphere from satellites to receivers. The amount of ionospheric delay of GPS varies from a few meters to decades of meters, but it could reach more than 100 m during severe ionosphere storms. In contrast, the GPS ionospheric delay may provide some useful information on the ionosphere. In 1993, Bassiri and Hajj introduced the model for GPS ionospheric delay based on realistic modeling of the electron in the ionosphere using a dipole moment approximation for the Earth’s

magnetic field. After knowing the relationship between the total electron content (TEC) of signal path and the GPS ionospheric delay, ground-GNSS ionospheric sounding become possible.

Ware (1992) suggested limb sounding the Earth atmosphere using GPS atmospheric delay signals. On 3 April 1995, the small research satellite of Microlab-1 was successfully put into a Low Earth Orbit (LEO) to validate the GPS radio occultation method (Feng and Herman 1999). Since then, the ground and space based GPS has been used to provide accurate, all weather, global refractive index, pressure, density profiles in the troposphere, temperature with up to the lower stratosphere (35–40 km), and the ionospheric total electron content (TEC) as well as electron density profiles (Rocken 1997; Syndergaard 2000), to improve weather analysis and forecasting, monitor climate change, and monitor ionospheric events. Furthermore, GPS satellites in high altitude orbits of ~20,200 km are capable of providing details on the structure of the entire topside ionosphere, even the plasmasphere. Additionally, GPS is a low-cost, all-weather, near real time, and high-temporal resolution (30 s) technique (Klobuchar 1991). Therefore, GPS has become the most widely used method for investigations of ionospheric irregularities and related sciences (Mannucci et al. 1998). For example, Calais and Minster (1995) found the ionospheric perturbations following Northridge earthquake using the vertical TEC series derived GPS dual-frequency data.

In 1998 the ionosphere working group of the international GNSS serve (IGS) was created with the goal of generating reliable global ionospheric maps (GIM). Since then, the scientific community behind IGS, especially CODE (Center for Orbit Determination in Europe), ESA (European Space Agency), JPL (Jet Propulsion Laboratory) and UPC (Technical University of Catalonia), have been continuously contributing to reliable IGS combined vertical TEC maps. In addition, as lots of regional density GPS networks have been set up, such as GPS Network (GEONET) in Japan, high spatial and temporal resolution for regional ionospheric mapping can be derived. For some (grid) ionospheric models established by GPS, the parameters of the ionospheric models are usually determined by fitting all GPS data in the large area, which limits the precision of the model due to neglecting the local character of ionosphere and also is not suitable for analyzing the local effects of ionospheric parameters (e.g. Jin et al. 2004). For a small and local region, many methods are used to investigate grid ionospheric model using GPS data from ground GPS networks in the past several years, such as the methods of distance weight function of WAAS (e.g. Skone 1998), spherical harmonic function and the polynomial function (e.g. Schaer 1999).

However, in the past time, most scientists used ground-based GPS data to monitor ionospheric irregularities based on a single layer model (SLM) of the ionosphere at the altitude of electron density peak (generally 350 km above the Earth) (Schaer 1999; Otsuka et al. 2002). In fact, the single layer model ignored the vertical variation information of the ionosphere. Therefore, to better monitor the ionospheric activities in full dimensions, it is a new challenge to map 3-D ionosphere with GPS. Since Austen et al. (1988) first proposed the possibility of studying the ionosphere using satellite radio tomography, tomographic reconstruction techniques

have been applied recently to ionospheric imaging. Computer aided tomography is a well known technique in medicine, where two dimensional cross section images of the body are derived from measurements of the attenuation of X-rays passing through a human body from many different angles. In X-ray tomography the attenuation is proportional to the line integral of the X-ray absorption along the ray path through the body. Tomographic imaging of ionospheric electron density involves measurements of the total electron content (TEC) along trans-ionospheric ray paths between global positioning satellites (GPS) and ground-based receivers. In computerized ionospheric tomography (CIT) the line integrals comprise the slant TEC (STEC) of GPS ray path. Therefore, using ground based GPS STEC measurements and computerized ionospheric tomography it is possible to get 3-D ionospheric structures (Yin et al. 2004). In the following sections, the methods, 2-D and 3-D ionospheric sounding and applications from ground-based GPS observations are presented and discussed.

4.2 GNSS Ionospheric Sounding

The Global Positioning System (GPS) consists of a constellation of up to 30 operating satellites in six circular orbits 20,200 km above the Earth at an inclination angle of 55° with a 12-h (sidereal) period. Each GPS satellite broadcasts two spread spectrum L-band radio signals with the frequencies $f_1 = 1.57542$ GHz and $f_2 = 1.2276$ GHz. As the ionosphere is a dispersive medium, dual-frequency GPS receivers are able to evaluate the ionospheric effect by measuring the modulations on the codes and the carrier phases. The equations of carrier phase (L) and code observations (pseudorange P) of dual-frequency GPS are expressed as:

$$L_{k,j}^i = \lambda_k \phi_{k,j}^i = \rho_{0,j}^i - d_{ion,k,j}^i + d_{trop,j}^i + c (\tau^i - \tau_j) - \lambda_k (b_{k,j}^i + N_{k,j}^i) \quad (4.1)$$

$$P_{k,j}^i = \rho_{0,j}^i + d_{ion,k,j}^i + d_{trop,j}^i + c (\tau^i - \tau_j) + d_{q,k}^i + d_{q,k,j} + \varepsilon_j^i \quad (4.2)$$

where subscript k stands for the frequency ($k = 1, 2$), superscript i and subscript j represent the satellite and ground-based GPS receiver, respectively, and other parameters are:

- ρ_0 , the true distance between the GPS receiver and satellite;
- d_{ion} and d_{trop} , the ionospheric and tropospheric delays;
- c , the speed of light in vacuum space;
- τ , the satellite or receiver clock offset;
- b , the phase delay of satellite and receiver instrument bias;
- d_q , the code delay of satellite and receiver instrument bias;
- λ , the carrier wavelength;
- ϕ , the total carrier phase between the satellite and receiver;

N , the ambiguity of the carrier phase; and
 ε , other residuals.

One can easily obtain the following equations from Eqs. (4.1) and (4.2):

$$P_4 = P_{1,j}^i - P_{2,j}^i = \left(d_{ion,1,j}^i - d_{ion,2,j}^i \right) + DCB^i + DCB_j \quad (4.3)$$

$$L_4 = L_{1,j}^i - L_{2,j}^i = -\left(d_{ion,1,j}^i - d_{ion,2,j}^i \right) - \lambda \left(b_{1,j}^i - b_{2,j}^i \right) - \lambda \left(N_{1,j}^i - N_{2,j}^i \right) \quad (4.4)$$

where $DCB^i = d_1^i - d_2^i$, and $DCB_j = d_{1,j} - d_{2,j}$ stand for differential code biases of the satellites and differential code biases of the receivers, respectively. Since the pseudorange observations P_4 have larger noise, the carrier phases are used to smooth the pseudorange (Liu et al. 1998). Smoothed $P_{4,sm}$ observations can be expressed as follows:

$$P_{4,sm} = \omega_t P_4(t) + (1 - \omega_t) P_{4,prd}(t) \quad (t > 1) \quad (4.5)$$

where t stands for the epoch number, ω_t is the weight factor related with epoch t and

$$P_{4,prd}(t) = P_{4,sm}(t-1) + [L_4(t) - L_4(t-1)] \quad (t > 1) \quad (4.6)$$

when t is equal to 1, which means the first epoch of one observation arc, $P_{4,sm}$ is equal to P_4 . Cycle slips and gross errors in the carrier phase observations should be removed before using the carrier phase observations to smooth the pseudorange observations. Here both dual-frequency pseudorange code observations (Melbourne-Wubena combination) and ionospheric residual observations are used to detect cycle slips and gross errors.

Only the first order of ionospheric refraction is considered while estimating the ionosphere delay in GPS processing, due to the minor effect of the higher orders. The ionosphere delay can be expressed as follows:

$$d_{ion} = \frac{40.3}{f^2} STEC \quad (4.7)$$

where f stands for the frequency of the carrier, and $STEC$ stands for the slant total electron content along the path of the signal (see Fig. 4.1). Substituting Eqs. (4.7) into (4.3), and replacing P_4 by smoothed $P_{4,sm}$, we get:

$$P_{4,sm} = 40.3 \left(\frac{1}{f_1^2} - \frac{1}{f_2^2} \right) STEC + DCB^i + DCB_j \quad (4.8)$$

After smoothing, more reliable DCB estimate values can be extracted from GPS data and then the STEC can be determined.

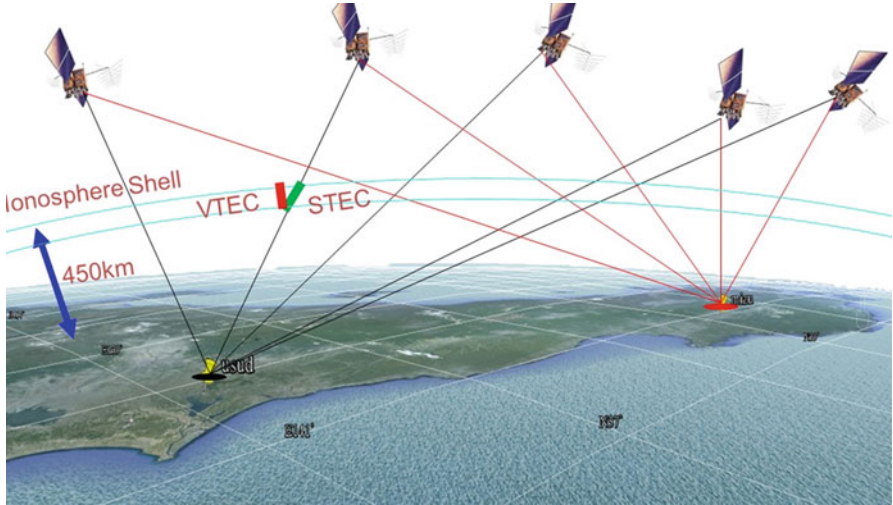


Fig. 4.1 Geometry of GPS-TEC estimation

4.2.1 DCB Determination

From Eq. (4.8), it is easy to extract slant total electron content (STEC) from GNSS dual-frequency observations as follow

$$STEC = -\frac{f_1^2 f_1^2}{40.3(f_1^2 - f_2^2)} (P_{4,sm} - cDCB_j - cDCB^i) \quad (4.9)$$

where DCB's unit is the time. The earth's ionosphere ranges in altitude from 60 to $\sim 1,000$ km. It is assumed that all electrons in the ionosphere are concentrated in a thin shell at altitude H (see Fig. 4.1), so the STEC can be translated into the vertical total electron content (VTEC) using the modified single-layer model (MSLM: http://aiuws.unibe.ch/spec/ion.php#processing_description), namely

$$\begin{aligned} VTEC &= MF(z)STEC \\ MF &= \cos \left(\arcsin \left(\frac{R}{R+H} \sin(\alpha z) \right) \right) \end{aligned} \quad (4.10)$$

where z is the satellite elevation angle, R is the earth's radius, and H is the attitude of the ionosphere thin shell (normally the approximate peak height of the F2 layer). R is set to 6,371 km. H and α can be set by users. Here they are defaulted as $H = 506.7$ km and $\alpha = 0.9782$ which are consistent with the values used by the CODE group. An ionospheric spherical harmonic function is applied in the M_DCB software. The VTEC, $E(\beta, s)$ can be expressed as follows (Schaer 1999):

$$E(\beta, s) = \sum_{n=0}^{n_{\max}} \sum_{m=0}^n \tilde{P}_{nm} (\sin \beta) (a_{nm} \cos ms + b_{nm} \sin ms) \quad (4.11)$$

where β is the geocentric latitude of the ionosphere pierce point (IPP), $s = \lambda - \lambda_0$ is the sun-fixed longitude of the IPP, λ, λ_0 are the longitude of the IPP and the apparent solar time, respectively, a_{nm}, b_{nm} are the global or regional ionosphere model coefficients, $\tilde{P}_{nm} = \Lambda(n, m) P_{nm}$ are normalized Legendre polynomials. The Λ denotes the normalization function, and P_{nm} are unnormalized Legendre polynomials, with

$$\Lambda = \sqrt{2 \frac{2n+1}{1 + \delta_{0m}} \frac{(n-m)!}{(n+m)!}} \quad (4.12)$$

and with δ being the Kronecker Delta. Substituting Eqs. (4.9) and (4.10) into Eq. (4.11), the following expression can be obtained:

$$\begin{aligned} & \sum_{n=0}^{n_{\max}} \sum_{m=0}^n \tilde{P}_{nm}(\sin \beta) (a_{nm} \cos ms + b_{nm} \sin ms) \\ &= \cos \left(\arcsin \left(\frac{R}{R+H} \sin(\alpha z) \right) \right) \left[-\frac{f_1^2 f_1^2}{40.3 (f_1^2 - f_2^2)} (P_4 - cDCB_j - cDCB^i) \right] \end{aligned} \quad (4.13)$$

where P_4 are the smoothed observations, and a_{nm}, b_{nm}, DCB_j and DCB^i are unknown parameters to be estimated, respectively. The order of spherical harmonics expansion depends on the areas. Users can set the appropriate order in the main program(s) on the command line. For the regional, continental and global size, normally it uses 4th, 8th and 15th order, respectively. Here for our small areas tests, the spherical harmonics expansion is defaulted as fourth order. A set of ionosphere coefficients is assumed every 2 h, but of course can be changed. For one GPS station, there are more than 20,000 measurements every day. Thus the number of observations is much more than the number of unknown parameters. According to the theory described above, the DCB and ionosphere coefficients can be estimated from GPS dual-frequency observations by the least squares (LS) method. Before the LS estimate, carrier phase smoothing using pseudo-ranges is used in the data pre-processing. Since Eq. (4.13) is singular, one exterior constraint condition must be added in order to separate the DCBs of satellites and receivers. It is routinely assumed that the sum of all GPS satellite DCB values is zero. Under this constraint condition, Eq. (4.13) reaches full rank and the DCBs of the satellites and receivers can be separated.

The M_DCB software was developed in Matlab (version: 2010b), which is available at http://www.ngs.noaa.gov/gps-toolbox/m_dcb.htm. GPS RINEX observation files and precise ephemerides are the input for M_DCB. Here GPS RINEX observations containing P_1 and P_2 observations are defaulted. The outputs are the DCB estimates of the satellites and receivers and TEC ionosphere coefficients for the relative region. IONEX files are used to check our DCB estimates. Figure 4.2 shows the flowchart for the M_DCB calculation.

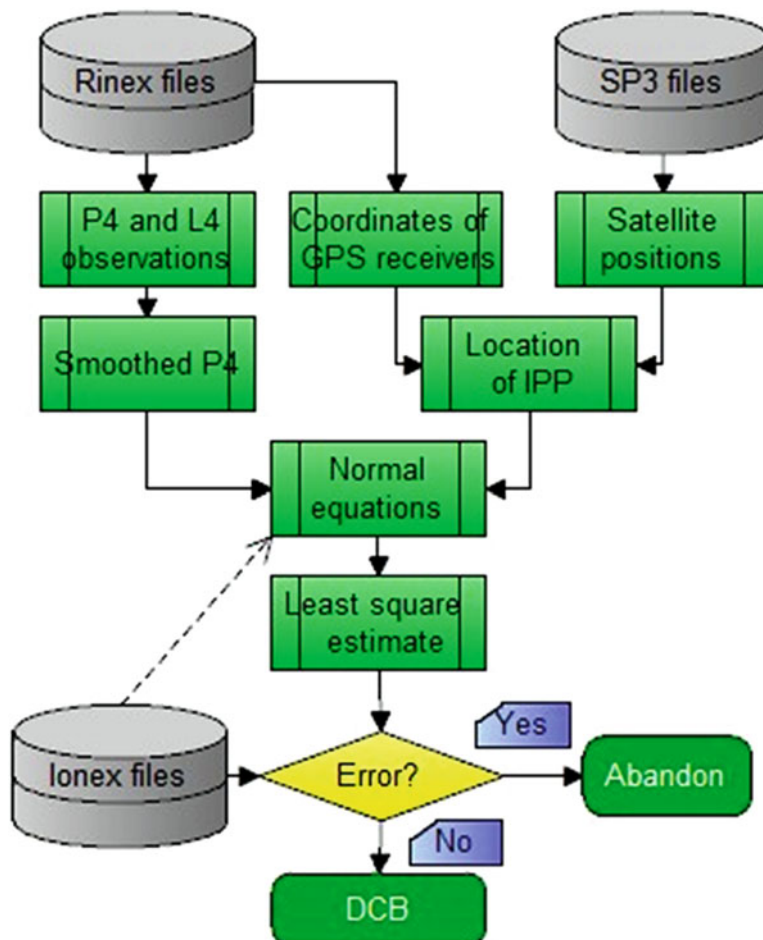


Fig. 4.2 Flowchart of GNSS DCB calculations

The M_DCB software package can estimate the DCB for a single station or for multiple stations. For a single station, usually not all the GPS satellites are available in one GPS receiver view. It is not convenient to use the constraint condition mentioned in Sect. 2.2 for such a case. Here, IONEX files are used to confirm our estimate using the same constraint conditions. The DCBs of satellites without observations are set as known parameters.

IGS stations that were chosen to test the M_DCB estimates are shown in Fig. 4.3. RINEX files (<http://sopac.ucsd.edu/cgi-bin/dbDataBySite.cgi> or <ftp://cddis.gsfc.nasa.gov/gps/data/>), SP3 files (<ftp://igscc.jpl.nasa.gov/igscc/>) and IONEX files (<ftp://cddis.nasa.gov/pub/gps/products/ionex/>) are used in our experiment. For some users, they may have only one GPS station or a multi-station network. The M_DCB

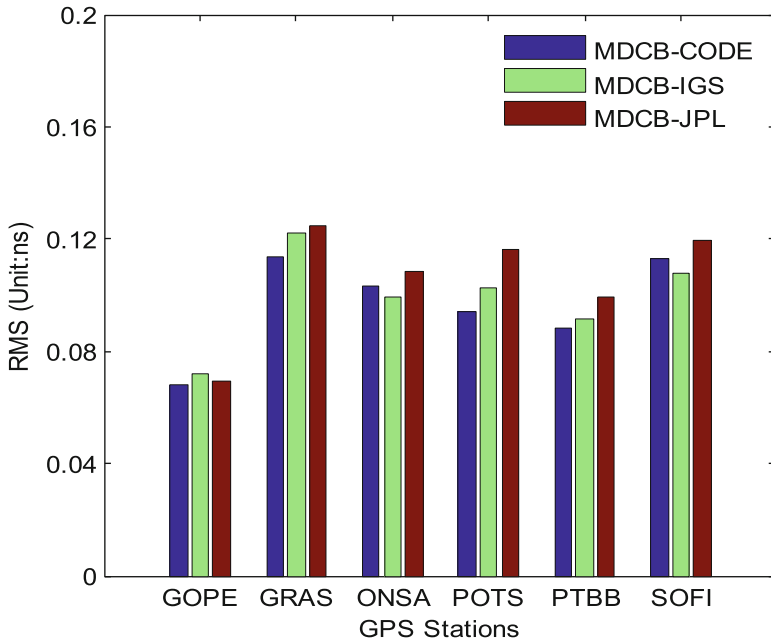


Fig. 4.3 The RMSs of the differences between receiver DCB values estimated by M_DCDB and those released by CODE, JPL, and IGS-combined

can estimate the DCB for multiple stations or one station. In the following subsections, the test results using a multi-station network and a single station are presented, respectively, which are evaluated using the IGS solutions, such as those by CODE, JPL, and IGS-combined.

4.2.1.1 Test Results of Multi-stations

The DCB values of the satellites and receivers are estimated from January 1–31, 2010 using the M_DCDB software. Here DCB estimate values released by CODE are regarded as reference values to validate the M_DCDB result. CODE uses 15 orders of spherical harmonic functions to describe the global total electron content of the earth's ionosphere every 2 h. Both global GPS and GLONASS observations are used during DCB estimation (<http://www.aiub.unibe.ch/>). DCB values estimated by M_DCDB and those released by CODE are compared in Table 4.1. Receiver DCB biases are slightly larger than those for satellites, but most of them are less than 0.4 ns except PRN1 whose DCB bias reaches 0.746 ns. The RMS of all differences is lower than 0.3 ns. Since the number of valid observations (when the elevation angle is more than 20°) for PRN 1 is approximately a quarter of the other satellites each day from January 1–31, the larger bias in PRN 1 is probably caused by fewer observations.

Table 4.1 The RMS and mean differences of satellite and receiver DCB estimates from January 1–31, 2010 using multiple GNSS stations (M_{DCB} minus CODE)

Satellite	RMS	Differences	Satellite	RMS	Differences
PRN1	0.251	0.746	PRN17	0.138	0.038
PRN2	0.087	-0.073	PRN18	0.100	-0.044
PRN3	0.066	0.194	PRN19	0.066	0.381
PRN4	0.123	0.003	PRN20	0.073	0.004
PRN5	0.111	-0.236	PRN21	0.088	-0.121
PRN6	0.061	0.169	PRN22	0.109	0.050
PRN7	0.085	-0.233	PRN23	0.053	0.052
PRN8	0.085	-0.271	PRN24	0.076	-0.221
PRN9	0.088	0.038	PRN25	0.085	-0.220
PRN10	0.095	-0.343	PRN26	0.092	-0.020
PRN11	0.063	0.202	PRN27	0.088	0.060
PRN12	0.051	0.049	PRN28	0.107	-0.340
PRN13	0.062	0.140	PRN29	0.091	-0.277
PRN14	0.126	0.150	PRN30	0.074	0.020
PRN15	0.117	-0.164	PRN31	0.138	0.057
PRN16	0.084	0.096	PRN32	0.077	0.115
BOGO	0.080	0.065	POTS	0.094	0.237
BRUS	0.111	0.309	PTBB	0.095	0.201
GOPE	0.068	0.142	SOFI	0.113	0.081
GRAS	0.131	0.370	WTZA	0.083	0.270
ONSA	0.103	0.178			

The RMS between DCBs estimated by M_{DCB} and those from CODE, JPL, and the IGS combination during January 1–30, 2010 are shown in Fig. 4.3. The M_{DCB} estimates are most consistent with the CODE solutions and the differences between M_{DCB} estimates and the JPL solutions are larger. CODE’s results have been estimated with an external calibration. The database and order of the spherical harmonic functions during DCB estimation are different. Here we use GPS observations from just 19 IGS stations, while the JPL uses the triangular mesh model to describe the ionosphere while estimating DCB and TEC coefficients, and the IGS values are from the combination of several GNSS analysis centers. Some systematic differences may be from the processing strategies and models used, while the RMS values have almost no significant difference with respect to each other.

4.2.1.2 Test Results of Single Station

Sometimes, one must estimate a DCB for a single station. In order to test the validation of a single station DCB estimate using the M_{DCB} software, the single station DCB is tested at GOPE, GRAS, ONSA, POTS, PTBB and SOFI, respectively.

Table 4.2 The RMSs and mean differences of single station DCB estimate from January 1–31, 2010 (M_DCB minus IGS combined)

	Differences (ns)	RMS(ns)
GOPE	0.530	0.209
GRAS	0.577	0.280
ONSA	0.623	0.338
POTS	0.637	0.216
PTBB	0.483	0.247
SOFI	-0.205	0.257

Table 4.2 shows the mean differences and RMSs for these 30 days between the IGS combined DCB values and single station's DCB estimated by M_DCB. It has been shown that one station also can get reliable results for a DCB estimate with a mean difference of less than 0.7 ns and an RMS of less than 0.4 ns. However the result is not as good as the DCB estimate based on multiple stations. A multi-station estimate is recommended for local network receiver DCB computation. When we estimate a new receiver DCB, we should take advantage of the nearest IGS stations for more accurate DCB estimates.

4.2.2 TEC Estimate

After determining the DCB, the STEC can be estimated from Eqs. (4.3) and (4.4), i.e.,

$$L_4 = L_{1,j}^i - L_{2,j}^i = -40.3 \left(\frac{1}{f_1^2} - \frac{1}{f_2^2} \right) STEC + B_4 \quad (4.14)$$

$$P_4 = P_{1,j}^i - P_{2,j}^i = 40.3 \left(\frac{1}{f_1^2} - \frac{1}{f_2^2} \right) STEC + b_4 \quad (4.15)$$

where STEC is the slant total electron content (STEC) of the GPS signal ray path, b_4 is $DCB^i + DCB_j$, and B_4 is ($B_4 = -\lambda_1(b_{1,j}^i + N_{1,j}^i) + \lambda_2(b_{2,j}^i + N_{2,j}^i)$), which can be obtained as $\sum_{i=1}^N (P_4 + L_4 - b_4)/N$, where N is the number of samples for one arc of GPS observations. Thus, the precise STEC can be derived from dual-frequency GPS carrier phase and code observations (Jin et al. 2004, 2006).

Earth's ionosphere ranges from 60 km to more than 1,000 km altitude. When satellites are not located at the zenith of stations, the latitude and longitude of each point on the signal path are different. It is very complex to model the Earth's ionosphere in this situation. Usually, it is assumed that all electrons in the ionosphere are concentrated in a thin shell at altitude H (see Fig. 4.4), which is called as the shell central ionospheric layer. The altitude H will be defined as at 300 ~ 600 km altitude, where the electron density reaches up to the peak. The Vertical TEC (VTEC),

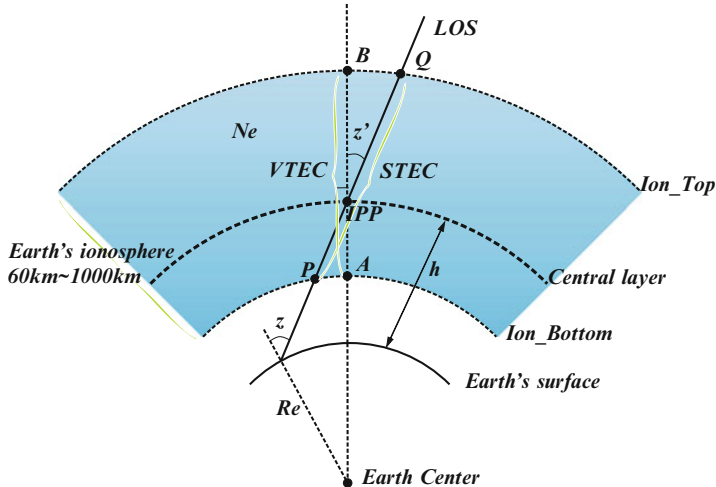


Fig. 4.4 Geometry of a thin shell GNSS ionospheric mapping

which is total electron content in zenith, can be obtained from the STEC using an appropriate mapping function, see Eq. (4.10).

4.3 2-D Ionospheric Mapping

Two-dimensional region and global VTEC models can be established using some functions, e.g., surface fitting, distance-weighted, hardy function interpolation, spherical harmonics functions and triangular grid methods as well as differential areas for differential stations (DADS) (Yuan and Ou 2002).

4.3.1 Method of 2-D Ionospheric Mapping

4.3.1.1 Surface Fitting Method

Surface fitting model is based on the mathematic expression. In this model, VTEC is a function of differential latitude and differential solar time angle.

$$VTEC = \sum_{i=0}^n \sum_{j=0}^m E_{ij} (\varphi - \varphi_0)^i (S - S_0)^j \quad (4.16)$$

where φ_0 is the geographic latitude of the central point of the surveyed area, and $(S - S_0)$ is the differential solar time angle. i, j are the order.

4.3.1.2 Distance-Weighted Method

Ionospheric distance-weighted model is based on the meshing technology. Mesh VTEC values are computed by distance weighted average method using the measured VTEC.

$$VTEC^j = \frac{\sum_{i=1}^n \frac{VTEC^i}{D_{ij}}}{\sum_{i=1}^n \frac{1}{D_{ij}}} \quad (4.17)$$

$$(D_{ij} \leq DR)$$

where i, j are the number of the grid network. DR is the threshold of distance-weighted. If the distance between the grid and the ionospheric pierce point is larger than the threshold, measurement VTEC of this point will not be considered for distance-weighted average.

4.3.1.3 Hardy Function Interpolation (HFI) Method

In 1977, Hardy developed the Hardy Function Interpolation (HFI) method. We here apply the HFI method to establish GPS grid ionospheric model over a small local region. For the GPS site coordinates (B_i, L_j) , the VTEC of fitting model can be written as (Jin et al. 2004):

$$VTEC(B, L) = \sum_{i=1}^n a_i Q(B, L, B_i, L_i) \quad (4.18)$$

where $VTEC(B, L)$ is the VTEC of the measurement points in a single plane, $(B_i$ and $L_i)$ is the coordinate of grid node, and a_i is the vector of the VTEC value at the grid point. The corresponding core function can be expressed as follows:

$$Q(B, L, B_i, L_i) = [(B - B_i)^2 + (L - L_i)^2 + \varepsilon^2]^\beta \quad (4.19)$$

where ε^2 and β are the smooth factor, whose empirical values are 0.01 and 0.5 respectively. If there are m measurement points (B_j, L_j) and n grid nodes (B_i, L_i) , and let n grid nodes (B_i, L_i) as central sites of core function Q . Thus, the VTEC of each GPS epoch in the Eq. (4.18) can be written as follows:

$$v_{(VTEC)} = Qa \quad (4.20)$$

Namely:

$$\begin{bmatrix} v_1(B_1, L_1)_{VTEC} \\ v_1(B_2, L_2)_{VTEC} \\ \vdots \\ v_1(B_m, L_m)_{VTEC} \end{bmatrix} = \begin{bmatrix} Q(B_1, L_1, B_{i1}, L_{i1}) & \cdots & Q(B_1, L_1, B_{in}, L_{in}) \\ \vdots & & \vdots \\ Q(B_m, L_m, B_{i1}, L_{i1}) & \cdots & Q(B_m, L_m, B_{in}, L_{in}) \end{bmatrix} \begin{bmatrix} a_1 \\ a_2 \\ \vdots \\ a_n \end{bmatrix} \quad (4.21)$$

The error equation is as follows:

$$\Delta v = Qa - v_{VTEC} \quad (4.22)$$

Through the Eq. (4.22) we can obtain the vector a by a weighted least squares adjustment to all GPS observations in each epoch, namely

$$a = (Q^T P_v Q)^{-1} Q^T P_v v \quad (4.23)$$

where P_v is the weight matrix of the VTEC. And that, we can obtain the VTEC of random grid sites, namely: $VTEC_h = Q_h^t a$, where $Q_h^t = (Q_{h1} \ Q_{h2} \ \cdots \ Q_{hi})$.

4.3.1.4 Spherical Harmonics Functions

For global VTEC expression, spherical harmonics functions are widely used (Schaer 1999).

$$VTEC(\varphi, \lambda) = \sum_{n=0}^{n_{\max}} \sum_{m=0}^n \tilde{P}_{nm}(\sin \beta) (a_{nm} \cos ms + b_{nm} \sin ms) \quad (4.24)$$

β is the latitude of the ionosphere pierce point, $s = \lambda - \lambda_0$ is the sun-fixed longitude. λ, λ_0 are the longitude of the ionosphere pierce point and the apparent solar time. a_{nm}, b_{nm} are the ionosphere model's coefficients. \tilde{P}_{nm} are normalized Legendre polynomials. Normalization function is as follow.

$$\Lambda = \sqrt{\frac{(n-m)! (2n+1) (2-\delta_{om})}{(n+m)!}} \quad (4.25)$$

4.3.1.5 Triangular Grid Method

Another VTEC description is used in JPL's global VTEC computation. They use triangular grid to express the global VTEC distribution and variation. For each grid

point, a stochastic process is used to describe VTEC's variation as time. Parameters which need to be estimated are the VTEC values of grids.

$$VTEC_{IPP} = \sum_{i=V_A, V_B, V_C} W(\theta, \varphi, i) VTEC_i + b_r + b_s \quad (4.26)$$

b_r, b_s are instrument biases. $W(\theta, \varphi, i)$ is the weight which is related to the distance between the grid points to the ionosphere pierce points.

4.3.2 Applications of 2-D GNSS TEC

Nowadays, ground-GNSS observations have been widely used to monitor the Earth's ionosphere, particularly for global and mid-small scales ionospheric variations and disturbances from continuous GNSS observations. On one hand, the global ionospheric models (GIM) with more and more accuracy could correct ionospheric delay for L-band observations, e.g., InSAR and Radar Altimetry. On the other hand, GNSS-derived TEC can be used for ionospheric research and useful signals or indicators of some activities from natural sources (e.g., earthquake and volcano) and anthropogenic sources (such as rocket launching, explosion and so on).

4.3.2.1 TEC Climatology

The total electron content (TEC) is one of important parameters in the Earth's ionosphere, related to various space weather and solar activities. However, understanding of the complex ionospheric environments is still a challenge due to the lack of direct observations, particularly in the polar areas, e.g., Antarctic. Now more and more continuous operational GPS stations are set up, GPS has become a powerful tool to monitor global and region TEC. The international GNSS service (IGS) has routinely produced global vertical TEC maps every 2 h for more than 10 years, which can be used to investigate the ionospheric TEC climatology at seasonal and secular scales. Figure 4.5 (upper) shows obviously annual variation of long GPS TEC time series over Antarctica at the point (120°E , -87.5°S), and the mean values of vertical TEC over the Antarctica have a slight decrease (Jin and Jin 2013). The 2,880 MHz solar flux variations during 2002–2012 are also shown in Fig. 4.5 (bottom). The vertical TEC variation shows agreement with the solar activities. Higher amplitudes of vertical TEC time series are found in around 2003 and 2011, which are higher solar activities years. Although, for the most time, the Sun is not visible in areas near the South Pole in Antarctica, the variation of amplitudes is obvious. In addition, the mean values and the standard deviations of about 10 years GPS TEC series over Antarctica increase with the latitude degrease at latitudinal circles. Probably, this phenomenon can be explained due to the differences of solar radiation in different latitude. Solar fluxes become smaller and smaller when the location is getting closer

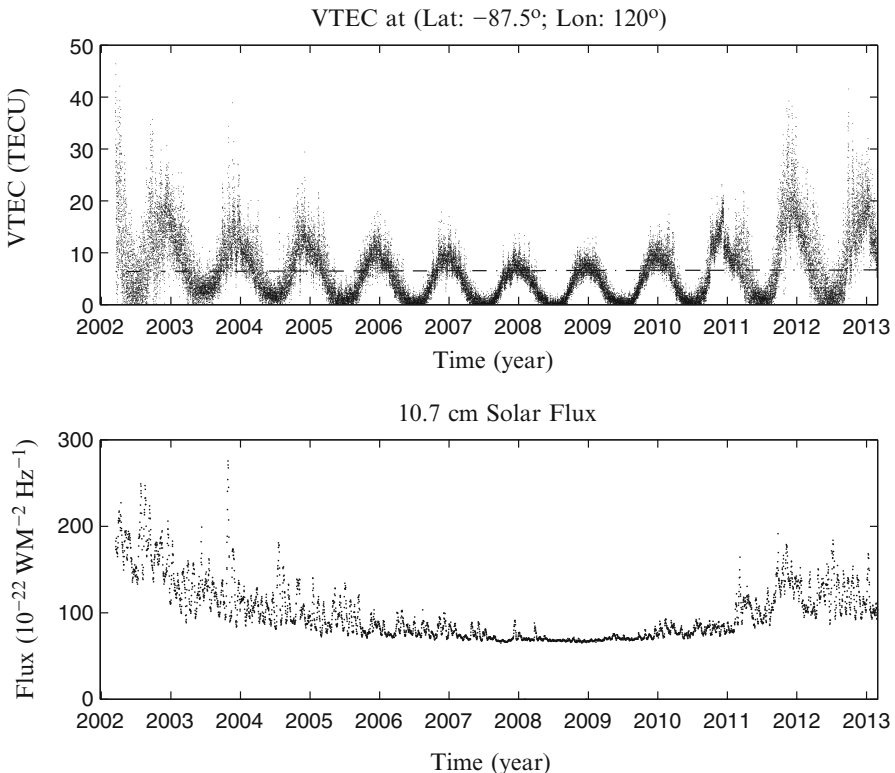


Fig. 4.5 Long term variation and Fluctuation of TEC from 2002 to 2012 over Antarctica

to the South Pole. Earth's ionosphere gets less energy for ionization near the South Pole. Lower vertical TEC and fewer fluctuations are shown in long-term vertical TEC in higher latitude areas over Antarctica. Figure 4.6 shows the distribution of the annual amplitudes and phases of GPS TEC times series from day 076, 2002 to day 252, 2012. The amplitudes and phases are both related to the longitude and latitude. The average amplitudes range from 4 to 6 TECU, and increase as the decrease of latitudes. And for 0°W to 120°W , the average amplitudes are relatively large. Initial phases also changes with the latitude variations exclude from 120°E to 170°E .

4.3.2.2 TEC Responses to Solar Flare and Storms

During solar flares, X-rays and ultraviolet rays emission enhance, which will make the ionosphere disturbances. This phenomenon can be detected by ground-based incoherent scatter radars, high-frequency Doppler and some other technologies. In addition, intense electromagnetic emission triggered by solar flare will lead the Earth magnetic field change dramatically, which is called the Earth magnetic storm.

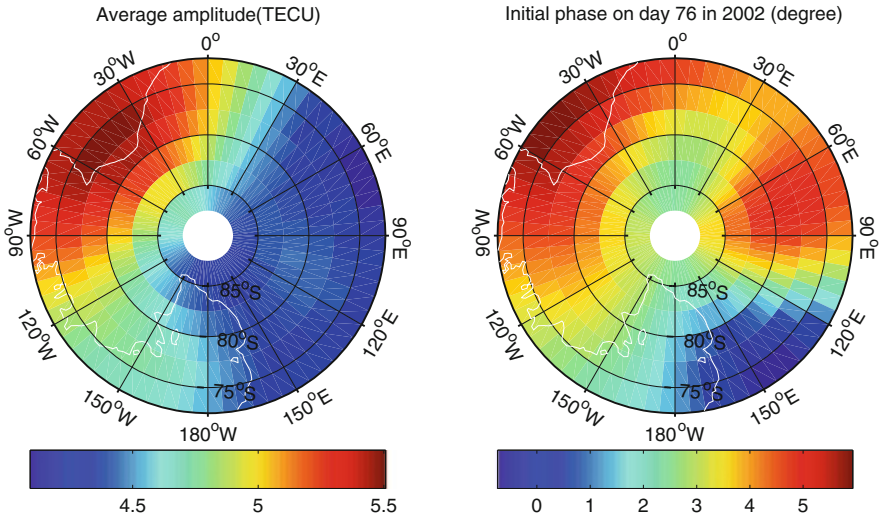


Fig. 4.6 GPS TEC average annual amplitudes and initial phases over Antarctica

These storms also can disturb Earth's ionosphere from several hours to several days. Nowadays, GNSS will be a new and powerful tool for solar flare and its effects monitoring. For example, Fig. 4.7b shows the VTEC time series at the grid points of different latitudes, (-15° S, 145° E), (-30° S, 145° E) and (-45° S, 145° E) in Australia during the geomagnetic storm from 19 to 21 Nov 2003 with the time series of the Dst index, and geomagnetic activity index Kp (Fig. 4.7a). The Dst profile is the solid line and Kp indexes are the dash line. The Dst index is used to define the occurrence, duration and magnitude of a storm, whose unit is nT, nanotesla. And the Kp index is a disturbed level of geomagnetic field. The Kp indexes reach a value of -9 (close to its maximum, from 20:00 on 20 Nov and 4:00 UT on 21 Nov 2003, indicating a severely disturbed geomagnetic condition during these time. The Dst index also reaches the summit at 20:00 on 20 Nov, indicating a stronger geomagnetic activity. The TECs normally vary from day to night on 19 Nov 2003. But it suddenly reduces from 8:00 to 16:00 20 Nov 2003, and rarely varies from day to night on 21 Nov 2003. It is obvious to see that the TEC has a severe effect due to suffering a great geomagnetic storm.

4.3.2.3 TEC Disturbances Following Earthquakes

Robust seismic signals around the globe could estimate the gross nature of earthquakes, but the details are usually unclear due to the lack of near-field observations. Although ground measurements, e.g., GNSS/InSAR and strong motion measurements, provide unique insights on the kinematic rupture and nature of the earthquake, but the temporal-spatial resolutions are still limited. It may help

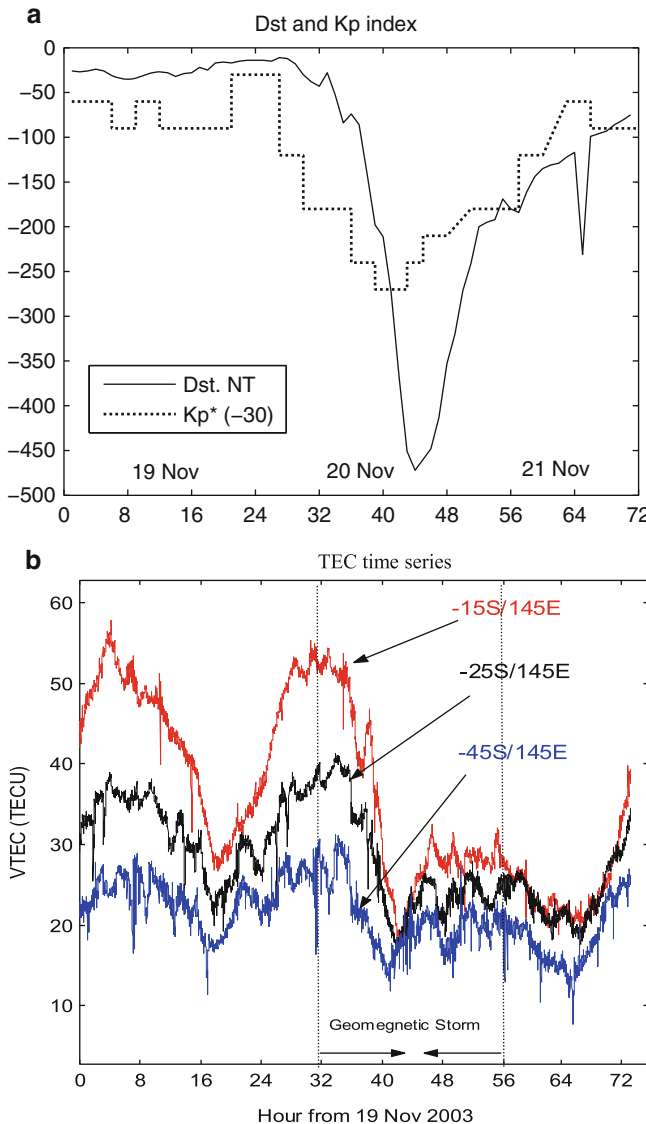


Fig. 4.7 The Dst index and geomagnetic activity Kp index on 19–21 Nov, 2003 (a) and VTEC series at three grid points from 19 to 21 Nov 2003 (b)

from non-seismic measurements, e.g., atmospheric, ionospheric or electromagnetic observations. Here a case study of the 2008 Wenchuan earthquake is carried out using the ground GNSS observations.

The Mw = 8.0 Wenchuan earthquake occurred on May 12, 2008 at the Longmen Shan fault, which is a thrust structure along the border of the Tibetan Plateau

and the western Sichuan Basin. This event was a deadly earthquake to hit China since the 1976 Tangshan earthquake, which lead to ten thousands of lives death and huge economic losses in several cities along the western Sichuan basin in China (Jin et al. 2010; Afraimovich et al. 2010). After the Wenchuan earthquake, a lot of scientists and volunteers quickly rescued and investigated this event on the sites in time, including monitoring crustal deformation, landslide, aftershocks, and landslide dam. Although robust seismic signals around the globe could estimate the gross nature of this event, but the details of rupture are obscure due to the lack of near-field observations. Local ground geodetic measurements provided more details on this continental event, e.g., co-/post-seismic deformation, rupture and slip, but it still difficult to determine the rupture direction and velocity. While GPS signals propagate the atmosphere, the GNSS signals are delayed by the atmospheric (tropospheric and ionospheric) refraction, which results in lengthening of the geometric path of the ray, usually referred to as the tropospheric and ionospheric delays. Since the GNSS atmospheric delays may be disturbed by the seismic waves, the GNSS atmospheric seismology is proposed. A case study of the 2008 Wenchuan earthquake is investigated. Here, dense GNSS network observation data are collected from China national continuous and campaign GNSS network, and the coseismic ionospheric disturbances are investigated following this event.

At the time t , each i -th element of the vertical TEC is denoted by the measured TEC value $I_i(t)$. TEC time series reflect regular changes of the ionosphere, e.g., seasonal and diurnal scales, and abnormal variations caused by irregularities of electron concentration of various scales, such as solar flares, geomagnetic storms, geohazard events due to the coupling of the solid-Earth and the ionosphere, and so on. We here filtered TEC series $dI(t)$ by removing the trend and regular changes with a time window of 5–20 min in order to show characteristic ionospheric disturbances. Significant coseismic ionospheric disturbances are found at continuous GPS sites within 500 km from the epicenter. We check the solar activity indices (e.g. Auroral Electrojet (AE) and F10.7 cm solar radio flux) and geomagnetic indices (e.g. Kp and Dst) and found that the day of May 12 2008 is a geomagnetic quiet day. Therefore, these co-seismic ionospheric characteristics mainly reflect the coupling of the ionosphere and Wenchuan earthquake. For example, Fig. 4.8 shows the filtered TEC series $dI(t)$ for LUZH-PRN22 (a) with black, red, and gray lines on 11, 12 and 13 May, respectively. (b) demonstrates the evolution of N-shaped response with distance from epicenter increase; the first maximums of N-response for LUZH-PRN14 and LUZH-PRN22 are superposed. On the panels (c) and (d) the black lines show the accumulated TEC series $dIP(t)$, obtained on the experimental stage of processing for the plane and spherical wave front, respectively (*QOA* method) (Kiryushkin and Afraimovich 2007). The red gray lines on the panels (c) and (d) marks the modeled $dIP(t)$ for which the maximum of function C was reached. The moment of the main shock of the Wenchuan earthquake is marked by blue shaded triangles. It has found that an intensive N-shape shock-acoustic waves with a plane waveform and with half-period of about 200 s propagated toward northeast with a mean velocity 600 m/s for a distance of about 1,000 km from the epicenter, in

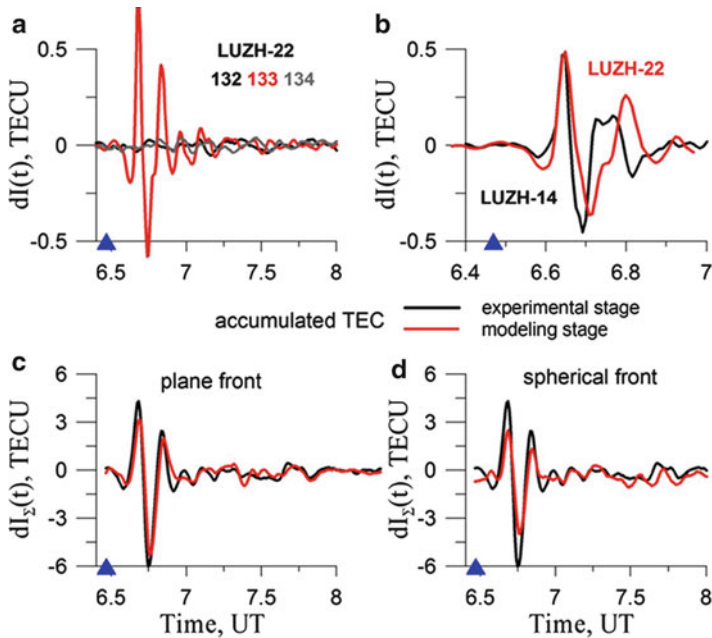


Fig. 4.8 The filtered TEC series $dI(t)$ for LUZH-PRN22 (a) with black, red, and gray lines on 11, 12 and 13 May, respectively. (b) demonstrates the evolution of N-shaped response with distance from epicenter increase; the first maximums of N-response for LUZH-PRN14 and LUZH-PRN22 are superposed. On the panels (c) and (d) the black lines show the accumulated TEC series $dI_\Sigma(t)$, obtained on the experimental stage of processing for the plane and spherical wave front, respectively (*QOA* method). The red gray lines on the panels (c) and (d) marks the modeled $dI_\Sigma(t)$ for which the maximum of function C was reached. The moment of the main shock of the Wenchuan earthquake is marked by blue shaded triangles

parallel with the rupture direction. More detailed description of methods and results are referred to Afraimovich et al. (2010). In the future, we will further investigate the coupling processes and mechanism of the seismo-ionospheric TEC variations.

4.4 3-D GNSS Ionospheric Mapping

4.4.1 3-D Ionospheric Topography

The *STEC* is defined as the line integral of the electron density as expressed by:

$$STEC = \int_{R_{receiver}}^{R_{satellite}} N_e(\lambda, \varphi, h) ds \quad (4.27)$$

where $N_e(\lambda, \varphi, h)$ is the ionospheric electron density, λ , φ and h are the longitude, latitude and height, respectively. To obtain N_e , the ionosphere is divided into grid pixels with a small cell where the electron density is assumed to be constant, so that the *STEC* in Eq. (4.27) along the ray path i can be approximately written as a finite sum over the pixels j as follows:

$$STEC_i = \sum_{j=1}^M a_{ij} n_j \quad (4.28)$$

where a_{ij} is a matrix whose elements denote the length of the path-pixel intersections in the pixel j along the ray path i , and n_j is the electron density for the pixel j . Each set of *STEC* measurements along the ray paths from all observable satellites at consecutive epochs are combined with the ray path geometry into a linear expression:

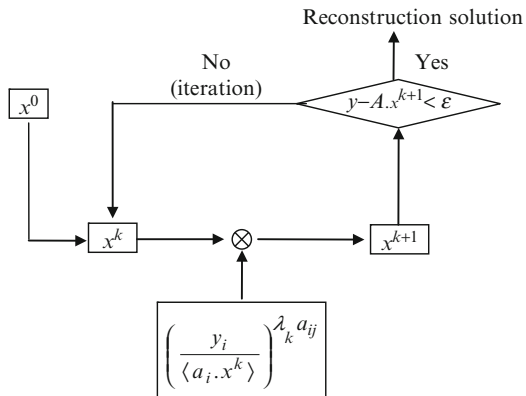
$$Y = Ax + \varepsilon \quad (4.29)$$

where Y is a column of m measurements of *STEC*, x is a column of n electron density unknowns for cells in the targeted ionosphere region, and A is an $m \times n$ normal matrix with elements a_{ij} . The unknown electron densities x can be estimated by the ionospheric tomographic reconstruction technique. Many tomography algorithms are used in different ways, e.g. singular value decomposition (Wall et al. 2001), correlation function (Ruffini et al. 1998), and algebraic reconstruction technique (Gordon et al. 1970). One of the most common approaches is the algebraic reconstruction technique (ART), which was first introduced in Computerized Ionospheric Tomography (CIT) by Austen et al. (1988). This is an iterative procedure for solving a linear equation. A modified version of ART is the so-called multiplicative ART (MART), where the correction in each iteration is obtained by making a multiplicative modification to x (Raymund et al. 1990; Tsai et al. 2002). The ART generally produces estimates of the unknown parameters by minimization of the L2 norm, while the MART follows maximum entropy criteria and thus underlies different statistics. In addition, the MART performs a multiplicative modification in each iteration, and thus the inversion results are always positive. Therefore, MART has the advantage over ART in determining the electron densities that avoid unreasonable negative values and is the one used in this study. Basically, the MART algorithm is iterated cyclically:

$$x_j^{k+1} = x_j^k \cdot \left(\frac{y_i}{\langle a_i, x^k \rangle} \right)^{\lambda_k a_{ij}} \quad (4.30)$$

where y_i is the i th observed *STEC* in a column of m measurements, x_j is the j th resulted cell electron density in a column of n unknowns, a_{ij} is the length of link i that lies in cell j , λ_k is the relaxation parameter at the k th iteration with $0 < \lambda_k < 1$, and the inner product of the vectors x and a_i is the simulated *STEC* for the i th path.

Fig. 4.9 Flowchart of 3-D GNSS ionospheric tomography

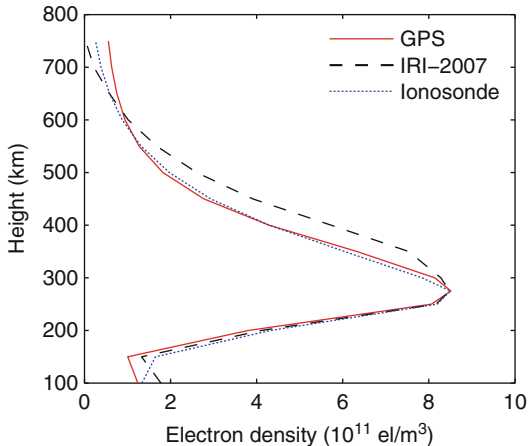


The electron density matrix x is therefore corrected iteratively by the ratio of the measured *STEC* and the simulated *STEC* with a relaxation parameter of λ_k until the residual does not change (see Fig. 4.9) (Jin and Park 2007; Jin et al. 2008). This relaxation parameter value is chosen from experience in which the best λ_k value is identified where the solution converges quickly with a reasonable number of iterations and the residuals are a minimum. Here $\lambda_k = 0.01$ has been chosen for all iterations. In addition, it is noted that any iterative algorithm requires an initial condition before the iteration begins. Due to the poor *STEC* geometry, the initialization could be extremely important for the tomographic reconstruction. In practice, the closer the initial condition is to the true electron density distribution, the more accurate the reconstruction will be. Here the latest IRI-2007 model (<http://nssdcftp.gsfc.nasa.gov/models/ionospheric/iri/iri2007>) is used as an initial guess for the reconstruction iteration.

4.4.2 Validation of GNSS Ionospheric Tomography

The ionospheric reconstruction algorithm MART can integrate the *STEC* from all available GPS receivers to all GPS satellites visible from each site of the KGN network above a user-specified elevation cut-off angle (usually 15°). The unknown electron density profile is expressed in 4-D (longitude-latitude-height and time) voxel basis functions over the following grid: longitude 124E°–130E° in 1° increments, latitude 33 N°–39 N° in 0.5° increments, altitude 100–1,000 km in 25 km increments and time: 1 h increments of linear change in the electron density per voxel. As there are a sparse number of ions in the ionosphere above 1,000 km, the effect on the inversion for ionospheric electron density profiles is very small and the ionosphere is only considered up to an altitude of 1,000 km. Furthermore, it is faster to invert the unknown ionospheric density parameters because of the reduced number of unknown variables. In addition, the fewer leaving rays from the ionospheric space of above defined latitude and longitude range are not used, but

Fig. 4.10 Comparison of the electron density profiles derived from the ground-based GPS tomography reconstruction (solid line), ionosonde observation at Anyang stations (37.39°N , 126.95°E) (dot line) and IRI-2007 estimation (dashed line) at 9:00 UT on 1 October 2003

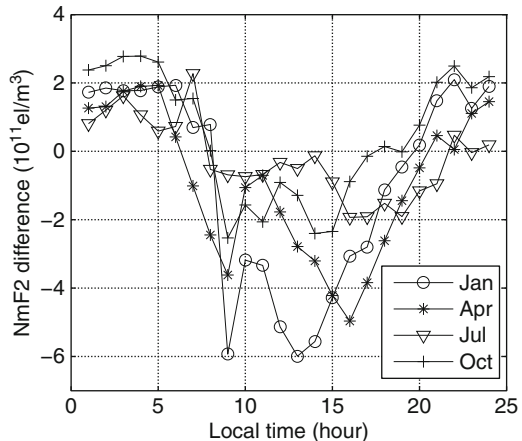


are useful to further obtain ionospheric profiles outside the latitudinal/longitudinal boundaries space. Using the STEC of all ray paths passing the ionospheric grid cells from the Korean GPS network, the 4-D ionospheric electron density profiles can be derived through the tomography reconstruction algorithm. To verify the reliability of GPS ionospheric tomography reconstruction results, the available ionosonde station (Anyang) in South Korea provides an independent comparison with the GPS tomographically reconstructed electron density profiles (Jin et al. 2008). The electron density profiles at 25 km height steps from GPS reconstruction and ionosonde data match well in October and November with a root-mean-square (RMS) of $0.3 \times 10^{11} \text{ el/m}^3$. For example, Fig. 4.10 shows a comparison of the GPS reconstructed electron density profile at 9:00 UT on 1 October 2003 with the available ionosonde data at Anyang station (37.39°N , 126.95°E) and the profiles from the IRI-2007 model. It can be seen that the GPS tomographically reconstructed density profile is in a good agreement with ionosonde data and the IRI-2007 model, but is closer to the ionosonde, which confirms the validity of our GPS ionospheric reconstruction approach (Jin et al. 2007).

4.4.3 Assessment of IRI-2001 Using GNSS Tomography

In order to check the validity of the IRI-2001 for predicting the seasonal variation over South Korea, we further compare the IRI-2001 model with real GPS observation results in terms of main ionospheric parameters, the electron density F2 peak (NmF2) and TEC (Jin and Park 2007). The monthly averaged diurnal GPS results of these main parameters in January, April, July and October 2003 are considered to represent winter, spring, summer and autumn seasons, respectively. As GPS ionospheric reconstruction profiles are in very close agreement with the ionosonde, e.g. the F2 peak parameter NmF2, we here didn't compare the ionosonde with

Fig. 4.11 NmF2 differences of monthly averaged median of GPS reconstruction with the IRI-2001 model



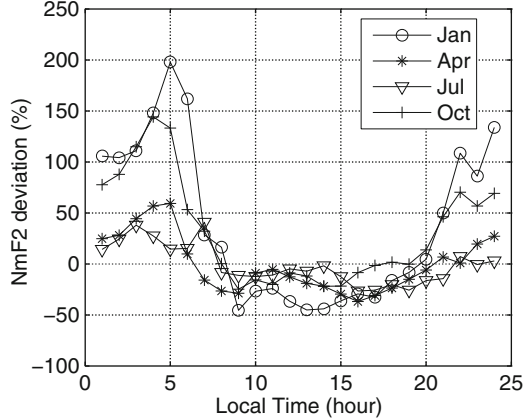
the IRI-2001, and just GPS reconstruction with the IRI-2001. Figure 4.11 shows the comparison of the monthly averaged diurnal NmF2 difference (DNmF2) from GPS reconstruction with respect to the IRI-2001 model at the grid point (37.5°N , 127.0°E) in winter, spring, summer and autumn, 2003, where the standard URSI foF2 peak model for the IRI-2001 was used to estimate NmF2. It can be seen that the GPS-derived NmF2 is larger than the estimation of the IRI-2001 model in nighttime for all seasons (00:00–07:00 LT and 21:00–24:00 LT), but much smaller in daytime for all seasons from 08:00 to 20:00 LT, indicating that the IRI-2001 model underestimates NmF2 values in nighttime for all seasons, and significantly overestimates NmF2 values in daytime for all seasons.

For a good ionospheric model, its electron density profiles $N(\varphi, \lambda, t)$ should give a good F2-layer peak electron density $NmF2(\varphi, \lambda, t)$. To assess the IRI-2001 model with GPS reconstruction, a simple deviation percentage can be defined as following:

$$DNmF2(\varphi, \lambda, t) = [(NmF2_{GPS}(\varphi, \lambda, t) - NmF2_{IRI}(\varphi, \lambda, t)) / NmF2_{IRI}(\varphi, \lambda, t)] \times 100 \% \quad (4.31)$$

where $NmF2_{GPS}(\varphi, \lambda, t)$ and $NmF2_{IRI}(\varphi, \lambda, t)$ are the electron density peak values of GPS reconstruction and IRI-2001, respectively, and $DNmF2(\varphi, \lambda, t)$ is the deviation percentage value of maximum ionospheric electron density $NmF2_{GPS}(\varphi, \lambda, t)$ with respect to the $NmF2_{IRI}(\varphi, \lambda, t)$. Thus, the monthly averaged diurnal percentage variations of the monthly median $DNmF2(t)$ can be obtained. Figure 4.12 shows a comparison of monthly averaged density peak deviation percentage as calculated from GPS reconstruction with respect to the IRI-2001 at the grid point (37.5°N , 127.0°E) in winter, spring, summer and autumn, 2003. It can be seen that the IRI-2001 model underestimates the NmF2 values by $\sim 30\%$ in nighttime for all seasons, and significantly overestimates NmF2 values in daytime for all seasons, especially in autumn and winter.

Fig. 4.12 Monthly averaged diurnal NmF2 variation percentage of the GPS reconstruction with respect to the IRI-2001 model



The $TEC(\varphi, \lambda, h)$, relating with latitude φ , longitude λ and height h , is the integrated electron density along a path through the ionosphere, namely

$$TEC(\varphi, \lambda, h) = \int_{R_{receiver}}^{S_{satellite}} N_e(\varphi, \lambda, h) ds \quad (4.32)$$

where $N_e(\varphi, \lambda, h)$, ionospheric electron density, was obtained from GPS tomography reconstruction in small cells (i, j, k) of $0.5^\circ \times 1.0^\circ \times 25$ km pixels. Therefore, the vertical $TEC(\varphi, \lambda, h)$ can be written as follows

$$VTEC(\varphi, \lambda, h) = \sum_i \sum_j \sum_k (N_e)_{i,j,k} h_{i,j,k} \quad (4.33)$$

Thus, the vertical TEC can be obtained from the GPS reconstructed 3-D electron density at any specific grid points. Although the IRI model can calculate the TEC by really updating F2 peak parameters with measured peak values, we here focus on evaluating the average behaviours of the IRI-2001 model with empirical standard models' parameters. So we here didn't use the measured peak values (e.g. ionosonde) and just used empirical standard models' peak values for IRI TEC calculation. Figure 4.13 is the comparison of TEC at grid point (37.5°N , 127.0°E) estimated from GPS and IRI-2001 in different seasons. Both show the diurnal behavior of the monthly TEC median of the ionosphere averaged over 1 month. Independently of the season, the maximum TEC values are arrived at about the noon, between 11:00 and 15:00 LT. The IRI-2001 gives a smoother TEC than GPS reconstruction. However, averaged monthly TEC medians from the IRI-2001 model are overestimated in daytime in winter, but underestimated in other time for all seasons. In addition, the maximum GPS-derived TEC values are found during equinoxes (spring equinox especially). Furthermore, the daytime TEC values in winter (January) are slightly greater (about 5–16 %) than those in summer (July)

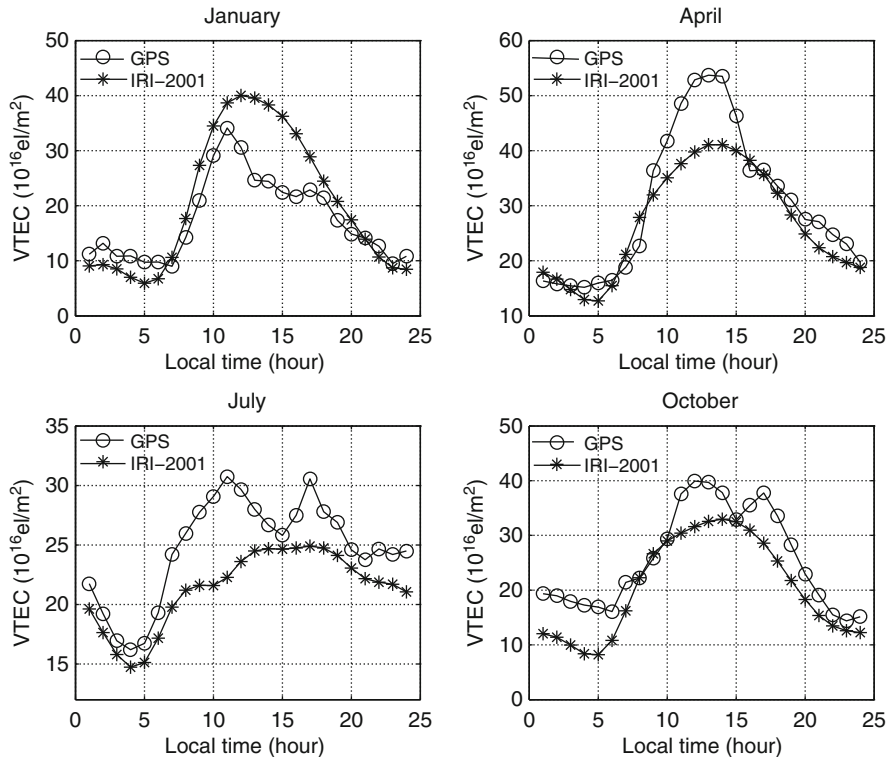


Fig. 4.13 Comparison of TEC at grid point (37.5N, 127.0E) between GPS reconstruction and IRI-2001

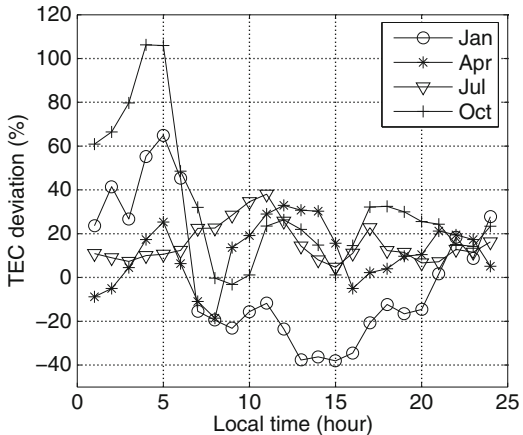
from around 10:00 to 12:00 LT, namely so-called winter anomaly. However, the nighttime behavior shows that TEC values are higher in summer than in winter, which indicates that this phenomenon vanishes at night near the maximum of the solar cycle in 2003.

Similar with the $NmF2$ deviation percentage as Eq. (4.31), the monthly averaged diurnal variation percentages of the GPS reconstruction TEC with respect to the IRI-2001 model are obtained (Fig. 4.14). It has been seen that the IRI-2001 significantly overestimates the TEC in daytime in winter and almost underestimates the TEC in other time by about 30 %.

4.4.4 Ionospheric Slab Thickness

The ionospheric slab thickness is defined as the ratio of the total electron content (TEC) to the maximum electron density of the F-region ($NmF2$, proportional to the square of the F2-layer critical frequency $foF2$). It represents the equivalent slab

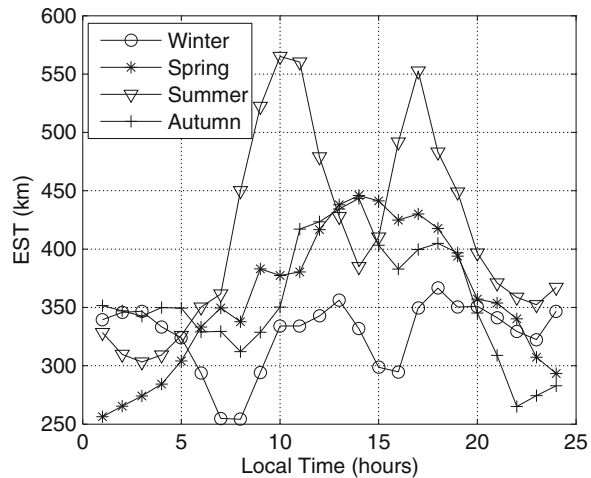
Fig. 4.14 Monthly averaged diurnal TEC variation percentage of GPS reconstruction with respect to the IRI-2001 model



thickness (EST) of the ionosphere having a constant uniform density of the F2 peak. The equivalent slab thickness is of great influence on the shape of ionospheric electron density profile $N_e(h)$, and also a convenient one-parameter summary of the electron density profile that may be related to the various physical processes. Therefore, the ionospheric slab thickness is thus very helpful in understanding the nature of variations of upper atmosphere and is therefore employed in modelling the ionosphere such as International Reference Ionosphere, IRI (Bilitza 2001). The equivalent slab thickness contains information regarding the neutral temperature and, for an assumed electron density profile, can be related directly to the scale height of the ionizable parameters (Bhonsle et al. 1965). Besides, the equivalent slab thickness is a useful parameter in satellite-to-ground radio communication as the relations between the EST and the F2 layer peak electron density N_{mF2} , which can provide an estimate of TEC and the refraction and the rotation of electric field of the radio wave. Therefore, the equivalent slab thickness is capable of addressing many useful ionospheric parameters and a study of this parameter at any location provides information about the nature of the distribution of ionization (Huang 1983). Over the last five decades, a number of studies have been performed on the variation of this parameter under different geophysical conditions, but the equivalent slab thickness and its variability were generally studied with several independent data, such as the TEC from the GOES satellite and the f_0F2 from the ionosonde (Jayachandran et al. 2004; Mansilla et al. 2005), or with other expensive techniques, such as incoherent scatter radar (Pandey et al. 2001). It maybe induces unreliable estimations in equivalent slab thickness as each observation technique has its feature and representative. Here the equivalent slab thickness and its seasonal variation are first studied from the most low-cost and convenient GPS observations in South Korea in the following.

Once the TEC and maximum electron density N_{mF2} are extracted from GPS measurements, and the equivalent slab thickness τ , in km, for each hour is computed from the following formula:

Fig. 4.15 Averaged diurnal variations of the seasonal median of the EST (equivalent slab thickness)



$$\tau = TEC/NmF2 \quad (4.34)$$

where $NmF2$ is the maximum electron density of the F-region in el/m^{-3} . The EST is then obtained as a function of local time at intervals of 1 h for each day separately. The averaged diurnal medians for December-January-February (DJF), March-April-May (MAM), June-July-August (JJA) and September-October-November (SON) have been considered to represent the winter, spring, summer and autumn seasons, respectively. Here some days with no or bad observation data are not used.

Using the Eq. (4.34), the equivalent slab thickness (EST) was determined from the GPS-derived TEC and $NmF2$ (Jin et al. 2007). Figure 4.15 shows the corresponding diurnal variation of EST in four seasons. An oscillating hourly variability is observed. A clear diurnal variation as well as considerable variability is observed. The large scatter at any fixed local time shows the importance of significant day-to-day variability of values between 250 and 580 km. It can also be noted that the daytime (07–20 LT) EST shows seasonal variations, with higher values during summer and equinox as compared to the winter, and their magnitude of diurnal variation is also reflected by the EST ratio. In addition, the nighttime (00–07 LT and 20–24 LT) values, however, do not show significant seasonal variations. During 07–20 LT in daytime, in general the larger EST values are observed in summer while the smaller ones are in winter, and the lower values for all seasons are observed during 0–07 LT and 20–24 LT in nighttime. The EST is significantly smaller in winter than in summer but with a consistent variation pattern. During 13–16 LT, in general the larger EST values are observed in spring and autumn while the smaller ones are in summer and winter. In addition, two peaks appear to dominate the EST diurnal variation around 10–18 LT, especially strong dual peaks in summer. The first peak is around 10–14 LT (pre/postnoon) and the second peak is around 17–18 LT (postsunset).

4.4.5 3-D ionospheric Behaviours to Storms

4.4.5.1 Geomagnetic Conditions

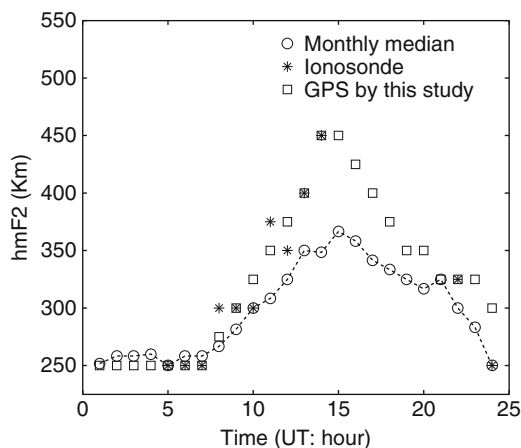
A strong geomagnetic storm commenced on 20 November 2003, as confirmed by the Dst index time series in Fig. 4.7 (upper) obtained from the World Data Center in Kyoto (<http://wdc.kugi.kyoto-u.ac.jp/>). The Dst or disturbance storm time index in nanoteslas (nT), is a measure of geomagnetic activity used to assess the severity of magnetic storms based on the average value of the horizontal component of the Earth's magnetic field measured hourly at four near-equatorial geomagnetic observatories. The storm started with the arrival of the shock at about 8:00 UT on 20 November and reached a minimum Dst value of -472 nT at 20:00 UT, accompanied with an AE index up to 2,600 nT and a maximum Kp value of 9 at about 16:00 UT. Here the AE index is the auroral electrojet index obtained from a number of stations distributed in local time in the latitude region that is typical of the northern hemisphere auroral zone, which provides a measure of the overall horizontal current strength. The planetary K-index (Kp) is a disturbed level of geomagnetic field, which can be obtained from a number of magnetometer stations at mid-latitudes. As can be seen from these indices, the magnetic activity returned to normal level by 22 November.

4.4.5.2 Disturbance of F2-Layer Parameters

As the F2-layer peak electron density (NmF2) and its height (hmF2) are of great influence on the shape of the ionospheric electron density profile Ne (h), the NmF2 and hmF2 are key parameters for monitoring ionospheric conditions in order to understand the nature of ionospheric activities. Therefore, the behaviour of the ionospheric F2-layer was investigated in detail over South Korea in terms of the NmF2 and hmF2 during the geomagnetic storm (20 November 2003). The peak density (NmF2) and its corresponding height (hmF2) can be easily obtained from the ground-based GPS reconstructed results of electron density profiles with the ionospheric height. By checking the solar geophysical index series (Dst, Kp and AE) from the World Data Center in Kyoto in November 2003, the days 1–19 and 22–30 November are magnetically quiet. The monthly median value of electron density profiles during these quiet days is taken as the reference and the deviation can be regarded as the variation of ionospheric F2 peak density and height during the geomagnetic storm.

The NmF2 and hmF2 hourly time series of monthly median, ionosonde data and GPS observations are analyzed at the grid site (37.5°N , 127.0°E) on 20 November 2003, where the monthly median is calculated from 1 month of GPS-derived electron density profiles. It can be seen that there are anomalous variations during this storm, which is also confirmed by independent ionosonde observations at

Fig. 4.16 Comparison of F2-layer peak heights (hmF2) from the monthly median, ionosonde and GPS observations on 20 November 2003



Anyang station. The GPS-derived F2-layer peak density (NmF2) has an anomalous change at 9:00 UT and increases from 10:00 UT until 19:00 UT. The F2-layer peak height (hmF2) suddenly rises from 8:00 UT when the shock of this storm just started, and reaches the maximum height at about 16:00 UT with a maximum K_p value of 9, and then gradually descends until 21:00 UT (Fig. 4.16). The significant increases of F2-layer peak height and density last for about 10 h and is classified as a long-duration ionospheric positive storm (Huang et al. 2005). The electron density profile comparison also shows the same enhancements of the F2-region from 10:00 UT to 19:00 UT. For example, Fig. 4.17 is a comparison of electron density profiles between the GPS, ionosonde data and monthly median at 13:00 UT. It can be clearly seen that the electron density profiles are significantly increased above the F region on 20 November 2003, especially the NmF2 which increased by about 45 % accompanied by a significant uplift in the height of the F2 layer peak (the hmF2), while on the quiet day (23 November) the electron density profiles are almost close to the monthly median value. In addition, the responses of the NmF2 and hmF2 to this storm at different latitudes (i.e. different grid sites) were analyzed, and almost similar results were obtained, which is mainly due to the small area of South Korea. As the TEC is the integrated electron density along a path through the ionosphere, the TEC variations over South Korea during this storm are similar to the NmF2 behaviour.

The uplift of the F2 layer is mainly associated with a strong eastward electric field. The increase of electron density in the F2-layer peak depends mainly on the molecular nitrogen concentration [N_2] with some contribution from molecular oxygen concentration [O_2], while the production rate depends on the atomic oxygen concentration [O]. However, the O/N_2 ratio from the GUVI instrument on board the TIMED satellite shows no significant change during this geomagnetic storm. It suggests that the increase in NmF2 is not caused by changes in neutral composition,

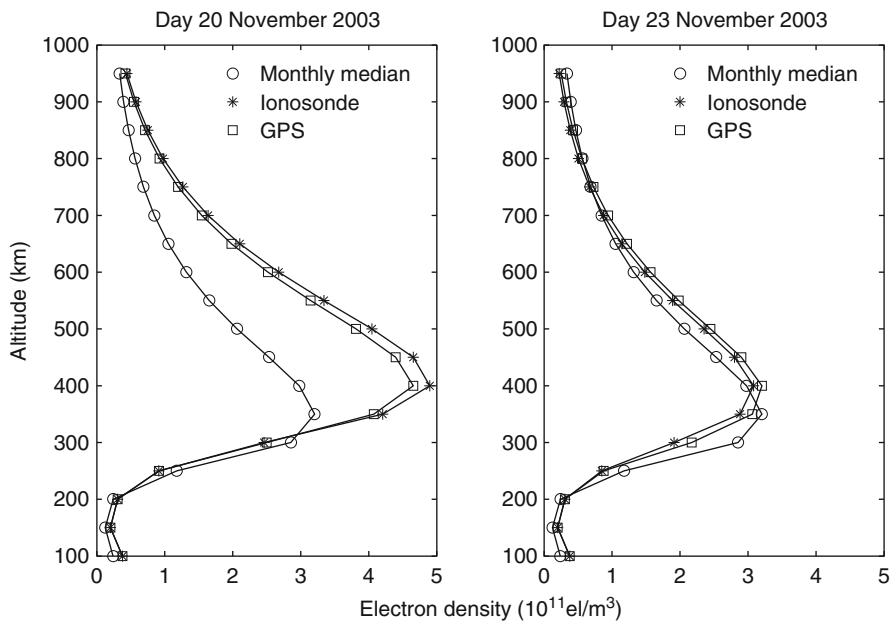


Fig. 4.17 Comparison of the GPS and ionosonde observations and monthly median from GPS-derived electron density profiles at 13:00 UT, 20 and 23 November 2003 (Note: Only values at 50 km height step are plotted for better readability)

but is related to other possible non-chemical effects, such as dynamical changes of vertical ion motions induced by winds and $E \times B$ drifts, tides and waves in the mesosphere/lower thermosphere (MLT) region, which can be dynamically coupled upward to generate ionospheric perturbations and oscillations.

References

- Afraimovich E, Ding F, Kiryushkin V, Astafyeva E, Jin SG, Sankov V (2010) TEC response to the 2008 Wenchuan earthquake in comparison with other strong earthquakes. *Int J Remote Sens* 31(13):3601–3613. doi:[10.1080/01431161003727747](https://doi.org/10.1080/01431161003727747)
- Austen JR, Franke SG, Liu CH (1988) Ionospheric imaging using computerized tomography. *Radio Sci* 23:299–307
- Bassiri S, Hajj GA (1993) Higher-order ionospheric effects on the global positioning systems observables and means of modeling them. *Manuscr Geodetica* 18:280–289
- Bhonsle RV, Da Rosa AV, Garriott OK (1965) Measurement of total electron content and the equivalent slab thickness of the mid latitude ionosphere. *Radio Sci* 69(7):929–939
- Bilitza D (2001) International reference ionosphere 2000. *Radio Sci* 36:261–275
- Calais E, Minster JB (1995) GPS detection of ionospheric perturbations following the January 17, 1994, Northridge Earthquake. *Geophys Res Lett* 22(9):1045–1048

- Feng D, Herman BM (1999) Remotely sensing the Earth's atmosphere using the Global Positioning System (GPS)- The GPS/MET data analysis. *J Atmos Ocean Technol* 16:989–1002
- Gordon R, Bender R, Therman G (1970) Algebraic reconstruction techniques (ART) for three dimensional electron microscopy and X-ray photography. *J Theor Biol* 29:471–481
- Huang YN (1983) Some result of ionospheric slab thickness observations at Lunping. *J Geophys Res* 88:5517–5522
- Huang C-Y, Kuo Y-H, Chen S-H, Vandenberghe F (2005) Improvements in typhoon forecasts with assimilated GPS occultation refractivity. *Weather Forecast* 20:931–953
- Jayachandran B, Krishnankutty T, Gulyaeva T (2004) Climatology of ionospheric slab thickness. *Ann Geophys* 22:25–33
- Jin R, Jin SG (2013) Secular variations and fluctuations of GPS TEC over Antarctica. In: Proceeding of IAU symposium 288, Beijing, China, 20–31 Aug 2012, pp 322–325. doi:[10.1017/S1743921312017139](https://doi.org/10.1017/S1743921312017139)
- Jin SG, Park J (2007) GPS ionospheric tomography: a comparison with the IRI-2001 model over South Korea. *Earth Planets Space* 59(4):287–292
- Jin SG, Wang J, Zhang H, Zhu W (2004) Real-time monitoring and prediction of the total ionospheric electron content by means of GPS observations. *Chin Astron Astrophys* 28(3): 331–337. doi:[10.1016/j.chinastron.2004.07.008](https://doi.org/10.1016/j.chinastron.2004.07.008)
- Jin SG, Park J, Wang J, Choi B, Park P (2006) Electron density profiles derived from ground-based GPS observations. *J Navig* 59(3):395–401. doi:[10.1017/S0373463306003821](https://doi.org/10.1017/S0373463306003821)
- Jin SG, Cho J, Park J (2007) Ionospheric slab thickness and its seasonal variations observed by GPS. *J Atmos Sol Terr Phys* 69(15):1864–1870. doi:[10.1016/j.jastp.2007.07.008](https://doi.org/10.1016/j.jastp.2007.07.008)
- Jin SG, Luo OF, Park P (2008) GPS observations of the ionospheric F2-layer behavior during the 20th November 2003 geomagnetic storm over South Korea. *J Geod* 82(12):883–892. doi:[10.1007/s00190-008-0217-x](https://doi.org/10.1007/s00190-008-0217-x)
- Jin SG, Zhu WY, Afraimovich E (2010) Co-seismic ionospheric and deformation signals on the 2008 magnitude 8.0 Wenchuan Earthquake from GPS observations. *Int J Remote Sens* 31(13):3535–3543. doi:[10.1080/01431161003727739](https://doi.org/10.1080/01431161003727739)
- Kiryushkin V, Afraimovich E (2007) Determining the parameters of ionospheric perturbation caused by earthquakes with using the quasi-optimum algorithm of spatiotemporal processing of TEC measurements. *Earth Planets Space* 59:267–278
- Klobuchar JK (1991) Ionospheric effects on GPS. *GPS World*:48–51
- Liu J, Chen J, Zhang Y et al (1998) The theory and method of wide area differential GPS. Surveying and Mapping Press, Beijing
- Mannucci AJ, Wilson B, Yuan DN (1998) A global mapping technique for GPS-derived ionospheric total electron content measurements. *Radio Sci* 33(3):565–574
- Mansilla G, Mosert M, Ezquer R (2005) Seasonal variation of the total electron content, maximum electron density and equivalent slab thickness at a South-American station. *J Atmos Sol Terr Phys* 67:1687–1690
- Otsuka Y, Ogawa T, Saito A, Tsugawa T, Fukao S, Miyazak S (2002) A new technique for mapping of total electron content using GPS network in Japan. *Earth Planets Space* 54:63–70
- Pandey VK, Sethi NK, Mahajan KK (2001) Equivalent slab thickness and its variability: a study with incoherent scatter measurements. *Adv Space Res* 27:61–64
- Raymund TD, Austen JR, Franke SJ (1990) Application of computerized tomography to the investigation of ionospheric structures. *Radio Sci* 25:771–789
- Reinisch BW, Haines DM, Benson RF, Green JL, Sales GS, Taylor W (2001) Radio sounding in space: magnetosphere and topside ionosphere. *J Atmos Sol Terr Phys* 63:87–98
- Rocken C (1997) Analysis and validation of GPS/MET data in the neutral atmosphere. *J Geophys Res* 102:29849–29866
- Ruffini G, Flores A, Rius A (1998) GPS tomography of the ionospheric electron content with a correlation functional. *IEEE Trans Geosci Remote Sens* 36(1):143–153
- Schaer S (1999) Mapping and predicting the Earth's ionosphere using the Global Positioning System. Ph.D. dissertation. Astronomical Institute, University of Berne, Switzerland

- Skone S (1998) Wide area ionosphere grid modeling in the Auroral Region. Ph.D. thesis, The University of Calgary, Calgary, Alberta, Canada
- Syndergaard S (2000) On the ionosphere calibration in GPS radio occultation measurements. *Radio Sci* 35(3):865–883
- Tsai LC, Liu CH, Tsai WH, Liu CT (2002) Tomographic imaging of the ionosphere using the GPS/MET and NNSS data. *J Atmos Sol Terr Phys* 64:2003–2011
- Tsunoda RT (1988) High-latitude F-region irregularities: a review and synthesis. *Rev Geophys* 26:719–760
- Wall ME, Dyck PA, Brettin TS (2001) SVDMAN – singular value decomposition analysis of microarray data. *Bioinformatics* 17:566–568
- Ware R (1992) GPS sounding of the earth atmosphere. *GPS World* 3:56–57
- Yin P, Mitchell CN, Spencer PS, Foster JC (2004) Ionospheric electron concentration imaging using GPS over the USA during the storm of July 2000. *Geophys Res Lett* 31:L12806. doi:[10.1029/2004GL019899](https://doi.org/10.1029/2004GL019899)
- Yuan Y, Ou J (2002) Differential Areas for Differential Stations (DADS): a new method of establishing grid ionospheric model. *Chin Sci Bull* 47(12):1033–1036

Chapter 5

Theory of GNSS Radio Occultation

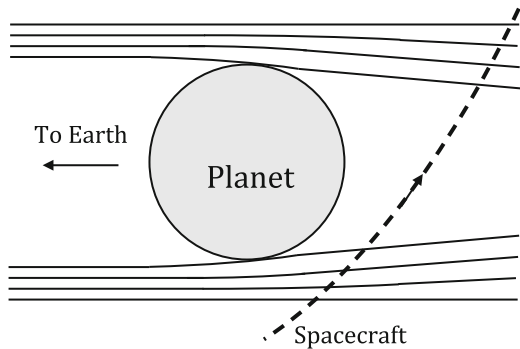
5.1 Introduction

The word “*occult*” is original from Latin word “*occultus*” referring to “hide”. The usage of “occultation” in science field starts in astronomy. An occultation refers to an event that occurs when one celestial body is occulted (or hidden) by another celestial body of interest that passes between it and the observer. During an occultation event, the signal from the occulted object travel through the limb (or edge) of the middle object could be distorted due to the existence of medium, such as atmosphere at the limb. The change of the signal can then be used to infer the atmospheric structure of the celestial body of interest. This is called the occultation technique. Various signal sources at different wavelength have been used to apply the occultation remote sensing technique. For example, by looking at the stars that is setting or rising behind a celestial body of interest is called stellar occultation. The way in which the star’s signals bend and change relative to the observer can be used to characterize the atmospheres and/or ring systems in the solar system or beyond.

5.1.1 *Radio Occultation in Planetary Sciences*

The radio occultation (RO) technique, which uses the radio signals, emerged at the dawn of interplanetary space exploration in the 1960s. It was pioneered by two independent research groups at Stanford University and the NASA’s Jet Propulsion Laboratory (JPL), for determining the size and atmospheric composition of distant planets. The first planetary radio occultation profile were collected in 1965, when the Mariner-4 spacecraft flied by Mars and sent the radio signals through its atmosphere and ionosphere and intercepted at the Earth (Fjeldbo and Eshleman 1965; Kliore et al. 1965). As seen in Fig. 5.1, by precisely recording the change of the radio signals scanning through the planetary atmosphere, the vertical structure of the atmosphere can be precisely measured. Since then, the radio occultation technique

Fig. 5.1 Schematic plot of planetary occultation geometry with radio signal ray paths (*solid line*) connecting a flyby spacecraft (trajectory in *dashed line*) with a distant receiver or transmitter on the Earth



has been widely used to probe the planetary atmosphere and ionosphere of nearly every planets in the solar system: e.g., Venus, Mars and Mercury (e.g., Kliore et al. 1967; Fjeldbo and Eshleman 1968; Howard et al. 1974), the gas giants Jupiter, Saturn, Uranus and Neptune (e.g., Fjeldbo et al. 1975; Kliore et al. 1980; Lindal et al. 1987; Tyler et al. 1989). In addition, the RO technique has also been used to study the moons of the outer planet, such as Jupiter's satellites: Io, Europa, Ganymede and Callisto (Kliore et al. 1975, 1997), Saturn's satellite Titan (Lindal et al. 1983) and Neptune's satellite Triton (Tyler et al. 1989), as well as the planetary ring structure (e.g., Marouf and Tyler 1986).

Other than the US interplanetary missions, the former USSR also launched multiple planetary missions and applied RO technique for sensing the planetary atmosphere and ionosphere (e.g., Kolosov et al. 1976; Ivanov et al. 1979). Table 5.1 shows a list of celestial bodies in the solar system that have been investigated by the radio occultation technique in the past half century. The RO technique continues to thrive and provide highly valuable atmospheric measurements that contribute to an improved understanding of structure, circulation, dynamics, and transport in the planetary atmosphere.

5.1.2 GNSS Radio Occultation in Earth Sciences

The application of the radio occultation technique to probe the Earth's atmosphere was first suggested in the mid-1960s (Fishbach 1965; Kliore 1969; Lusignan et al. 1969). Several more studies of satellite configurations were carried out by a group of Russian scientists later (Kalashnikov and Yakovlev 1978; Gurvich and Krasil'nikova 1987; Eliseev and Yakovlev 1989; Yakovlev et al. 1995).

A few pioneering RO experiments from satellite-to-satellite tracking link demonstrated the feasibility and the great benefit of the technique for the Earth's atmosphere research. The first radio occultation experiment to sense the Earth's atmosphere was carried out within the framework of the historical (joint US-Soviet) Apollo-Soyuz mission using the ATS-6 (Applications Technology Satellite-6)

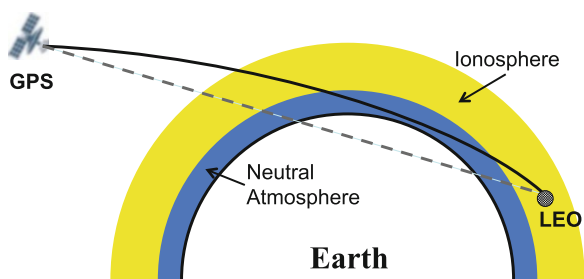
Table 5.1 Celestial bodies investigated by the radio occultation technique except the Earth

Celestial bodies	Spacecraft	Years
Mars	Mariner 4, 6, 7	1965, 1969
	Mars 2, 4, 6	1971, 1974
	Mariner 9	1971
	Viking 1, 2	1976
	MGS (Mars Global Surveyor)	1998
	MEX (Mars Express)	2003
Venus	MRO (Mars Reconnaissance Orbiter)	2005
	Mariner 5, 10	1967, 1974
	Venera 9, 10	1975
	Pioneer Venus	1979
	Venera 15, 16	1983
	Magellan	1991
Mercury	Mariner 10	1974
Jupiter	Pioneer 10, 11	1974
Saturn (and Saturnian rings)	Voyager 1, 2	1979
	Galileo	1995
	Pioneer 11	1976
	Voyager 1, 2	1980, 1981
Uranus (and Uranian rings)	Cassini	2005
	Voyager 2	1986
Neptune	Voyager 2	1988
Moon	Earth's Moon	Luna 19, 22
Titan	Saturn's Moon	Voyager 1
Io	Cassini	1980
	Jupiter's Moon	Pioneer 10
	Galileo	1997
Europa, Ganymede, Callisto	Galileo	1996–1997
	Vega 1, 2	1986
Halley's Comet		
Triton	Neptune's Moon	Voyager 2
Pluto		New Horizons

geostationary satellite in July 1975 (Rangaswamy 1976). Another RO experiment based on the radio link between ATS-6 and GEOS-3 (Geodynamics Experimental Ocean Satellite-3) on a circular polar orbit was documented by Liu (1978). Yakovlev et al. (1995) presented preliminary results of radio occultation experiments, which were performed by using the orbital station MIR and a retranslating geostationary satellite.

Note that the RO observation requires a pair of a radio source and a suitable receiver off the Earth. To monitor the state of the atmosphere will require a sufficient number of daily RO soundings to fulfill the meteorological tasks. However, the high cost of implementing a large number of new transmitters and receivers in the space to achieve the sampling goal makes the technique not attractive by then.

Fig. 5.2 Schematic plot of GPS radio occultation geometry



In the 1980s, the emergence of the Global Navigation Satellite System (GNSS) constellation that provides reliable and low-cost radio signal sources, enabled the RO application for Earth's atmospheric sounding. The US Global Positioning System (GPS) and the Russian Globalnaya Navigatsionnaya Sputnikovaya Sistema (GLONASS) became the first two operational GNSS in the world. The RO concept to profile Earth's atmosphere using the GNSS radio signal was first proposed in 1980s (e.g., Gurvich and Krasil'nikova 1987; Yunck 1988). Figure 5.2 shows a schematic view of a setting occultation as a Low-Earth-Orbit (LEO) receiver satellite tracks the GPS transmitter while it sets behind the Earth. The dashed straight line is the line-of-sight without the presence of the medium. Whereas, the bended black line represents the GPS signal ray path travels through the ionosphere and neutral atmosphere before reaching the LEO receiver.

On 3 April 1995, the proof-of-concept GPS/MET (for GPS Meteorological experiment) led by the University Corporation for Atmospheric Research (UCAR) was launched and became the first GPS RO satellite mission to probe the Earth's atmosphere (Feng et al. 1995; Ware et al. 1996; Rocken et al. 1997). The RO measurement precisely reveals the fine vertical structure of temperature across the tropopause inversion as indicated in the closely coincident radiosonde sounding and the weather model profile. The temperature retrievals agreed well with co-located analyses and radiosondes to within 1 K between ~ 5 and 25 km.

The GPS/MET RO receiver aboard the small research satellite MicroLab-1 continued to collect over a hundred RO soundings per day until the end of the mission in mid 1997. The remarkably successful mission demonstrated the capability of GPS RO technique to provide global coverage, accurate and high-vertical resolution soundings of the Earth's atmosphere in all-weather conditions. The breakthrough success of the mission paves the road for developing a worldwide constellation of LEO satellites, which shall operationally provides a dense global observation of fundamental atmospheric variables. The RO observations will provide a great complement to the conventional nadir-viewing satellite sounders and the sparse in-situ measurements from radiosondes and aircrafts.

Following the pioneering example of GPS/MET, the same type of GPS RO receiver were launched into the space aboard two small international flight projects in 1999 and one US Air Force (USAF) satellite mission in 2001, i.e., Denmark's *Ørsted* mission, designed primarily for magnetic field mapping, South Africa's

Sunsat, a student-built satellite carrying a high-resolution imager, and USAF's *IOX* for ionosphere sensing (Yunck et al. 2000).

The GPS/MET type of basic receiver built by NASA's Jet Propulsion Lab (JPL) is a dual-frequency Turbo Rogue GPS receiver that produces only a small number of RO soundings (~ 125) each day. Many of the soundings failed in the lower troposphere ($\sim 3\text{--}5$ km above surface), in particular over the moist regions in tropics and mid-latitudes. Nevertheless, such unique GPS/MET measurements provided not only pioneering atmospheric science but also enormous insight into the behavior of RO signals, which ultimately benefited and led to the new design for the next generation occultation receivers.

In 2000, the JPL-built second-generation occultation receivers (known as the "BlackJack") were launched on two international satellite missions. One is on the German satellite CHAMP (CHAllenging Minisatellite Payload) for magnetometry and gravity mapping (Wickert et al. 2001). Another is on the Argentina spacecraft SAC-C (Satellite de Aplicaciones Cientificas-C) carrying a multispectral imager and magnetometer (Hajj et al. 2004). SAC-C became the first RO mission to carry occultation antennas in both the fore and aft velocity directions, and thus was the first to observe rising occultations. One unique feature of SAC-C is that all flight software can be modified and reloaded after launch. Both satellite missions provide much stable daily RO soundings measurements as compare to earlier RO missions. For several years, CHAMP and especially SAC-C have served as developmental test beds for GPS sounding. In 2001, the BlackJack receivers were placed on one of the twin spacecraft GRACE-A (Gravity Recovery and Climate Experiment-A). However, the RO occultation measurements were not activated until 2006 to avoid the potential disturbance to the major gravity field measurement mission (Wickert et al. 2009).

On 15 April 2006, the joint Taiwan-US six RO satellite constellation, FORMOSAT-3/COSMIC (Formosa Satellite mission #3/Constellation Observing System for Meteorology, Ionosphere, and Climate), were successfully launched. Each COSMIC satellite is equipped with a newer generation GPS RO receiver (called IGOR, Integrated GPS and Occultation Receiver). The RO receiver preserves a high degree of the Blackjack heritage and the hardware architecture. In addition it offers open-loop tracking capability that is highly desirable for moist lower troposphere soundings where the BlackJack close-loop receivers from earlier missions encounter problems. COSMIC was the first constellation of satellites dedicated primarily to RO and delivering 1,500–2,500 daily RO soundings in near-real-time to operational weather centers around the world shortly after its launch (Anthes et al. 2008). On the same horizon, the MetOp-A, the Europe's first polar orbiting satellite for operational meteorology, was launched on October 19, 2006. The satellite payload includes a GPS RO receiver (GRAS – Global Navigation Satellite System Receiver for Atmospheric Sounding), which was independently developed by the European Space Agency (ESA) (Luntama et al. 2008).

Following the success of these missions, a series of RO missions were launched on many international satellite payloads. For example, the UC C/NOFS, the German TerraSAR-X and its sister satellite TanDEM-X; OceanSat2 and Megha Tropiques

(a joint India-France mission); the SAC-D/Aquarius from Argentina; and a follow-on MetOp-B from ESA. Moreover, a series of single-receiver RO missions have been planned to be launched in the near future such as Chinese FY-3C equipped with GNOS (GNSS Radio Occultation Sounder); ROHP-PAZ from Spain; KOMPSAT-5 from South Korea and EQUARS from Brazil.

In general, a single GPS RO receiver satellite can recover \sim 500 rising and setting RO profiles each day, distributed almost uniformly around the globe; a large constellation would recover many thousands of profiles, which could have a profound impact on both long term climatological studies and short term weather predictions.

The follow-on mission of COSMIC-II are planned to have 12 satellites with 6 satellites on low-inclination (equatorial) orbits and another 6 satellites on high inclination orbits to produce uniform global sounding coverage. The next generation RO receiver (e.g., TriG developed by JPL) will be capable of tracking the GPS, GLONASS and Galileo satellites at the same time and will significantly increase the sounding densities. The likely over 10,000 daily profiles will provide extremely valuable atmospheric observations that are essential for mesoscale weather forecasting, such as hurricane/typhoon, thunderstorms etc. The GNSS RO also attracts strong interests from the private sectors. The CICERO (Community Initiative for Cellular Earth Remote Observation) was form to seek private funds for launching many micro-satellites in Low-Earth Orbit and providing dense RO soundings.

All these RO missions provide essential global atmospheric measurements with high vertical resolution and significantly benefit the weather and climate research communities. A comprehensive list of the past and current RO missions as well as many on plan is summarized in the Table 5.2.

5.2 Principle of GNSS Radio Occultation

As the LEO satellite equipped with a GNSS receiver orbits around the Earth, an occultation event occurs (Fig. 5.2) when the received navigation signal from a setting (rising) GNSS satellite scan through successively deeper (higher) layers of the Earth's atmosphere until the GNSS signals descend below the Earth surface (rise above the atmosphere). The GNSS signal is bent or delayed before arriving at the LEO due to the Earth's atmosphere.

Strictly speaking, the propagation of the GNSS signal through the atmosphere obeys Maxwell's equation in which the propagation medium (e.g., the Earth's atmosphere) is characterized by a three-dimensional spatial distribution of a complex and dispersive refractive index. The GNSS radio occultation technique takes advantage of the extremely precise phase and amplitude measurement of the GNSS navigation signals that pass through the Earth's atmosphere to provide accurate retrieval of the vertical profiles of refractive index of the atmosphere. Consequently, the atmospheric properties such as air density, temperature, pressure, and humidity can be inferred (Kursinski et al. 1997; Rocken et al. 1997).

Table 5.2 Radio occultation technique for the Earth's atmosphere

Mission	Years	Sounding # per day	Remarks/receiver
Apollo-Soyuz & ATS-6	1975	N/A	Joint USA and Soviet Union
Mir-AST-6	1990	N/A	Soviet Union
GPS/MET (Microlab)	04/1995–03/1997	~125	USA/Turbo Rogue (JPL)/CL
Sunsat	01/1999–02/2001	N/A	South Africa/Turbo Rogue (JPL)/CL
Ørsted	01/1999–present	~125	Denmark/Turbo Rogue (JPL)/CL
IOX	09/2001–11/2004	~125	USA/Turbo Rogue (JPL)/CL
CHAMP	07/2000–10/2008	~250	Germany-USA/Blackjack (JPL)/CL
SAC-C	11/2000–present	~500	Argentina-USA/Blackjack (JPL)/OL
GRACE-A	01/2006–present	~125	Germany-USA/Blackjack (JPL)/CL
FORMOSAT-3/COSMIC (6-satellite)	04/2006–present	~1,500–2,000	Taiwan-USA/IGOR (JPL/BRE)/OL
METOP-A	10/2006–present	~650	ESA/GRAS/OL
TerraSAR-X	06/2007–present	~400	German/IGOR (JPL/BRE)/OL
C/NOFS	04/2008–present	~250	USA/CORISS (Aerospace Corporation)/CL
OCEANSAT-2	09/2009–present	~500	India/ROSA (ISRO/Italy)
TanDEM-X	06/2010–present	~400	German/IGOR (JPL/BRE)/OL
Megha-Tropiques	10/2011–present	~500	India-France/ROSA (ISRO/Italy)
SAC-D/Aquarius	06/2011–present	~500	Argentina-USA/ROSA (ISRO/Italy) /OL
METOP-B	09/2012–present	~600	ESA/GRAS/OL
FY-3C	Launch 2013	~250	China/GNOS (CMA/China)
ROHP-PAZ	Launch 2013	~500	Spain/IGOR + (JPL/BRE)/OL
KOMPSAT-5/Arirang-5	Launch 11/2013	~400	South Korea/ IGOR + (JPL/BRE)/OL
FORMOSAT-7/ COSMIC-II (6–12 satellites)	Launch 2016	~6,000–12,000	USA-Taiwan/TriG (JPL)/OL
EQUARS	Launch 2017	~250	Brazil/IGOR (JPL/BRE)/OL
CICERO (18–24 satellites)	First launch ~2014	~30,000	USA/Pyxis-RO (BRE)/OL

Note *CL* Close-loop tracking, *OL* Open-loop tracking

5.2.1 Atmospheric Refraction

Before the introduction of the RO retrieval process, we first explore how the atmospheric properties influence the refractive index n .

The refractive index (or index of refraction) n in a medium is defined as the ratio between the speed of light in a vacuum and the speed of light in the medium. In the neutral atmosphere, n is very close to unity, such that it is conveniently

expressed in terms of refractivity defined as $N = (n - 1) \times 10^6$. The refractivity at GPS frequencies contains contributions from four major components, i.e., the dry neutral atmosphere (N^{dry}), water vapor (N^{vapor}), free electrons in the ionosphere (N^{iono}), and particulates (primarily liquid water and ice water content, N^{scatt}) through the following relationship (Kursinski et al. 1997; Hajj et al. 2002):

$$N = 77.6 \frac{P}{T} + 3.73 \times 10^5 \frac{P_w}{T^2} - \left(40.3 \times 10^7 \frac{n_e}{f^2} + O\left(\frac{1}{f^3}\right) \right) + (1.4W_{liquid} + 0.6W_{ice})$$

$$= N^{dry} + N^{vapour} + N^{iono} + N^{scatt} \quad (5.2)$$

where P and P_w are total pressure and water vapor partial pressure in hectopascal (hPa), T is temperature in Kelvin (K), n_e is electron number density per cubic meter, f is signal frequency in Hertz (Hz), and W_{liquid} and W_{ice} are referred to liquid water content and ice water content in gram per cubic meter, respectively.

Dry refractivity is proportional to molecular number density and is dominant below 60–90 km. The dry refractivity term is due to the polarizability of molecules in the atmosphere, i.e., the ability of an incident electric field to induce an electric dipole in the molecules. The moist refractivity term is due primarily to the large permanent dipole moment of water vapor and becomes significant in the lower troposphere, especially in the tropics and subtropics (Kursinski et al. 2000). The ionospheric term in Eq. (5.1) includes a first-order approximation ($1/f^2$) to the Appleton-Hartree equation (Papas 1965), which is mainly due to free electrons in the ionosphere and becomes important above 60–90 km. The second-order term ($1/f^3$) is generally neglected (e.g., Kursinski et al. 1997). The scattering term given in Eq. (5.1) is due to liquid water droplets and ice crystals suspended in the atmosphere. For realistic suspensions of water or ice, the scattering term is small in comparison with the other terms and is therefore neglected in most RO applications.

5.2.2 Geometric Optics Approximation

At GNSS frequencies, it is convenient to assume that the refractive index is real (i.e., zero absorption). For simplicity, we can further assume that the signals are monochromatic, which is largely valid in the dry atmosphere. Because the wavelengths of the GNSS radio signals are generally small compared to the characteristic scale of the atmospheric problem, the geometric optics (or ray optics) concept can be applied to describe the GPS radio occultation measurements. The signals (light waves) propagate in a direction orthogonal to the geometrical wavefronts defined as the surface on which the signal phase is constant (i.e., stationary phase) (Born and Wolf 1980). Lines representing these signal propagating trajectories are called ray paths (e.g., black solid curve in Fig. 5.2).

In the geometric optics (GO) approximation to the propagation of electromagnetic radiation, the path of a ray passing through a region of varying refractive index is determined globally by Fermat's principle of least time and locally by Snell's law. Therefore, the differential equation of the ray path can be described by the Eikonal equation (Born and Wolf 1980) as

$$\frac{d}{ds} \left(n \frac{d\vec{r}}{ds} \right) = \vec{\nabla} n, \quad (5.3)$$

where \vec{r} is the position vector of a typical point on a ray, $\vec{\nabla} n$ is the gradient of the refractive index n , and ds is an incremental length along the ray path (i.e., $d\vec{r} = \vec{s} ds$).

5.2.3 Spherically Symmetric Atmosphere Assumption

Consider the variation of the vector $\vec{r} \times (n \vec{s})$ along the ray. We have

$$\frac{d}{ds} (\vec{r} \times n \vec{s}) = \frac{d\vec{r}}{ds} \times n \vec{s} + \vec{r} \times \frac{d}{ds} (n \vec{s}), \quad (5.4)$$

Since $d\vec{r} = \vec{s} ds$, the first term on the right vanishes. The second term, on account of Eq. (5.3), can be rewritten as:

$$\frac{d}{ds} (\vec{r} \times n \vec{s}) = \vec{r} \times \vec{\nabla} (n), \quad (5.5)$$

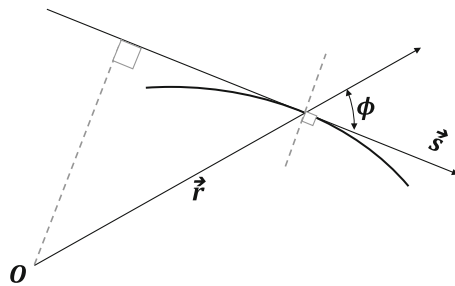
Equation (5.5) shows that only the non-radial portion of the refractive index gradient contributes to changes in $\vec{r} \times (n \vec{s})$. Now, let's consider rays in a medium with spherical symmetry, i.e., where the refractive index only varies on the radial direction. This is a simple approximation of the earth's atmosphere, when the curvature of the earth is taken into account.

$$n = n(\vec{r}) \quad (5.6)$$

Therefore, $\vec{\nabla} n = \frac{\vec{r}}{r} \frac{dn}{dr}$, i.e., the refractive index gradient is only in the radial direction. The second term on the right-hand side of Eq. (5.4) also vanishes. Hence $\vec{r} \times (n \vec{s}) = const$. This relation implies that all the rays are plane curves and along each ray,

$$nr \sin \phi = a, \quad (5.7)$$

Fig. 5.3 A ray path (thick line) in a medium with spherical symmetry that satisfies the Bouguer's formula



where ϕ is the angle between the position vector \vec{r} and the tangent of the ray path (see Fig. 5.3), and the constant a in a spherically symmetric atmosphere is called impact parameter and is also known as Bouguer's rule, which represents Snell's law in a spherically symmetric medium.

5.2.4 Bending Angle and Refractive Index

The accumulated change in the ray path direction along a ray path is defined as the bending angle. According to Eq. (5.3), the rate of change in ray path tangential direction is given as

$$\frac{d\vec{s}}{ds} = \frac{1}{n} \left(\vec{\nabla} n - \vec{s} \frac{dn}{ds} \right) = \frac{1}{n} \left(\vec{\nabla}_{\perp \vec{s}} n \right), \quad (5.8)$$

Thus, the bending is only due to the refractive index gradient that is orthogonal to the ray path tangent direction \vec{s} , i.e., the projection of $\vec{\nabla} n$ into the plane perpendicular to the ray direction \vec{s} (i.e., $\vec{\nabla}_{\perp \vec{s}} n$). Now we can define a local coordinate system where x is orthogonal to r and lies in the plane defined by s and r , and y is in the direction orthogonal to the r - x plane (Kursinski et al. 2000). The bending angle increment along the ray path can be written as

$$d\alpha = \frac{|d\vec{s}|}{|\vec{s}|} = \frac{ds}{n} \left[\left(\frac{\partial n}{\partial r} \sin \phi + \frac{\partial n}{\partial x} \cos \phi \right)^2 + \left(\frac{\partial n}{\partial y} \right)^2 \right]^{1/2}. \quad (5.9)$$

The largest gradients of refractivity are generally found in the lower level of the atmosphere near the tangent point ($\phi \approx 90^\circ, \cos \phi \approx 0$) along a ray path. Since the magnitude of horizontal gradient is generally much smaller than those of vertical gradients in the Earth's atmosphere, the bending of a ray path is largely caused by the refractivity gradient in radial direction. But it is worth noting that the greatest horizontal gradient contribution will come from the gradient in y direction (i.e., perpendicular to the ray tangent direction).

The variation of n along a limb path in the Earth's atmosphere is dominated by the vertical density gradient so that, to the first order, we can assume the gradient of n is directed radially and the local refractive index field is spherically symmetrical, i.e., $n = n(r)$. Combining Eq. (5.9) with the Bouguer's rule in Eq. (5.7), the bending angle increment along the ray path can be simplified as

$$d\alpha = -\frac{d \ln(n)}{dr} \frac{a}{\sqrt{n^2 r^2 - a^2}} dr. \quad (5.10)$$

Since the refractivity generally decreases at higher altitudes, to allow the bending angle to be positive values, a negative sign is added. The total bending angle thus becomes

$$\alpha(a) = 2 \int_{r_t}^{\infty} d\alpha = -2a \int_{r_t}^{\infty} \frac{d \ln(n)}{dr} \frac{dr}{\sqrt{n^2 r^2 - a^2}} \quad (5.11)$$

where r is distance from the center of curvature of a ray path and the integral is over the portion of the atmosphere above r_t , the radius of the tangent point (i.e., the point on the ray path that is closest to the Earth's center). By introducing the integration variable $x = nr$, Eq. (5.11) can be modified as

$$\alpha(a) = -2a \int_a^{\infty} \frac{d \ln(n)}{dx} \frac{dx}{\sqrt{x^2 - a^2}} \quad (5.12)$$

Equation (5.12) provides the forward calculation of bending angle α given the refractive index profile $n(r)$. By inverting the equation through the Abelian transformation, the $n(r)$ can be expressed as a function of α and a (Fjeldbo et al. 1971):

$$n(r) = \exp \left[\frac{1}{\pi} \int_a^{\infty} \frac{\alpha(x) dx}{\sqrt{x^2 - a^2}} \right]. \quad (5.13)$$

Given impact parameter a and the refractive index n , the radius r at each tangent point can be derived according to Bouguer's formula:

$$r = \frac{a}{n(r)}. \quad (5.14)$$

Note that Eq. (5.13) embeds the assumption of local spherically symmetric atmosphere, i.e., the refractive index only varies along radius direction. However, the ellipsoidal shape of the Earth (with an equatorial radius roughly 20 km larger than its polar radius) and horizontal gradients in atmospheric structure produce non-spherical symmetry in the refractive index field. Moreover, the ray paths for a given occultation do not necessarily scan the atmosphere vertically nor are they coplanar. Therefore, measurement of $\alpha(a)$ will be affected by the tangential refractivity gradients and occultation geometry, and Eq. (5.13) could introduce systematic errors

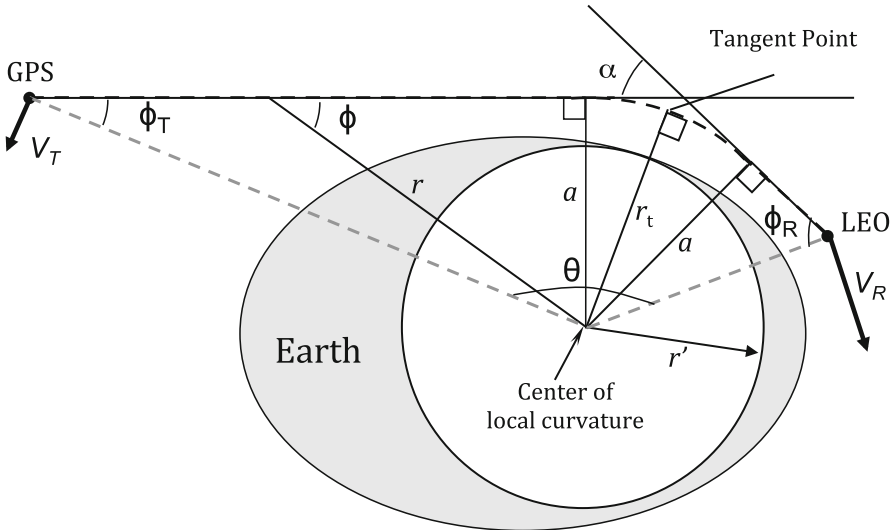


Fig. 5.4 GPS radio occultation geometry. The bending angle, impact parameter and curvature radius are denoted by α , a and r' , respectively

into the retrieved refractive index profile $n(r)$. As shown in Fig. 5.4, First-order errors due to the ellipticity of the Earth can be eliminated by selecting a center and radius of curvature (r') appropriate to the latitude and orientation of the occultation near the tangent point, where most of the bending is accumulated (Kursinski et al. 1997; Hajj et al. 2002).

5.3 GNSS Radio Occultation Processing

Based on the physical principle of the GNSS RO sensing technique described in previous section, the GNSS RO retrieval process generally consists of three major steps. Firstly, the GNSS signal phase and amplitude records are calibrated to derive the precise occultation geometry (e.g., positions and velocities of GNSS/LEO satellites) and the excess phase delay due to the atmosphere (Sect. 5.3.1). Secondly, the bending angle and the refractivity profiles are retrieved based on the physical principle of GNSS RO technique. Thirdly, the geophysical parameters in the neutral atmosphere and ionosphere can be retrieved, which will be described in Chaps. 6 and 7, respectively.

5.3.1 Calibrating and Extracting GNSS RO Observables

As the GNSS signal goes through the Earth's atmosphere, the signal is bent and delayed due to the media. The difference between the observed phase delay and

the geometric phase of the occultation link is referred as the *excess atmospheric delay*, i.e., a combination of the phase delay caused by the neutral atmosphere and ionosphere. By precisely measuring the excess phase delay and its differential form, or call Doppler, the bending angle and therefore the vertical structure of atmospheric refractive index can be derived. In following sections, we will focus on retrieving the excess atmospheric delay from the RO observations through the calibration process.

The basic observables at a LEO receiver for an occultation event are the occulting GPS signal amplitude and phase measurements. Specifically for a GPS occultation, the phase observations consist of L1 (C/A) and L2 (P2) phase measurements between the LEO receiver satellite and the occulting GPS satellite. These raw phase measurements L can be modeled (in dimension of distance) as (e.g., Hajj and Romans 1998; Hajj et al. 2002):

$$L_k^{TR} = -\frac{c}{f_k} \phi_k^{TR} = \rho^{TR} + \Delta_k^{TR} + C^T + C^R + \varepsilon_k \quad (5.15)$$

$$\Delta_k^{TR} = \Delta_k^{neutral} + \Delta_k^{iono} = \Delta_k^{neutral} + \left(d \frac{TEC_k^{TR}}{f_k^2} + O(f^2) \right) \quad (5.16)$$

with

ϕ_k^{TR} the recorded phase in cycles for the signal propagated from transmitter (T) to receiver (R);

c the speed of light in vacuum; $k = 1$ or 2 for L1 and L2, respectively;

ρ^{TR} the geometric range (distance) between the transmitter and the receiver;

Δ_k^{TR} the total excess delay due to neutral atmosphere ($\Delta_k^{neutral}$) and ionosphere (Δ_k^{iono});

C^T , C^R time dependent clock errors of the transmitter and the receiver, respectively;

ε_k measurement noise due to the receiver's thermal noise and local multipath;

d a constant;

TEC_k^{TR} the integrated electron density along the raypath, and

$O(f^2)$ the higher order ionospheric terms (order $1/f^3$ or higher).

Subscript k in Eqs. (5.15 and 5.16) implies the dependency on the frequency. The ionosphere is dispersive media whereas the neutral atmosphere is non-dispersive at radio frequencies. However, since the electromagnetic signal has to travel through the ionosphere before and after it reaches the lower neutral atmosphere, the L1 and L2 signals received at a given time also sense slightly different parts of the neutral atmosphere. This is why the neutral atmospheric delay term $\Delta_k^{neutral}$ remains frequency dependent (Hajj et al. 2002).

Here we assume the phase errors caused by the transmitter and receiver antennas' relative orientation as well as the phase center variations have been modeled and removed. Also, a constant bias (additive constant) corresponding to a large integer number (constant) of cycles during an occultation is ignored, since the derivative of the phase but not the absolute phase delay is of interest for an occultation measurement. It is worth noting that the high order ionospheric terms

$O(f^2)$ (Bassiri and Hajj 1993) is normally small and can be ignored, but it becomes a dominant error term at high altitudes ($>40\text{--}60$ km) during solar-maximum day-time conditions (Kursinski et al. 1997).

In Eq. (5.15), the dominant term on the right-hand-side is the geometrical range ρ between the transmitter and receiver. Whereas the excess atmospheric phase delay accumulated in the GPS L1 and L2 phase measurements in the neutral atmosphere ($\Delta_k^{neutral}$) and ionosphere (Δ_k^{iono}) is of primary interest. By differentiating the excess phase delay, the excess Doppler due to the atmosphere can be derived, which is the fundamental building blocks for retrieving the vertical profile of bending angle and refractive index of the atmosphere.

The process of extracting the excess phase delay due to the atmosphere is generally referred as the *calibration* processes, which consists of two major steps. Firstly, *Precision-Orbit-Determination* (POD) is performed to derive the precise orbits (positions and velocities) for both the transmitter (e.g., GPS) and LEO RO receiver satellites on the occultation link. This process will allow removal of the dominant geometrical range term (ρ) in Eq. (5.15) between the transmitting and receiving satellites. Secondly, through the differential technique with simple linear combination, the clock errors of both GPS transmitter and LEO receiver can be removed. Consequently, the sum of the neutral and the ionospheric delays is isolated (up to a constant). The details of the calibration process is presented in the following two sessions.

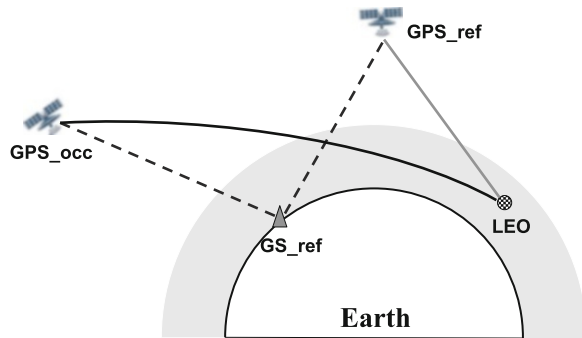
5.3.1.1 Precision Orbit Determination (POD) Method

In order to derive useful atmospheric profiles from radio occultations, the velocities of both GPS and LEO satellites need to be estimated with high accuracy within sub-mm/s level, as it is directly related to the excess Doppler due to the atmosphere. Given the fast movement of GPS (~ 3.8 km/s) and LEO (~ 7 km/s) satellites, this is a daunting challenge. The way to achieve highly accurate orbit information is referred as Precision Orbit Determination (POD) process.

The objective of POD is to obtain an accurate orbit (position and velocity vectors) that accounts for the dynamical environment in which the motion occurs, including all relevant forces affecting the satellite's motion. In practice, each LEO satellite is generally equipped with at least two upward-looking antennas, with one to track a high-elevation GPS satellite for POD purpose and another to track a reference GPS satellite. In addition one or two downward-looking (forward or rear-looking along satellite trajectory) are to the limb of the Earth's atmosphere for occultation measurements (Fig. 5.5). For example, each COSMIC spacecraft is equipped with four antennas, with two upward-looking antennas and two limb viewing occultation antennas.

Since the beginning of the space age the POD technique has been used in the geodesy research community as a means to improve or even determine geodetic models. As a major legacy of GPS geodesy, the International GPS Service for

Fig. 5.5 Data links used for various differencing technique



Geodesy (IGS) was formed in 1992, to oversee the deployment and operation of a permanent global reference ground network to provide precise GPS orbits and reference data to geodesists (Mueller and Beutler 1992). These reference data are critical for the occultation missions.

For each occultation, the POD process consists of the orbit determination for the occulting and reference GPS transmitters and for the LEO receiver. The POD of GPS involves processing the ground reference stations data to estimate the high-rate clock offsets and precise orbits for the GPS satellites. Once the ground-based processing is completed, the space-based LEO POD processing is executed to solve for the LEO orbits and clock offsets with several processing options, which includes the dynamic approach, kinematic or geometric approach, and the reduced-dynamic approach (e.g., Rim and Schutz 2002).

The dynamic orbit determination approach (Tapley 1973) directly solves for the equation of the motion and thus requires precise models of the forces acting on the satellite. This can be achieved by accurate modeling various forces on the satellite, including the gravitational forces (e.g., gravitational effects of sun, moon and planets, tides and relativistic effects), non-gravitational forces (e.g., atmospheric drag, solar and Earth radiation pressure and thermal radiation). Some other unmodeled forces will generally need to be estimated. Dynamic model errors are the limiting factor for this technique, which, however, can be reduced by the continuous, global, and high precision GPS tracking data.

Alternatively, the kinematic approach doesn't require modeling the orbit dynamics except for possible interpolation between solution points for the satellite (i.e., relies purely upon observation data), and the orbit solution is referenced to the phase center of the on-board GPS antenna instead of the satellite's center of mass. However, kinematic solutions are more sensitive to geometrical factors, such as the direction of the GPS satellites and the GPS orbit accuracy, and they require the resolution of phase ambiguities, which are not always available.

The reduced-dynamic approach (Wu et al. 1987), on the other hand, uses both kinematic and dynamic information and optimally weighs their relative strength by solving for local geometric position corrections using a process noise model to absorb dynamic model errors.

There are various software packages for POD process in the radio occultation research community. For example, the GFZ group (Geoforschungszentrum, German Research Center for Geosciences) use the EPOS-OC; NASA Jet Propulsion Laboratory (JPL) utilize the GIPSY-OASIS (GNSS-Inferred Positioning System and Orbit Analysis) software and apply the reduced-dynamic strategy; The UCAR COSMIC group use the Bernese GPS data processing package to solve for satellite orbits with a reduced-dynamic approach (e.g., Ho et al. 2009).

5.3.1.2 Differencing Technique to Remove Clock Errors

Once the effect of satellite motion is removed, the GPS and LEO satellite clock errors need to be eliminated through the differencing technique to derive the atmospheric excess phase of the occultation link.

In the ideal case, when both GPS and LEO satellite clocks are sufficiently stable and require no calibrations, i.e., the LEO and GPS clock offset are zero or known, the total excess phase delay due to the atmosphere can be directly resolved from Eq. (5.15) after removing the satellite geometric term. This is referred as zero-difference (or un-difference), i.e., no differencing is needed. Beyerle et al. (2005) demonstrate the zero-difference processing can produce highly accurate excess phase data by applying prior estimated LEO and GPS clocks in GRACE-B occultation measurements. Note that the twin GRACE (Gravity Recovery and Climate Experiment A&B) spacecrafnts are equipped with an ultra-stable-oscillator (USO), which allows highly accurate clock measurements without need for clock calibration.

However, for most of the other GPS occultation missions, the less stable LEO receiver's clocks generally require calibration. Sometimes the GPS clocks are also need to be calibrated. A commonly known calibration process is the differencing technique. Differential GPS/GNSS (DGPS/DGNSS) is a technique for reducing the error in GPS-derived positions by using additional data from a reference GNSS receiver at a known position. The technique was originally developed by GPS geodesists to significantly improve the precision of ground GPS measurement, in the presence of large errors due to the selective availability (SA) process. The SA was introduced by the U.S. Department of Defense to degrade the performance of GPS. The intentional, time varying errors of up to 100 m were intentionally added to the L1 publicly available navigation signals to destabilize GPS signals for “unauthorized” users. This significantly limited the usage of the civilian GPS application that requires much higher precision of measurements without a costly classified receiver. In the early and mid 1980s, the pioneering work of GPS geodesists leads to a DGPS technique. Generally, the DGPS involves determining the combined effects of navigation message ephemeris and satellite clock errors (including the effects of propagation) at a reference station and transmitting corrections, in real time, to a user's receiver. Given a reference receiver with known exact position, the vector displacement or differential, between the known position and the position the reference receiver get from the GPS satellites, can be calculated. This differential or

correction can then be applied to achieve higher accuracy of positioning for the GPS receiver of interest that collects the exact same data from the same GPS satellites at the same time. The DGPS technique eliminates selective availability and other clock errors and allows civilian receivers with broad-beam antennas to achieve millimeter precision in phase measurements (e.g., Wu 1984). The widespread usage of differential GPS services as well as the new technologies to deny GPS service to potential adversaries on a regional basis by the US military eventually leads to the termination of the SA service in 2 May, 2000.

The similar technique can be applied for deriving high-precision LEO satellite orbits. The two most widely applied procedures are called double-differencing and single-differencing, and they differ in how the effect of the GPS satellite oscillator fluctuations are removed from the LEO phase data (Kursinski et al. 1997; Wickert et al. 2002; Hajj et al. 2002; Beyerle et al. 2005). Figure 5.5 shows a diagram that illustrates differencing geometry.

The *single-differencing* procedure requires the LEO receiver viewing simultaneously an occulting transmitter (GPS_occ) and a non-occulting reference transmitter (GPS_ref) during the occultation (Fig. 5.5). The occultation link (LEO-GPS_occ) and reference link (LEO-GPS_ref) data are differenced to remove the effect of the receiver clock errors, and the solved-for high-rate GPS clock offsets are interpolated based on the IGS final clock products to remove the effects of the transmitter clock errors (Wickert et al. 2002; Schreiner et al. 2010).

However, in some situations, especially before the deactivation of Selective Availability (S/A), the GPS clock can be sufficiently unstable and need to be calibrated. In such case, the *double-differencing* procedure is needed to remove both the GPS and LEO clock errors (Hajj et al. 2002; Wickert et al. 2002; Schreiner et al. 2010). Therefore, other than the two data links between LEO and the occulting/reference GPS transmitters, two additional data links between a ground reference station (GS_ref, precisely known position) and the same occulting/reference transmitters need to be measured (Fig. 5.5). The similar single-differencing technique needs to be applied twice to eliminate the clock errors of both the GPS transmitters and LEO receiver.

One significant disadvantage of double-difference processing is its susceptibility to availability of ground fiducial network station data (Galas et al. 2001; Wickert et al. 2001) as well as error sources including multipath, residual atmospheric and ionospheric noise, data interpolation, and thermal noise. Since deactivation of Selective Availability (S/A), the GPS clock errors are reduced by orders of magnitude. Without S/A GPS clocks are sufficiently stable, therefore, double differencing can be replaced by the single difference technique to eliminate the need for concurrent high-rate ground station observations (Wickert et al. 2002).

After the POD and differencing process, the L1 and L2 atmospheric excess phases can be derived along with the precise orbits (positions and velocities) of both the LEO and occulting GPS satellites. The further derivation of the atmospheric properties based on these occultation measurements will be explored in the next section.

5.3.2 Bending Angle Retrieval

After the phase delays are calibrated to remove special and general relativistic effects and to remove the GPS and LEO clock errors, a time series of excess phase delay at both GNSS frequencies (e.g., L1 and L2 for GPS) are derived. Then the atmospheric bending in the ionosphere and neutral atmosphere can be inferred.

In the ionosphere and upper part of the neutral atmosphere, the radio signals can be assumed to be monochromatic (e.g., single-tone or single-ray), i.e., only one ray connects the transmitter and receiver at one instant. The geometric optics (or ray optics) concept can be applied to describe the radio signal propagation, as the diffraction effect can be neglected. The computation of bending angles is thus straightforward as they are unambiguously related to the instantaneous frequency of the received signal.

In the lower troposphere, however, radio signals become non-monochromatic (e.g., multiple-tone) and may have a very complex structure due to multipath effects caused mainly by water vapor structures (Gorbunov and Gurvich 1998; Sokolovskiy 2001). The atmospheric multipath occurs when sharp vertical variations in atmospheric refractivity structure create multiple, simultaneous signal paths connecting the transmitter and receiver through the atmosphere. In the multipath regions, the bending angles cannot be derived directly from the instantaneous frequency of the measured signal because the instantaneous frequency will be related, not to a single ray, but to two or more rays.

Generally, it is practical to split the bending angle retrieval into two altitude ranges. Above the lower troposphere where atmospheric multipath is not significant, the bending angles at both frequencies are derived based on geometric optics from the differential form of the excess phase (or excess Doppler) after appropriate noise filtering (Vorob'ev and Krasil'nikova 1994; Kursinski et al. 1997; Hajj et al. 2002). In the lower troposphere, where atmospheric multipath cannot be neglected, the radio-holographic (wave optics) techniques are needed to accurately reconstruct the bending angle from the phase and amplitude measurements (e.g., Gorbunov 2002; Jensen et al. 2003).

5.3.2.1 Geometric Optics Method

The sum of the extra phase delay due to the ionosphere and neutral atmosphere is determined after the calibration process. The differential form of the excess phase delay, also called extra Doppler shift can be derived. Based on geometric optics assumption, the accumulation of atmospheric bending along a ray path can be measured as an extra Doppler shift relative to that expected for a straight-line (in vacuum) signal path (Vorob'ev and Krasil'nikova 1994; Kursinski et al. 1997; Hajj et al. 2002). By using the geometry and notation in Fig. 5.4, the extra Doppler

shift f_D in the GPS transmitter frequency f_T at the receiver can be expressed as the projection of the satellite velocities on the ray paths (Kursinski et al. 1997), such as

$$\begin{aligned} f_D &= \frac{f_T}{c} \left(\vec{V}_T \cdot \vec{k}_T + \vec{V}_R \cdot \vec{k}_R \right), \\ &= -\frac{f_T}{c} \left(V_T^r \cos \phi_T + V_T^\theta \sin \phi_T + V_R^r \cos \phi_R + V_R^\theta \sin \phi_R \right), \end{aligned} \quad (5.17)$$

where \vec{V}_R and \vec{V}_T are velocity vectors for receiver and transmitter, and \vec{k}_R and \vec{k}_T are unit vectors representing the direction of the ray path at the receiver and transmitter, and c is the velocity of light in vacuum. The superscripts (r and θ) represent the radial and tangential components of the velocity vectors, and ϕ_T and ϕ_R are the angels between the ray path and the satellite position vectors at the transmitter and receiver (Fig. 5.4).

According to Bouguer's rule in Eq. (5.7) and the geometry of Fig. 5.4, we have:

$$a = n(r_T) r_T \sin \phi_T = n(r_R) r_R \sin \phi_R = n(r_t) r_t. \quad (5.18)$$

As the transmitter and the receiver are at reasonably high altitudes, we can simply setting the refractive index equals to unity at both transmitter and receiver, thus we have

$$a = r_T \sin \phi_T = r_R \sin \phi_R. \quad (5.19)$$

The total bending angle α according to the geometry in Fig. 5.4 follows

$$\alpha = \phi_T + \phi_R + \theta - \pi, \quad (5.20)$$

where, r_T , r_R , and r_t are the distance of the transmitter, receiver and the tangent point from the center of curvature, and θ is the open angle between the transmitter and receiver vectors.

Given the precise measurements of the occultation geometry (transmitter and receiver position and velocity vectors) and extra Doppler shift, the bending angle can be derived iteratively from Eqs. (5.17, 5.18, 5.19, and 5.20) under the assumption of local spherically symmetric atmosphere.

5.3.2.2 Radio-Holographic (RH) Method

In the lower troposphere, the multipath problem due to the water vapor gradients could result in large error in the geometric optics bending retrieval. Also the vertical resolution of GO retrieval is limited by the size of the Fresnel zone (Kursinski et al. 1997). In order to tackle the multipath problem and improve the vertical resolution

of the bending angle retrieval, it is necessary to use the radio-holographic (RH) methods, which is based on the analysis of the records of complex radio signals, or radio holograms.

There are many RH methods proposed for processing radio occultation signals in multipath regions: (1) back-propagation (BP) (also referred to as diffraction correction), which propagates signals backward in the vacuum toward a plane located in a single-ray area (Hinson et al. 1997; Gorbunov and Gurvich 1998); (2) radio-optics, which analyzes the local spatial spectra of the measured complex wave field through Fourier analysis (Lindal et al. 1987; Pavelyev 1998; Hocke et al. 1999; Sokolovskiy 2001); (3) Fresnel diffraction theory (Marouf et al. 1986; Mortensen and Høeg 1998); (4) canonical transform (CT) (Gorbunov 2002); (5) full-spectrum-inversion (FSI) (Jensen et al. 2003) and (6) phase matching method (Jensen et al. 2004).

The widely used CT method consists of using Fourier Integral Operators (FIO) to find directly the dependence of the bending angle on the impact parameter for each physical ray in multi-path conditions. The CT method requires that the electromagnetic field is back-propagated to a straight line before the canonical transformation can be applied to transform the coordinate to impact parameter representation (Gorbunov 2002). The back-propagation from the observation trajectory to the auxiliary straight-line trajectory results in the most computational time in CT processing. The Fourier transform method has theoretical limitation that requires circular satellite orbits. The approximation developed by Jensen et al. (2003) in FSI method expands the Fourier method to be applied for near-circular/realistic satellite orbits. The FSI method utilizes the relation between the derivative of the phase of a physical ray on the instantaneous frequency in the full Fourier spectrum of the RO signal and the time of intersection of the physical ray with LEO satellite orbit. Similar to FSI method, the phase-matching method is based on the synthetic aperture concept and the method of the stationary phase and thus preserves the high vertical resolution properties. Moreover, it is a more general method that is directly applicable for noncircular/realistic orbits and eliminates the intermediate step of propagation of complex electromagnetic field to circular orbits (e.g., for FSI) or straight line (e.g., for CT). However the phase-matching method comes with higher computational cost, as it can't apply Fast-Fourier-Transform (FFT).

All the RH methods are based on stationary electromagnetic theory. Other than BP method, the other RH methods provide the bending angle as a single-valued function of impact parameter in the multi-path region. The BP method, however, may result in multi-valued function in particular in the presence of ducting or super-refraction (Gorbunov 2002).

In terms of resolution and ability to handle multipath, the most efficient radio-holographic methods are currently the Fourier operator based methods such as canonical transform and FSI. Both methods are widely adapted by many GNSS occultation data processing centers. For GPS and close to circular LEO orbit, the FSI method is an optimal method (most accurate and fast) for bending angle retrieval in the multi-path condition.

5.3.3 Ionosphere Retrieval

After the calibration process, the sum of the neutral and the ionospheric delays is isolated (up to a constant). When the tangent point of the occultation link is in the ionosphere, the excess phase delay due to the neutral atmosphere is negligible. There are two types of processing technique for extracting ionospheric delay along the ray path (Hajj and Romans 1998; Schreiner et al. 1999): (1) single-frequency approach, i.e., deriving the ionospheric delay at each carrier frequency (e.g., L1 and L2) separately; (2) a dual-frequency approach that directly isolates the ionospheric delay through linear combination by assuming L1 and L2 signals travel along the same ray path in the ionosphere.

The first approach results in less noisy determination of ionospheric delay but requires the a-priori calibration processes (Sect. 5.3.1) to remove the orbit and clock errors. The second approach is inherently simpler by eliminating the calibration process, as the orbit and clocks errors cancel out when forming the L1 and L2 linear combination. However, the simplicity in the dual-frequency approach is at the cost of lower precision due to the noise added by L2. Also it assumes L1 and L2 signals travel along the same ray path in the ionosphere, which could be violated and result in extra errors in the presence of significant bending in the ionosphere (Hajj and Romans 1998).

By using the single-frequency approach, the bending angle at each signal frequency can be retrieved from the ionospheric delay or Doppler. Following the Abel transform in Eq. (5.13), the vertical profile of refractive index can be derived. Note that the Abel integral requires knowledge of bending all the way up to the top of the ionosphere. GPS is above most of the ionosphere, however, the LEO receiver satellite are generally located inside the ionosphere. Therefore the bending due to the ionosphere above LEO altitude might not be neglected and needs to be modeled (e.g., Hajj and Romans 1998).

The electron density profile n_e (in per cubic meter) can then be derived through the following relation (Hajj and Romans 1998):

$$n_e(r) = [1 - n(r)] \cdot f^2 / (40.3). \quad (5.21)$$

In the ionosphere, the total electron content (TEC in electrons numbers per square meters) along a ray is related to electron density n_e , refractive index n and the excess phase S (in meters) by

$$TEC = \int n_e dl = -\frac{f^2}{40.3 \times 10^{16}} \int (n - 1) dl = -\frac{f^2 S}{40.3}. \quad (5.22)$$

Due to the dispersive characteristics of the ionosphere, the L1 and L2 signals propagate on slightly different paths and thus result in slightly different TECs. TEC may be calculated from excess ionospheric phase delay (S_1 and S_2 at two carrier frequencies) after removing the orbit and clock errors through calibration process.

While the bending angle is rather small in the F2 layer of the ionosphere, a straight-line propagation assumption (i.e., the path difference is negligible) can be applied, such that the TEC is related to the calibrated phase $\Delta S = (S_1 - S_2)$ as

$$TEC = \frac{\Delta S}{40.3} \frac{f_1^2 f_2^2}{f_1^2 - f_2^2}, \quad (5.23)$$

where f_1 and f_2 are the GPS L1 and L2 carrier frequencies, respectively. The phase difference (ΔS) cancels out the orbit and clock errors automatically and eliminates the complicated calibration process. The dual-frequency approach greatly reduces the amount of data processing and allows electron density profile n_e to be computed on orbit and disseminated in near real time that is essential for space weather forecast.

Note that the total TEC is the integral of electron density from the GPS transmitter to LEO receiver. With the assumption of spherical symmetric ionosphere, the ionosphere contribution above the LEO can be removed. The TEC along the section of a ray below the LEO, $\overline{TEC}(r_0)$, is a function of electron density (Schreiner et al. 1999)

$$\overline{TEC}(r_0) = 2 \int_{r_0}^{r_{LEO}} \frac{n_e(r) \cdot r}{\sqrt{r^2 - r_0^2}} dr. \quad (5.24)$$

Therefore, the electron density profile can be reconstructed similar to the Abel transform through the following:

$$n_e(r) = -\frac{1}{\pi} \int_{r_0}^{r_{LEO}} \frac{d(\overline{TEC})}{dr_0} \frac{dr_0}{\sqrt{r_0^2 - r^2}}. \quad (5.25)$$

The inversion of the electron density $n_e(r)$ is based on the assumption of local spherical symmetry of the electron density in a large region (a few thousand kilometers in radius) around the ray path tangent points. This assumption may be violated due to the presence of large horizontal gradients in electron density, in particular below the F-layer (sometimes giving large negative or positive electron density). At the same time the geographical location of the ray path tangent points at the top and at the bottom of a profile may differ by several hundred kilometers (horizontal smear). Therefore, retrieved electron density profiles should generally not be interpreted as actual vertical profiles, but rather as a mapping of both vertical and horizontal ionospheric structure into a 1D profile, given particular occultation geometry.

5.3.4 Neutral Atmosphere Retrieval

In the neutral atmosphere (generally below 70 km), the inversion process includes removing the ionospheric effects, deriving the neutral atmosphere bending angle, retrieving refractivity, and further inferring the geophysical parameters.

5.3.4.1 Ionospheric Calibration on Bending

When the tangent points descend into the neutral atmosphere, the bending angles at both GPS frequencies include the bending contribution from both the ionosphere and neutral atmosphere. In the most general situation, an ionospheric correction is needed in order to derive the neutral atmospheric bending. The process to separate the neutral atmospheric bending (or ionosphere-free bending) by removing the ionosphere induced bending is referred as ionospheric calibration.

Because of the dispersive nature of the ionosphere, the L1 and L2 signals travel along slightly different paths and have slightly different bending. The separation of the two signal paths in the ionosphere near the tangent point varies from 100 to 5 km, depending on the tangent height and location of the occultation, the local time and the solar conditions (e.g., Hajj and Romans 1998; Hajj et al. 2002).

Generally, a first-order ionospheric correction is accomplished through a simple linear combination of the L1 and L2 bending angle profiles following a procedure first suggested by Vorob'ev and Krasil'nikova (1994), such that

$$\alpha_{neutral}(a) = \frac{f_{L1}^2}{f_{L1}^2 - f_{L2}^2} \alpha_{L1}(a) - \frac{f_{L2}^2}{f_{L1}^2 - f_{L2}^2} \alpha_{L2}(a), \quad (5.26)$$

where α_{L1} and α_{L2} , the bending at two GPS frequencies f_{L1} and f_{L2} , are interpolated to the same level of impact parameter (a).

Note that the L2 phase measurements are usually noisier and less accurate than L1 due to lower frequency (i.e., more prone to the ionospheric scintillation and delay) and lower SNR (signal to noise ratio) (e.g., Hajj et al. 2002). To reduce the effect of larger noise on L2, a slightly modified linear combination is used (Rocken et al. 1997):

$$\alpha_{neutral}(a) = \alpha_{L1}(a) + \frac{f_{L2}^2}{f_{L1}^2 - f_{L2}^2} [\bar{\alpha}_{L1}(a) - \bar{\alpha}_{L2}(a)], \quad (5.27)$$

where $\bar{\alpha}_{L1}(a)$ and $\bar{\alpha}_{L2}(a)$ are obtained from L1 and L2 excess phases subjected to filtering with larger smoothing window (e.g., longer intervals) than that used for $\alpha_{L2}(a)$. This results in overall error reduction by reducing the effects of L2 noise, however, at the expense of a certain increase of uncalibrated ionospheric effects.

Deeper into the lower atmosphere (e.g., below ~ 10 km), the L2 signal becomes too weak for robust tracking due to the low L2 signal power, incomplete knowledge of P-code modulation as well as large atmospheric defocusing effects. In such case, the ionospheric correction term (i.e., $\bar{\alpha}_{L1}(a) - \bar{\alpha}_{L2}(a)$), is linear extrapolated from higher altitudes downward to the surface for continuing ionospheric correction in the lower altitudes with the absence of L2 measurement. Also note that the ionospheric calibration should not be applied above a certain height, when the neutral atmosphere signature on the occulted signal is comparable to residual ionospheric effects or the receiver's thermal noise. This tends to occur at the altitude of $\sim 50\text{--}90$ km, depending on the ionospheric conditions (Hajj et al. 2002).

The ionospheric calibration process described above effectively removes the first order ionospheric term ($1/f^2$) in Eq. (5.1). Higher order contributions constitute the major source of error during day-time solar maximum at high altitudes (e.g., Kursinski et al. 1997) will require further calibration (e.g., Bassiri and Hajj 1993).

5.3.4.2 Refractivity Retrieval from Abel Inversion

Under the assumption of spherically symmetric atmosphere, the refractive index profile can be derived from the neutral atmospheric bending through the Abel transform in Eq. (5.13). As the upper limit of the Abel integral requires knowledge of the bending angle as a function of impact parameter up to the top of the atmosphere. However, the estimated bending is reasonable accurate only up to a certain upper height (e.g., $\sim 50\text{--}90$ km dependent on the ionospheric condition as discussed in previous section). Therefore, the a-priori (or background) bending angle is needed to extend the observational neutral bending angle at higher altitudes. This a-priori bending is often referred as the upper boundary condition for Abel inversion. In practice, the a-priori bending can be derived from weather or climate models (e.g., Hedin 1991) or from a simple model (e.g., exponential extrapolation of bending upward from a certain altitudes (Hajj et al. 2002)). The uncertainty in the a-priori bending model could introduce errors in the refractivity retrieval from Abel integral. To reduce the effects of error propagation downward from the upper stratosphere, the optimization technique that mixes the observational neutral atmospheric bending with the a-priori model can be used (e.g., Lohmann 2005).

After the refractive index as a function of impact parameter $n(a)$ at the tangent point, is derived from the Abel inversion, the tangent point radius is obtained from (5.14), i.e., $r = a/n$. The radius in turn is converted into height above an ellipsoidal fit to the mean sea-level geoid.

5.3.4.3 Quality Control

In the GNSS RO data processing centers, various quality control methods are applied and they are used at different processing stages. For example, in the early processing stage, the quality of the measured signal SNR, excess phase and

excess Doppler are examined; whereas in the later stages, the bending angle and/or refractivity profiles are compared with either climatology or weather model analysis or reanalysis products. Various criteria can be applied to ensure the quality of RO retrieval dataset for suited research or operational usage (e.g., Ho et al. 2009).

After going through the calibration and retrieval processes, the bending angle and refractivity profiles can be derived from occultation measurements. Further process will lead to the derivation of the atmospheric properties in the neutral atmosphere and ionosphere, which will be elaborated in the following Chaps. 6 and 7, respectively.

References

- Anthes RA, Bernhardt PA, Chen Y, Cucurull L, Dymond KF, Ector D, Healy SB, Ho SP, Hunt DC, Kuo Y-H, Liu H, Manning K, McCormick C, Meehan TK, Randel WJ, Rocken C, Schreiner WS, Sokolovskiy SV, Syndergaard S, Thompson DC, Trenberth KE, Wee TK, Yen NL, Zeng Z (2008) The COSMIC/FORMOSAT-3 mission-early results. *Bull Am Meteorol Soc* 89:313–333
- Bassiri S, Hajj GA (1993) Higher-order ionospheric effect on the Global Positioning System observables and means of modeling them. *Manuscr Geod* 18:280–289
- Beyerle G, Schmidt T, Michalak G, Heise S, Wickert J, Reigber C (2005) GPS radio occultation with GRACE: atmospheric profiling utilizing the zero difference technique. *Geophys Res Lett* 32:L13806. doi:[10.1029/2005GL023109](https://doi.org/10.1029/2005GL023109)
- Born M, Wolf E (1980) Principles of optics. Electromagnetic theory of propagation interference and diffraction of light. Pergamon Press, Oxford/New York
- Eliseev SD, Yakovlev OI (1989) On the radio occultation measurements in the Earth's atmosphere using millimeter radio waves (in Russian). *Izv Vyssh Uchebn Zaved Radiofiz* 32:3–10
- Feng D, Herman B, Exner M, Schreiner B, Anthes R, Ware R (1995) Space-borne GPS remote sensing for atmospheric research. *Proc Synth Apert Radar Passiv Microw Sens* 2584:448–455
- Fishbach FF (1965) A satellite method for temperature and pressure below 24 km. *Bull Am Meteorol Soc* 9:528–532
- Fjeldbo G, Eshleman VR (1965) The bistatic radar-occultation method for the study of planetary atmosphere. *J Geophys Res* 70(1965):3217–3226
- Fjeldbo G, Eshleman VR (1968) The atmosphere of Mars analyzed by integral inversion of the Mariner IV occultation data. *Planet Space Sci* 16:1035–1059
- Fjeldbo GF, Eshleman VR, Kliore AJ (1971) The neutral atmosphere of Venus as studied with the Mariner V radio occultation experiments. *Astron J* 76:123–140
- Fjeldbo (Lindal) G, Kliore AJ, Seidel B, Sweetnam D, Cain D (1975) The Pioneer 10 radio occultation measurement of the ionosphere of Jupiter. *Astron Astrophys* 39:91
- Galas R, Wickert J, Burghardt W (2001) High rate low latency GPS ground tracking network for CHAMP. *Phys Chem Earth (A)* 26:649–652
- Gorbunov ME (2002) Canonical transform method for processing radio occultation data in lower troposphere. *Radio Sci* 37(5):1076. doi:[10.1029/2000RS002592](https://doi.org/10.1029/2000RS002592)
- Gorbunov ME, Gurvich AS (1998) Microlab-1 experiment: multipath effects in the lower troposphere. *J Geophys Res* 103(D12):13,819–13,826
- Gurvich AS, Krasil'nikova TG (1987) On the use of navigational satellites in radio occultation measurements in the Earth's atmosphere (in Russian). *Issled Zemli Kosmosa* 6:89–93
- Hajj GA, Romans LJ (1998) Ionospheric electron density profiles obtained with the Global Positioning System: results from the GPS/MET experiment. *Radio Sci* 33(1):175–190
- Hajj GA, Kursinski ER, Romans LJ, Bertiger WI, Leroy SS (2002) A technical description of atmospheric sounding by GPS occultation. *J Atmos Solar Terr Phys* 64:451–469

- Hajj GA, Ao CO, Iijima BA, Kuang D, Kursinski ER, Mannucci AJ, Meehan TK, Romans LJ, de la Torre Juarez M, Yunck TP (2004) CHAMP and SAC-C atmospheric occultation results and intercomparisons. *J Geophys Res* 109:D06109. doi:[10.1029/2003JD003909](https://doi.org/10.1029/2003JD003909)
- Hedin AE (1991) Extension of the MSIS thermosphere model into the middle and lower atmosphere. *J Geophys Res* 96:1159–1172. doi:[10.1029/90JA02125](https://doi.org/10.1029/90JA02125)
- Hinson DP, Flasar FM, Schinder AJKPJ, Twicken JD, Herrera RG (1997) Jupiter's ionosphere: results from the first Galileo radio occultation experiment. *Geophys Res Lett* 24(17):2107–2110
- Ho S-P, Kirchengast G, Leroy S, Wickert J, Mannucci AJ, Steiner A, Hunt D, Schreiner W, Sokolovskiy S, Ao C, Borsche M, von Engeln A, Foelsche U, Heise S, Iijima B, Kuo Y-H, Kursinski ER, Pirscher B, Ringer M, Rocken C, Schmidt T (2009) Estimating the uncertainty of using GPS radio occultation data for climate monitoring: intercomparison of CHAMP refractivity climate records 2002–2006 from different data centers. *J Geophys Res* 114:D23107. doi:[10.1029/2009JD011969](https://doi.org/10.1029/2009JD011969)
- Hocke KA, Pavelyev AG, Yakovlev OI, Barthes L, Jakowski N (1999) Radio occultation data analysis by the radioholographic method. *J Atmos Sol Terr Phys* 61(15):1169–2117
- Howard HT, Tyler GL, Esposito PB, Anderson JD, Reasenberg RD, Shapiro II, Fjeldbo G, Kliore AJ, Levy GS, Brunn DL, Dickinson R, Edelson RE, Martin WL, Postal RB, Seidel B, Sesplaukis TT, Shirley DL, Stelzried CT, Sweetnam DN, Wood GE, Zygielbaum AI (1974) Mercury: results on Mass, radius, ionosphere and atmosphere obtained from the Mariner 10 dual frequency radio signals. *Science* 185(4146):179–183
- Ivanov GS, Kolosov MA, Savich NA et al (1979) Daytime ionosphere of Venus as studied with Venera 9 and 10 dual-frequency experiments. *Icarus* 39(2):209
- Jensen AS, Lohmann M, Benzon H-H, Nielsen AS (2003) Full spectrum inversion of radio occultation signals. *Radio Sci* 38(3):1040. doi:[10.1029/2002RS002763](https://doi.org/10.1029/2002RS002763)
- Jensen AS, Lohmann MS, Nielsen AS, Benzon H-H (2004) Geometrical optics phase matching of radio occultation signals. *Radio Sci* 39:RS3009. doi:[10.1029/2003RS002899](https://doi.org/10.1029/2003RS002899)
- Kalashnikov IE, Yakovlev OI (1978) Possibility of investigation of the Earth's atmosphere using the radio occultation method (in Russian). *Kosm Issled* 16:943–946 (English translation, *Cosm Res* 16:943–946, 1978)
- Kliore AJ (1969) Some remarks on meteorological measurements with occultation satellites. In: Space research, vol IX. North-Holland Publishing Company, Amsterdam, pp 590–602
- Kliore A, Cain DL, Levy GS, Eshleman VR, Fjeldbo G, Drake FD (1965) Occultation experiment: results of the first direct measurement of Mar's atmosphere and ionosphere. *Science* 149:1243–1248
- Kliore A, Levy GS, Cain DL, Fjeldbo G, Rasool SI (1967) Atmosphere and ionosphere of Venus from the Mariner V S-band radio occultation measurement. *Science* 158(3809):1683–1688
- Kliore AJ, Fjeldbo G, Siedel BL, Sweetnam DN, Sesplaukis TT, Woiceshyn PM, Rasool SI (1975) The atmosphere of Io from Pioneer 10 radio occultation measurements. *Icarus* 24:407–410
- Kliore AJ, Patel IR, Lindal GF, Sweetnam DN, Hotz HB, Waite JH Jr, McDonough TR (1980) Structure of the ionosphere and atmosphere of Saturn From Pioneer 11 Saturn radio occultation. *J Geophys Res* 85(A11):5857–5870. doi:[10.1029/JA085iA11p05857](https://doi.org/10.1029/JA085iA11p05857)
- Kliore AJ, Hinson DP, Flasar FM, Nagy AF, Cravens TE (1997) The ionosphere of Europa from Galileo radio occultations. *Science* 277:355–358
- Kolosov MA, Yakovlev OI, Trusov BP et al (1976) Radio occultation investigation of the atmosphere of Venus by use of satellites Venera-9 and Venera-10. *Radio Eng Electron Phys* 21(8):1585
- Kursinski ER, Hajj GA, Schofield JT, Linfield RP, Hardy KR (1997) Observing Earth's atmosphere with radio occultation measurements using the Global Positioning System. *J Geophys Res* 102(D19):23429–23465
- Kursinski ER, Hajj GA, Leroy SS, Herman B (2000) The GPS radio occultation technique. *Terr Atmos Ocean Sci* 11:53–114
- Lindal GF, Wood GE, Hotz HB, Sweetnam DN, Eshleman VR, Tyler GL (1983) The atmosphere of Titan: an analysis of the Voyager 1 radio-occultation measurements. *Icarus* 53:348–363

- Lindal GF, Lyons JR, Sweetnam DN, Eshleman VR, Hinson DP, Tyler GL (1987) The atmosphere of Uranus: results of radio occultation measurements with voyager 2. *J Geophys Res* 92:14987–15001
- Liu AS (1978) On the determination and investigation of the terrestrial ionospheric refractive indices using GEOS-3/ATS-6 satellite-to-satellite tracking data. NASA-CR-156848, Nov 1978, Jet Propulsion Laboratory, Pasadena
- Lohmann M (2005) Application of dynamical error estimation for statistical optimization of radio occultation bending angles. *Radio Sci* 40:RS3011. doi:[10.1029/2004RS003117](https://doi.org/10.1029/2004RS003117)
- Luntama J-P, Kirchengast G, Borsche M, Foelsche U, Steiner A, Healy S, von Engeln A, O’Clerigh E, Marquardt C (2008) Prospects of the EPS GRAS mission for operational atmospheric applications. *Bull Am Meteorol Soc* 89:1863–1875
- Lusignan B, Modrell G, Morrison A, Pomalaza J, Ungar SG (1969) Sensing the Earth’s atmosphere with occultation satellites. *Proc IEEE* 57(4):458–467
- Marouf EA, Tyler GL (1986) Detection of two satellites in the Cassini division of Saturn’s rings. *Nature* 6083:31–35
- Marouf EA, Tyler GL, Rosen PA (1986) Profiling Saturn rings by radio occultation. *ICARUS* 68:120–166
- Mortensen MD, Høeg P (1998) Inversion of GPS occultation measurements using Fresnel diffraction theory. *Geophys Res Lett* 25(13):2446–2449
- Mueller II, Beutler G (1992) The international GPS service for geodynamics development and current status. In: Proceedings of the 6th international geodetic symposium on satellite positioning, Columbus, March, pp 823–835
- Papas CH (1965) Theory of electromagnetic wave propagation. McGraw-Hill, New York
- Pavelyev AG (1998) On the feasibility of radioholographic investigations of wave fields near the Earth’s radio-shadow zone on the satellite-to-satellite path. *J Commun Technol Electron* 43(8):875–879
- Rangaswamy S (1976) Recovery of atmospheric parameters from the Apollo/Soyuz-ATS-F radio occultation data. *Geophys Res Lett* 3(8):483–486. doi:[10.1029/GL003i008p00483](https://doi.org/10.1029/GL003i008p00483)
- Rim HJ, Schutz BE (2002) Geoscience Laser Altimeter System (GLAS) algorithm theoretical basis document version 2.2: Precision Orbit Determination (POD), Center for Space Research, The University of Texas at Austin, October 2002
- Rocken C, Anthes R, Exner M, Hunt D, Sokolovskiy S, Ware R, Gorbunov M, Schreiner W, Feng D, Herman B, Kuo Y-H, Zou X (1997) Analysis and validation of GPS/MET data in the neutral atmosphere. *J Geophys Res* 102:29849–29866. doi:[10.1029/97JD0240](https://doi.org/10.1029/97JD0240)
- Schreiner WS, Sokolovskiy SV, Rocken C, Hunt DC (1999) Analysis and validation of GPS/MET radio occultation data in the ionosphere. *Radio Sci* 34:949–966
- Schreiner W, Rocken C, Sokolovskiy S, Hunt D (2010) Quality assessment of COSMIC/FORMOSAT-3 GPS radio occultation data derived from single- and double-difference atmospheric excess phase processing. *GPS Solut* 14:13–22. doi:[10.1007/s10291-009-0132-5](https://doi.org/10.1007/s10291-009-0132-5)
- Sokolovskiy SV (2001) Modeling and inverting radio occultation signals in the moist troposphere. *Radio Sci* 36(3):441–458
- Tapley BD (1973) Statistical orbit determination theory. In: Tapley BD, Szebehely V (eds) Advances in dynamical astronomy. D. Reidel Publishing Co, Holland, pp 396–425
- Tyler GL, Sweetnam DN, Anderson JD, Borutzki SE, Campbell JK, Kursinski ER, Levy GS, Lindal GF, Lyons JR, Wood GE (1989) Voyager radio science observations of Neptune and Triton. *Science* 246:1466–1473
- Vorob’ev VV, Krasil’nikova TG (1994) Estimation of accuracy of the atmospheric refractive index recovery from Doppler shift measurements at frequencies used in the NAVSTAR system. *Izv Russ Acad Sci Atmos Ocean Phys Engl Transl* 29:602–609
- Ware R, Exner M, Feng D, Gorbunov M, Hardy K, Herman B, Kuo HK, Meehan T, Melbourne W, Rocken C, Schreiner W, Sokolovskiy S, Solheim F, Zou X, Anthes R, Businger S (1996) GPS sounding of the atmosphere: preliminary results. *Bull Am Meteorol Soc* 77:19–40

- Wickert J, Reigber C, Beyerle G, König R, Marquardt C, Schmidt T, Grunwaldt L, Galas R, Meehan TK, Melbourne WG, Hocke K (2001) Atmosphere sounding by GPS radio occultation: first results from CHAMP. *Geophys Res Lett* 28:3263–3266
- Wickert J, Beyerle G, Hajj GA, Schwieger V, Reigber C (2002) GPS radio occultation with CHAMP: atmospheric profiling utilizing the space-based single difference technique. *Geophys Res Lett* 29(8):28-1–28-4. doi:[10.1029/2001GL13982](https://doi.org/10.1029/2001GL13982)
- Wickert J, Michalak G, Schmidt T, Beyerle G, Cheng CZ, Healy SB, Heise S, Huang CY, Jakowski N, Köhler W, Mayer C, Offiler D, Ozawa E, Pavelyev AG, Rothacher M, Tapley B, Arras C (2009) GPS radio occultation: results from CHAMP, GRACE and FORMOSAT-3/COSMIC. *Terr Atmos Ocean Sci* 20(1):35–50. doi:[10.3319/TAO.2007.12.26.01\(F3C\)](https://doi.org/10.3319/TAO.2007.12.26.01(F3C))
- Wu JT (1984) Elimination of clock errors in a GPS based tracking system. In: Paper AIAA-84-2052, AIAA/AAS astrodynamics conference, Seattle, August
- Wu SC, Yunck TP, Thornton CL (1987) Reduced-dynamic technique for precise orbit determination of low Earth satellite. In: Proceedings of AAS/AIAA astrodynamics specialist conference, Paper AAS 87-410, Kalispell, Montana, August 1987
- Yakovlev OI, Matyugov SS, Vilkov IA (1995) Attenuation and scintillation of radio waves in the Earth's atmosphere from radio occultation experiments on satellite-to-satellite links. *Radio Sci* 30(3):591–602. doi:[10.1029/94RS01920](https://doi.org/10.1029/94RS01920)
- Yunck TP, Lindal GF, Liu C-H (1988) The role of GPS in precise Earth observation. In: Proceedings of the IEEE position location and navigation symposium (PLANS 88), 29 November–2 December
- Yunck T, Liu C-H, Ware R (2000) A history of GPS sounding. *Terr Atmos Oceanic Sci* 11:1–20

Chapter 6

Atmospheric Sensing Using GNSS RO

6.1 GNSS RO Atmospheric Sounding

6.1.1 Parameters Retrieval from GNSS RO

The Eqs. (5.3) and (5.4) in Chap. 5 shows the dependency of atmospheric refractivity on various atmospheric properties in the GPS RO frequencies. In the neutral atmosphere, which includes the stratosphere and the troposphere (i.e., below ~ 70 km), the refractivity primarily depends on the dry atmosphere and water vapor as firstly described by Smith and Weintraub (1953). For realistic suspensions of water or ice, contribution due to the liquid water and ice water content are generally small in comparison with other terms and will be neglected here. Therefore, the refractivity variation with tangent radius r becomes a simple function of atmospheric pressure P (in hPa), water vapor partial pressure P_w (in hPa) and temperature T (in Kelvin), such as

$$N(r) = c_1 \frac{P(r)}{T(r)} + c_2 \frac{P_w(r)}{T^2(r)}. \quad (6.1)$$

The constants are $c_1 = 77.6$ (K hPa^{-1}) and $c_2 = 3.73 \times 10^5$ ($\text{K}^2 \text{ hPa}^{-1}$). Generally, the first term on the right-hand-side (RHS) of the equation is referred as a dry term, which dominates throughout the neutral atmosphere. However, the second term on the RHS is referred as a wet term (i.e., water vapor contribution), which is generally smaller than the dry term but becomes significant in the middle and lower troposphere and can constitute to $\sim 30\%$ of refractivity near the Earth's surface in lower latitudes.

Given the GNSS RO refractivity measurement, the conventional geophysical parameters, such as air density, pressure, temperature and humidity can be further derived. However, beside Eq. (6.1), other physical relations or assumptions are necessary.

6.1.2 Dry Atmosphere Retrieval (Density, Pressure and Temperature)

In the regions where the water vapor is negligible, Eq. (6.1) reduces to $N = c_1 P/T$. As the saturation vapor pressure decreases rapidly with decreasing temperature according to Clausius-Clapeyron equation, the water vapor pressure P_w can be neglected in the upper troposphere where temperature is low (e.g., $T < 250$ K) (Kursinski et al. 2000a; Hajj et al. 2002). Combining the Eq. (6.1) with the ideal gas law (i.e., $P = \rho \cdot (R/m) \cdot T$, where m is the mean molecular mass of air), the atmospheric density $\rho(r)$ (in kg m^{-3}) can be expressed as a function of refractivity by

$$\rho(r) = \frac{N(r)m_d}{c_1 R} = \frac{P(r)m_d}{T(r)R}, \quad (6.2)$$

where $R = 8.314 \text{ (J K}^{-1} \text{ mol}^{-1}\text{)}$ is the universal gas constant. The m_d is the mean molecular mass of dry air, which can be deemed as a constant as the atmosphere is well-mixed below the homopause (~ 100 km altitude) (Kursinski et al. 1997). With a further assumption of hydrostatic equilibrium:

$$\frac{\partial P(r)}{\partial r} = -\rho(r)g, \quad (6.3)$$

where g is the gravitational acceleration, the atmospheric pressure (P) can be derived from the density by integrating the hydrostatic equation given the density profile obtained from the refractivity in Eq. (6.2).

$$P(r) = P(r_{top}) + \int_r^{r_{top}} \rho(r)g(r)dr = \frac{1}{c_1} N(r_{top}) T(r_{top}) + \frac{m_d}{c_1 R} \int_r^{r_{top}} N(r)g(r)dr \quad (6.4)$$

Note that an upper boundary condition of pressure, $P(r_{top})$ is required to obtain the pressure profile at any given altitude. The simplest option is to use zero pressure at the top of the atmosphere (e.g., $P = 0$ when $r \rightarrow \infty$). However, the vertical extent of the density profile is constrained by the RO refractivity retrieval. In practice the temperature from weather model analysis or climatology at a high altitude (e.g., in the upper stratosphere) is generally used. Fractional pressure errors due to such initial temperature guess decrease rapidly as the integration moves deeper into the atmosphere (Kursinski et al. 1997). Given the pressure and refractivity (or density) profiles, accurate temperature profiles can be easily derived based on Eq. (6.2) throughout the stratosphere down to mid-troposphere and below depending on latitudes, where the water vapor is negligible, e.g.,

$$T(r) = c_1 \frac{P(r)}{N(r)}. \quad (6.5)$$

Note that when the water vapor is non-negligible in the lower altitudes, the temperature derived from Eq. (6.5) is generally called dry temperature, which will be colder than the real temperature. In addition, given the density and pressure profiles as a function of geometric height (or absolute altitude), the geopotential heights of constant pressure levels can also be derived. As RO provides independent values of pressure and height, the geopotential height at a constant pressure level from RO can be retrieved only based on the density profile above the level of interest (Leroy 1997). Such derivation will therefore have the advantage of not relying on the surface pressure and temperature measurements that are generally required for conventional geopotential heights calculation.

6.1.3 *Moist Atmosphere Retrieval*

When the water vapor becomes significant in the middle and lower troposphere, derivation of water vapor, temperature and pressure from refractivity measurement becomes under-determined. It requires independent knowledge of one of the three parameters (T , P or P_w) in order to solve for the other two parameters. Combining Eq. (6.1) and the ideal gas law, the density can be expressed as

$$\rho(r) = \frac{m_v}{c_1 R} \left(N(r) - \frac{c_2 P_w(r)}{T^2(r)} \right), \quad (6.6)$$

where m_v is the mean molecular mass of moist air. And the Eq. (6.1) can be rearranged to solve for water vapor:

$$P_w(r) = [N(r)T^2(r) - c_1 P(r)T(r)] / c_2. \quad (6.7)$$

or solve for temperature given a-priori water vapor after simple iteration

$$T(r) = \frac{c_1 P(r)}{N(r)} + \frac{c_2 P_w(r)}{T(r)}. \quad (6.8)$$

Due to the large water vapor variation and the lacking of observational constraint in models, the water vapor uncertainty generally far exceeds the pressure and temperature uncertainties. Therefore given the precise measurement of refractivity from GNSS RO as well as the independent knowledge of temperature (e.g., from in-situ observations, global model analysis and reanalysis or climatology), the water vapor pressure can be derived iteratively from Eqs. (6.4, 6.5, 6.6 and 6.7). While the approach is relatively simple, the RO water vapor retrieval (given the a-priori temperature) or temperature retrieval (given the a-priori humidity) will contain measurement error in RO refractivity and uncertainties in the a-priori information.

6.1.4 1D-Var (*Variational Method*)

Another approach to obtain optimal estimation of the water vapor, temperature and pressure is through the variational methods. These methods combine the occultation measurements (e.g., refractivity) with the a-priori (or background) atmospheric information in a statistically optimal way (e.g., Zou et al. 1995; Healy and Eyre 2000; Kursinski et al. 2000a). For example, the optimal solution to the state vectors \mathbf{x} (e.g., T , P_w and P) can be found by adjusting the state vector elements in a way that is consistent with the estimated background errors, to produce simulated measurement values that fit the observations to within their expected observational errors (Healy and Eyre 2000). When assuming Gaussian error distribution, the optimal solution of the state vectors can be achieved by minimizing a cost function $J(\mathbf{x})$ given by,

$$J(\mathbf{x}) = \frac{1}{2} (\mathbf{x} - \mathbf{x}^b)^T \mathbf{B}^{-1} (\mathbf{x} - \mathbf{x}^b) + \frac{1}{2} (\mathbf{y}^o - \mathbf{y}(\mathbf{x}))^T (\mathbf{O} + \mathbf{F})^{-1} (\mathbf{y}^o - \mathbf{y}(\mathbf{x})) \quad (6.9)$$

where \mathbf{x} is the state vectors (e.g., T , P_w and P), \mathbf{y} is the measurement vector (e.g., RO refractivity N), $\mathbf{y}(\mathbf{x})$ is the forward model to map the state vectors into the measurement space (e.g., Eq. (6.1) for refractivity), the superscript b and o denote the background (or a-priori) and measurement information, \mathbf{O} and \mathbf{F} represents the error covariance of the measurement and the forward model, respectively. The superscripts T and -1 denote matrix transpose and inverse. Similarly bending angle α can be the measurement vectors instead of refractivity, however, the forward model becomes much more complicated and computation cost also becomes much higher. Nevertheless, the measurement errors covariance of bending is relatively simpler as compared with refractivity, as the RO refractivity generally includes vertically correlated errors as a result of the Abel integration.

The variational method demonstrates that the retrieval results are less sensitive to the errors in the a-priori information than the simpler direct retrieval method (e.g., Eqs. 6.6, 6.7 and 6.8). However, the errors of the geophysical parameters derived from the variational method could become more challenging to interpret as the errors will consist of the model background errors (generally less understood) with the RO measurement errors.

6.2 Characteristics of GNSS RO Observations

The limb sounding geometry of the GNSS RO technique leads to high vertical resolution measurements but with relatively coarse horizontal resolution and is a highly complementary to the conventional nadir-viewing infrared and microwave satellite sounders. The RO L-band microwave signals are not sensitive to aerosol, cloud and precipitation. Such all-weather sounding capability makes the high

Table 6.1 Summary of the key characteristics for GNSS RO soundings

GNSS RO Characteristics	Note
Limb sounding geometry	Complementary to spaceborne nadir-viewing and ground-based instruments
Full global coverage	From tropics to poles, including regions near the north/south poles
Profile ionosphere, stratosphere and troposphere	Cover full vertical range of neutral atmosphere and the ionosphere up to the RO receiver satellite altitude
All-weather sounding	Minimally affected by aerosols, clouds and precipitation
High accuracy	~ 1 K of single temperature profile and ~ 0.1 K of average accuracy in the upper troposphere and lower stratosphere
High precision	0.02–0.05 K from upper troposphere to lower stratosphere
High vertical resolution	~ 0.1 km near surface to ~ 1 km near tropopause
Relative low horizontal resolution	~ 100 –300 km dependent on atmospheric vertical structures
Independent height and pressure measurements	Refractivity, density and pressure are measured at absolute positions/heights
No first-guess needed in bending angle retrieval	Independent of external constraints in the basic RO parameter retrieval
Self calibration	No external calibration required
No instrument drift	Independent of satellite mission
No satellite-to-satellite bias	Independent of satellite platform
Independent of processing center	Relatively retrieval algorithm independent
Compact sensor, low power and low cost	Can be carried as a secondary payload on many satellite platforms

vertical resolution RO soundings very valuable for sensing many important weather phenomena with the presence of clouds and precipitation, such as hurricane, severe thunderstorm etc.

Also noted that the fundamental quantity in the RO measurement is light travel time, therefore, it is insensitive to calibration difficulties and instrument drift problem common to conventional radiometric measurements. This quality also makes the RO measurement insensitive to instrument generation that is highly desirable for long term climate monitoring.

For a typical GNSS RO sounding, it generally takes 1–2 min to scan the atmosphere from ~ 100 km down to the surface. The bending angle is ~ 1 – 2° near the surface, corresponding to the refractivity ~ 300 –400 N-unit, falling exponentially with height. The scale-height of the decay is approximately the density scale-height. Tangent point drifts in the horizontal by ~ 150 km during a typical RO sounding measurement.

The key features of the RO soundings are summarized in Table 6.1. The spaceborne GNSS RO sounding consists of a unique combination of characteristics, such as, global coverage, self-calibrated, high accuracy, high vertical resolution and all-weather sounding capability (e.g., Kursinski et al. 1997; Anthes et al. 2008; Anthes 2011).

6.2.1 Spatial Resolution (Vertical and Horizontal Resolution)

The vertical resolution of RO sounding retrieved through the geometric optic method is constrained by the diffraction limit (i.e., the diameter of the first Fresnel zone) as well as the vertical refractivity gradient (Kursinski et al. 1997). The first Fresnel zone is defined as the region within which the path lengths differences are within a half wavelength of the path of minimum phase delay. The diameter of first Fresnel zone decreases as refractivity increases, such that the vertical resolution improves from ~ 1.4 km in the upper troposphere and stratosphere to ~ 0.2 km near the moist boundary layer top where large refractive gradient is generally found (Kursinski et al. 2000a). For a GNSS RO limb sounding geometry, the bending angle retrieval at a tangent point is not a local point measurement but an integration of bending along the ray path. The bending generally increases exponentially at lower altitude due to the denser atmosphere. Therefore, most of the bending occurs near the tangent point (e.g., over $\sim 50\%$ (Kursinski et al. 1997)), where the ray path is closest to the Earth's surface. For simplicity, the horizontal resolution (Δl) can be defined by the distance traversed by a ray path as it enters and exits a spherically symmetric atmospheric layer with thickness represented by the vertical resolution (Δz) (Kursinski et al. 2000a). The relation between the horizontal and vertical resolution can be expressed as

$$\Delta l \sim 2\sqrt{2R\Delta z}, \quad (6.10)$$

where R is the radius of the atmosphere at the tangent height. Given the improving vertical resolution from ~ 1.4 km in the upper troposphere and stratosphere to ~ 0.2 km near the boundary layer, the horizontal resolution also improves from ~ 270 to ~ 100 km.

The more sophisticated radio-holographic retrieval methods (e.g., Canonical-Transform or Full-Spectrum-Inversion) eliminate the Fresnel diffraction limit of vertical resolution imposed by the geometric optics assumption. Gorbunov et al. (2004) demonstrates the theoretical estimation of vertical resolution to be ~ 60 m in their simulation studies. Such high vertical resolution measurement is not achievable by the passive nadir-viewing satellite sounders. In such case, much finer horizontal resolution (~ 60 km) can be achieved.

6.2.2 Accuracy and Precision Analysis

The theoretical estimation of RO measurement accuracy was first discussed in Yunck et al. (1988) and later updated by Kursinski (1994). A much more comprehensive analysis of the RO theoretical accuracy was carried out through analytical and simulation studies in Kursinski et al. (1997). Based on these studies, under certain mean conditions, the refractivity retrieval error is generally large in the lower

troposphere with a maximum of $\sim 1\%$ near the surface; the error decrease sharply upward and reach the minimum of $\sim 0.2\%$ at around 20 km; and then increases again to $\sim 1\%$ at 40 km (Kursinski et al. 1997).

As described in Chap. 5, the derivation of atmospheric properties from GNSS RO observations involves in RO raw amplitude and phase measurements (e.g., Eq. 5.17 in Chap. 5) along with multiple retrieval steps that are affected by various error sources. Individual error sources can be grouped into three major categories: measurement errors, calibration errors and retrieval errors. Here we briefly discuss the effects of these errors.

6.2.3 *Measurement Errors*

During an occultation event, the principal observables are the RO signal phase and amplitude, which could be affected by the measurement errors including the thermal noise, the clock instability, local multipath and receiver tracking errors.

6.2.3.1 Thermal Noise

The thermal noise is generally random and un-correlated for any two occultations and is caused by the finite GNSS signal strength and the receiver amplifier noise. The thermal noise can produce random phase errors. Because thermal errors vary rapidly with height, they could contribute significantly to refractivity and temperature error at high altitudes but produce little pressure error (Kursinski et al. 1997).

6.2.3.2 Clock Instability

The signal phase is also affected by the phase stability of the clocks of the GPS occultation and reference satellites as well as the LEO and possibly ground reference receivers. The clock errors can largely be removed through differencing technique in the retrieval process. However the residual clock errors could still be important at high altitudes but should not dominate retrieval error in general (Kursinski et al. 1997).

6.2.3.3 Local Multipath

The widely used broad-beam GPS receiver antennas significantly simplify GPS instrumentation but are sensitive to the local multipath caused by the multiple signals arriving at the antenna after scattering off structures near the antenna. The local multipath could create slowly varying phase errors, which could potentially

introduce significant errors in the upper stratosphere (Kursinski et al. 1997). The more directional antennas may reduce such error but at a cost of instrumental complexity, cost, and size. Another way of minimizing the local multipath errors is through better modeling of the multipath signals near the receiver antenna.

6.2.3.4 Receiver Tracking (Open Loop vs. Close Loop)

In the early RO missions, such as GPS/MET, CHAMP, SAC-C (before 2006) and GRACE, the RO receiver applied the so-called close-loop (CL) tracking technique. Such receivers use phase-locked-loop (PLL) to model (or predict) the phase of the RO signal by extrapolation from the previously measured phase (Stephens and Thomas 1995). The CL tracking is an optimal and reliable tracking technique for RO signals when there is sufficient signal-to-noise ratio (SNR) and the signal dynamics are not too high (e.g., single-tone signals).

In the moist lower troposphere, however, the complicated signal dynamics due to the rapid fluctuations in phase and amplitude (caused by multipath propagation), as well as the decreasing SNR due to the atmospheric attenuation effect (caused by the increasing pressure and humidity) could lead to unreliable CL tracking of the RO signals (Sokolovskiy 2001). The significant tracking errors result in systematic biases in the RO refractivity in the lower troposphere in the early RO missions (e.g., Rocken et al. 1997; Ao et al. 2003; Beyerle et al. 2003; Hajj et al. 2004). Besides, the loss tracking of RO signals results in the insufficient penetration of the high quality retrieved profiles deep into the lower troposphere. In addition, the CL tracking cannot be applied to record the rising occultation in the troposphere, as the RO signal starts with very low SNR as it emerges from the shadow of the Earth in a rising occultation event.

To overcome the limitation of the CL tracking technique, a model-based open-loop (OL) tracking technique was developed for use in the moist troposphere to track complicated RO signals under low SNR for both setting and rising occultations (Sokolovskiy 2001). The OL tracking allows deep penetration of the retrieved profiles below the top of the moist atmospheric boundary layer where sharp refractivity gradient and severe multipath frequently occurs. It is worthy noting that OL tracking has long been successfully applied in planetary RO experiments (e.g., Tyler 1987; Steffes et al. 1994). However, a key difference with GPS RO is that the GPS signals are modulated whereas the planetary RO measurements were almost always carried out with signal modulation turned off (Ao et al. 2009). The need for demodulation in the receiver makes the OL tracking for GPS RO more complicated (Sokolovskiy et al. 2006a; Ao et al. 2009).

In OL tracking, the receiver signal reference model does not use feedback (i.e., the signal recorded at an earlier time), but it is instead based on a reasonably accurate atmospheric (e.g., Doppler shift or bending angle) model in addition to a geometric model (e. g., real-time navigation solution of satellite orbits). Such

an approach can be implemented within the existing flight receiver hardware that applied CL tracking through software modification (Sokolovskiy 2001). The OL tracking was successfully implemented for the first time by JPL in the SAC-C RO receiver in 2005, and significantly led to a much higher percentage of RO soundings to penetrate deep into the lower troposphere (Sokolovskiy et al. 2006b). OL tracking is later being routinely applied on the RO receivers aboard COSMIC (Sokolovskiy et al. 2009; Ao et al. 2009) and most of the follow-on RO missions as shown in Table 5.2 in Chap. 5. Besides eliminating the large tracking errors and improving the ability to probe deeper into the lower troposphere, OL tracking enables the acquisition of rising occultations, thereby doubling the number of occultations from the same instrument.

6.2.4 Calibration Errors

After the POD processing, the satellite orbits and velocities can be precisely determined. The precision of RO GNSS transmitter and LEO receiver satellite orbits can be within meter and several centimeter levels, respectively (Bertiger et al. 1994). Such position errors primarily affect the altitudes of the retrieved bending angle and refractivity profiles. The altitude error is in the order of ~ 10 cm for typical occultation geometry and is generally negligible (Kursinski et al. 1997).

The satellite velocity errors, especially the component along the ray path directly affects the atmospheric Doppler measurement and so the atmospheric property retrievals. Given the LEO receiver velocity errors of ~ 0.05 (mm s^{-1}) (Bertiger and Wu 1996), the corresponding root-mean-square (RMS) errors in geopotential height and temperature is ~ 10 m and 0.3 K near 50 km altitude. The errors decrease rapidly at lower altitudes and should not have significant impact at lower altitudes.

In general, the differencing procedure is necessary to removes the clock errors (especially for LEO receiver clock) that could affect the signal phase measurements. The differencing technique allows the unclassified receiver to achieve high accuracy clock solutions even with SA modulation on, which allows the usage of much smaller size, power and less expensive LEO receiver. The downside is the additional thermal and local multipath noise on each differencing link, which, however, can be significantly reduced with higher SNR measurements.

When applying zero differencing (e.g., no differencing), clock errors could leak into the phase measurements and so the retrievals. Beyerle et al. (2005) demonstrate the zero-difference processing can produce highly accurate excess phase data with GRACE-B (equipped with an ultra-stable-oscillator) occultation measurements. On the other hand, when the ground reference station is used in double differencing, the troposphere related errors could add to the clock errors and result in retrieval errors. Such tropospheric noise induced errors is generally small compared with other sources of noise (Treuheft and Lanyi 1987).

6.2.5 Retrieval Errors

To derive the neutral atmospheric bending angle profile, the ionospheric induced bending can be removed via the simple linear combination approach (Sect. 5.4.4.1), by assuming spherically symmetric atmosphere and that the two frequency (e.g., L1 and L2) signals travel in straight line and are along the same path (Vorobev and Krasilnikova 1994).

This ionospheric calibration process effectively removes the first order ionospheric term ($1/f^2$). Higher order term contributions constitute the major source of error during day-time solar maximum at high altitudes (e.g., Kursinski et al. 1997) and require further calibration (e.g., Bassiri and Hajj 1993). In addition, the spherically symmetric atmosphere assumption could become less accurate due to the long signal travel distance within the ionosphere. The presence of horizontal gradient of electron density, small-scale variation (e.g., over E -region) and the ionospheric scintillations (e.g., over low latitudes due to magnetic storms) could produce residual ionospheric residual errors that can't be removed by the simple linear combination calibration process.

The ionospheric residual errors decrease rapidly at lower altitude in the neutral atmosphere, but could be the dominant error source in the upper stratosphere. Explicit consideration for the ionosphere yields more accurate neutral atmospheric bending angles, especially for high altitudes where the ionospheric bending is significant (e.g., Wee et al. 2010). The magnitude and long-term drift of such errors are not well understood and could be very important for climate monitoring and warrant additional study.

6.2.5.1 Upper Boundary Condition

Derivation of refractivity requires the Abelian integration of the bending angle extended to the top of the atmosphere (e.g., Eq. 5.15). Similarly, the temperature retrieval requires the hydrostatic integration of refractivity up to the top of the atmosphere (e.g., Eq. 6.4) and practically uses a-priori temperature at a high altitude (e.g., upper stratosphere).

Therefore, the errors in the high-altitude bending angle or density used in the Abelian integrals, or the a-priori temperature error will result in errors in the refractivity, pressure and temperature retrievals. Such upper boundary condition induced errors decrease rapidly at lower altitudes, but will limit the accuracy of the refractivity and temperature retrievals near the altitudes where upper boundary condition is applied.

6.2.5.2 Spherically Symmetric Atmosphere Assumption

The bending angle derivation from excess Doppler (e.g., geometric optics method) or excess phase and amplitude (e.g., radio-holographic method), assumes local

spherically symmetric atmosphere near the tangent point. Same assumption is embedded in the derivation of the refractivity from bending angle through the Abel transform.

Departures from the spherical symmetry assumption come from the horizontal gradients of the refractive index and also the ellipsoidal shape of the earth. The latter kind of errors becomes significant below 40 km and can be removed through an oblateness correction (e.g., Kursinski et al. 1997; Syndergaard 1998). Such correction is performed by referring the occultation geometry to a local center of refraction, defined by the origin of a sphere tangential to the ellipsoid at the profile location (Syndergaard 1998).

In the lower troposphere, the water vapor can vary appreciably on horizontal scales of a few tens of kilometers, which may result in significant horizontal gradients in refractive index (e.g., Healy et al. 2001). The horizontal gradients in the atmosphere could lead to systematic representative errors (i.e., difference from the in-situ local measurements at the tangent points) in bending and refractivity retrievals (Melbourne et al. 1994; Kursinski et al. 1997; Ahmad and Tyler 1999; Healy 2001; Zou et al. 2002; Poli 2004; Poli and Joiner 2004; Syndergaard et al. 2005).

Kursinski et al. (1997) shows that the along-track refractive index gradients (i.e., parallel with the ray path) causes refractivity errors of order of $\sim 1\%$ near the surface, falling linearly with height to $\sim 0.2\%$ at 10 km and then remaining relatively constant up to 30 km. Healy (2001) further demonstrated that the cross-track refractive index gradient (i.e., perpendicular to the ray path, which cause out of plane bending) can cause larger systematic errors in both the bending angle and the impact parameter, but the latter is more significant. For example, the impact parameter error can be off by as large as ~ 100 m near the surface corresponding to $\sim 10\%$ errors in bending angle in certain cases. Statistic analysis based on the simulations with various realistic atmospheric field represented by high-resolution mesoscale model reveals RMS errors of $\sim 3\%$ in bending angle or $\sim 1.4\%$ in refractivity near the surface caused by the cross-track horizontal gradients.

In the real occultations, the often non-coplanar orbits for occultation transmitter and receiver result in tangent points drifting horizontally as the ray path descends deep into the atmosphere. Such horizontal drift leads to refractivity retrieval error due to Abel transform, because the bending angle at higher altitudes is not the bending directly above the present tangent point. However, The ray path tangent point drift is generally of the order of the horizontal averaging interval or less (e.g. ~ 200 km below 10 km), and the resulting errors are therefore relatively small. The ratio of horizontal drift to vertical descent is greatest near the surface where the largest error is expected (Kursinski et al. 1997). The effects due to tangent point drift can be accounted for by considering a slanted profile that follows the tangent point trajectory (e.g., Poli and Joiner 2004).

It is worth noting that the magnitude of errors introduced by large-scale horizontal inhomogeneity in refractivity can vary depending on horizontal gradients, but, statistically, they should not introduce a significant bias. To fully exploit the benefit of the RO measurements, it is necessary to take into account the spherical

symmetry constraint especially in the lower troposphere where horizontal gradient could be significant. Several studies have developed computational efficient ways of assimilating the RO observations (e.g., refractivity, bending or excess phase) into numerical weather models by using the 2D linearized forward operator (i.e., to convert the model field into the RO observables) (Ahmad and Tyler 1999; Syndergaard et al. 2005; Poli and Joiner 2004; Sokolovskiy et al. 2005).

6.2.5.3 Atmospheric Multipath

In the earlier RO missions (e.g., GPS/MET and CHAMP), relatively few soundings penetrated into the lower half of the troposphere, in addition, significant refractivity errors including negative biases was present in the lower moist troposphere (Rocken et al. 1997). The receiver tracking errors (close-loop) is one of the dominant error sources (Ao et al. 2003; Beyerle et al. 2003). In addition, the presence of frequent atmospheric multipath in the lower troposphere is another major source of retrieval errors when applying the geometric optics retrieval method.

As discussed earlier, the geometric optics retrieval method is highly accurate when the RO signals are monochromatic (single-tone). High accuracy in refractivity and temperature retrieval near the tropopause and above has been demonstrated (e.g., Kursinski et al. 1997). In the lower troposphere, however, radio signals become non-monochromatic (multiple-tone) and may have very complex structure due to multipath effects mainly caused by water vapor variation. The GO retrieval method could introduce significant errors and the radio-holographic retrieval method is necessary to entangle the multipath problem. To a large extent, the multipath problem has been resolved by the advanced radio-holographic inversion methods (e.g. Gorbunov 2002; Jensen et al. 2003) and the implementation of the open-loop tracking technique (e.g. Sokolovskiy 2001).

6.2.5.4 Ducting (or Super-Refraction)

The atmospheric boundary layer (ABL, i.e., the lowest 1–2 km of the troposphere that is directly affected by the Earth’s surface) is generally capped by a stable inversion layer with negative moisture gradient. Since the refractivity is a function of pressure, temperature and water vapor pressure according to Eq. (6.1), the vertical refractivity gradient can be expressed as

$$\frac{dN}{dz} = \frac{c_1}{T} \frac{dP}{dz} - \left(\frac{c_1 P}{T^2} + 2c_2 \frac{P_w}{T^2} \right) \frac{dT}{dz} + \frac{c_2}{T^2} \frac{dP_w}{dz}. \quad (6.11)$$

The three terms on the right-hand-side (RHS) represent the contributions from vertical pressure, temperature and water vapor gradients. For typical atmospheric conditions, the first term due to the pressure gradient is approximately -30 N-units/km near the surface and decrease in magnitude roughly exponentially with

increasing height. The generally decreasing temperature and moisture at higher altitudes in the troposphere result in cancelation of their contribution to the refractivity gradient.

However, near the top of the atmospheric boundary layer, the temperature inversion (e.g., $dT/dz > 0$) and the often collocated negative moisture gradient (e.g., $dPw/dz < 0$) will contribute constructively to negative refractivity gradient. In the moist lower troposphere especially near to ABL top, the moisture gradient can dominate the refractivity gradient. Note that a small change of 1 g/kg in specific humidity (or 1.5 hPa in Pw) is approximately equivalent to a change in temperature of 10 K across a thin layer in contributing to the vertical refractivity gradient.

When the vertical refractivity gradient becomes so large and exceeds a threshold value that the radius of the curvature of the ray is smaller than the radius of the curvature of the atmosphere r , i.e.,

$$-\frac{dN}{dz} > 10^6 \cdot \left(\frac{1}{r}\right), \quad (6.12)$$

the so-called ducting (also referred as super-refraction, SR, by some authors) condition occurs. For a typical mean value of r (e.g., 6,371 km), the refractivity gradient threshold ($-dN/dz = 10^6/r \approx 157$ (N-unit/km)) is called critical refraction.

A large number of high-resolution Island and ship-borne radiosonde soundings have shown that ducting occurs about 90 % of the time in a year over the subtropical and tropical eastern oceans and even ~ 50 % at some high-latitude islands during the summer time (Xie 2006; Ao 2007). The ducting results in negative errors in the Abel-retrieved refractivity below the SR layer (Kursinski et al. 1997, 2000a). In the presence of ducting, the reconstruction of refractivity from RO data becomes an ill-posed non-unique inversion problem (Sokolovskiy 2003; Ao et al. 2003), i.e., a given RO bending angle profile is consistent with a continuum (an infinite number) of refractivity profiles (Xie et al. 2006; Ao 2007). The standard Abel retrieval gives the minimum refractivity solution of the continuum and thus produces the largest negative bias, consistent with a negative bias that is often present in the retrieved refractivity profiles inside the boundary layer. Simulation studies indicate a large variation in the magnitude of the negative refractivity biases (could exceed -15 %) dependent on the ducting height, thickness and strength (Xie et al. 2006; Ao 2007).

Note that the implementation of open-loop receiver tracking and the radioholographic retrieval method significantly reduced the systematic negative bias in the RO refractivity soundings in the lower troposphere (Ao et al. 2003; Beyerle et al. 2003; Hajj et al. 2004). However, systematic negative refractivity biases (~ -1 to -5 %) in RO sounding remain pronounced over the subtropical eastern oceans (Xie et al. 2010a). Over this region, the persistent sharp temperature and moisture gradient at the top of the stratocumulus or trade-cumulus covered ABL result in frequent ducting conditions (e.g., von Engeln and Teixeira 2004; Lopez 2009). It is therefore reasonable to believe that the residual negative N -bias is likely caused by the presence of duct.

Xie et al. (2006) proposed a retrieval method that is capable of removing the ducting induced N -bias after introducing an external constraint inside the ABL (e.g., surface refractivity etc.) and assuming a simple linear ducting layer structure. The approach is successful applied in a COSMIC RO sounding near Hawaii (Xie et al. 2010a). However, several challenges (such as identification of the ducting from RO sounding, acquiring the independent constraint etc.) need to be addressed before the approach can be widely applied to the occultation measurements. Another potentially approach is to employ a nonlinear optimization method based on the assimilation of bending angles (Palmer et al. 2000; Zou et al. 2000). This method could work because unlike refractivity, the bending angles derived from RO measurements are in principle not biased in the presence of ducting. For now, however, it is important to take the negative bias from ducting into account when lower troposphere refractivity (or a derived product such as water vapor) is used (Ao 2007), especially over subtropical eastern oceans (Xie et al. 2010a).

6.2.5.5 Refractivity Constant Uncertainty

Note that the coefficients used in the refractivity equation have been determined empirically. The refractivity equation (6.1) has been simplified from a more general expression that contains three terms representing dry gas polarizability, water vapor polarizability and the permanent dipole moment of water vapor, as well as the effects of compressibility (e.g., Thayer 1974):

$$N = 77.6 \frac{P_d}{T} Z_d^{-1} + 64.8 \frac{P_w}{T} Z_w^{-1} + 3.776 \times 10^5 \frac{P_w}{T^2} Z_w^{-1}, \quad (6.13)$$

where P_d and P_w (in hPa) are the partial pressure of the dry gas and water vapor, T (in Kelvin) is temperature, and Z_d , Z_w are the compressibility of the dry air and water vapor representing the non-ideal properties of the gas (Owens 1967).

There is a wide list of published values and uncertainties associated with these empirically derived coefficients for frequencies in the microwave range of the spectrum (e.g., review by Rüeger 2002 and references therein). The accuracy of these coefficients will affect the pressure, temperature and water vapor retrieval based on the RO refractivity. The uncertainty associated to these coefficients is not negligible when the refractivity equation is used as a forward model in the RO data assimilation (e.g., Kursinski et al. 1997; Aparicio et al. 2009; Cucurull 2010; Aparicio and Laroche 2011; Healy 2011). A more robust determination of these values within the GPS community is needed.

6.2.5.6 Water Vapor Ambiguity

In the lower troposphere, water vapor could contribute a significant fraction of atmospheric refractivity. Given the RO refractivity measurements, the water vapor

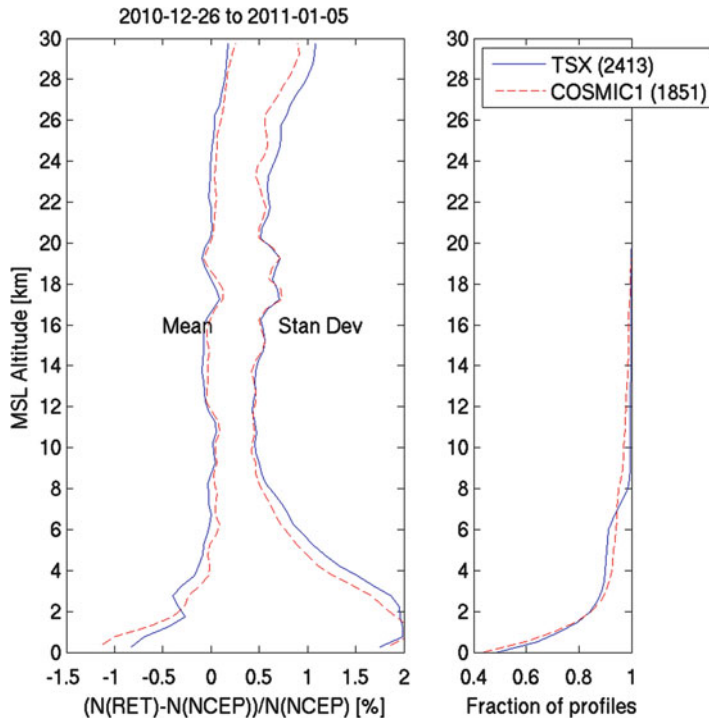


Fig. 6.1 Refractivity difference between RO occultation soundings (COSMIC-LEO#01, in *red* and TerraSAR-X, TSX, in *blue*) and the near-coincident NCEP analyses (interpolated into the time and place of the RO soundings) from December 26, 2010 to January 5, 2011. The mean differences and the standard deviation (*left*) as well as the number of RO soundings reaching various levels in the atmosphere are shown (Courtesy of C. O. Ao at NASA Jet Propulsion Laboratory)

(or temperature) cannot be independently derived and require the a-priori information of temperature (or water vapor) as well as hydrostatic balance assumption. With the variational methods, e.g., the one dimensional variational (1DVar) to 4DVar analysis method, temperature, and water vapor profiles can be derived simultaneous (e.g., Kuo et al. 2000; Kursinski et al. 2000b; Palmer et al. 2000; Poli et al. 2002). The errors in the a-priori information will propagate into the derived temperature or water vapor retrieval.

6.2.6 Experimental Validation of RO Accuracy and Precision

The accuracy of the RO measurements can be determined through comparisons with independent data (e.g., high-quality radiosondes and model analyses). For example, Fig. 6.1 shows the mean and standard deviation of the 1 month of COSMC (only LEO#01 satellite) and TerraSAR-X RO refractivity as compared with the

coincident NCEP analysis. However, a numerical estimate of the accuracy could be challenging, since it is affected by the measurement and representativeness errors of both data sets, also, the RO accuracy may well be greater than many other temperature observing system (Anthes 2011). Kuo et al. (2004) showed error estimation comparable to, but slightly larger than the theoretical estimates obtained by Kursinski et al. (1997). Ho et al. (2010a) compared numerous COSMIC RO dry temperatures with collocated radiosondes (Vaisala-RS92, one of the most accurate sondes), and found a mean bias difference of -0.01 K and a mean absolute bias difference of 0.13 K, suggesting that the accuracy of RO dry temperatures is better than 0.13 K between 10 and 200 hPa. Similar results were also found by Gobiet et al. (2007) and He et al. (2009).

With the increasing number of RO satellites on the orbits, the precision estimation of RO measurements becomes possible by comparing close-by RO soundings from different RO satellites. The first experimental estimation of the precision was obtained by Hajj et al. (2004) by comparing close-by occultations (within 30 min and 200 km) from CHAMP and SAC-C satellites. The results indicate that individual profiles agree to 0.86 K (~ 0.4 % fractionally), standard deviation between 5 and 15 km altitude. In the early months after the launch of the COMIC constellation, the six satellites were orbiting very close to each other at the initial altitude of 512 km. The close-by RO soundings (within tens of kilometers or less) from different COSMIC satellites provide a unique opportunity to estimate the precision of RO measurements. Schreiner et al. (2007) demonstrate that the RMS difference of refractivity between 10 and 20 km altitude is less than 0.2 %, increasing to about 0.7 % at 30 km altitude. In the lower troposphere, the maximal RMS is ~ 0.8 % at 2 km altitude and decreases abruptly to ~ 0.2 % between 6 and 8 km altitude. Similar study carried out by Ho et al. (2009a) also indicates that the precision of COSMIC RO observations is better than 0.05 K from surface up to ~ 40 km by quantitative comparison of numerous pairs of COSMIC RO soundings within 10 km of each other. Foelsche et al. (2011) also found that refractivity and temperature climate records from multiple RO satellites were consistent within 0.05 %.

6.3 Dynamic Processes Studies with GNSS RO

Since the GPS/MET mission in 1995, the GPS radio occultation data have been widely used for studying various atmospheric phenomena. The powerful remote sensing technique has become more and more appreciated by an expanding research community. The high vertical resolution RO soundings from troposphere to the stratosphere enable dynamic process studies of tropopause and various waves in the upper troposphere and stratosphere. The unique all-weather sounding capability of RO observation also makes it extremely valuable for investigating various weather phenomena, such as front and tropical cyclone, where large coverage of thick clouds and precipitation are present.

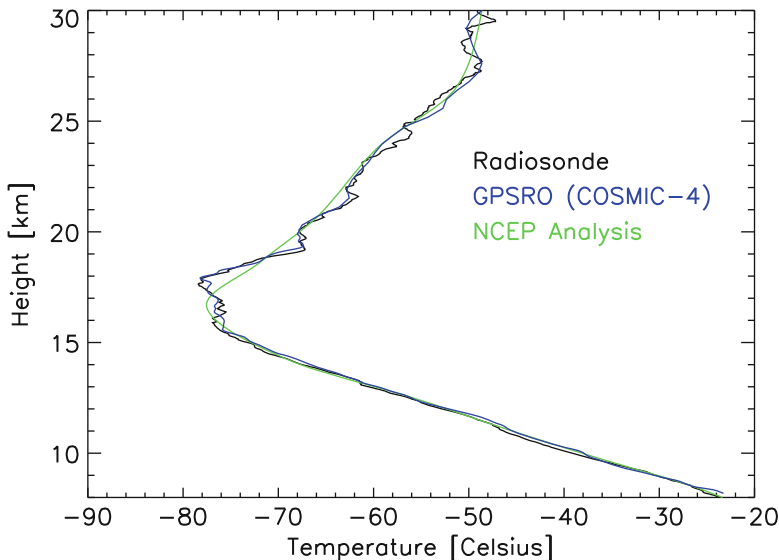


Fig. 6.2 Temperature comparison of radiosonde at Lihue, Hawaii (12UTC, black) with the near-coincident COSMIC (LEO#4 RO sounding (11:50UTC, blue) and NCEP analysis (12UTC, green) on December 10, 2006. Note the tangent point of the COSMIC RO sounding is about 147 km away from the radiosonde site

6.3.1 Tropopause and Stratospheric Waves

Starting with GPS/MET, the high accuracy and high vertical resolution temperature in the upper troposphere and lower stratosphere (UTLS) gained immediate attention from the broad research community. Figure 6.2 shows the COSMIC RO sounding is capable of resolving the fine vertical structure temperature variations near the cold-point tropopause (~ 18 km) as seen in the near-coincident radiosonde sounding. Note the NCEP analysis temperature profile is much smoothed and is likely due to its lower vertical resolution.

The gravity wave signatures in the RO temperature profiles were soon revealed by Tsuda et al. (2000) and Steiner and Kirchengast (2000). The global map of gravity waves climatology were successfully developed based on GPS/MET data (Tsuda et al. 2000). Various propagating waves in the stratosphere, including Kelvin waves, Rossby-gravity waves, as well as waves associated with Quasi-Biennial-Oscillation were identified (Randel et al. 2003; Randel and Wu 2005). Schmidt et al. (2005) further derive a 9-year record of QBO based on the long-term CHAMP and SAC-C RO soundings.

The global soundings of highly accurate and high vertical resolution RO temperature observations are ideal for tropopause and related UTLS research (e.g., Randel et al. 2003; Borsche et al. 2007; Schmidt et al. 2006, 2008, 2010; Steiner et al. 2009). Randel et al. (2003) firstly demonstrate that the GPS/MET data is

capable of resolving the sharp temperature structure at the tropopause as seen in the high-resolution radiosondes and the thermal variability of the tropical tropopause region.

6.3.2 Tropical Tidal Waves

Driven by the daily persistent solar heating, the diurnal cycle is one of the fundamental variations in the Earth's weather and climate system, which modulates dynamical, hydrological, radiative, and chemical processes throughout the atmosphere. Contrary to most of sun-synchronized orbits, several of RO satellite orbits process with time. For example, the CHAMP RO sounding allows a complete diurnal coverage within 130 days. Zeng et al. (2008) firstly derive the amplitude of the diurnal tide at altitudes of 10–30 km in the tropical regions based on CHAMP temperature profiles, which compares well but also shows distinct difference with two stratosphere models. The launch of six-satellite COSMIC constellation yields much denser global sampling (over 2,000 profiles per day) and allows full diurnal sampling within 1 month in the low latitudes. Also the implementation of open-loop tracking significantly improves the RO sounding quality in the lower troposphere.

The vertical structure of the diurnal phase and amplitude for both temperature (e.g., Pirscher et al. 2010; Xie et al. 2010b) and refractivity as seen in Fig. 6.3, were derived based on the COSMIC observations in the tropics (Xie et al. 2010b). The propagating tidal wave, which migrates with the sun, dominates the tropical diurnal variation in the stratosphere and higher altitudes (e.g. McLandress 1997). Its propagation nature is evident in the temperature and refractivity data, showing a downward progressing phase profile (Fig. 6.3, right panels) with growing amplitude above 14 km. The vertical wavelength of the diurnal tidal wave is about 25 km, which is observed in both the temperature and refractivity phase profiles (Xie et al. 2010b). The migrating tidal wave observed by COSMIC is consistent with one obtained by Zeng et al. (2008) from the multiyear CHAMP data, and with those from the classical tidal theory and model results (e.g., Chapman and Lindzen 1970 and McLandress 1997). In the stratosphere the maximum refractivity amplitude reaches $\sim 1\%$, or $\sim 2.5\text{ K}$ in temperature (Xie et al. 2010b).

6.3.3 Weather Front

A weather front is a boundary separating two air masses of different densities, and is the principal cause of meteorological phenomena. Kuo et al. (1998) show that GPS/MET RO profile is capable of distinguishing a frontal system, which is observed by a nearby radiosonde observation, but missed by the global model analyses. Another high-impact weather phenomenon known as “atmospheric river” represents a narrow corridor of concentrated moisture in the atmosphere, which

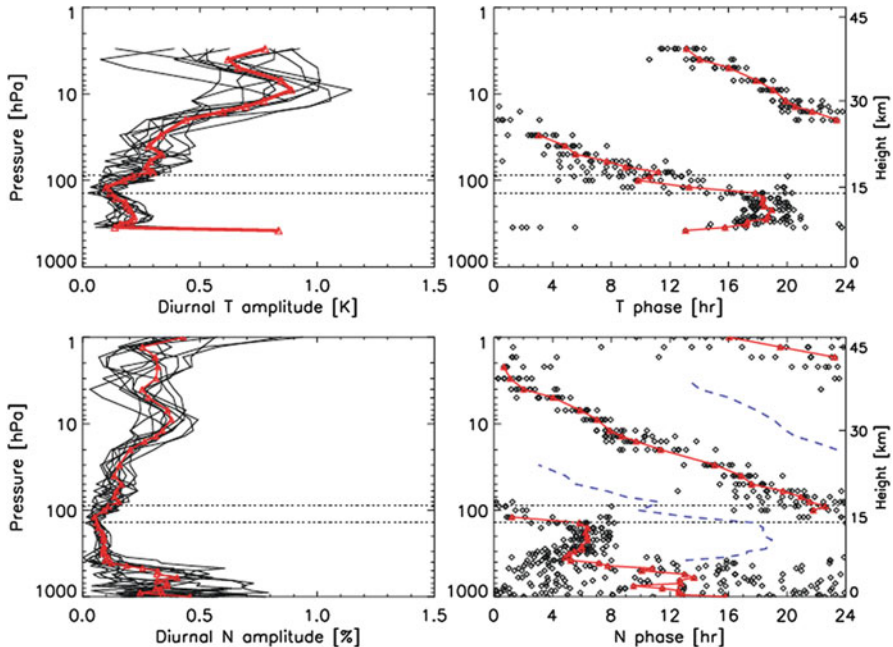


Fig. 6.3 Vertical structure of the temperature (*upper panels*) and refractivity (*lower panels*) amplitude (*left panels*) and phase (*right panels*) of diurnal variations over 10°S – 10°N based on COSMIC RO observations in 2007. Each thin line (*left panels*) represents one monthly mean amplitude profile whereas phases from the monthly data are shown as *open diamond* (*right panels*). The *RED thick lines* show the annual median values. The *blue dashed lines* in (*lower-right panel*) represent the temperature phase as shown in (*upper-right panel*) (Note the COSMIC RO data are provided by NASA Jet Propulsion Laboratory.)

could significantly enhance water vapor transport. It occurs when winds draw moisture together into a narrow region ahead of a cold front, in a region of very strong winds. They can be thought of as tropical connectors that feed tropical moisture into more northern latitudes. Neiman et al. (2008) demonstrates the strong horizontal gradient in temperature and water vapor that are resolved by the COSMIC soundings during an “atmospheric river” event.

6.3.4 Tropical Cyclones (TC)

The limited understanding of tropical cyclone (TC) genesis has largely restrained by the sparse high-quality atmospheric observations in the vicinity of the cyclones. The high-vertical resolution RO sounding is insensitive to the cloud and precipitation and could provide the highly desired observation. Several case studies show the close agreement between RO soundings with the close-by dropsondes near a

tropical cyclone (Anthes 2011). Such high-quality RO soundings could provide the thermodynamic temperature and water vapor structure that are essential for cyclone genesis studies. The current number RO LEO satellites only produce relatively sparse RO soundings in a regional scale (e.g., ~ 1 sounding per day per 4-degree grid, given $\sim 3,000$ soundings per day globally). However, occasionally, the RO soundings provide critical information near the cyclone and can make significant positive impact on forecast. For example, Huang et al. (2005) and Chen et al. (2009) showed that GPS RO had positive impacts on TC simulations by conducting data assimilation experiments using 3D-Var. Liu et al. (2012) use the Weather Research and Forecast (WRF) model to simulate the hurricane Ernesto in 2006. After assimilating COSMIC soundings, the lower troposphere is moistening and leads to hurricane genesis as seen in the observations. Studies also demonstrates that assimilating COSMIC observations in the NCEP operational model improved the temperature, water vapor, geopotential and wind fields (Cucurull and Derber 2008), which provides the key thermodynamic background for correctly simulating the cyclone genesis. With multiple RO missions planned for launch in the near future, it is reasonably to believe that such improvement in the dynamic field will significantly improve the tropical cyclone prediction when RO soundings density increases considerably near the cyclone.

6.3.5 Atmospheric Boundary Layer (ABL)

The shallow atmospheric boundary layer (1–2 km) and the frequent cloud and aerosol presence make it extremely difficult to observe from the space. GPS RO is currently the only satellite remote sensing technique that can profile the temperature and water vapor with high vertical resolution inside the ABL. A typical well-mixed boundary layer is capped by a temperature inversion and negative water vapor gradient and therefore is characterized by a negative refractivity gradient. The large refractivity gradient results in a sharp increase in bending angle observation, produces large defocusing (e.g., reduction of mean signal amplitude) and multipath propagation. The implementation of the open-loop receiver tracking along with the application of radio-holographic retrieval method allow the routinely RO profiling into the ABL with very high vertical resolution (~ 100 m). Such well-mixed ABL top height can be precisely determined from the RO bending angle or refractivity profiles (Sokolovskiy et al. 2006b, 2007). The spatial and temporal variations of ABL height climatology can also be derived based on the multiple-year RO observations (von Engeln and Teixeira 2004; Sokolovskiy et al. 2007; Ratnam and Basha 2010; Guo et al. 2011; Ao et al. 2012; Xie et al. 2012a). Diurnal variation of the ABL heights over subtropical eastern oceans (Sokolovskiy et al. 2010) and Sahara desert (Ao et al. 2012) has also been derived from multiple year COSMIC data. Xie et al. (2012a) demonstrates the highly accurate ABL height detection from COSMIC RO soundings over the subtropical eastern Pacific Oceans as comparing with close-by high-resolution radiosondes, whereas the high-resolution ECMWF

model analysis is biased low. It is worth noting that the RO refractivity gradient over these subtropical eastern oceans are biased low in comparison with the close-by radiosonde and ECMWF analysis. The bias is likely caused by the ducting (or super-refraction) as discussed earlier. Even though the systematic N -bias should not affect the precise detection of the ABL height, the vertical profile of refractivity and its derivable such as temperature and water vapor inside the ABL could be also biased and need to be used with special attention (Xie et al. 2012a).

6.4 Weather Prediction Applications

With a unique combination of global coverage, high vertical resolution, high precision and accuracy and insensitivity to clouds and precipitation, GNSS RO provides a great complement to the conventional nadir viewing infrared and microwave radiance observations. Since the launch of the proof-of-concept GPS/MET, recognition for the potential of GNSS RO for global atmosphere observation has grown significantly. The sequential launches of the six-satellite COSMIC constellation and the GRAS on MetOp in 2006 offers over 3,000 near real-time RO profiles per day, a much-needed dense sampling for global weather monitoring. GNSS RO measurement has become an important new component of the global observing system and significantly contributed to the improvement of global and regional weather forecasting.

6.4.1 GNSS RO Data Assimilation

Accurate initial conditions are one of the key factors that influence the predictability of high-impact weather and climate systems. Modern data assimilation techniques combine observations and model information to form dynamically and physically consistent initial conditions for numerical models and can therefore more effectively use the satellite observations. GNSS RO data products include the raw phase delay and amplitude, bending angle and refractivity as well as temperature, water vapor and geopotential height. Generally, the variational or ensemble based data assimilation techniques can be used to assimilate RO observations into the global or regional weather models. The phase delay measurements are very challenging to be assimilated into the NWP model due to the complex and computationally expensive forward model operator. On the other hand, the water vapor ambiguity in the lower troposphere makes the direct assimilation of RO temperature and water vapor retrieval not appealing as the RO measurement errors could be masked by the errors in the a priori information used in the retrieval process (e.g., Sect. 6.2.5.6). Generally, assimilation of the bending angle or refractivity is considered to be better and more feasible than the others (Kuo et al. 2000).

Assimilating the RO refractivity is relatively straightforward for its simple forward model (e.g., Eq. 6.1). On the other hand the forward model used for assimilating the bending becomes more complicated and computationally expensive. However, the bending angle assimilation could be preferable because the use of bending angle reduces the preprocessing of RO data before being assimilated and increase the vertical range of useful RO data. More specifically, it circumvents the complication of refractivity observation errors associated with the upper boundary condition in the refractivity retrieval, which requires a priori information (e.g., climatology) above a certain altitude (above ~ 30 km). In addition, the vertical correlation of the observation errors in the RO refractivity due to the Abel inversion also make the error covariance used for refractivity data assimilation more complicated (Healy and Thepaut 2006).

Most numerical weather prediction (NWP) operational centers assimilate either bending angle or refractivity profiles using one-dimensional (1D) observation operators, with the assumption of local spherically symmetric atmosphere. In the lower troposphere, however, specific humidity can vary appreciably on horizontal scales of a few tens of kilometers, which may result in significant horizontal gradients in refractivity (e.g., Healy 2001). It is likely that the errors of representativeness due to the violation of the spherical symmetry assumption could dominate over measurement errors in the moist lower troposphere as they appear to do in the upper troposphere and lower stratosphere (Kuo et al. 2004; Syndergaard et al. 2005). In this regard, the two-dimensional (2D) observation operators could be used to reduce the representative errors of the RO observation particularly in the presence of strong horizontal gradients. In addition the 2D operators should also reduce the forward model error. Two-dimensional (2D) observation operators make use of *a priori* knowledge of the horizontal gradients in the atmosphere provided by an NWP forecast when simulating the observation. Due to the high computational cost of simulating the bending angel through the conventional 2D geometric optics ray-tracing (Zou et al. 2000), some simplified 2D mapping operators, i.e., the “non-local” refractivity (Syndergaard et al. 2005) and phase operator (Sokolovskiy et al. 2005) have been proposed. Also, faster refractivity and bending angle operators have also been developed to incorporate both the tangent point drifting and horizontal gradient effects on the RO measurements (Poli 2004). Note that the increasing NWP model resolution will make the benefits of 2D operator more obvious due to the better-resolved horizontal structure of the atmosphere.

6.4.2 *Operational Assimilation of GNSS RO in NWP Models*

Since the launch of GPS/MET, several NWP studies using GPS RO observations have yielded promising positive impact on weather forecasting, which is especially evident in the upper troposphere and lower stratosphere (UTLS) regions (Healy and Thepaut 2006; Cucurull et al. 2006; Aparicio and Deblonde 2008). The RO data (e.g., GPS/MET) have also been used to identify the biases in NWP analysis

product (Anthes et al. 2000). Improvement of the southern hemisphere (SH) 500 hPa height field after assimilating CHAMP data was also shown (Zou et al., 2004). The RO soundings provide independent information, moreover, the self-calibrated measurements can be assimilated without bias correction. As most other satellite observations require bias correction to the model, RO measurements, therefore, could be used to anchor the bias correction of radiance measurements (e.g., Healy 2008).

GNSS RO has quickly evolved from an experimental concept to become a major component of the global observing system, providing data assimilated without bias correction by several NWP national agencies worldwide. Soon after the launch of COSMIC constellation, the European Centre for Medium-Range Weather Forecasts (ECMWF) and the US National Center for Environmental Prediction (NCEP) started assimilating real-time COSMIC soundings into their operational models and immediately demonstrated positive impact in the operational analysis and forecasts (Cucurull and Derber 2008; Healy 2008). Later on, the GRAS and TerraSAR-X and C/NOFS RO data have also been operational assimilated by many weather centers (e.g., Luntama et al. 2008; Cucurull et al. 2010; Poli et al. 2010). For example, ECMWF started assimilating GPSRO data operationally on December 12, 2006. Clear improvement in the ECMWF operational short-range forecast in both temperature and height field at 100 hPa after assimilating COSMIC data is indicated by the reduced bias when comparing the forecast to the radiosonde temperature at 100 hPa in the southern hemisphere (e.g., Fig. 6.4, adapted from Healy (2007)). Similar improvements have also been reported by many other operational weather centers, such as Environmental Canada, Meteo France, UK Met Office, Japan Meteorological Agency and the Australian forecast system (Poli et al. 2007; Rennie 2008; LeMarshall et al. 2010).

Other than being successfully assimilated into the global models, numerous regional NWP models (e.g., the Weather Research and Forecasting, WRF, model) also assimilate RO data to improve forecast. Generally, assimilation of refractivity has been undertaken using a local observation operator or a nonlocal observation operator (Huang et al. 2005; Chen et al. 2009). Positive impacts on the tropical cyclone simulations were demonstrated after assimilating RO data through variational (e.g., 3D-Var or 4D-Var) (Huang et al. 2005; Chen et al. 2009) or ensemble based (Liu et al. 2012) data assimilation systems.

6.5 Climate Applications

The fundamental RO observable is the phase delay of the GNSS radio signals (related to the propagation time between satellites). Since the time is calibrated very precisely by ultra stable atomic clocks, no additional satellite or inter-satellite calibration is needed for the RO observations. In contrary, passive thermal radiation measurements require periodic calibration to account for the drift of sensitivity of the sensors, and thus also inter-satellite calibration. Another important feature of

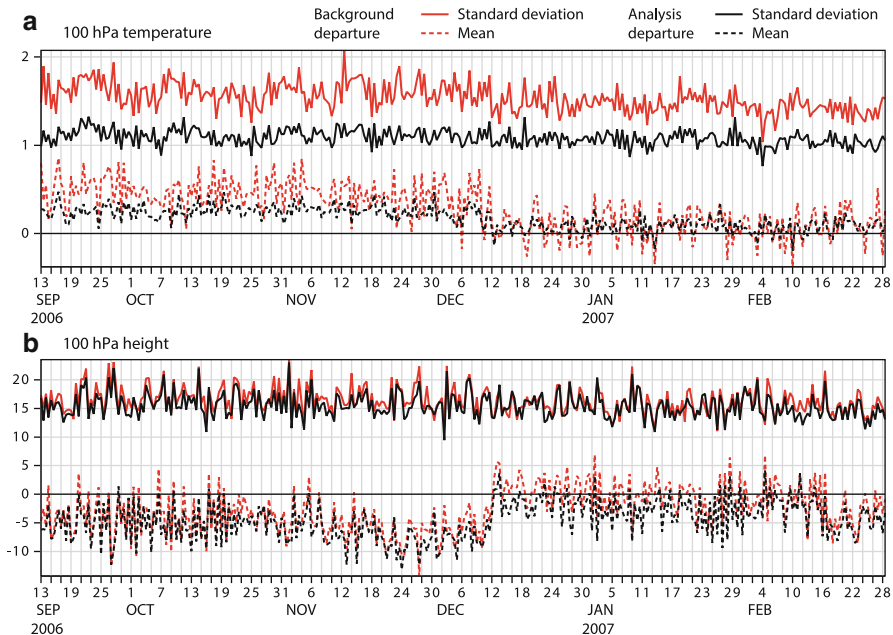


Fig. 6.4 Time series of the mean and standard deviation of the operational background departure and analysis departure for (a) temperature and (b) height from radiosonde measurements at 100 hPa in the southern hemisphere. Note the bias reduction after the assimilation of COSMIC RO data on December 12, 2006. (Plot is adapted from Healy (2007), courtesy of ECMWF)

RO observation is the all-weather character. Most clouds have a negligible effect on the measured signal. Even when the signal is attenuated by precipitation, the measurements are not significantly degraded, since the important measurements are the frequency but not the amplitude. For the same reason, the frequency (or time) measurements have intrinsically a long-term stability, with no significant calibration problems. In addition, the relative coarse horizontal resolution (~ 300 km) has been considered a limitation for resolving mesoscale features of the atmosphere (Anthes et al. 2000). However, such property has significant advantages for climate observations, as the RO observables do not have the representativeness errors associated with small-scale atmospheric variability that in-situ point measurements (e.g., radiosondes) have (Anthes 2011). These unique characters makes GNSS RO observations especially valuable for monitoring climate where both high accuracy (i.e. degree of veracity) and high precision (i.e. degree of reproducibility) measurements are desired, and monitoring climate trends which, generally, requires stable and high precision measurements that are consistent from satellite to satellite. The 2007 National Research Council (NRC) “Decadal Survey” report identified GNSS RO as a key element in the global climate observing system and GNSS RO is a critical data set to be assimilated into climate analyses.

The stringent climate monitoring requires a long-term measurement with 0.5 K accuracy and better than 0.10 (K decade $^{-1}$) stability (Ohring et al. 2005; Luntama et al. 2008). As discussed earlier, no any other atmospheric observing system but GNSS RO observations could meet these accuracy, stability and global sampling requirements (Anthes 2011). Studies using COSMIC temperature data have verified the theoretical high precision of RO soundings. The precision of individual profiles in the upper troposphere/lower stratosphere is equivalent to about 0.05 K or higher (Ho et al. 2009a). RO provides relatively uniform spatial/temporal coverage with an accuracy of approximately 0.1 K or higher (e.g., Gobiet et al. 2007; He et al. 2009; Ho et al. 2010a), a precision of 0.05 K or better, and a satellite-to-satellite bias less than 0.05 K (Ho et al. 2009a). The accuracy and stability of RO observations verifies that RO observations meet the high standards of climate benchmark observations.

Several other RO observables have also been identified to be optimal for climate trend detection, such as geopotential height (e.g., Leroy et al. 2006; Foelsche et al. 2008) and bending angle (Ringer and Healy 2008). The basic RO phase (or time delay) observations are mission or sensor independent (Ho et al. 2009a; Foelsche et al. 2011), implying that observations from previous and current RO missions can be compared directly to the future RO missions and the measurement time series can be easily pieced together to build up a long-term climate record. RO retrievals are also nearly independent of the data processing carried out at different data center (Ho et al. 2009b), which is another desirable property of climate benchmark observations.

Based on the intercomparison study of monthly-mean zonal-mean fields of 7-year COSMIC RO data from six international RO processing center, the structural uncertainty in trends over 7 year is <0.03 % for the bending angle, refractivity, and pressure, <3 m for geopotential height of pressure levels, and <0.06 K for temperature over the mid-latitude (50°S–50°N) UTLS region (Steiner et al. 2013). Such low structural uncertainty enables for detecting a climate change signal within about a decade. Even though RO observations have only been available since 1995, several studies have taken advantage of unique climate benchmark characteristics of RO soundings (i.e., high accuracy, mission independent and low structure uncertainty) and detected the climate trends from the relative short-term RO data (e.g., Steiner et al. 2009; Lackner et al. 2011).

In the previous section, we discussed that GNSS RO data can be assimilated into the NWP model without the need for bias correction. Such bias-free RO data can be used to anchor the radiance measurements that could potentially be biased. Similarly for climate application, the RO observations not only can be used to establish an independent climate record, they can also be used to assess the quality of the radiance measurements from other microwave and infrared sensors like the Microwave Sounder Unit (MSU) and Advanced MSU (AMSU) or Atmospheric Infrared Sounder (AIRS) (e.g., Ho et al. 2007; Steiner et al. 2007; Ladstädter et al. 2011). COSMIC data have also been used to calibrate radiance measurements from microwave sensors (AMSU) on different NOAA satellites (Ho et al. 2009a). Similarly, RO observations can be used to validate AIRS infrared satellite data from both

LEO and geostationary satellites (Ho et al. 2010b). The radiosonde soundings have long been deemed as the ground truth for the upper-air in-situ observations. However, the evolving instrumentation upgrade over the past decades as well as the various brands of radiosonde units used at different countries raise the concerns about how accurate the radiosondes are for long-term climate monitoring. The highly accurate and precise RO measurements provide a unique opportunity to assess the quality of radiosonde data. The diurnal bias due to radiative effects and the difference among various radiosonde brands have been revealed after being compared with the near coincident RO soundings (e.g., Kuo et al. 2005; He et al. 2009).

6.6 Future Application of Radio Occultation

6.6.1 Future GNSS and GNSS RO Missions

According to Table 5.2, the current RO sounding number ($\sim 3,000$ per day), produced mainly by COSMIC and GRAS and a couple of other LEO satellites, is still a relative small sample in regional scale. Most of the current available LEO RO satellites only track the GPS satellites. The current number of RO daily soundings (~ 1 daily profile per $4^\circ \times 4^\circ$ grid) significantly limits the impact of RO observations on the regional weather prediction such as tropical cyclone and severe weather and thunderstorm prediction, since the average spacing of about 400 km cannot adequately resolve the storm structures and their environment.

A COSMIC follow-on constellation is now being planned by the US and Taiwan and will produce five to ten times as many RO soundings as COSMIC. The new RO receiver (Tri-G) developed by NASA JPL will take advantage of the expanding GNSS transmitters and will be able to track different GNSS signals, including the GPS, GLONASS, Galileo and Compass/Beidou. Each of these GNSSs will consist of 24–30 transmitting satellites when fully operated. This will allow a significant increase in the number of possible RO soundings obtained by an individual LEO RO receiver. It is expected that COSMIC-II will provide over 10,000 daily soundings (i.e., ~ 1 profile per 2° grid) (Anthes 2011). Such dense global sampling will lead to a major, positive impact on regional severe weather and tropical cyclone prediction, climate monitoring as well as weather, climate and ionospheric research.

6.6.2 Airborne and Mountain-Top GNSS RO

While the GNSS radio occultation measurement from the space has the advantage of global coverage (e.g., one LEO receiver provides ~ 500 global distributed soundings per day), the sampling in a particular region is still relatively sparse without a large number of LEO receivers. Therefore with the current number of LEO RO satellites,

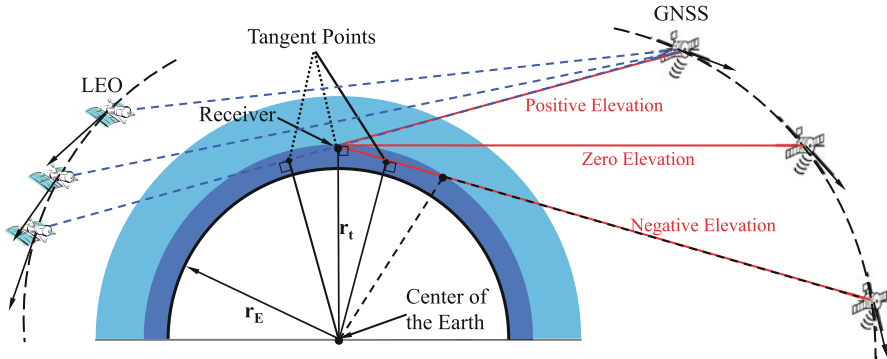


Fig. 6.5 Schematic diagram of radio occultation geometry with a receiver inside (e.g. aircraft or mountain-top) and outside (LEO) the atmosphere. The red lines connecting the GPS with the receiver represent three raypaths going through the atmosphere with different elevation relative to the local horizon (zero elevation). The blue dashed lines represent the descending of raypath received at LEO. Note the bending of the raypath is neglected and the relative scales of the plot are exaggerated for illustration purposes

it is difficult to provide dense sounding measurements in a specific region within a limited time period. With a GNSS receiver inside the atmosphere on a mountain top or onboard an airplane, the RO technique offers much denser regional soundings while retaining the high vertical resolution RO sounding capability which could greatly facilitate studies of regional weather and climate.

The possibility of making RO measurements with a receiver inside the atmosphere was originally considered by Zuffada et al. (1999). Even though fundamentally very similar to the spaceborne RO measurements, the mountain-top or air-borne RO measurements must be corrected for the asymmetric sampling geometry as the GNSS receiver is located inside the Earth's atmosphere. Zuffada et al. (1999) noticed that it is possible to measure both positive and negative elevation rays. These refer to rays that intersect the receiver from above and below the local horizon, as shown in Fig. 6.5. Note however that it is not possible to retrieve information unambiguously from the positive elevation angle rays alone.

For an occultation ray with elevation angle below the local horizon, the bending angle measured at the receiver is a sum of bending accumulated due to the atmosphere between the tangent height and the receiver height and the bending from the atmosphere above the receiver up to the GNSS satellite (e.g., Healy et al. 2002; Xie et al. 2008). The negative elevation bending is theoretically given by

$$\alpha_N(a) = -2a \cdot \int_{r_t}^{r_R} \frac{1}{n} \frac{dn}{dr} \frac{dr}{\sqrt{(nr)^2 - a^2}} - a \cdot \int_{r_R}^{r_T} \frac{1}{n} \frac{dn}{dr} \frac{dr}{\sqrt{(nr)^2 - a^2}}. \quad (6.14)$$

where r_T and r_R refer to the radius of the transmitter and receiver altitude, respectively, and r_t is the radius at the tangent altitude. The constant a , for a given ray, is known as the impact parameter. Assuming spherically symmetric

atmosphere, for every negative elevation angle ray with bending angle α_N , there is a corresponding positive elevation angle ray, with bending angle α_P with the same impact parameter, and is in fact equal to the second term in Eq. (6.14). These two bending angles can be differenced to derive the so-called “partial bending angle”. The partial bending angle corresponds to the accumulated bending from a segment of the ray path below the altitude of the receiver.

$$\alpha'(a) - \alpha_N(a) - \alpha_P(a) = -2a \cdot \int_{r_t}^{r_R} \frac{1}{n} \frac{dn}{dr} \frac{dr}{\sqrt{(nr)^2 - a^2}} r_t. \quad (6.15)$$

The refractive index below the receiver can then be retrieved through the slightly modified Abel transform (Healy et al. 2002), which is similar to the spaceborne GPS occultation case, but the refractive index at the receiver, n_R can no longer be neglected:

$$n(a) = n_R \exp \left[\frac{1}{\pi} \int_{x=a}^{n_R r_R} \frac{\alpha'(x) dx}{\sqrt{x^2 - a^2}} \right]. \quad (6.16)$$

The refractive index profile is transformed to a function of altitude rather than impact parameter using the relation $a = nr$ at the tangent point. In practice, α_N and α_P , as functions of a , are derived from the measured excess Doppler shifts in a similar way to that used for the spaceborne RO case. Consequently, the atmospheric thermodynamic parameters such as density temperature, pressure and humidity can be inferred based on the airborne RO refractivity measurement following the approach used in spaceborne RO retrieval as described in Sect. 6.1.

The geometric optics retrieval technique has been adapted from the spaceborne RO to the airborne measurements, and simulation studies have been carried out by several authors (Healy et al. 2002; Lesne et al. 2002; Mousa and Tsuda 2004; Xie et al. 2008). A number of field campaigns have also been conducted, and preliminary comparisons of measurements with radiosonde observations and numerical weather prediction (NWP) model analyses have been reported (Aoyama et al. 2004; Xie et al. 2008; Muradyan et al. 2010). Due to the multipath effect in the lower troposphere, the geometric optics retrieval technique encounter challenges, the more advanced radio-holographic retrieval method is thus needed to derive more accurate and higher vertical resolution RO soundings (e.g., Xie et al. 2012b).

Contrary to the spaceborne RO observation, with a GNSS receiver inside the atmosphere, the receiver is either still (e.g., on mountain-top) or moving (e.g., airborne, in the order of ~ 0.25 km/s) much slower than the GNSS occultation satellite (~ 3.87 km/s) and the LEO satellites (~ 7.8 km/s). A typical airborne/mountain-top radio occultation generally takes ~ 20 – 30 min to sample the atmosphere from the altitude (~ 5 – 10 km) of the receiver down to the surface. The sampling rate requirement for the airborne/mountain-top RO measurements is thus lower than that for the spaceborne RO, such that it can be satisfied by an off-the-shelf commercial GPS receiver (Xie et al. 2008).

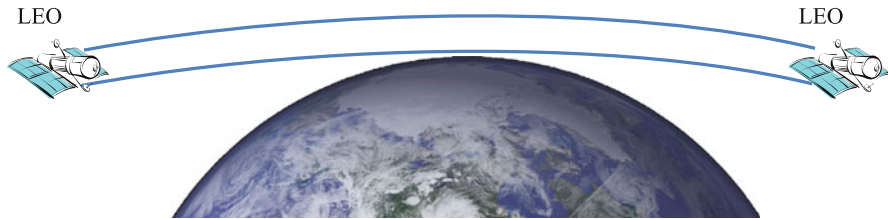


Fig. 6.6 LEO to LEO occultation geometry

On the other hand, the horizontal drift of the airborne/mountain-top RO tangent point is generally larger for an airborne case than for a space based receiver because the receiver is moving at a much slower speed than the transmitter. The errors due to the spherical symmetry assumption in the presence of significant horizontal gradients are compounded by the horizontal drift of the tangent point. Xie et al. (2008) demonstrates significant representative errors can be induced by the combination of limb sounding geometry and the horizontal tangent point drifting. Therefore, it is important to note that the airborne/mountain-top RO bending or refractivity profile derived from an occultation measurement should not be treated as local or in-situ measurement. Various data assimilation technique used in the spaceborne RO community could be adapted to maximize the benefit of airborne/mountain-top RO measurements for regional numerical weather forecasting.

6.6.3 *LEO-to-LEO Occultation*

Note the GNSS radio occultation sounding technique makes use of the L-band dual frequency signals and only measures the real part of the atmospheric refractivity, i.e., neglecting the absorption effect of the atmosphere. Since the late 1990s, many other frequencies that are significantly higher than GNSS signals have also been explored with similar types of limb sounding technique. By mounting the transmitter and receiver on two separated LEO satellites that are moving away or toward to each other (Fig. 6.6), the LEO to LEO occultation can be recorded. The LEO to LEO occultation measuring both refraction and absorption of coherent microwave and infrared signals could provide a much more complete set of atmospheric variables that includes thermodynamics (temperature, pressure, water vapor), dynamics (line-of-sight winds), climate/chemistry (ozone, carbon dioxide, methane, and other greenhouse gases and trace species) as well as cloud, aerosol and turbulence information (Kursinski et al. 2002; Kirchengast and Hoeg 2004; Kursinski et al. 2009; Kirchengast and Schweitzer 2011; Schweitzer et al. 2011).

The measurement of LEO-LEO occultation signals phase and amplitude in the microwave bands (MW occultation) near 22 GHz (~ 1.36 cm) and 183 GHz (~ 1.6 mm) water vapor absorption lines and 184 and 195 GHz (~ 1.5 mm) ozone

absorption lines will provide the fundamental thermodynamic variables of the atmosphere (temperature, pressure, geopotential height, humidity) from near the surface to the mesopause and ozone concentration through the middle atmosphere down into the upper troposphere (Kursinski et al. 2002; Kirchengast and Schweitzer 2011). Another MW band between 500 and 600 GHz (i.e., \sim 0.5–0.6 mm) would also be quite useful for profiling water vapor and its isotopes in the middle atmosphere (Kursinski et al. 2002).

On the other hand, the LEO-LEO occultation measurements in the short-wave infrared band (IR-laser occultation at 2–2.5 μm) will provide the line-of-sight wind, greenhouse gases (GHGs) and key chemical species (H_2O , CO_2 , CH_4 , N_2O , O_3 , CO) and four CO_2 and H_2O isotopes (HDO , H_2^{18}O , $^{13}\text{CO}_2$, C^{18}OO) in the upper troposphere and lower stratosphere. Furthermore, profiles of aerosol extinction, cloud layering, and turbulence can also be obtained (Kirchengast and Hoeg 2004; Kirchengast and Schweitzer 2011).

By directly measurement of water vapor, the LEO-LEO occultation in MW band is conceived to overcome the wet-dry ambiguity that limits direct interpretation of the GNSS RO refractivity profiles in the warmer regions of the troposphere because the wet and dry contributions to refractivity cannot be separated using refractivity measurements alone. In addition, the higher frequencies used by LEO-LEO occultation results in negligible ionospheric residual errors and could leads to highly accurate and independent upper air temperature and water vapor observations with climate benchmark quality (Kursinski et al. 2009).

Such a LEO-LEO occultation (often referred as the “next-generation RO”) observing system could complement the GNSS RO and provide long-term global free atmosphere observation (above the boundary layer), which will strongly benefit the climate community as well as the NWP and atmospheric chemistry communities. Due to the relatively high cost of building the constellation of the LEO-LEO occultation observing system, the technique is still in the testing phases. However, significant support and appreciation of the values of such novel observations have grown immensely in recent years.

References

- Ahmad B, Tyler GL (1999) Systematic errors in atmospheric profiles obtained from Abelian inversion of radio occultation data: effects of large-scale horizontal gradients. *J Geophys Res* 104(D4):3971–3992. doi:[10.1029/1998JD200102](https://doi.org/10.1029/1998JD200102)
- Anthes RA (2011) Exploring Earth’s atmosphere with radio occultation: contributions to weather, climate and space weather. *Atmos Meas Tech* 4:1077–1103. doi:[10.5194/amt-4-1077-2011](https://doi.org/10.5194/amt-4-1077-2011)
- Anthes RA, Rocken C, Kuo Y-H (2000) Applications of COSMIC to meteorology and climate. *Terr Atmos Ocean Sci* 11:115–156
- Anthes RA, Bernhardt PA, Chen Y, Cucurull L, Dymond KF, Ector D, Healy SB, Ho SP, Hunt DC, Kuo Y-H, Liu H, Manning K, McCormick C, Meehan TK, Randel WJ, Rocken C, Schreiner WS, Sokolovskiy SV, Syndergaard S, Thompson DC, Trenberth KE, Wee TK, Yen NL, Zeng Z (2008) The COSMIC/FORMOSAT-3 Mission-Early results. *Bull Am Meteorol Soc* 89: 313–333

- Ao CO (2007) Effect of ducting on radio occultation measurements: an assessment based on high-resolution radiosonde soundings. *Radio Sci* 42:RS2008. doi:[10.1029/2006RS003485](https://doi.org/10.1029/2006RS003485)
- Ao CO, Meehan TK, Hajj GA, Mannucci AJ, Beyerle G (2003) Lower troposphere refractivity bias in GPS occultation retrievals. *J Geophys Res* 108(D18):4577. doi:[10.1029/2002JD003216](https://doi.org/10.1029/2002JD003216)
- Ao CO, Hajj GA, Meehan TK, Dong D, Iijima BA, Mannucci AJ, Kursinski ER (2009) Rising and setting GPS occultations by use of open-loop tracking. *J Geophys Res* 114:D04101. doi:[10.1029/2008JD010483](https://doi.org/10.1029/2008JD010483)
- Ao CO, Waliser DE, Chan SK, Li J-L, Tian B, Xie F, Mannucci AJ (2012) Planetary boundary layer heights from GPS radio occultation refractivity and humidity profiles. *J Geophys Res* 117:D16117. doi:[10.1029/2012JD017598](https://doi.org/10.1029/2012JD017598)
- Aoyama Y, Shoji Y, Mousa A, Tsuda T, Nakamura H (2004) Temperature and water vapor profiles derived from downward-looking GPS occultation data. *J Meteorol Soc Jpn* 82:433–440
- Aparicio J, Deblonde G (2008) Impact of the assimilation of CHAMP refractivity profiles on Environment Canada global forecasts. *Mon Weather Rev* 136(1):257–275
- Aparicio JM, Laroche S (2011) An evaluation of the expression of the atmospheric refractivity for GPS signals. *J Geophys Res Atmos* 116:D11104
- Aparicio J, Deblonde G, Garand L, Laroche S (2009) The signature of the atmospheric compressibility factor in COSMIC, CHAMP and GRACE radio occultation data. *J Geophys Res* 114:D16114. doi:[10.1029/2008JD011156](https://doi.org/10.1029/2008JD011156)
- Bassiri S, Hajj GA (1993) Higher-order ionospheric effect on the Global Positioning System observables and means of modeling them. *Manuscr Geodaet* 18:280–289
- Bertiger WI, Wu S (1996) Single frequency GPS orbit determination for low Earth orbiters. Paper presented at the National Technical Meeting, Institute of Navigations, Santa Monica, CA, January
- Bertiger WI et al (1994) GPS precise tracking of TOPEX/POSEISON: results and implications. *J Geophys Res* 99:24,449–24,464
- Beyerle G, Gorbunov ME, Ao CO (2003) Simulation studies of GPS radio occultation measurements. *Radio Sci* 38(5):1084. doi:[10.1029/2002RS002800](https://doi.org/10.1029/2002RS002800)
- Beyerle G, Schmidt T, Michalak G, Heise S, Wickert J, Reigber C (2005) GPS radio occultation with GRACE: atmospheric profiling utilizing the zero difference technique. *Geophys Res Lett* 32:L13806. doi:[10.1029/2005GL023109](https://doi.org/10.1029/2005GL023109)
- Borsche M, Kirchengast G, Foelsche U (2007) Tropical tropopause climatology as observed with radio occultation measurements from CHAMP compared to ECMWF and NCEP analyses. *Geophys Res Lett* 34:L03702. doi:[10.1029/2006GL027918](https://doi.org/10.1029/2006GL027918)
- Chapman S, Lindzen RS (1970) Atmospheric tides: thermal and gravitational. Gordon and Breach, New York, NY, 200 pp
- Chen S-Y, Huang C-Y, Kuo Y-H, Guo Y-R, Sokolovskiy S (2009) Assimilation of GPS refractivity from FORMOSAT-3/COSMIC using a nonlocal operator with WRF 3DVAR and its impact on the prediction of a typhoon event. *Terr Atmos Ocean Sci* 20:133–154
- Cucurull L (2010) Improvement in the use of an operational constellation of GPS radio-occultation receivers in weather forecasting. *Weather Forecast* 25(2):749–767. doi:[10.1175/2009WAF2222302.1](https://doi.org/10.1175/2009WAF2222302.1)
- Cucurull L, Derber JC (2008) Operational implementation of COSMIC observations into NCEP's Global Data Assimilation System. *Weather Forecast* 23:702–711
- Cucurull L, Kuo YH, Barker D, Rizvi SRH (2006) Assessing the impact of simulated COSMIC GPS radio occultation data on weather analysis over the Antarctic: a case study. *Mon Weather Rev* 134:3283–3296
- Foelsche U, Kirchengast G, Steiner AK, Kornblueh L, Manzini E, Bengtsson L (2008) An observing system simulation experiment for climate monitoring with GNSS radio occultation data: setup and test bed study. *J Geophys Res* 113:D11108. doi:[10.1029/2007JD009231](https://doi.org/10.1029/2007JD009231)
- Foelsche U, Scherlin-Pirscher B, Ladstädter F, Steiner AK, Kirchengast G (2011) Refractivity and temperature climate records from multiple radio occultation satellites consistent within 0.05%. *Atmos Meas Tech* 4:2007–2018

- Gobiet A, Kirchengast G, Manney GL, Borsche M, Retscher C, Stiller G (2007) Retrieval of temperature profiles from CHAMP for climate monitoring: intercomparison with Envisat MIPAS and GOMOS and different atmospheric analyses. *Atmos Chem Phys* 7:3519–3536. doi:[10.5194/acp-7-3519-2007](https://doi.org/10.5194/acp-7-3519-2007)
- Gorbunov ME (2002) Radio-holographic analysis of Microlab-1 radio occultation data in the lower troposphere. *J Geophys Res* 107(D12):4156. doi:[10.1029/2001JD000889](https://doi.org/10.1029/2001JD000889)
- Gorbunov ME, Benzoni H-H, Jensen AS, Lohmann MS, Nielsen AS (2004) Comparative analysis of radio occultation processing approaches based on Fourier integral operators. *Radio Sci* 39:RS6004. doi:[10.1029/2003RS002916](https://doi.org/10.1029/2003RS002916)
- Guo P, Kuo Y-H, Sokolovskiy S, Lenschow DH (2011) Estimating atmospheric boundary layer depth using COSMIC radio occultation data. *J Atmos Sci* 68:1703–1713. doi:[10.1175/2011JAS3612.1](https://doi.org/10.1175/2011JAS3612.1)
- Hajj GA, Kursinski ER, Romans LJ, Bertiger WI, Leroy SS (2002) A technical description of atmospheric sounding by GPS occultation. *J Atmos Solar Terr Phys* 64:451–469
- Hajj GA, Ao CO, Iijima BA, Kuang D, Kursinski ER, Mannucci AJ, Meehan TK, Romans LJ, de la Torre Juarez M, Yunck TP (2004) CHAMP and SAC-C atmospheric occultation results and intercomparisons. *J Geophys Res* 109:D06109. doi:[10.1029/2003JD003909](https://doi.org/10.1029/2003JD003909)
- He W, Ho S, Chen H, Zhou X, Hunt D, Kuo Y (2009) Assessment of radiosonde temperature measurements in the upper troposphere and lower stratosphere using COSMIC radio occultation data. *Geophys Res Lett* 36:L17807. doi:[10.1029/2009GL038712](https://doi.org/10.1029/2009GL038712)
- Healy SB (2001) Radio occultation bending angle and impact parameter errors caused by horizontal refractive index gradients in the troposphere: a simulation study. *J Geophys Res* 106:11,875–11,889
- Healy SB (2007) Operational assimilation of GPS radio occultation measurements at ECMWF. European Centre for Medium-range Weather Forecasts (ECMWF) Newsletter No. 111, Reading, UK
- Healy SB (2008) Forecast impact experiment with a constellation of GPS radio occultation receivers. *Atmos Sci Lett* 9:111–118
- Healy SB (2011) Refractivity coefficients used in the assimilation of GPS radio occultation measurements. *J Geophys Res* 116:D01106. doi:[10.1029/2010JD014013](https://doi.org/10.1029/2010JD014013)
- Healy SB, Eyre JR (2000) Retrieving temperature, water vapour and surface pressure information from refractive index profiles derived by radio occultation: a simulation study. *Q J R Meteorol Soc* 126:1661–1683
- Healy SB, Thepaut JN (2006) Assimilation experiments with CHAMP GPS radio occultation measurements. *Q J R Meteorol Soc* 132:605–623
- Healy SB, Haase J, Lesne O (2002) Abel transform inversion of radio occultation measurements made with a receiver inside the Earth's atmosphere. *Ann Geophys* 20(8):1253–1256
- Ho S-P, Kuo Y-H, Zeng Z, Peterson T (2007) A comparison of lower stratosphere temperature from microwave measurements with CHAMP GPS RO data. *Geophys Res Lett* 34:L15701. doi:[10.1029/2007GL030202](https://doi.org/10.1029/2007GL030202)
- Ho S-P, Goldberg M, Kuo Y-H, Zou C-Z, Schreiner W (2009a) Calibration of temperature in the lower stratosphere from microwave measurements using COSMIC radio occultation data: preliminary results. *Terr Atmos Ocean Sci* 20:87–100
- Ho S-P, Kirchengast G, Leroy S, Wickert J, Mannucci AJ, Steiner A, Hunt D, Schreiner W, Sokolovskiy S, Ao C, Borsche M, von Engeln A, Foelsche U, Heise S, Iijima B, Kuo Y-H, Kursinski ER, Pirscher B, Ringer M, Rocken C, Schmidt T (2009b) Estimating the uncertainty of using GPS radio occultation data for climate monitoring: intercomparison of CHAMP refractivity climate records 2002–2006 from different data centers. *J Geophys Res* 114:D23107. doi:[10.1029/2009JD011969](https://doi.org/10.1029/2009JD011969)
- Ho S-P, Kuo Y-H, Schreiner W, Zhou X (2010a) Using SI-traceable Global Positioning System radio occultation measurements for climate monitoring, in: State of the Climate in 2009. Bull Am Meteorol Sci 91:S36–S37

- Ho S-P, Zhou X, Kuo Y-H, Hunt D (2010b) Climate calibration observatory in orbit: calibration and validation of measurements of AMSU and AIRS using Global Positioning System Radio Occultation Observations. Joint OPAC-4 and GRAS SAF climate workshop, Graz, Austria, September 610 pp
- Huang C-Y, Kuo Y-H, Chen S-H, Vandenberge F (2005) Improvements in typhoon forecasts with assimilated GPS occultation refractivity. *Weather Forecast* 20:931–953
- Jensen AS, Lohmann M, Benzon H-H, Nielsen AS (2003) Full spectrum inversion of radio occultation signals. *Radio Sci* 38(3):1040. doi:[10.1029/2002RS002763](https://doi.org/10.1029/2002RS002763)
- Kirchengast G, Hoeg P (2004) The ACE + Mission: an Atmosphere and Climate Explorer based on GPS, GALILEO, and LEO-LEO radio occultation. In: Kirchengast G et al (eds) *Occultations for probing atmosphere and climate*. Springer, Berlin, pp 201–220
- Kirchengast G, Schweitzer S (2011) Climate benchmark profiling of greenhouse gases and thermodynamic structure and wind from space. *Geophys Res Lett* 38:L13701. doi:[10.1029/2011GL047617](https://doi.org/10.1029/2011GL047617)
- Kuo Y-H, Zou X, Chen SJ, Huang W, Guo Y-R, Anthes RA, Exner M, Hunt D, Rocken C, Sokolovskiy S (1998) A GPS/MET sounding through an upper-level front. *Bull Am Meteorol Soc* 79:617–626
- Kuo Y-H, Sokolovskiy S, Anthes RA, Vandenberge F (2000) Assimilation of GPS radio occultation data for numerical weather prediction. *Terr Atmos Ocean Sci* 11:157–158
- Kuo YH, Wee TK, Sokolovskiy S, Rocken C, Schreiner W, Hunt D, Anthes RA (2004) Inversion and error estimation of GPS radio occultation data. *J Meteorol Soc Jpn* 82(1B):507–531
- Kuo Y-H, Schreiner WS, Wang J, Rossiter DL, Zhang Y (2005) Comparison of GPS radio occultation soundings with radiosondes. *Geophys Res Lett* 32:L05817. doi:[10.1029/2004GL021443](https://doi.org/10.1029/2004GL021443)
- Kursinski ER (1994) Monitoring the Earth's atmosphere with GPS. *GPS World* 5:50–54
- Kursinski ER, Hajj GA, Schofield JT, Linfield RP, Hardy KR (1997) Observing Earth's atmosphere with radio occultation measurements using the Global Positioning System. *J Geophys Res* 102(D19):23429–23465
- Kursinski ER, Hajj GA, Leroy SS, Herman B (2000a) The GPS radio occultation technique. *Terr Atmos Ocean Sci* 11:53–114
- Kursinski ER, Healy SB, Romans LJ (2000b) Initial results of combining GPS occultations with ECMWF global analyses within a 1DVar framework. *Earth Planets Space* 52:885–892
- Kursinski ER, Syndergaard S, Flittner D, Feng D, Hajj G, Herman B, Ward D, Yunck T (2002) A microwave occultation observing system optimized to characterize atmospheric water, temperature and geopotential via absorption. *J Atmos Ocean Technol* 19:1897–1914
- Kursinski ER, Ward D, Otarola A, Frehlich R, Groppi C, Albana S, Shein M, Bertiger W, Pickett H, Ross M (2009) The Active Temperature, Ozone and Moisture Microwave Spectrometer (ATOMMS). In: Steiner A et al (eds) *New horizons in occultation research: studies in atmosphere and climate*. Springer, Berlin, pp 295–313. doi:[10.1007/978-3-642-00321-9_24](https://doi.org/10.1007/978-3-642-00321-9_24)
- Lackner BC, Steiner AK, Hegerl GC, Kirchengast G (2011) Atmospheric climate change detection by radio occultation data using a fingerprinting method. *J Clim* 24:5275–5291
- Ladstädter F, Steiner AK, Foelsche U, Haimberger L, Tavolato C, Kirchengast G (2011) An assessment of differences in lower stratospheric temperature records from (A)MSU, radiosondes, and GPS radio occultation. *Atmos Meas Tech* 4:1965–1977. doi:[10.5194/amt-4-1965-2011](https://doi.org/10.5194/amt-4-1965-2011)
- LeMarshall J, Xiao Y, Norman R, Zhang K, Rea A, Cucurull L, Seecamp R, Steinie P, Puri K, Le T (2010) The beneficial impact of radio occultation observations on Australian regional forecasts. *Aust Meteorol Ocean J* 62:121–125
- Leroy S (1997) Measurement of geopotential heights by GPS radio occultation. *J Geophys Res* 102:6971–6986
- Leroy SS, Anderson JG, Dykema JA (2006) Testing climate models using GPS radio occultation: a sensitivity analysis. *J Geophys Res* 111:D17105. doi:[10.1029/2005JD006145](https://doi.org/10.1029/2005JD006145)
- Lesne O, Haase J, Kirchengast G, Ramsauer J, Poetzi W (2002) Sensitivity analysis for airborne sounding of the troposphere by GNSS radio occultation. *Phys Chem Earth* 27(4–5):291–299

- Liu H, Anderson J, Kuo Y-H (2012) Improved analyses and forecasts of Hurricane Ernesto's genesis using radio occultation data in an Ensemble Filter Assimilation System. *Mon Weather Rev* 140:151–166
- Lopez P (2009) A 5-yr 40-km-resolution global climatology of superrefraction for ground-based weather radars. *J Appl Meteorol Climatol* 48(1):89–110. doi:[10.1175/2008JAMC1961.1](https://doi.org/10.1175/2008JAMC1961.1)
- Luntama J-P, Kirchengast G, Borsche M, Foelsche U, Steiner A, Healy S, von Engeln A, O'Clerigh E, Marquardt C (2008) Prospects of the EPS GRAS mission for operational atmospheric applications. *Bull Am Meteorol Soc* 89:1863–1875
- McLandress C (1997) Seasonal variability of the diurnal tide: results from the Canadian Middle atmospheric general circulation model. *J Geophys Res* 102:29,747–29,764
- Melbourne WG, Davis ES, Duncan CB, Hajj GA, Hardy KR, Kursinski ER, Meehan TK, Young LE, Yunck TP (1994) The application of GPS to atmospheric limb sounding and global change monitoring. *JPL Publ* 94-18, Pasadena, CA, 147 pp
- Mousa A, Tsuda T (2004) Inversion algorithms for GPS downward looking occultation data: simulation analysis. *J Meteorol Soc Jpn* 82:427–432
- Muradyan P, Haase JS, Xie F, Garrison JL, Voo J (2010) GPS/INS navigation precision and its effect on airborne radio occultation retrieval accuracy. *GPS Solut.* doi:[10.1007/s10291-010-0183-7](https://doi.org/10.1007/s10291-010-0183-7)
- Neiman PJ, Ralph FM, Wick GA, Kuo Y-H, Wee T-K, Ma Z, Taylor GH, Dettinger MD (2008) Diagnosis of an intense atmospheric river impacting the Pacific Northwest: storm summary and offshore vertical structure observed with COSMIC satellite retrieval. *Mon Weather Rev* 136:4398–4420
- Ohring G, Wielicki B, Spencer R, Emery B, Atlas R (2005) Satellite instrument calibration for measuring global climate change – report of a workshop. *Bull Am Meteorol Soc* 86:1303–1313
- Owens JS (1967) Optical refractive index of air: dependence on pressure, temperature and composition. *Appl Opt* 6:51–58
- Palmer PI, Barnett JJ, Eyre JR, Healy SB (2000) A non-linear optimal estimation inverse method for radio occultation measurements of temperature, humidity, and surface pressure. *J Geophys Res* 105:17513–17526
- Pirscher B, Foelsche U, Borsche M, Kirchengast G, Kuo Y-H (2010) Analysis of migrating diurnal tides detected in FORMOSAT-3/COSMIC temperature data. *J Geophys Res* 115:D14108. doi:[10.1029/2009JD013008](https://doi.org/10.1029/2009JD013008)
- Poli P (2004) Effects of horizontal gradients on GPS radio occultation observation operators. II: A Fast Atmospheric Refractivity Gradient Operator (FARGO). *Q J R Meteorol Soc* 130. doi:[10.1256/qj.03.229](https://doi.org/10.1256/qj.03.229)
- Poli P, Joiner J (2004) Effects of horizontal gradients on GPS radio occultation observation operators. I: Ray tracing. *Q J R Meteorol Soc* 130:2787–2805
- Poli P, Joiner J, Kursinski ER (2002) 1DVAR analysis of temperature and humidity using GPS radio occultation refractivity data. *J Geophys Res* 107(D20):4448. doi:[10.1029/2001JD000935](https://doi.org/10.1029/2001JD000935)
- Poli P, Moll P, Puech D, Rabier F, Healy SB (2007) Quality control, error analysis, and impact assessment of FORMOSAT-3/COSMIC in numerical weather prediction. *Terr Atmos Ocean Sci* 20:101–113
- Poli P, Healy SB, Dee DP (2010) Assimilation of Global Positioning System radio occultation data in the ECMWF ERA-Interim reanalysis. *Q J R Meteorol Soc* 136:1972–1990. doi:[10.1002/qj.722](https://doi.org/10.1002/qj.722)
- Randel WJ, Wu F (2005) Kelvin wave variability near the equatorial tropopause observed in GPS radio occultation measurements. *J Geophys Res* 110:D03102. doi:[10.1029/2004JD005006](https://doi.org/10.1029/2004JD005006)
- Randel WJ, Wu F, Rivera Ríos W (2003) Thermal variability of the tropical tropopause region derived from GPS/MET observations. *J Geophys Res* 108(D1):4024. doi:[10.1029/2002JD002595](https://doi.org/10.1029/2002JD002595)
- Ratnam MV, Basha SG (2010) A robust method to determine global distribution of atmospheric boundary layer top from COSMIC GPS RO measurements. *Atmos Sci Lett* 11:216–222. doi:[10.1002/asl.277](https://doi.org/10.1002/asl.277)

- Rennie M (2008) The assimilation of GPS radio occultation data into the Met Office global model, Met R&D technical report 510, Met Office, UK
- Ringer MA, Healy SB (2008) Monitoring twenty-first century climate using GPS radio-occultation bending angles. *Geophys Res Lett* 35:L05708. doi:[10.1029/2007GL032462](https://doi.org/10.1029/2007GL032462)
- Rocken C, Anthes R, Exner M, Ware R, Feng D, Gorbunov M, Herman B, Hunt D, Kuo Y-H, Schreiner W, Sokolovskiy S, Zou X (1997) Verification of GPS/MET data in the neutral atmosphere. *J Geophys Res* 102:29,849–29,866
- Rüeger J (2002) Refractive index formulae for electronic distance measurements with radio and millimetre waves, Unisurv Report 109. University of New South Wales, Sydney, pp 758–766
- Schmidt T, Heise S, Wickert J, Beyerle G, Reigber C (2005) GPS radio occultation with CHAMP and SAC-C: global monitoring of thermal tropopause parameters. *Atmos Chem Phys* 5:1473–1488. doi:[10.5194/acp-5-1473-2005](https://doi.org/10.5194/acp-5-1473-2005)
- Schmidt T, Beyerle G, Heise S, Wickert J, Rothacher M (2006) A climatology of multiple tropopauses derived from GPS radio occultations with CHAMP and SAC-C. *Geophys Res Lett* 33:L04808. doi:[10.1029/2005GL024600](https://doi.org/10.1029/2005GL024600)
- Schmidt T, Wickert J, Beyerle G, Heise S (2008) Global tropopause height trends estimated from GPS radio occultation data. *Geophys Res Lett* 35:L11806. doi:[10.1029/2008GL034012](https://doi.org/10.1029/2008GL034012)
- Schmidt T, Wickert J, Haser A (2010) Variability of the upper troposphere and lower stratosphere observed with GPS radio occultation bending angles and temperatures. *Adv Space Res* 46:150–161. doi:[10.1016/j.asr.2010.01.021](https://doi.org/10.1016/j.asr.2010.01.021)
- Schreiner W, Rocken C, Sokolovskiy S, Syndergaard S, Hunt D (2007) Estimates of the precision of GPS radio occultations from the COSMIC/FORMOSAT-3 mission. *Geophys Res Lett* 34:L04808. doi:[10.1029/2006GL027557](https://doi.org/10.1029/2006GL027557)
- Schweitzer S, Kirchengast G, Proschek V (2011) Atmospheric influences on infrared-laser signals used for occultation measurements between Low Earth Orbit satellites. *Atmos Meas Tech* 4:2273–2292. doi:[10.5194/amt-4-2273-2011](https://doi.org/10.5194/amt-4-2273-2011)
- Smith EK, Weintraub S (1953) The constants in the equation for atmospheric refractive index at radio frequencies. *Proc IRE* 41:1035–1037
- Sokolovskiy SV (2001) Tracking tropospheric radio occultation signals from low Earth orbit. *Radio Sci* 36(3):483–498
- Sokolovskiy S (2003) Effect of superrefraction on inversions of radio occultation signals in the lower troposphere. *Radio Sci* 38(3):1058. doi:[10.1029/2002RS002728](https://doi.org/10.1029/2002RS002728)
- Sokolovskiy SV, Kuo Y-H, Wang W (2005) Assessing the accuracy of a linearized observation operator for assimilation of radio occultation data: case simulations with a high-resolution weather model. *Mon Weather Rev* 133:2200–2212
- Sokolovskiy S, Rocken C, Hunt D, Schreiner W, Johnson J, Masters D, Esterhuizen S (2006a) GPS profiling of the lower troposphere from space: inversion and demodulation of the open-loop radio occultation signals. *Geophys Res Lett* 33:L14816. doi:[10.1029/2006GL026112](https://doi.org/10.1029/2006GL026112)
- Sokolovskiy S, Kuo Y-H, Rocken C, Schreiner WS, Hunt D, Anthes RA (2006b) Monitoring the atmospheric boundary layer by GPS radio occultation signals recorded in the open-loop mode. *Geophys Res Lett* 33:L12813. doi:[10.1029/2006GL026112](https://doi.org/10.1029/2006GL026112)
- Sokolovskiy SV, Rocken C, Lenschow DH, Kuo Y-H, Anthes RA, Schreiner WS, Hunt DC (2007) Observing the moist troposphere with radio occultation signals from COSMIC. *Geophys Res Lett* 34:L18802. doi:[10.1029/2007GL030458](https://doi.org/10.1029/2007GL030458)
- Sokolovskiy S, Rocken C, Schreiner W, Hunt D, Johnson J (2009) Postprocessing of L1 GPS radio occultation signals recorded in open-loop mode. *Radio Sci* 44:RS2002. doi:[10.1029/2008RS003907](https://doi.org/10.1029/2008RS003907)
- Sokolovskiy S, Lenschow D, Rocken C, Schreiner W, Hunt D, Kuo Y-H, Anthes R (2010) Variability of the boundary layer depth over certain regions of subtropical ocean from 3 years of COSMIC data. Presentation at the 90th AMS annual meeting, Atlanta, GA, USA, 17–21 January
- Steffes PG, Jenkins JM, Austin RS, Asmar SW, Lyons DT, Seale EH, Tyler GL (1994) Radio occultation studies of the Venus atmosphere with the Magellan spacecraft, 1. Experiment description and performance. *Icarus* 110:71–78

- Steiner AK, Kirchengast G (2000) Gravity wave spectra from GPS/MET occultation observations. *J Atmos Ocean Technol* 17:495–503
- Steiner AK, Kirchengast G, Borsche M, Foelsche U, Schoengassner T (2007) A multi-year comparison of lower stratospheric temperatures from CHAMP radio occultation data with MSU/AMSU records. *J Geophys Res* 112:D22110. doi:[10.1029/2006JD008283](https://doi.org/10.1029/2006JD008283)
- Steiner AK, Kirchengast G, Lackner BC, Pirscher B, Borsche M, Foelsche U (2009) Atmospheric temperature change detection with GPS radio occultation 1995 to 2008. *Geophys Res Lett* 36:L18702. doi:[10.1029/2009GL039777](https://doi.org/10.1029/2009GL039777)
- Steiner AK, Hunt D, Ho S-P, Kirchengast G, Mannucci AJ, Scherllin-Pirscher B, Gleisner H, von Engeln A, Schmidt T, Ao C, Leroy SS, Kursinski ER, Foelsche U, Gorbunov M, Heise S, Kuo Y-H, Lauritsen KB, Marquardt C, Rocken C, Schreiner W, Sokolovskiy S, Syndergaard S, Wickert J (2013) Quantification of structural uncertainty in climate data records from GPS radio occultation. *Atmos Chem Phys* 13:1469–1484. doi:[10.5194/acp-13-1469-2013](https://doi.org/10.5194/acp-13-1469-2013)
- Stephens SA, Thomas JB (1995) Controlled-root formulations for digital phase-locked loops. *IEEE Trans Aerosp Electron Syst* 31(1):78–95
- Syndergaard S (1998) Modeling the impact of the Earth's oblateness on the retrieval of temperature and pressure profiles from limb sounding. *J Atmos Solar-Terr Phys* 60(2):171–180
- Syndergaard S, Kursinski ER, Herman BM, Lane EM, Flittner DE (2005) A refractive index mapping operator for assimilation of occultation data. *Mon Weather Rev* 133:2650–2668
- Thayer GD (1974) An improved equation for the radio refractive index of air. *Radio Sci* 9:803–807
- Treuhaft RN, Lany GE (1987) The effect of the dynamic wet troposphere on radio interferometric measurements. *Radio Sci* 22:251–265
- Tsuda T, Nishida M, Rocken C, Ware RH (2000) A global morphology of gravity wave activity in the stratosphere revealed by the GPS Occultation Data (GPS/MET). *J Geophys Res* 105:7257–7273
- Tyler GL (1987) Radio occultation experiments in the outer solar system with Voyager. *Proc IEEE* 75:1404–1431
- von Engeln A, Teixeira J (2004) A ducting climatology derived from the European Centre for Medium-Range Weather Forecasts global analysis fields. *J Geophys Res* 109, D18104. doi:[10.1029/2003JD004380](https://doi.org/10.1029/2003JD004380)
- Vorobev VV, Krasilnikova TG (1994) Estimation of accuracy of the atmospheric refractive index recovery from Doppler shift measurements at frequencies used in the NAVSTAR system, *Izv Russ Acad Sci Atmos Ocean Phys Engl Transl* 29:602–609
- Wee T-K, Kuo Y-H, Lee D-K (2010) Development of a curved ray tracing method for modeling of phase paths from GPS radio occultation: a two-dimensional study. *J Geophys Res* 115:D24119. doi:[10.1029/2010JD014419](https://doi.org/10.1029/2010JD014419)
- Xie F (2006) Development of a GPS occultation retrieval method for characterizing the marine boundary layer in the presence of super-refraction. Dissertation, University of Arizona, 134 pp
- Xie F, Syndergaard S, Kursinski ER, Herman BM (2006) An approach for retrieving marine boundary layer refractivity from GPS occultation data in the presence of superrefraction. *J Atmos Ocean Technol* 23:1629–1644. doi:[10.1175/JTECH1996.1](https://doi.org/10.1175/JTECH1996.1)
- Xie F, Haase JS, Syndergaard S (2008) Profiling the atmosphere using the airborne GPS radio occultation technique: a sensitivity study. *IEEE Trans Geosci Remote Sens*. doi:[10.1109/TGRS.2008.2004713](https://doi.org/10.1109/TGRS.2008.2004713)
- Xie F, Wu DL, Ao CO, Kursinski ER, Mannucci AJ, Syndergaard S (2010a) Super-refraction effects on GPS radio occultation refractivity in marine boundary layers. *Geophys Res Lett* 37:L11805. doi:[10.1029/2010GL043299](https://doi.org/10.1029/2010GL043299)
- Xie F, Wu DL, Ao CO, Mannucci AJ (2010b) Atmospheric diurnal variations observed with GPS radio occultation soundings. *Atmos Chem Phys* 10:6889–6899. doi:[10.5194/acp-10-6889-2010](https://doi.org/10.5194/acp-10-6889-2010)
- Xie F, Wu DL, Ao CO, Mannucci AJ, Kursinski ER (2012a) Advances and limitations of atmospheric boundary layer observations with GPS occultation over southeast Pacific Ocean. *Atmos Chem Phys* 12:903–918. doi:[10.5194/acp-12-903-2012](https://doi.org/10.5194/acp-12-903-2012)
- Xie F, Haase JS, Muradyan P (2012b) Airborne GNSS radio occultation retrieval with a radio-holographic method. IROWG 2nd Workshop, Estes Park, CO, March 28–April 3

- Yunck TP, Lindal GF, Liu C-H (1988) The role of GPS in precise Earth observation. In: Proceedings of the IEEE position location and navigation symposium (PLANS 88), Nov 29–Dec 2
- Zeng Z, Randel W, Sokolovskiy S, Deser C, Kuo Y-H, Hagan M, Du J, Ward W (2008) Detection of migrating diurnal tide in the tropical middle atmosphere using the Challenging Minisatellite Payload radio occultation data. *J Geophys Res* 113:D03102. doi:[10.1029/2007JD008725](https://doi.org/10.1029/2007JD008725)
- Zou X, Kuo YH, Guo YR (1995) Assimilation of atmospheric radio refractivity using a nonhydrostatic adjoint model. *Mon Weather Rev* 123:2229–2249
- Zou X, Wang B, Liu H, Anthes RA, Matsumura T, Zhu Y-J (2000) Use of GPS/MET refraction angles in 3D variational analysis. *Q J R Meteorol Soc* 126:3013–3040
- Zou X, Liu H, Anthes RA (2002) A statistical estimate of errors in the calculation of radio occultation bending angles caused by a 2D approximation of raytracing and the assumption of spherical symmetry of the atmosphere. *J Atmos Ocean Technol* 19:51–64
- Zuffada C, Hajj GA, Kursinski ER (1999) A novel approach to atmospheric profiling with a mountain-based or airborne receiver. *J Geophys Res* 104(D20):24435–24447

Chapter 7

Ionospheric Sounding Using GNSS-RO

7.1 Introduction

The GNSS signal will be bent from GNSS transmitters and LEO satellites when the signal goes through Earth's atmosphere and ionosphere. As the movements of GNSS and LEO satellites, the signal paths finish scanning the atmosphere and ionosphere, and one occultation event is generated. If the scanning is up to down, it is called as the descending occultation, and in the contrary it is called as the ascending occultation. According to the occultation altitude from occultation point (i.e., tangent point) (Fig. 7.1), occultation events can be divided into two categories: atmospheric occultation events (lower than 90 km) and ionospheric occultation events (from 90 km to LEO altitude). Atmospheric occultation events' time span is 1–3 min, and ionosphere occultation events' time span is 10–20 min. With the improvement of GNSS-RO technique and more GNSS-RO missions, a huge number of occultation observations are available. Table 7.1 just lists the number of total atmospheric occultations and ionospheric occultations till January 15 23:25:02 in 2013. It is a useful database not only for military and civil users but also for Earth's space environment researchers.

7.2 Ionospheric Inversion

Figure 7.2 shows the geometric sketch of GNSS Radio Occultation. The GNSS satellites, LEO satellites and the ray path locate in the same plane, which is called occultation plane. The O, L, G, P are the refraction center, the LEO satellite's location, the GNSS satellite's location and the tangent point on the ray path, respectively. O is consistent with Earth's center with assuming the Earth as a sphere. The other parameters are showing below, respectively:

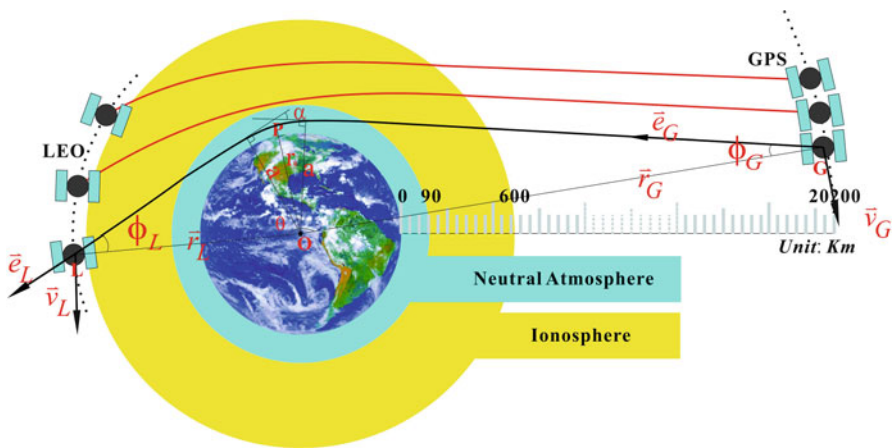


Fig. 7.1 Occultation geometry with GPS and LEO

Table 7.1 Total number of occultations at CDAAC till January 15, 2013

Missions	Total atmospheric occultation	Total ionospheric occultation
CHAMP	399,968	303,291
CNOFS	103,397	0
COSMIC	3,583,348	3,388,068
GPSMET	5,002	0
GPSMETAS	4,666	0
GRACE	229,083	110,677
METOPA	808,907	0
SACC	351,396	0
TSX	258,232	0
Total	5,743,999	3,802,036

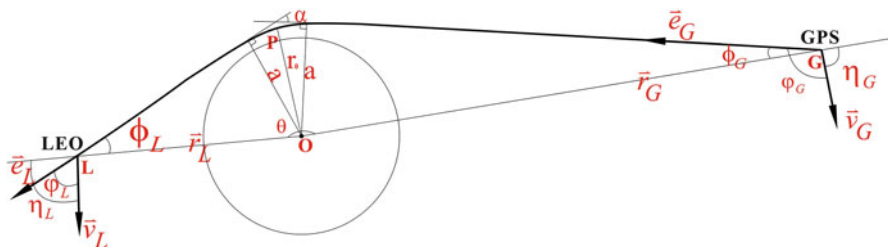


Fig. 7.2 Instantaneous geometric relationship of one occultation event

\vec{e}_L, \vec{e}_G : ray path direction vectors in the point of LEO and GNSS satellites.

\vec{v}_L, \vec{v}_G : projection of velocity vectors of LEO and GNSS satellites on the occultation plane.

\vec{r}_L, \vec{r}_G : location vectors of LEO and GNSS satellites in the refraction center.

- ϕ_L : angle between \vec{r}_L and \vec{e}_L (exit direction of signal).
 ϕ_G : angle between \vec{r}_G and \vec{e}_G (incident direction of signal).
 φ_L : angle between \vec{v}_L and \vec{e}_L (exit direction of signal).
 φ_G : angle between \vec{v}_G and \vec{e}_G (incident direction of signal).
 η_L : angle between \vec{r}_L and \vec{v}_L .
 η_G : angle between \vec{r}_G and \vec{v}_G .
 r_0 : distance between perigee and refraction center.
 a : impact parameter, which is the perpendicular distance between refraction center and asymptote of incident or exit direction of signal.
 α : bending angle.
 θ : angle between \vec{v}_L and \vec{r}_G .

7.2.1 Ionosphere Inversion Based on Doppler

According to Fermat's principle, the ray path range \widehat{LG} can be defined as:

$$L = \int n ds \quad (7.1)$$

Due to the refraction of Earth's atmosphere and ionosphere, excess phases exist in both carrier phases. Here ΔL_i is used to describe the excess phase.

$$\Delta L_i = L_i - r_{LG} = \int n ds - r_{LG} \quad (7.2)$$

where r_{LG} is the geometric distance between the GPS satellite and LEO satellite, and subscript i is the frequency ($i = 1, 2$). Differentiating Eq. (7.2) as

$$\frac{d\Delta L_i}{dt} = \frac{dL_i}{dt} - \frac{dr_{LG}}{dt} \quad (7.3)$$

As we known (Hocke 1997),

$$\frac{dL_i}{dt} = c \frac{\Delta f_i}{f_i} \quad (7.4)$$

where Δf_i is the Doppler shift of f_i . The relationship between satellites' velocities and $\frac{dL_i}{dt}$ is expressed as follow (Syndergaard 1998),

$$\frac{dL_i}{dt} = \left| \vec{v}_L \right| \cos \varphi_L(a) - \left| \vec{v}_G \right| \cos \varphi_G(a) \quad (7.5)$$

Using Eqs. 7.3 and 7.5,

$$\frac{d\Delta L_i}{dt} + \frac{dr_{LG}}{dt} - \left(\left| \vec{v}_L \right| \cos \varphi_L(a) - \left| \vec{v}_G \right| \cos \varphi_G(a) \right) = 0 \quad (7.6)$$

According to the geometrical relationship shown in Fig. 7.2,

$$\varphi_L(a) = \eta_L - \arcsin \left(\frac{a}{\left| \vec{r}_L \right|} \right) \quad (7.7)$$

$$\varphi_G(a) = \pi - \eta_G + \arcsin \left(\frac{a}{\left| \vec{r}_G \right|} \right) \quad (7.8)$$

$$\alpha = \theta - \arccos \left(\frac{a}{\left| \vec{r}_L \right|} \right) - \arccos \left(\frac{a}{\left| \vec{r}_G \right|} \right) \quad (7.9)$$

where $\frac{r_{LG}}{dt}$, $\left| \frac{d\vec{r}_L}{dt} \right|$, $\left| \frac{d\vec{r}_G}{dt} \right|$, θ , $\left| \vec{r}_L \right|$, $\left| \vec{r}_G \right|$ can be derived from satellites' locations and velocities and $\frac{d\Delta L_i}{dt}$ is the derivative with the time of excess phase. Using Eqs. (7.7, 7.8, and 7.9), the impact parameter can be derived by iteration. After getting the parameter a , bending angle α can be computed by Eq. (7.9).

With the spherical symmetry approximation of Earth's atmosphere and ionosphere, using the method of Abel inversion (Fjeldbo et al. 1971; Kursinski et al. 1997),

$$n(a_0) = \exp \left[\frac{1}{\pi} \int_{a_0}^{\infty} \frac{\alpha(a)}{\sqrt{a^2 - a_0^2}} da \right] \quad (7.10)$$

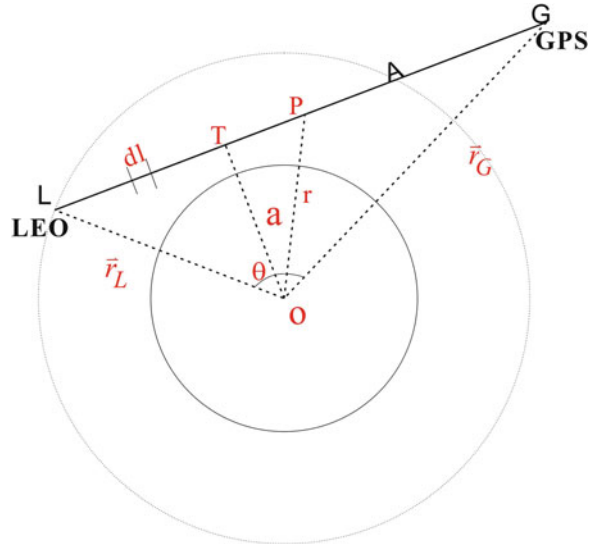
where a_0 the corresponding impact parameter of current radio occultation observation. The refractive index of Earth ionosphere can be expressed as (Bassiri and Hajj 1992; Hofmann-Wellenhof et al. 1992; Li and Huang 2005; Liu et al. 2006):

$$n = 1 - \frac{40.3}{f_i^2} Ne \quad (7.11)$$

where Ne is the electron density. Then, Ne can be derived as

$$Ne = \frac{f_i^2}{40.3} (1 - n) \quad (7.12)$$

Fig. 7.3 Occultation geometry with straight line



This method needs high precision orbit determination data and its processing procedure is complex. Usually, it will be used for atmosphere inversion and planetary radio occultation.

7.2.2 Ionosphere Inversion Based on TEC

Ionosphere inversion using TEC data is based on the fact that the bending angle due to the ionospheric refraction is very small (Hajj and Romans 1998), especially for upper ionosphere. Together another assumption of spherical symmetry in GNSS-RO inversion, the signal path from GNSS transmitter to the LEO satellite can be modeled as a straight line shown in Fig. 7.3.

The first step of ionosphere inversion based on TEC is to compute the slant total electron content along the signal path with GNSS dual-frequencies or single frequency data. TEC can be estimated by Eq. (7.13) with GNSS dual frequencies data, i.e.,

$$\begin{aligned} TEC &= \frac{f_1^2 f_2^2}{40.28(f_1^2 - f_2^2)} (L_1 - L_2 - (N_1 \lambda_1 - N_2 \lambda_2 + b_1 - b_2)) + \varepsilon_L \\ &= \frac{f_1^2 f_2^2}{40.28(f_2^2 - f_1^2)} (P_1 - P_2 - (B_1 - B_2)) + \varepsilon_P, \end{aligned} \quad (7.13)$$

where L_1 , L_2 , P_1 and P_2 are GNSS carrier phase and pseudorange observables, respectively, N_1 , N_2 , λ_1 and λ_2 are ambiguities and wavelengths for L_1 , L_2 ,

respectively, b_1 , b_2 , B_1 and B_2 are instrument biases, and ε_L and ε_P are noise. Here, the effect of propagation path difference and high order items of refraction are ignored. TEC error will increase in solar maximum year (Syndergaard 2000; Datta-Barua et al. 2008). Another method to compute TEC is based on L_1 and P_1 , i.e.,

$$TEC = \frac{f_1^2}{80.56} (P_1 - L_1) + N + \varepsilon \quad (7.14)$$

where N is the ambiguity and ε is the measurement error. The precision of TEC from single frequency GNSS data is lower because of greater noise of P_1 .

According to the definition of TEC and the assumption mentioned above, TEC can be expressed as the Abel transform of the electron density:

$$\begin{aligned} TEC(a) &= \left[\int_a^{r_{LEO}} + \int_a^{r_{GPS}} \right] Ne(r) dl = \left[\int_a^{r_{LEO}} + \int_a^{r_{GPS}} \right] \frac{Ne(r)r}{\sqrt{r^2 - a^2}} dr \\ &\approx 2 \int_a^{r_{LEO}} \frac{Ne(r)r}{\sqrt{r^2 - a^2}} dr \\ &\quad \left(l = \overline{LP} = \sqrt{r^2 - a^2} \Rightarrow dl = \frac{r}{\sqrt{r^2 - a^2}} dr \right) \end{aligned} \quad (7.15)$$

r : distance between the Earth geometrical center and one point on the ray path.

r_{LEO} : distance between the Earth geometrical center and the LEO satellite.

r_{GPS} : distance between the Earth geometrical center and the GPS satellite.

The electron content above the LEO satellite is neglected. Using the Abel inversion, the ionospheric electron density can be derived.

$$Ne(r) = -\frac{1}{\pi} \int_r^{r_{LEO}} \frac{\frac{dTEC(a)}{da}}{\sqrt{a^2 - r^2}} da \quad (7.16)$$

7.2.3 Recursive Inversion of TEC

Figure 7.4 shows the recursive scheme of the Abel inversion corresponding to the case in ionospheric GNSS-RO. Neglecting the discretization errors and with the same assumptions mentioned in last section, it can get

$$TEC \approx 2 \sum_{i=1}^n Ne(a_i) \cdot l_{i,n} \quad (7.17)$$

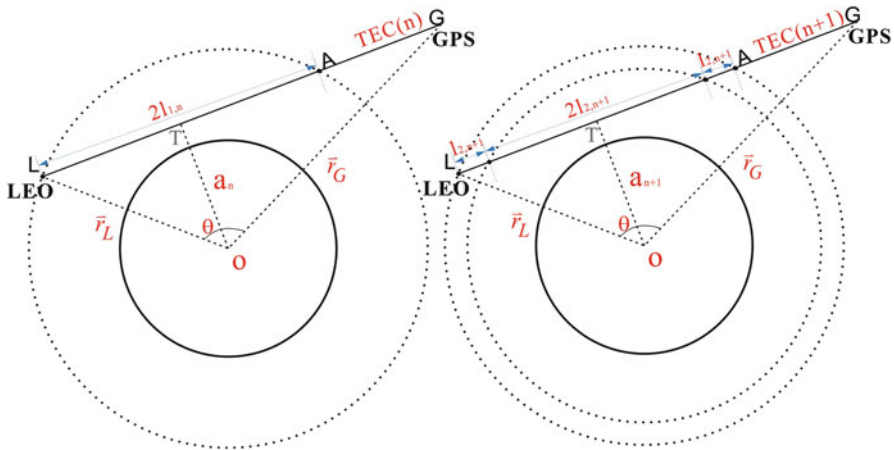


Fig. 7.4 a view of recursive scheme of the Abel inversion

Obviously, each TEC observation can determine a layer in the vertical profile. Further, the sampling rate of receivers equipped on the LEO satellites determines the vertical resolution of the profile.

$$Ne(a_n) = \frac{TEC(n) - 2 \cdot \sum_{i=1}^{n-1} Ne(a_i) \cdot l_{i,n}}{2 \cdot l_{n,n}} \quad (7.18)$$

Using Eq. (7.18), the electron density can be obtained layer by layer from the uppermost observation to the lowermost observation.

7.2.4 Amplitude Inversion

GNSS-RO observations contain not only phase observations but also amplitude variation information. Although the precision of bending angle derived from amplitude measurement is not as good as phase measurement, but it is applied in GNSS-RO physical inversion, such as back propagation algorithm (Gorbunov et al. 2000) and diffraction method (Melbourne et al. 1994). The variation of the amplitude is mainly caused by focusing or defocusing as well as associating with the atmosphere absorption and scattering effect. It may play an important role in optimizing phase inversion, monitoring multipath propagation, finding anomalies

of electron density et al. Amplitude measurement also can be used for ionosphere inversion as follow (Liou et al. 2002):

$$\frac{dNe}{dh} = \frac{f^2}{40.28\pi} \frac{1}{r} \int_r^\infty \frac{a \frac{d\alpha(a)}{da}}{\sqrt{a^2 - r^2}} da \quad (7.19)$$

$$\frac{d\alpha(a)}{da} = \left(1 - \frac{A_0^2}{A^2}\right) \left[\frac{1}{\sqrt{\left|\vec{r}_G\right|^2 - a^2}} + \frac{1}{\sqrt{\left|\vec{r}_L\right|^2 - a^2}} \right] \quad (7.20)$$

$$r = Re + h \quad (7.21)$$

where Re is the radius of Earth, A_0 and A are amplitudes before and after one occultation event.

7.3 Error Analysis

Errors in GNSS-RO technique include signal to noise performance, clock error, multipath propagation, orbit determination error, retrieval error et al. (Kursinski et al. 1997; Kuo et al. 2004). Here we just divide these errors in two categories: one is measurement error and the other one is the error in data processing.

7.3.1 Measurement Errors

7.3.1.1 Carrier Phase Measuring Errors

Both GNSS satellites and LEO GNSS receivers clock instability can cause errors in Doppler shift observation in GNSS-RO measuring. Usually, GNSS satellites' clock error is smaller than the receivers, which can be extracted from international GNSS services' products. The scale of receivers' clock errors is larger than satellites'. The receivers' clock errors are eliminated by single differential or double differential. For high precision analyses, the instrument error also should be considered. The other important error is the random error that is caused by thermal noise of receivers on the LEO or on the ground and atmosphere refraction noise. Thermal noise associates with the strength of signal, background radiation, hardware condition of receivers and some other factors. It is independent from sample to sample. In early stage, AS (Anti-spoofing) is also included in random errors.

7.3.1.2 Orbit Errors

Nowadays, the precision of GNSS satellites orbit can be determined with up to 1 cm. And for LEO satellites, it can be less than 10 cm. The LEO orbits are just used for geometrical computation. The precision of the orbit determination is enough for GPS-RO's purpose. Usually, orbit errors will be ignored.

7.3.2 Data Processing Errors

Since Earth's neutral atmosphere and ionosphere is very complex, it is difficult to use an exactly mathematic formula to describe the relationship between parameters of neutral atmosphere and ionosphere and variations of GNSS signal, including the phase variation and amplitude variation. Several approximations are used in the GNSS-RO inversion algorithms. The first approximation is that orbits of LEO and GNSS are circular. Moreover, each of them moves in the same orbit plane. The second one is that electromagnetic wave travel along the straight line. Another assumption is spherical symmetry of Earth's neutral atmosphere and ionosphere. All of these approximations will introduce some errors for GNSS-RO inversion results. Errors caused by approximations are related to the solar activity, occultation events location, and so on. In essence, errors will increase with ionosphere distribution anomalies or highly dynamic changes, especially for the approximation of spherical symmetry.

7.4 Ionospheric Products

Ionospheric products can be obtained from GNSS Radio Occultation, including total electron content (TEC) and electronic density. Figure 7.5 is an example of ionosphere inversion results from GNSS-RO at (39.7°W 53.7°S), 00:00:33 Jan 1, 2011. The blue line is the electron density profile derived from one GNSS RO measurement. The data is provided by CDDAC (COSMIC data analysis and archive center, <http://cdaac-www.cosmic.ucar.edu>). The source and receiver pair of this occultation event is C001 satellite of COSMIC (Constellation Observing System for Meteorology Ionosphere & Climate) constellation and PRN23 satellite of GPS constellation. The green line is electron density profile from IRI (International Reference Ionosphere) model –2011 (<http://iri.gsfc.nasa.gov/>). The IRI is an international project sponsored by the COSPAR (Committee on Space Research) and the URSI (International Union of Radio Science). The major data sources of IRI include the worldwide network of ionosondes, the powerful incoherent scatter radars et al. Generally, the result of GNSS-RO ionosphere inversion agrees well with IRI-2011 model. However, differences still exist, especially for low ionosphere. These differences may be caused by imperfection of GNSS-RO ionosphere inversion

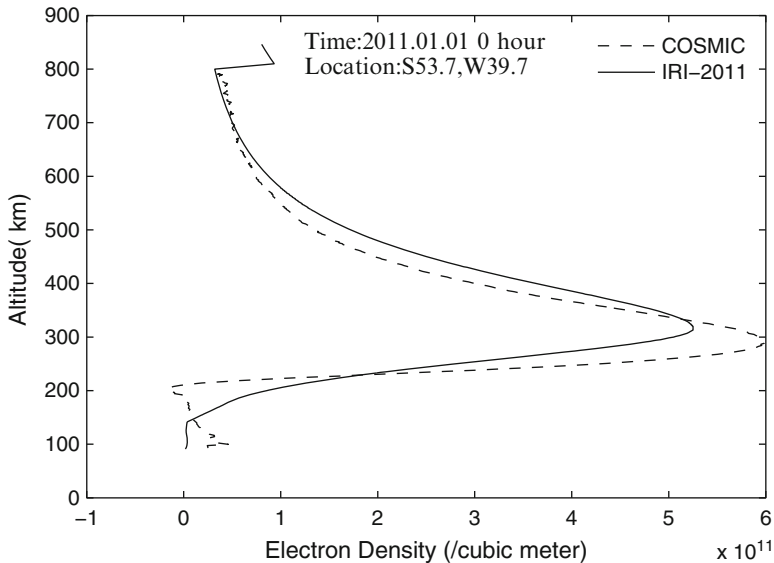


Fig. 7.5 Electron density from GNSS-RO at ($39.7W^\circ$ $53.7S^\circ$), 00:00:33 Jan 1, 2011

algorithm and errors of IRI input parameters system errors. Error sources of GNSS-RO ionosphere inversion and its effect are still a challenging topic, which needs to be further investigated and improved in the future.

7.5 GNSS-RO Ionospheric Applications

7.5.1 Establishing Ionospheric Models

GNSS-RO can provide global ionospheric products, such as total electron content (TEC) and electron density, which can monitor Earth's space environment. Together with TEC estimate from global ground GNSS observations, high resolution ionospheric model can be established, which can be used for ionospheric delay corrections and ionospheric climatology.

7.5.2 Ionospheric Tomography

The ground dual-frequency GNSS can provide total electron content or slant electron content, but lack of vertical ionospheric profile information. In order to obtain 3-D ionospheric information, ionospheric tomography was firstly proposed by (Austen et al. 1988). As shown in Fig. 7.6, the ionosphere is divided into

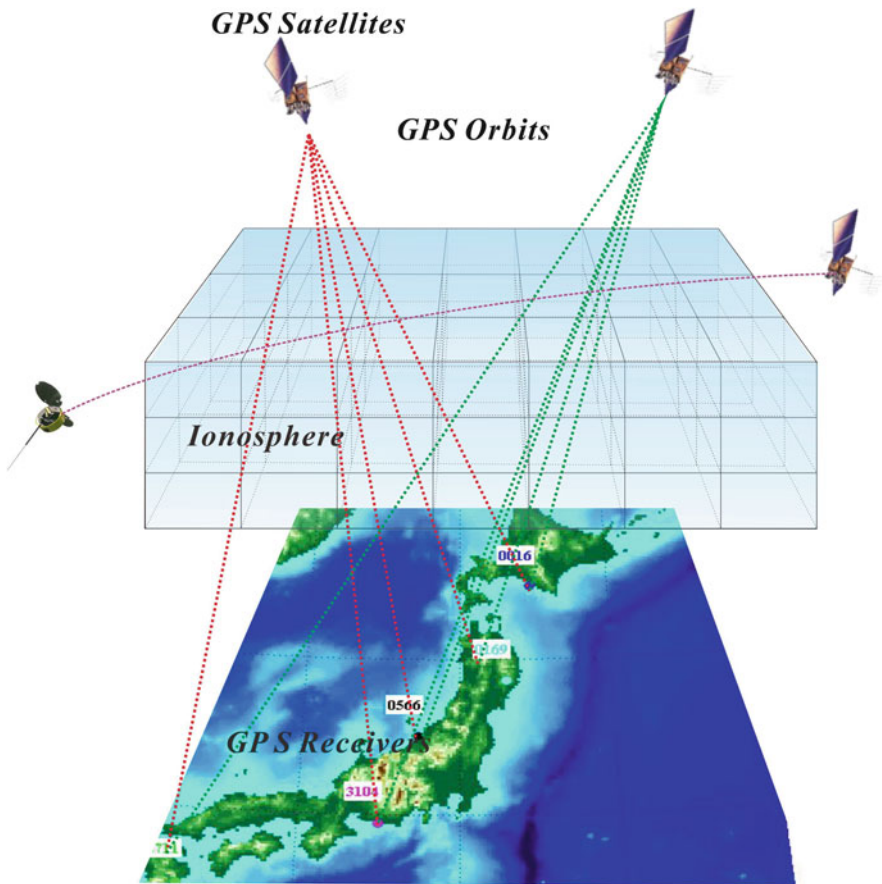


Fig. 7.6 Geometry of ionospheric tomography

small meshes, in which the electron density is a constant for a period. With TEC measurement, electron density of each mesh can be derived by inverting algorithm. However, some meshes may have no GNSS signals to cross, so there are still limitation for ground based GNSS ionospheric tomography (Jin et al. 2007b). While the space-borne GNSS RO can provide 3-D ionospheric profile information, together ground GNSS observations, 3-D ionospheric products can be obtained better, which can monitor the 3-D ionospheric structure and its variations.

7.5.3 Monitoring Ionospheric Anomalies

Earth's ionosphere is from about 60–1,000 km, which plays an important role in the globe electric circuit. Due to Earth's magnetic field and solar activities, the ionosphere is very complex. In addition, the ionospheric anomalies may be

related to the earthquake, tsunami, rocket launching and some other events (Calais and Minster 1995; Afraimovich and Kiryushkin 2002; Liu et al. 2006, 2011; Wan et al. 2005; Ding et al. 2008). The GNSS-RO provides 3-D ionospheric profile information, which better monitor ionospheric anomalies. Although there are dense continuous GNSS operational networks, such as in USA, Japan and Europe, but ground GNSS stations are still not enough to monitor global ionospheric variations, e.g., in the oceans and polar region, while GNSS-RO can provide long-term and global coverage observations. Therefore, GNSS-RO has wide advantages to monitor ionospheric anomalies, such as traveling ionospheric disturbances related to AGW (acoustic gravity wave), equatorial anomalies and so on.

7.5.4 Ionospheric Scintillation

Ionospheric scintillation is caused by small scale irregularities in the ionosphere, which will result in a rapid fluctuation of the radio signals when they go through the irregularities areas. The phase front of the signal will change because of the small-scale fluctuations in refractive index and subsequent scattering. Scintillation index can be derived using GNSS-RO amplitude observation (Pavelyev et al. 2007). Using GNSS-RO data to construct an ionospheric scintillation model, it will have wide applications.

References

- Afraimovich EL, Kiryushkin VV (2002) Space-multichannel reception for ionosphere monitoring during launches. *Quantum Electron Radio Phys* 11:46–53
- Austen JR, Franke SG, Liu CH (1988) Ionospheric imaging using computerized tomography. *Radio Sci* 23:299–307
- Calais E, Minster JB (1995) GPS detection of ionospheric perturbations following the January 17, 1994, Northridge Earthquake. *Geophys Res Lett* 22(9):1045–1048
- Datta-Barua S, Walter T, Blanch J, Enge P (2008) Bounding higher-order ionosphere errors for the dual-frequency GPS user. *Radio Sci* 43:RS5010. doi:[10.1029/2007RS003772](https://doi.org/10.1029/2007RS003772)
- Ding F, Wan W, Liu L et al (2008) A statistical study of large scale traveling ionospheric disturbances observed by GPS TEC during major magnetic storms over the years 2003–2005. *J Geophys Res* 113:A00A01. doi:[10.1029/2008JA013037](https://doi.org/10.1029/2008JA013037)
- Fjeldbo GF, Eshleman VR, Kliore AJ (1971) The neutral atmosphere of Venus as studied with the Mariner V radio occultation experiments. *Astron J* 76:123–140
- Gorbunov ME, Gurvich AS, Kornblueh L (2000) Comparative analysis of radioholographic methods of processing radio occultation data. *Radio Sci* 35(4):1025–1034
- Hajj GA, Romans LJ (1998) Ionospheric electron density profiles obtained with the Global Positioning System: results from the GPS/MET experiment. *Radio Sci* 33(1):175–190
- Hocke K (1997) Inversion of GPS meteorology data. *Ann Geophys-Atmos Hydrospheres Space Sci* 15(4):443–450
- Hofmann-Wellenhof B, Lichtenegger H, Collins J (1992) GPS theory and practice. Springer, Wien/New York

- Jin SG, Park J, Cho J, Park P (2007a) Seasonal variability of GPS-derived Zenith Tropospheric Delay (1994–2006) and climate implications. *J Geophys Res* 112:D09110. doi:[10.1029/2006JD007772](https://doi.org/10.1029/2006JD007772)
- Jin SG, Cho J, Park J (2007b) Ionospheric slab thickness and its seasonal variations observed by GPS. *J Atmos Sol-Terr Phys* 69(15):1864–1870. doi:[10.1016/j.jastp.2007.07.008](https://doi.org/10.1016/j.jastp.2007.07.008)
- Kuo YH, Wee TK, Sokolovskiy S, Rocken C, Schreiner W, Hunt D, Anthes RA (2004) Inversion and error estimation of GPS radio occultation data. *J Meteorol Soc Jpn* 82(1B):507–531
- Kursinski ER, Hajj GA, Schofield JT, Linfield RP, Hardy KR (1997) Observing Earth's atmosphere with radio occultation measurements using the Global Positioning System. *J Geophys Res* 102(D19):23429–23465
- Li ZH, Huang JS (2005) GPS surveying and data processing. Wuhan University Press, Wuhan, p 278
- Liou YA, Pavelyev AG, Huang CY, Igarashi K, Hocke K (2002) Simultaneous observation of the vertical gradients of refractivity in the atmosphere and electron density in the lower ionosphere by radio occultation amplitude method. *Geophys Res Lett* 29(19):1937. doi:[10.1029/2002GL015155](https://doi.org/10.1029/2002GL015155)
- Liu J-Y, Tsai Y-B, Ma K-F, Chen Y-I, Tsai H-F, Lin C-H, Kamogawa M, Lee C-P (2006) Ionospheric GPS total electron content (TEC) disturbances triggered by the 26 December 2004 Indian Ocean tsunami. *J Geophys Res* 111(A5):A05303
- Liu JY, Chen CH, Lin CH, Tsai HF, Chen CH, Kamogawa M (2011) Ionospheric disturbances triggered by the 11 March 2011 M9.0 Tohoku Earthquake. *J Geophys Res* 116:A06319. doi:[10.1029/2011JA016761](https://doi.org/10.1029/2011JA016761)
- Melbourne WG, Davis ES, Duncan CB, Hajj GA, Hardy KR, Kursinski ER, Meehan TK, Young LE, Yunck TP (1994) The application of GPS to atmospheric limb sounding and global change monitoring. *JPL Publ.*, 94–18, Pasadena, 147 pp
- Pavelyev AG, Liou YA, Wickert J, Schmidt T, Pavelyev AA, Liu SF (2007) Effects of the ionosphere and solar activity on radio occultation signals: application to Challenging Minisatellite Payload satellite observations. *J Geophys Res* 112, A06326. doi:[10.1029/2006JA011625](https://doi.org/10.1029/2006JA011625)
- Syndergaard S (1998) Modeling the impact of the Earth's oblateness on the retrieval of temperature and pressure profiles from limb sounding. *J Atmos Solar-Terr Phys* 60(2):171–180
- Syndergaard S (2000) On the ionosphere calibration in GPS radio occultation measurements. *Radio Sci* 35(3):865–883
- Wan W, Liu L, Yuan H et al (2005) The GPS measured SITEC caused by the very intense solar flare on July 14, 2000. *Adv Space Res* 36:2465–2469

Part III

GNSS Reflectometry and Remote Sensing

Chapter 8

Theory of GNSS Reflectometry

8.1 Introduction

This Chapter compiles different theoretical aspects to understand the GNSS signals after their reflection off the Earth surface. The concept was envisaged in early 1990s ([Martín-Neira 1993](#)) as a way to densify the Earth observations in a low cost effective way.

The GNSS-reflectometry works as a bi-static radar: a system in which the transmitter and the receiver are separated by a significant distance, comparable to the expected distance to the target, as sketched in Fig. 8.1. This definition can be extended to a system in which a single receiver can simultaneously track a diversity of bi-statically scattered signals, from a diversity of different transmitting sources. Then we call it multi-static (see Fig. 8.2).

The electromagnetic field at the receiver site has contribution from several GNSS sources (transmitting satellites). As explained in Chap. 1, different GNSS transmitters can be identified and separated from the rest of transmitters being received simultaneously by the modulation applied to each GNSS. These contributions correspond to signals that have propagated directly from the source to the receiver, crossing the atmosphere; as well as signals that have propagated down to the Earth surface, scattered off its surface, and up to the receiver coordinates. We will call “rays” or “radio-links” these different branches of the signal indistinctly. In principle, these two sort of contributions can be separated using two different antennas, one pointing to the transmitters to gather direct rays, and the other to the surface, to collect Earth-surface scattered signals. If the receiver is at air-borne or at higher altitudes, the delay and Doppler information can also be used to separate both radio-links. For some applications it is desirable that both direct and reflected signals interfere with each other, being then gathered by a single antenna pointing towards the horizon, the Earth limb, or at certain slant orientation.

Fig. 8.1 Geometry of a GNSS reflection, and conventions used along this chapter

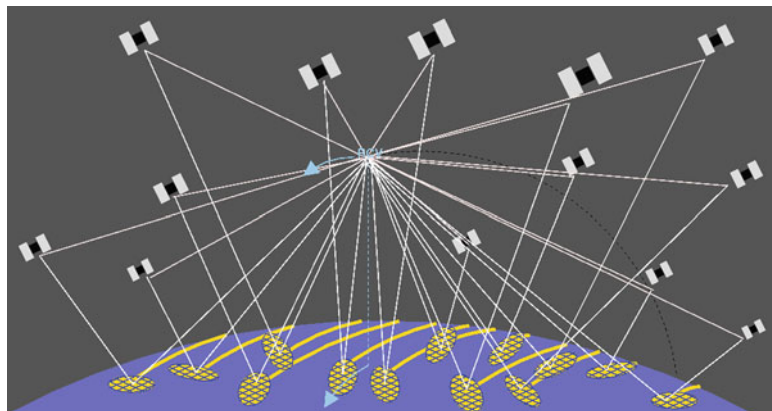
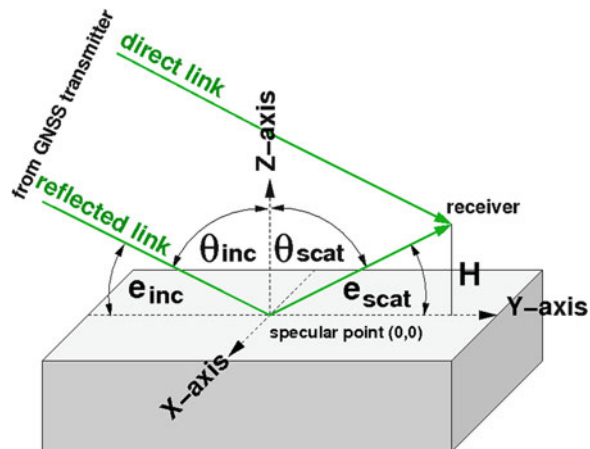


Fig. 8.2 Sketch of the GNSS-R as a multi-static system of observation. From each individual receiver, a large number of GNSS transmitted signals can be collected after their reflection off the Earth surface. This set of bi-static observations occur at different azimuth and elevation angles, providing a mosaic of “glistening zones”. As the receiver moves along its trajectory, the scanned surface takes an irregular, highly dense and wide swath comb-like pattern

Note that other contributions to the receiver electromagnetic field are also possible, such as those coming from atmospheric ducting (atmospheric multi-path), or from reflection off other objects surrounding the receiver or along the propagation path. These contributions will be neglected in this chapter.

8.2 Multi-static System: Geometry and Coverage

The GNSS-Reflectometry (GNSS-R) technique seeks to take the most of the large amount of GNSS signals reaching any spot on Earth simultaneously, in a wide range of incidence angles. The amount of reflected radio-links can be as large as the amount of direct radio-links. Currently, with more than 55 fully operational GNSS transmitters (GPS and GLONASS), it is easy to capture signals from 15 to 25 GNSS sources simultaneously using a receiver on the Earth surface (Fig. 8.3). This number increases with the altitude of the receiver. Moreover, this number will steadily increase with the deployment of new constellations: the European GALILEO (two prototypes in orbit); the Chinese COMPASS/Beidou2 (14 usable transmitters, 4 of them in Mid Earth Orbit, as of December 2012); and regional constellations (Chinese Beidou1, Indian IRNSS, and Japanese QZSS). All together will provide more than 130 GNSS transmitters globally distributed.

As a consequence of this large amount of simultaneously received signals, the spatial coverage obtained with a nadir-looking GNSS-R antenna corresponds to a gapped and irregularly sampled wide swath image of the surface beneath (Fig. 8.2). This image is compound by the mosaic of glistening zones produced by the reflected GNSS signals. In spite of the distance between glistening zones, the coverage potentially achievable from a space-based GNSS-R receiver gives a synoptic view of many hundreds of kilometers across-track. The time evolving pattern of the observed areas reminds an irregular comb.

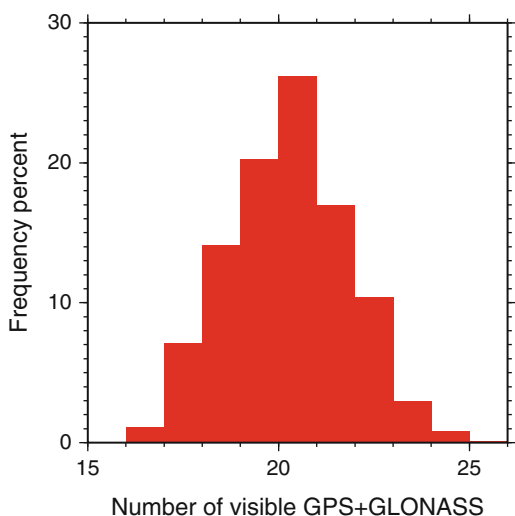


Fig. 8.3 Frequency percent of simultaneously visible GNSS transmitters from a receiver located at the surface-level, and mid latitudes (45°). Statistics performed with real orbits corresponding to the GPS and GLONASS constellations as in March 18 2012. These numbers would increase for reflected signals from a receiver at higher altitude

In order to analyze the potential time-space coverage of a hypothetical GNSS-R aboard a Low Earth Orbiter (LEO), it is useful to focus on the specular points of the reflections, rather than the entire reflection glistening zones. The specular point will here be understood as the point where the reflection would occur if the surface were perfectly smooth, with no diffuse scattering component. As the LEO receiver and the GNSS constellations move along their orbits, the ground-track locations of the specular points give an idea of the spatial coverage. Figure 8.4 illustrates the coordinates of the reflection specular points as they would be gathered from a LEO receiver at 800 km altitude, and with GNSS constellations as in March 18 2012 (32 GPS transmitters and 24 GLONASS receivers). As shown in these figures, the time required to irregularly cover the entire Globe at mesoscale resolution can be as short as 1 day, if all visible GNSS signals (constellation status as March 2012) could be used. As it will be explained in the subsequent Chapters, some applications constraint the range of elevation angles of observation from which sensitive data can be obtained. Figure 8.5 shows the 24-h coverage of GNSS-R data over three different regions (Central America, Europe, and Southeast Asia), at 10-s sampling rate. The orbits correspond to the same example as in Fig. 8.4-top.

Finally, the same example is used to illustrate the number of simultaneously reflected GNSS satellites as a function of the latitude-coordinate of their specular point on the Earth surface, and accumulated in 1 day of observations (Fig. 8.6).

8.3 Specular and Diffuse Scattering

As it will be explained in Sect. 8.6, the electromagnetic scattering is a complex process involving surface dielectric properties and topographic features as a whole system. Two limit-conditions are typically distinguished and contrasted: specular or *mirror-like* reflection vs. diffuse scattering. In most of the cases, the scattering process contains both types of contribution, that is, scenarios do not present either specular or diffuse scattering, but both of them in different proportions.

The specular reflection corresponds to scattering processes in which waves from a single direction are reflected into a single reflected direction. On the opposite side, in diffuse scattering the incoming waves are reflected in a broad range of directions. The specular-to-diffuse regime is determined by the roughness structures of the surface topography, rather than its dielectric properties.

Scattering with dominant specular component occurs in smooth surfaces, where the surface topography/roughness has not significant features of spatial scales similar to the electromagnetic wavelength. That is, the roughness spectrum has contributions at much higher and/or much lower wavenumbers than the electromagnetic wave. Specular reflection events are typically visualized in geometrical optics, in which the electromagnetic propagation is seen as a *ray*. A single ray bouncing off a smooth surface with a given incidence angle, reflects as another single ray, in the same plane defined by the incident ray and the vector normal to the surface at the incidence point, with opposite azimuth, and same incidence angle (panel *a* in Fig. 8.7). Using this simple model, the *specular point* is the 0-dimension point

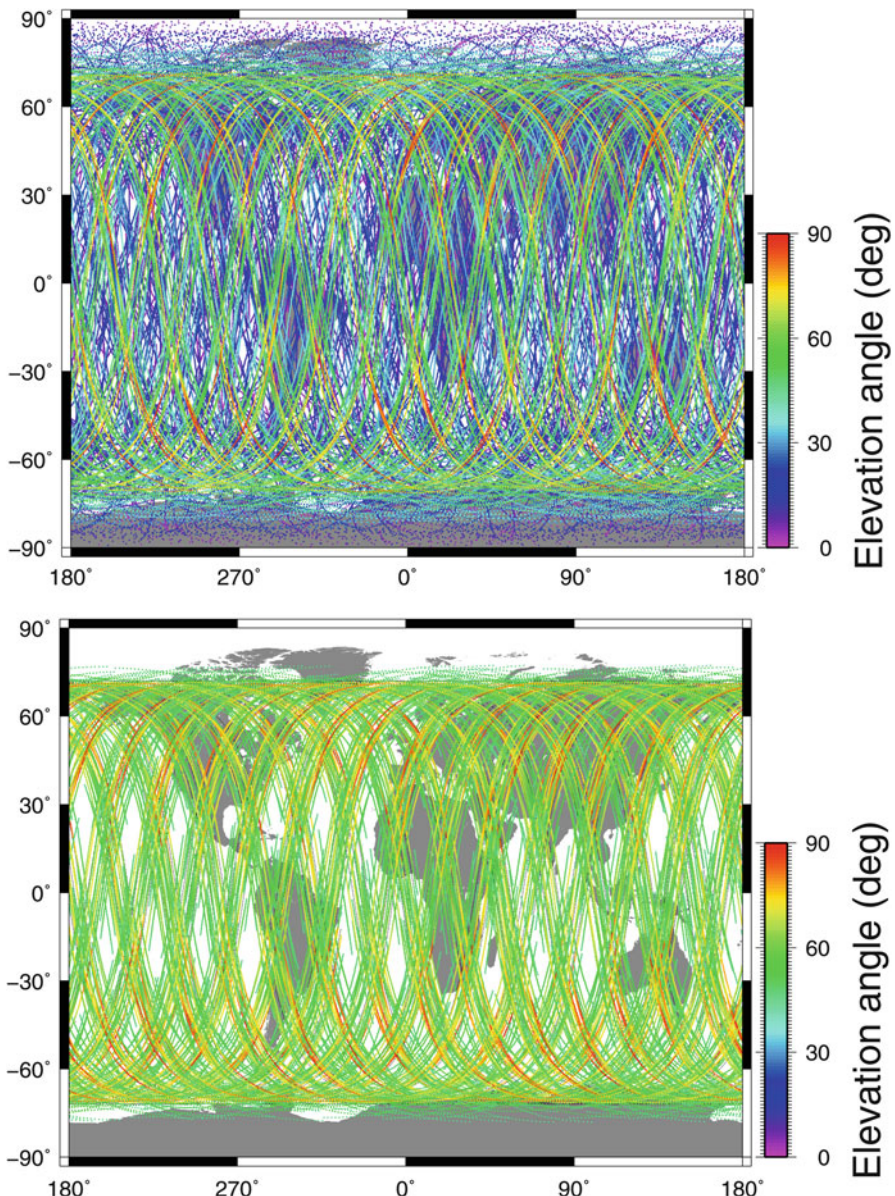


Fig. 8.4 Location of the GNSS reflections' specular points assuming a GNSS-R receiver aboard a LEO at 800 km altitude and 72° orbit inclination (one of the USA/Taiwan COSMIC satellite orbits has been used as example), and GNSS constellations as in March 18 2012 (32 GPS and 24 GLONASS). (top) 1-day coverage. (bottom) 3 days coverage using reflections occurring at elevation angles higher than 45°

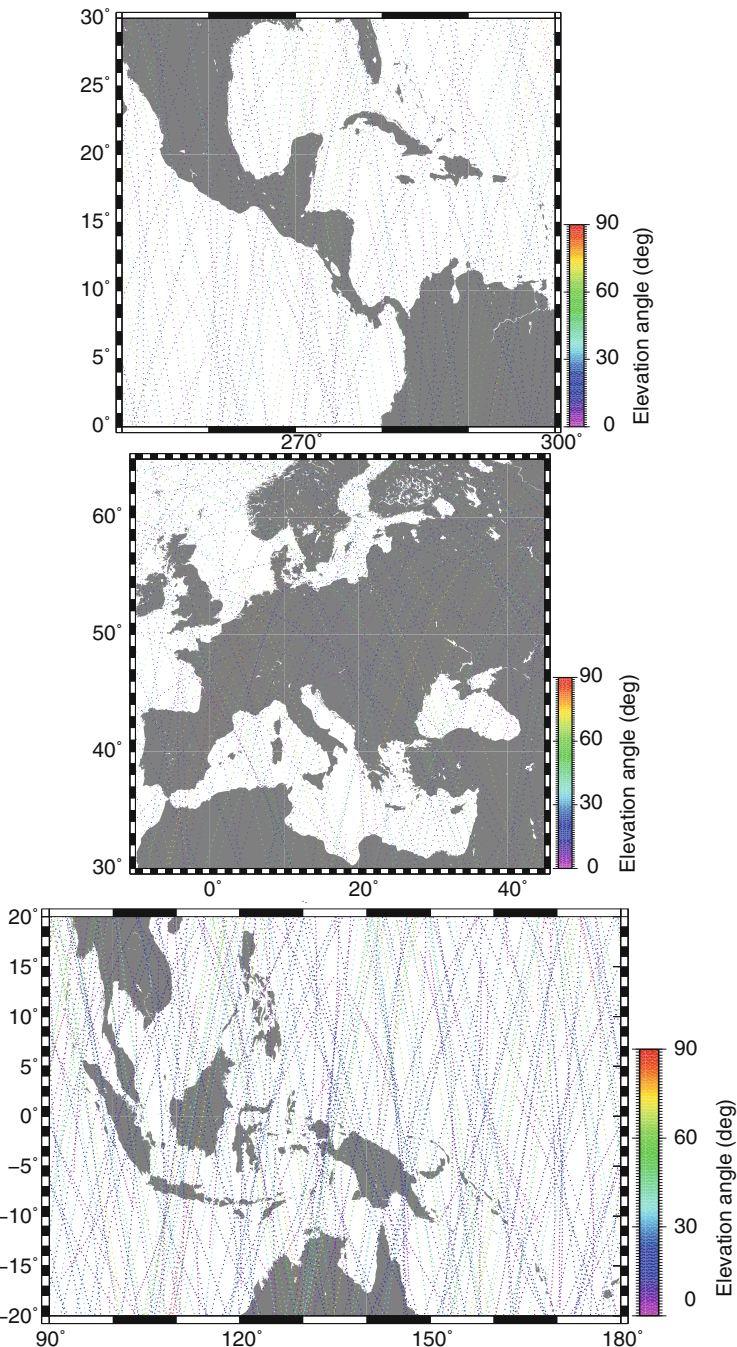


Fig. 8.5 Same as Fig. 8.4-top, but zooming into three different regions: Central America, Europe, and Southeast Asia. Time interval between subsequent along-track points: 10 s

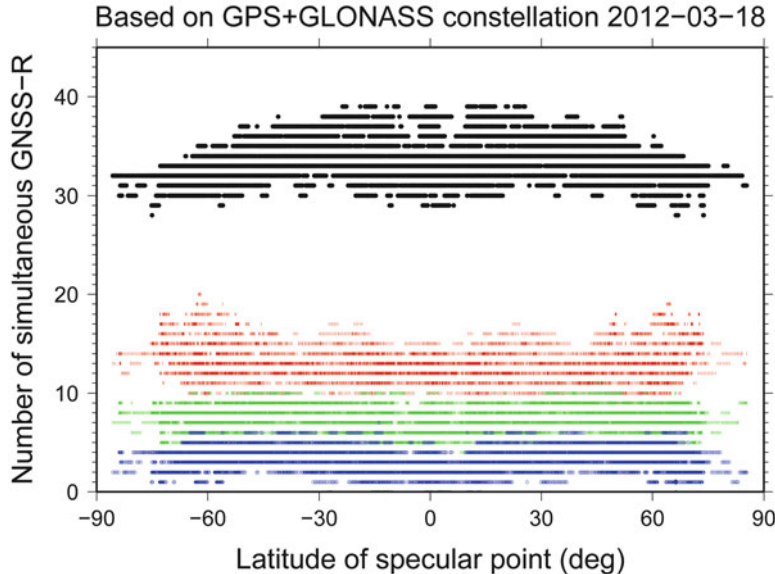


Fig. 8.6 Number of simultaneously reflected GNSS satellites as a function of the latitude-coordinate of their specular point on the Earth surface, and accumulated in 1 day of observations. The scenario is the same as in Fig. 8.4-top, using a 10-s time sampling. *Black* is for all visible GNSS transmitters (elevation cut-off = 0°); *red/green/blue* for elevation cut-off of $30^\circ/45^\circ/60^\circ$ respectively

where the two (incident and reflected) 1-dimension rays intersect the surface. The image generated in such reflection events is called specular image, and it appears with the same size than the source and at the same distance below the surface as the source is in the front (specular point being the reference).

A wave-optics picture of the specular reflection is also possible. Then, following Huygens-Fresnel principles, every point on the wave front, and in particular on the sea-surface, acts as a point-source of a secondary spherical wave. The scattered or reflected signal at any subsequent point between the surface and the observer is the sum of all these secondary spherical waves. If the incident signal is a planar wave of given incidence angle and azimuth, the reflected signal results in another planar wave, equal incidence and opposite azimuth; and most of the energy contribution comes from the point-sources of spherical waves located at a limited area on the surface (panel *b* in Fig. 8.7). This limited area surrounds the specular point. We could call it 2-dimensional specular zone, or Fresnel zone.

A particularity of the specular reflections is that the resulting scattered field has a well defined phase:

$$\exp\{\omega_0 t - \vec{k} \cdot \vec{r}\} \quad (8.1)$$

where ω_0 is the angular speed of the carrier, \vec{k} is the carrier's electromagnetic wavenumber, and \vec{r} position vector along the ray trajectory.

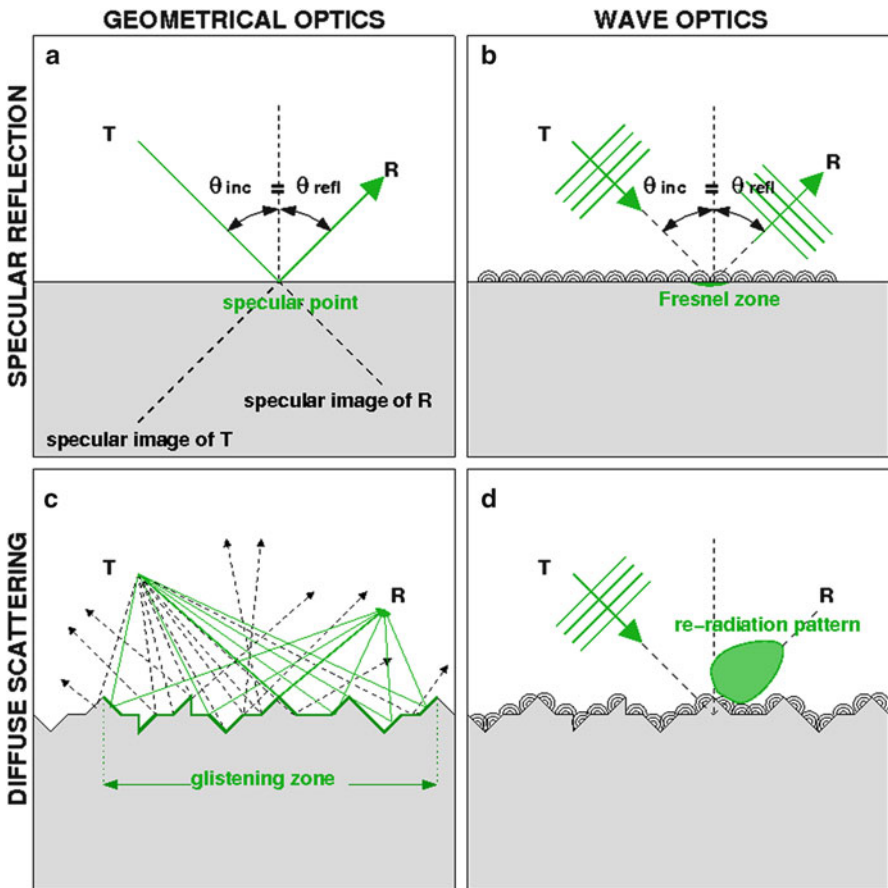


Fig. 8.7 Sketch of specular (panels **a** and **b**) and diffuse (panels **c** and **d**) scattering concepts, as pictured by the geometrical optics approach (panels **a** and **c**) and wave-optics or by Huygens-Fresnel principles (panels **b** and **d**)

The diffuse scattering can also be pictured as a Geometric Optics phenomena, or more accurately under wave-optics models. The former approach requires the concept of surface *facets*, surface patches of size and curvature of the order of or higher than a few electromagnetic wavelengths. Because of the roughness, different facets are oriented towards different directions. Incident rays reflect off the facets, each facet producing a mirror-like reflection, which forwards the reflected rays towards a direction determined by the facet's normal vector and the incident ray direction. In bi-static geometric conditions, the receiver only collects those rays reflected off facets with the appropriate tilt (panel **c** in Fig. 8.7). An appropriate tilt will occur at the surface coordinates x, y when the facet at x, y has its normal vector pointing towards the bisector of the angle formed by the incident ray at x, y and the vector connecting the surface point x, y and the receiver. The *glistening*

zone is then defined as the area from where well-oriented facets might exist above a probability threshold. The glistening zone corresponds to the deterioration of the specular image described above. Note that (1) points on the surface away from the nominal specular require higher slopes of the facet to forward the signal towards the receiver; and (2) the rougher the surface the higher the probability of largely tilted facets, meaning higher probability of well-oriented facets at coordinates far away from the nominal specular point. Therefore, the rougher the surface the largest the resulting glistening zone.

The wave-optics picture of the diffuse scattering results of the coherent sum of the spherical waves re-emitted by every point on the surface. We define then a *re-radiation pattern* or simply scattering beam, as the curve that relates each direction with the power forwarded towards it by the rough surface (panel *d* in Fig. 8.7).

Note that the field received after diffuse scattering can be seen as the coherent sum of many individual radio-link contributions, each introducing a phase-offset. Because in diffuse scattering the roughness scales are comparable or higher than the electromagnetic wavelength, the phase-offsets of each contribution, ϕ_i , can be any number within a cycle $[-\pi : +\pi]$:

$$\sum_i E_i \exp\{\omega_0 t - \vec{k}_i \cdot \vec{r}_i + \phi_i\} \quad (8.2)$$

As it will be shown in Sect. 8.7, moving receivers (air-borne and space-based) or dynamic surfaces (e.g. sea), make the individual contribution in Eq. 8.2 change, producing random-like time series of the total received phase (fading/speckle). Signal coherence thus requires strong specular components, or both platforms and surface static conditions.

As explained in Chap. 1, the detection of GNSS signals is done at the receiver by cross-correlating them against replicas or models. The result of this correlation will be called *waveform* hereafter. These replicas include modulations to identify the transmitters, working as nearly orthogonal codes: either the Binary Offset Carrier (BOC) modulation, or the Binary Phase Shift Keying (BPSK) in the Pseudo-Random Noise (PRN). Each code or part of a code is assigned to a different GNSS transmitter, so that a sufficiently long cross-correlation process yields power above the noise level if both signal and replica contain the same code modulation, or it yields just noise if they are not coincident. The shape of the matching cross-correlation response (waveform) is determined by the code itself. GPS C/A and P codes are series of phase-shifts, they can be seen as a train of rectangular chips. Its autocorrelation forms a triangle centered at the reception delay, and length $\pm \tau_{chip}$ (being τ_{chip} the length of the modulation chip). The new BOC modulations in GPS L5 and GALILEO are more complex, and they result in narrower waveforms, but with secondary peaks (see Chap. 1). Then, a purely specular reflection of GNSS signals produces a waveform shaped like the autocorrelation of its modulation code. That is, it produces the same waveform as the direct signal, but at a longer delay, corresponding to a reception at the specular image. For GPS C/A and P codes, it is the triangle function in amplitude, and squared triangle in power units. The delay

of the peak of such function corresponds to the time traveled by the specular ray path: time distance between the transmitter and the specular image (equivalent to the transmitter-specular point-receiver link).

When the reflection is not purely specular the waveform has contributions from the rest of the glistening zone. The scattered signal then spreads in both delay and frequency Doppler, as explained below.

8.4 Delay and Doppler

Under diffuse scattering the waveform has contributions from a broad area, the glistening zone. The radio-links between the transmitter, off-specular surface points, and the receiver, are longer than the path traveled through the specular point. The delay relative to the specular radio-link can be defined: $\Delta\tau(x, y) = \tau(x, y) - \tau_{spec}$, being $\tau(x, y)$ the traveling time along the radio-link that reaches the receiver after reflecting at surface coordinates (x, y) , and τ_{spec} after reflecting at the specular point ($x = y = 0$ in our convention). Then, the locus of surface points (x, y) such that all have the same relative delay, now expressed in units of length $\Delta\rho = \Delta\tau \cdot c$ describe an ellipse on the XY-plane, under flat surface approximation:

$$1 = \frac{y^2}{a^2} + \frac{x^2}{b^2} \quad (8.3)$$

where the scattering plane has been assumed along the Y-Z plane; the center of coordinates is the specular point; and

$$a = \frac{\sqrt{2H\Delta\rho}}{(\sin e)^{3/2}} \quad (8.4)$$

$$b = \frac{\sqrt{2H\Delta\rho}}{(\sin e)^{1/2}} \quad (8.5)$$

being e the elevation angle of observation (complementary to incidence angle θ), and H the receiver's altitude (Fig. 8.8).

Any contribution from areas away from the specular add power at the trailing edge of the waveform, that is, power accumulates at delays greater than the specular. The waveform thus distorts, its power scatters, the peak gets rounder and shifts towards positive delays. The distortion with respect to the code-autocorrelation function gives information about the roughness of the surface and its geophysical source (for example, wind blowing on the sea surface). Figure 8.9 shows the difference between waveforms obtained under specular and diffuse scattering conditions, because of the delay spreading.

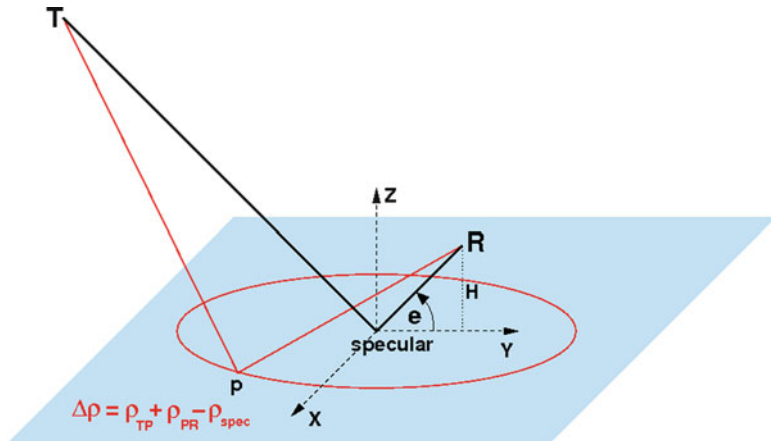


Fig. 8.8 Iso-delay ellipse in the flat-surface approximation

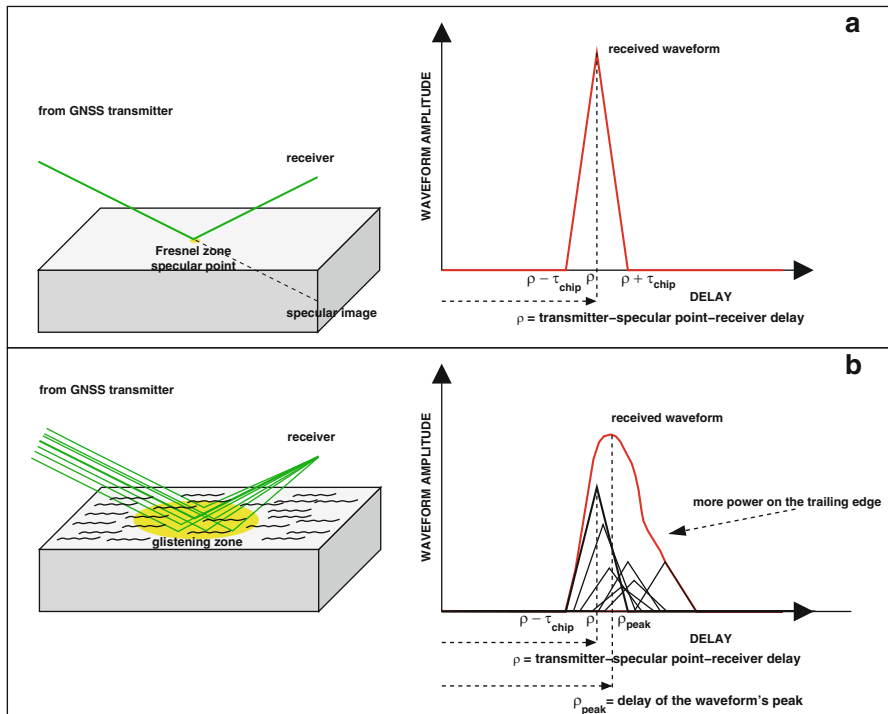


Fig. 8.9 (a) Waveform resulting of a specular reflection, corresponding to a C/A or P-like code (triangular autocorrelation function). (b) Conceptual sketch of a waveform resulting from a diffuse scattering process, corresponding to the same code than the sketch on the top panel

The signal contribution by reflections off areas away from the specular also have different Doppler frequency than the specular itself.

$$f_D(x, y) = \frac{1}{\lambda} (\vec{V}_T \cdot \hat{k}_i(x, y) - \vec{V}_R \cdot \hat{k}_s(x, y)) \quad (8.6)$$

being λ the GNSS carrier wavelength; \vec{V}_T and \vec{V}_R the transmitter and receiver velocities; and \hat{k}_i and \hat{k}_s the incident and scattering direction unitary vectors. If \vec{R} and \vec{T} are the receiver and transmitter positions, and \vec{P} is the position of a point on the reflecting surface, then: $\hat{k}_i = (\vec{P} - \vec{T})/|\vec{P} - \vec{T}|$; $\hat{k}_s = (\vec{R} - \vec{P})/|\vec{R} - \vec{P}|$. The iso-frequency lines on the surface, under the simplified assumption of flat surface ($z = 0$); receiver along the YZ plane; and only tangential velocity of the receiver considered ($V_{Rz} = 0$; $\vec{V}_T \cdot \hat{k}_i \sim Const.$), reduces to $x = \frac{-B \pm \sqrt{B^2 - 4AC}}{2A}$; where $A = V_{Rx}^2 - f_D^2 \lambda^2$; $B = -2 V_{Rx} V_{Ry} (R_y - y)$; and $C = V_{Ry}^2 (R_y - y)^2 - f_D^2 \lambda^2 (R_y - y)^2 - f_D^2 \lambda^2 H^2$.

Figure 8.10 shows the distribution of delay and Doppler parameters across the reflecting surface, considering also the effects of the curvature of the Earth.

The coherent integration process, characterized by the coherent integration time, τ_i , acts as a band-pass frequency filter given by the *sinc – exponential* function,

$$\frac{\sin(\pi \delta f \tau_i)}{\pi \delta f \tau_i} e^{-i\pi \delta f \tau_i} \quad (8.7)$$

where $\delta f = f - f_{central}$ is the difference between the frequency of the signal-component and the frequency of the replica used to correlate against the signal (*correlation central frequency*, $f_{central}$). This effectively blocks out frequencies beyond

$$f_{central} \pm \frac{1}{\tau_i} \quad (8.8)$$

Typically, the central frequency is chosen as the best estimate of the frequency at the specular point. In that case $\delta f = f - f_{spec}$, thus the integration process filters the contributions away from the central iso-Doppler line in Fig. 8.10. An example is given in the left panel of Fig. 8.11. Nevertheless, the correlation against the signal model can be done at other frequencies. Then, the correlation process might filter out the signal around the specular and *select* instead contributions from a given Doppler belt (see examples in Fig. 8.10 and right panel in Fig. 8.11).

This section has shown that, under diffuse scattering regime, the waveform maps the power reflected from areas delayed with respect to the specular point. These areas correspond to elliptical rings. Moreover, tuning the frequency of the replica in the code-correlation process, it is possible to select a given Doppler belt on the surface: the scattering contributions from the selected Doppler-belt region will be

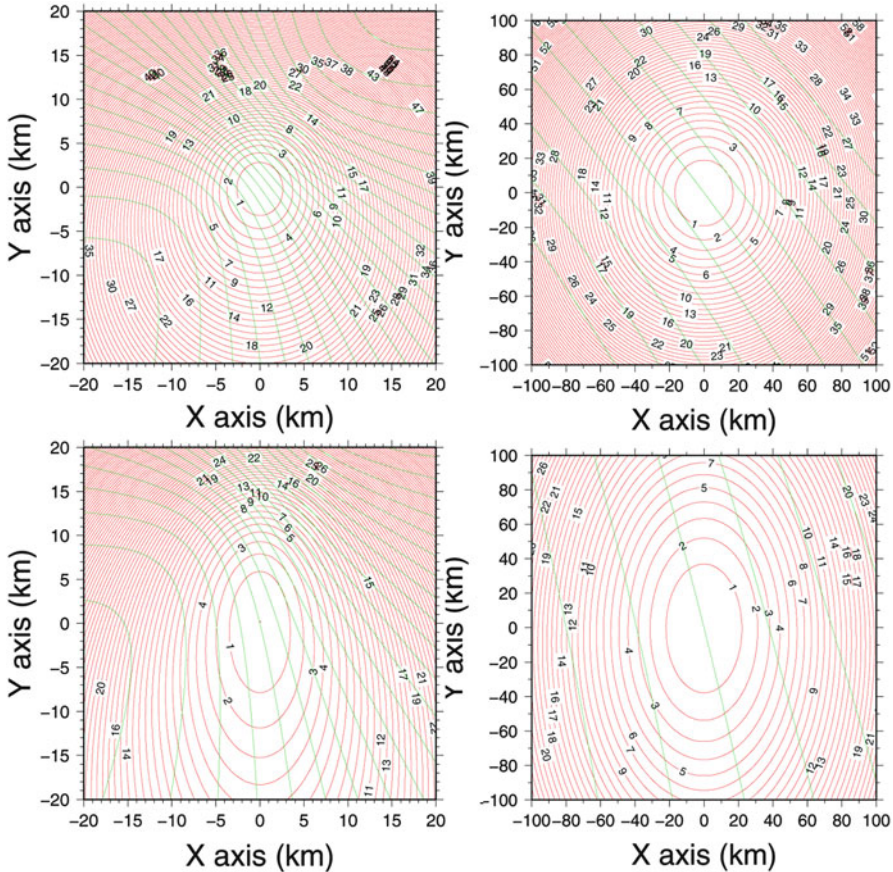


Fig. 8.10 Delay and Doppler frequency properties at each point on the reflecting surface, here given with respect to the specular point (coordinates: 0,0), under the form of iso-value contour lines (locii: ellipsoidal for iso-delay lines, parabolic-like for iso-frequency lines). The scattering plane is the Y-Z plane, the receiver laying in the positive side of the Y-axis, transmitter towards negative Y. Iso-delay contours given at 1 C/A code chip intervals (0.978 μ s delay, or 293.26 m range). Earth curvature has been taken into account. (left) Aircraft scenario at 10 km altitude, elevation angle of observation at 60° (top) and 30° (bottom). The receiver velocity is 250 m/s pointing towards 45° counter-clockwise from X-axis. Iso-frequency lines given at 100 Hz intervals. (right) LEO scenario at 500 km altitude, elevation angle of observation at 60° (top) and 30° (bottom). The receiver velocity is 7 km/s pointing towards 45° counter-clockwise from X-axis. Iso-frequency lines given at 1 kHz intervals

captured in the waveform, filtering out the contributions from other areas. That is, the technique permits to map the Doppler-frequency space (Fig. 8.12). Table 8.1 compiles the size of the Fresnel zone (specular reflection); of the first GPS C/A chip iso-delay; and of the first Doppler belt under different geometric conditions.

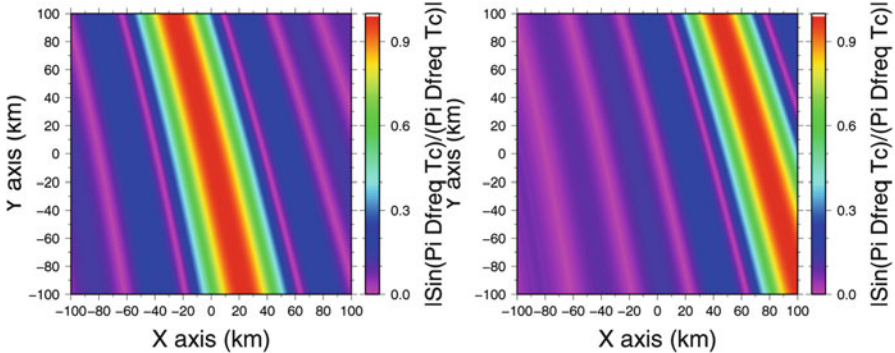


Fig. 8.11 $Sinc$ function in Eq. 8.7 corresponding to a coherent integration time of $\tau_i = 0.001$ s, for the LEO scenario in the bottom-right panel of Fig. 8.10. (left) Correlation frequency set to the frequency of the specular point $f_{central} = f_{spec}$. (right) Correlation frequency centered with an offset of 2 kHz with respect to the specular one, $f_{central} = f_{spec} + 2$ kHz

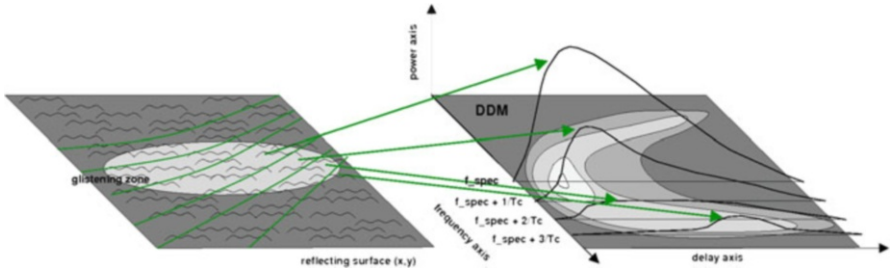


Fig. 8.12 Sketch of informational content of the delay-Doppler waveforms. Correlations performed at different $f_{central}$ frequency capture the reflected power from different Doppler belts on the surface (left). These produce different delay waveforms (right), with lower power levels and further delayed peaks as the frequency differs from the specular one. The grey shaded areas on the basis of the right panel correspond to the contour plot of the complete set of delay-Doppler waveforms, also called delay-Doppler map, DDM

8.5 Reflectivity Levels and Polarization Issues

The detailed formulation of the polarimetric behavior of the GNSS reflected signals is embedded in the theories listed under Sect. 8.6. However, the details of these theories are not required to understand some general polarization aspects of the reflectometry GNSS:

The GNSS signals are transmitted at right-hand circular polarization (RCHP). The dielectric properties of the reflecting surface, together with the geometry (incidence angle) determine which amount of RCHP signal is reflected as RCHP, and which one is reflected as left-hand circular (LHCP) in specular-like contributions. It follows the Fresnel reflectivity relationship:

Table 8.1 Approximate sizes of: Fresnel zone; first C/A chip ellipse along the scattering direction (major semi-axis); and first Doppler belt along the velocity direction (widest of the two contributing Doppler belts in the central waveform: $[f_{spec}: f_{spec} \pm 1/\tau_i]$). All given in km. Dimensions beyond reasonable visible extension are marked with “_”

	H	e	Fresnel	C/A chip	Doppler belt	
					V (m/s)	τ_i (s)
LEO	500	90°	0.4	17	7,000	0.001
		60°	0.5	21		20
		30°	1.2	48		130
	1,000	90°	0.6	24	7,000	0.001
		60°	0.8	30		40
		30°	1.7	68		250
AIRCRAFT	1	90°	0.019	0.7	100	0.001
						0.010
		60°	0.024	1	100	0.001
						0.010
	5	90°	0.055	2	100	0.001
						0.010
		30°	0.04	2	150	0.001
						0.010
	10	90°	0.05	2	150	0.001
						0.010
		60°	0.12	5	150	0.001
						0.010
	10	90°	0.06	2	250	0.001
						0.010
		60°	0.08	3	250	0.001
						0.010
		30°	0.17	7	250	0.001
						0.010
						11

$$E_p^{scat} = R_{pq} E_q^{inc} \quad (8.9)$$

where here R_{pq} is the Fresnel coefficient for incident q-polarized signals to p-polarized scattered electromagnetic fields. It depends on geometric parameters and the surface relative dielectric constant ϵ . The expressions of R for linearly polarized signals can be easily found in the literature (e.g. Ulaby et al. 1982; Ishimaru 1978). The change of polarization base can be applied and thus express R for incident and scattered circular polarized waves:

$$R_{RL} = \frac{1}{2}(R_{\parallel} - R_{\perp}) \quad (8.10)$$

$$R_{RR} = \frac{1}{2}(R_{\parallel} + R_{\perp}) \quad (8.11)$$

The dielectric constant varies between different types of reflecting surfaces. Scientific and engineering literature compiles the values measured at the L-band of the spectra for some types of interfaces. For example, Ulaby et al. (1982) gives the relative dielectric constant of the saline water as:

$$\epsilon = \epsilon_r + i\epsilon_i \quad (8.12)$$

$$\epsilon_r = \epsilon_\infty^{sw} + \frac{(\epsilon_0^{sw} - \epsilon_\infty^{sw})}{1 + (2\pi f \tau^{sw})^2} \quad (8.13)$$

$$\epsilon_i = \frac{2\pi f \tau^{sw} (\epsilon_0^{sw} - \epsilon_\infty^{sw})}{1 + (2\pi f \tau^{sw})^2} + \frac{S_i e^{-\phi}}{2\pi \epsilon_0 f} \quad (8.14)$$

where f is the frequency, $\epsilon_\infty^{sw} = 4.9$, and:

$$\begin{aligned} \phi &= (25 - T)(2.033^{-2} + 1.266^{-4}(25 - T) + 2.464^{-6}(25 - T)^2 \\ &\quad - S(1.849^{-5} - 2.551^{-7}(25 - T) + 2.551^{-8}(25 - T)^2)) \end{aligned} \quad (8.15)$$

$$S_i = S(0.18252 - 1.4619^{-3}S + 2.093^{-5}S^2 - 1.282^{-7}S^3) \quad (8.16)$$

where T is the temperature of the water in degrees Celsius and S the salinity in parts per thousand. And,

$$\epsilon_0^{sw} = (87.174 - 1.949^{-1}T - 1.279^{-2}T^2 + 2.491^{-4}T^3)A \quad (8.17)$$

$$A = 1 + 1.613^{-5}TS - 3.656^{-3}S + 3.21^{-5}S^2 - 4.232^{-7}S^3 \quad (8.18)$$

$$\tau^{sw} = \frac{\tau_0^{sw}}{2\pi}B \quad (8.19)$$

$$B = 1 + 2.282^{-5}TS - 7.638^{-4}S - 7.760^{-6}S^2 + 1.105^{-8}S^3 \quad (8.20)$$

$$\tau_0^{sw} = 1.1109^{-10} - 3.824^{-12}T + 6.938^{-14}T^2 - 5.096^{-16}T^3 \quad (8.21)$$

Recent studies, in support to the L-band radiometric missions (SMOS, Aquarius), have refined this model. See for example Blanch and Aguasca (2004).

Typical values for soil permittivity at L-band can be found in (e.g. Ulaby et al. 1986), and listed in Table 8.2.

Figure 8.13 compiles the reflectivity of several Earth surface types for co-polar and cross-polar circular polarized signals, at GNSS frequency bands. It is clear that at nadir and small incidence angles, the reflection process is essentially cross-polar, meaning that most of the incident, RHCP, signals swap to LHCP after reflection. At

Table 8.2 Permittivity of some soil surfaces as calculated for frequency = 1.5 GHz, using the semi-empirical model in Ulaby et al. (1986, E.111, p. 2103), setting the bulk soil density to 0.5 (consistent with Krotikov 1962)

Soil composition			Volumetric moisture (V_{wet} / V_{total})	Real part of the dielectric constant
Sand (%)	Silt (%)	Clay (%)		
51.1	35.0	13.5	0.0	1.55
			0.1	4.67
			0.2	9.22
			0.3	14.95
			0.4	21.74
			0.5	29.49
42.0	49.5	8.5	0.0	1.55
			0.1	4.66
			0.2	9.20
			0.3	14.92
			0.4	21.70
			0.5	29.45
30.6	55.9	13.5	0.0	1.55
			0.1	4.47
			0.2	8.85
			0.3	14.44
			0.4	21.13
			0.5	28.84
17.2	63.8	19.0	0.0	1.55
			0.1	4.27
			0.2	8.47
			0.3	13.91
			0.4	20.50
			0.5	28.16
5.0	47.6	47.4	0.0	1.55
			0.1	3.80
			0.2	7.56
			0.3	12.63
			0.4	18.95
			0.5	26.46

grazing angles of elevation (large incidence), the reflection is essentially co-polar: RCHP signals are reflected as RHCP. The transition between the co-polar and cross-polar regime is characterized by the Brewster angle, in which only horizontally polarized signal is scattered, and thus the RHCP and LHCP must have the same power (otherwise yielding elliptically polarized fields). The polarimetric features of the scattering around the Brewster angle are sensitive to the dielectric properties of the surface, especially for soil moisture (Brewster angle in the soil example shown in Fig. 8.13 presents variations between 58° and 80° incidence, for soil dry to 0.5 volumetric moisture). Sea water is in general more reflective than soil, but less sensitive to dielectric variations (given by salinity and Temperature), than soil moisture changes.

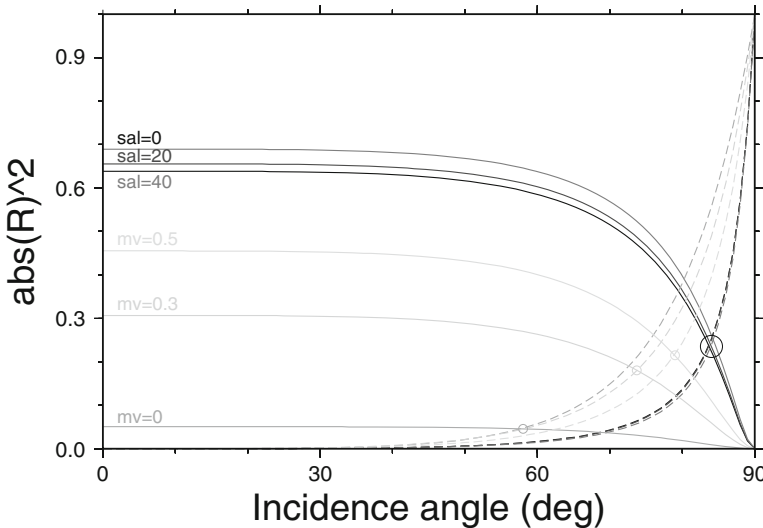


Fig. 8.13 Cross-polar (solid lines) and co-polar (dashed lines) Fresnel coefficients in circular base of polarization, for different surface types: darker hues of grey for sea water (darker to lighter for 0, 20, and 40 parts per thousand salinity respectively, and 25 °C temperature). Lighter hues of grey for soil (5 % sand, 48 % silt, 47 % clay) containing 0, 0.3 and 0.5 volumetric moisture (darker to lighter respectively). Brewster angles marked with circles

8.6 Scattering Theories

GNSS-R is based on the reflection of microwave signals off the Earth surface, which tends to be rough compared to the GNSS wavelengths. The study and modelling of the interaction of electromagnetic waves with random rough surfaces is a broad topic, vast enough to fill entire books (e.g. Bass and Fuks 1979; Beckmann and Spizzichino 1987), or complete chapters (e.g. Ishimaru 1978, Chap. 21), or (e.g. Ulaby et al. 1982, Chap. 12), or (e.g. Zhurbenko 2011, Chap. 10). This Section aims to (1) help understanding the limitations of a set of different, most used, approaches and approximations, providing bibliographic references for those interested in the details; and (2) focus on the bi-static radar equation for GNSS signals, under the Kirchoff Geometric Optics (KGO) limit. This Section is not meant to derive the formulae (references given where to check the details), yet it wants to remind about the starting point: the electromagnetic fields, \mathbf{E} and \mathbf{H} , connected by Maxwell's equations, in a 3-D domain V enclosed by a surface S may be determined by the Stratton-Chu integral equations (Stratton 1941)

$$\mathbf{E}(\mathbf{r}) = \mathbf{E}_i(\mathbf{r}) - \oint_S \{i\omega\mu_0(\mathbf{n} \times \mathbf{H})G + (\mathbf{n} \times \mathbf{E}) \times \nabla G + (\mathbf{n} \cdot \mathbf{E})\nabla G\}dS \quad (8.22)$$

$$\mathbf{H}(\mathbf{r}) = \mathbf{H}_i(\mathbf{r}) + \oint_S \{i\omega\epsilon_0(\mathbf{n} \times \mathbf{E})G - (\mathbf{n} \times \mathbf{H}) \times \nabla G - (\mathbf{n} \cdot \mathbf{H})\nabla G\}dS \quad (8.23)$$

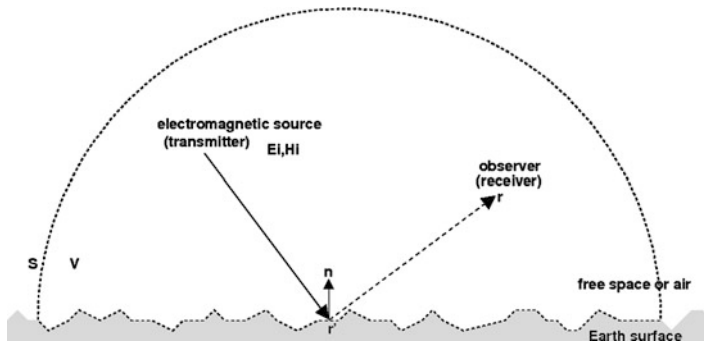


Fig. 8.14 Solving the scattered electromagnetic fields within an enclosed domain, V , limited by the surface S , which contains the sources (transmitter) and the observation point, \mathbf{r}

if the total surface fields are known. In the equation above the incident radiation is $(\mathbf{E}_i, \mathbf{H}_i)$, of angular frequency ω and wavenumber $k = 2\pi/\lambda$; ϵ_0 and μ_0 are the electric permittivity and magnetic permeability respectively of the medium (assuming free space); G is the Green's function of free space $G = \exp(i k R)/(4\pi R)$; being R the distance between the observation point \mathbf{r} and the surface scattering point \mathbf{r}' ; and \mathbf{n} is the unitary vector normal to the surface pointing inside the enclosing volume (see Fig. 8.14). Note that the surface fields need to be known, reason for which solving these equations for realistic scattering problems yields to insurmountable numerical complexity, and approximate models are necessary. This necessity has sprung the development of more than 30 approximate models, valid under different limits and conditions. An extensive review and classification is given in [Elfouhaily and Guérin \(2004\)](#). Next we focus on the Kirchhoff approximation, and later four other approaches are briefly introduced.

In most of the GNSS-R scenarios, the receiver is far away from the surface, in the so-called far-zone (mean distance from the observer to the scattering area, R_0 , is much larger than the scattering area, XY expressed in units of electromagnetic wavelength: $R_0 \gg XY/\lambda$). Accordingly, the following approximations apply: $G \sim \exp(i k R)/(4\pi R_0)$ and $\nabla G \sim -ikG\mathbf{n}_2$, \mathbf{n}_2 being the unitary vector in the scattered direction ([Valenzuela 1978](#)), and the scattered field reduces to (e.g. [Ulaby et al. 1982](#), Appendix 12J):

$$\mathbf{E}^s(\mathbf{r}) = K\hat{\mathbf{r}} \times \int_S \{(\hat{\mathbf{n}} \times \mathbf{E}(\mathbf{r}')) - \eta\hat{\mathbf{r}} \times (\hat{\mathbf{n}} \times \mathbf{H}(\mathbf{r}'))\} e^{i\mathbf{k}\cdot\mathbf{r}'} d^2r' \quad (8.24)$$

Note that Eq. 8.24 does not account for the polarization of the fields. This is simply introduced by replacing \mathbf{E}^s in the left-hand term by \mathbf{E}_{qp}^s (being q the incident polarization and p the received one); and replacing \mathbf{E} and \mathbf{H} in the right-hand term by \mathbf{E}_p and \mathbf{H}_p respectively.

However, the far-zone approximation still requires the computation of the tangential surface fields. The exact analytical expressions for such fields can be found in the form of integral equation (e.g. Zhurbenko 2011, Eqs. 2.2.11–2.2.16), but they cannot in general be solved analytically and further approximations have to be introduced.

8.6.1 Kirchhoff or Tangent Plane Approximation (KA)

In the Kirchhoff approach, the total fields (incident plus scattered) at any point on the surface are approximated by those that would be present on an infinitely extended tangent plane at the surface integration point. That is, each contribution to the scattering is considered to be locally specular and it depends only on the Fresnel reflection coefficients at the facet plane on each surface point. Note that this approximation is a local approximation: the supposed field at a point on the surface does not depend on the surface elsewhere. For this approximation to be valid, every point on the scattering surface should present a large radius of curvature (compared to the electromagnetic wavelength).

Following Ulaby et al. (1982), the terms $\hat{\mathbf{n}} \times \mathbf{E}$ and $\hat{\mathbf{n}} \times \mathbf{H}$ in Eq. 8.24 are functions of the Fresnel reflection coefficients and they both have a common factor $e^{-ik\hat{\mathbf{k}}_i \cdot \hat{\mathbf{r}}}$. Reason for which it first reduces to

$$\mathbf{E}^s(\mathbf{r}) = K \int_S \{\hat{\mathbf{q}} \cdot [\hat{\mathbf{k}}_s \times (\hat{\mathbf{n}} \times \mathbf{E}(\mathbf{r}')) + \eta(\hat{\mathbf{n}} \times \mathbf{H}(\mathbf{r}'))]\} e^{i(\mathbf{k}_s - \mathbf{k}_i) \cdot \mathbf{r}'} d^2 \mathbf{r}' \quad (8.25)$$

Still, no analytic solution has been obtained from Eq. 8.25 without additional simplifying assumptions, such as Stationary-Phase or Physical Optics.

8.6.1.1 KA in Stationary-Phase Approximation (Kirchhoff Geometrical Optics, KGO)

The geometrical optics limit of the Kirchhoff approximation is one of the most used approaches implemented in GNSS-R modelling work. It assumes that the phase factor in Eq. 8.25 is stationary, that is, it has null derivative with respect to displacements along the integration area. Note that physically this corresponds to those areas in the surface from where the received phase is nearly constant. It also corresponds to those areas in where the surface is locally oriented such that its local normal corresponds to the bisector angle between the incidence direction $-\hat{\mathbf{k}}_i$ and the direction pointing from that particular surface point towards the receiver $\hat{\mathbf{k}}_s$. This can be shown by taking the partial derivative of the phase term in Eq. 8.25, being the phase: $Q = (\mathbf{k}_s - \mathbf{k}_i) \cdot \mathbf{r}' \equiv \mathbf{q} \cdot \mathbf{r}' = q_x x' + q_y y' + q_z z'$

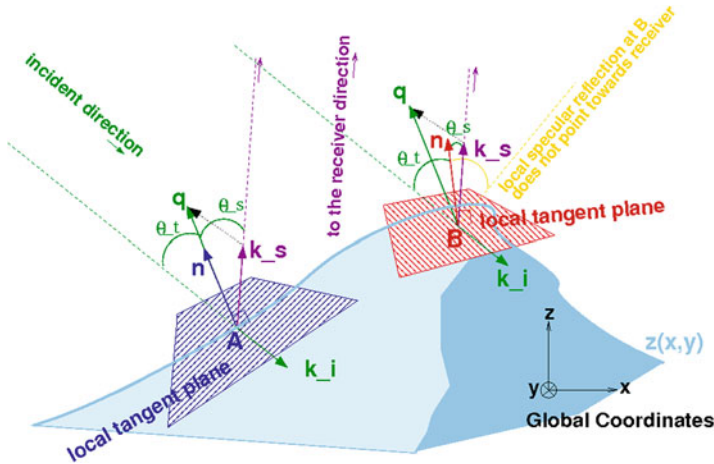


Fig. 8.15 Stationary phase conditions (Eqs. 8.28 and 8.29) apply at point A ($\mathbf{q} \parallel \hat{\mathbf{n}}_A$), but they do not apply at point B ($\mathbf{q} \nparallel \hat{\mathbf{n}}_B$) (Figure modified from Cardellach (2002))

$$\frac{\partial Q}{\partial x'} = q_x + q_z \frac{\partial z'}{\partial x'} = 0 \quad (8.26)$$

$$\frac{\partial Q}{\partial y'} = q_y + q_z \frac{\partial z'}{\partial y'} = 0 \quad (8.27)$$

which leads to the relationships

$$\frac{\partial z'}{\partial x'} = \frac{-q_x}{q_z} \quad (8.28)$$

$$\frac{\partial z'}{\partial y'} = \frac{-q_y}{q_z} \quad (8.29)$$

The above conditions only hold when the local incident and the scattered angles are the same: $\mathbf{q} \parallel \mathbf{n}$, local specular reflection, as illustrated in Fig. 8.15.

Under the stationary phase limit, it can be shown that (Ulaby et al. 1982, p. 930 and Appendix 12A) the received fields are

$$E_{hh}^s = M[R_{\parallel}(\hat{\mathbf{h}}_s \cdot \hat{\mathbf{k}}_i)(\hat{\mathbf{h}} \cdot \hat{\mathbf{k}}_s) + R_{\perp}(\hat{\mathbf{v}}_s \cdot \hat{\mathbf{k}}_i)(\hat{\mathbf{v}} \cdot \hat{\mathbf{k}}_s)] \quad (8.30)$$

$$E_{vh}^s = M[R_{\parallel}(\hat{\mathbf{v}}_s \cdot \hat{\mathbf{k}}_i)(\hat{\mathbf{h}} \cdot \hat{\mathbf{k}}_s) - R_{\perp}(\hat{\mathbf{h}}_s \cdot \hat{\mathbf{k}}_i)(\hat{\mathbf{v}} \cdot \hat{\mathbf{k}}_s)] \quad (8.31)$$

$$E_{vv}^s = M[R_{\parallel}(\hat{\mathbf{v}}_s \cdot \hat{\mathbf{k}}_i)(\hat{\mathbf{v}} \cdot \hat{\mathbf{k}}_s) + R_{\perp}(\hat{\mathbf{h}}_s \cdot \hat{\mathbf{k}}_i)(\hat{\mathbf{h}} \cdot \hat{\mathbf{k}}_s)] \quad (8.32)$$

$$E_{hv}^s = M[R_{\parallel}(\hat{\mathbf{h}}_s \cdot \hat{\mathbf{k}}_i)(\hat{\mathbf{v}} \cdot \hat{\mathbf{k}}_s) - R_{\perp}(\hat{\mathbf{v}}_s \cdot \hat{\mathbf{k}}_i)(\hat{\mathbf{h}} \cdot \hat{\mathbf{k}}_s)] \quad (8.33)$$

where R_{\parallel} and R_{\perp} are the Fresnel coefficients; $\hat{\mathbf{v}}$ and $\hat{\mathbf{h}}$ are unit polarization vectors for the incident vertical and incident horizontal waves respectively; $\hat{\mathbf{v}}_s$ and $\hat{\mathbf{h}}_s$ the same for the reflected waves; and M is

$$M = \frac{-ik_s e^{-ik_s R_0}}{4\pi R_0} \frac{q|q_z|}{k_i q_z} \frac{1}{(\hat{\mathbf{k}}_i \cdot \hat{\mathbf{h}}_s)^2 + (\hat{\mathbf{k}}_i \cdot \hat{\mathbf{v}}_s)^2} I \quad (8.34)$$

$$= \frac{-ik_s e^{-ik_s R_0}}{4\pi R_0} \frac{q|q_z|}{k_i q_z} \frac{1}{(\hat{\mathbf{k}}_i \cdot \hat{\mathbf{h}}_s)^2 + (\hat{\mathbf{k}}_i \cdot \hat{\mathbf{v}}_s)^2} \int e^{i(\mathbf{k}_s - \mathbf{k}_i) \cdot \mathbf{r}'} d^2 \mathbf{r}' \quad (8.35)$$

Finally, Ulaby et al. (1982) also develop the set of dot-products

$$\hat{\mathbf{v}}_s \cdot \hat{\mathbf{k}}_i = \sin \theta \cos \theta_s \cos(\phi_s - \phi) + \cos \theta \sin \theta_s \quad (8.36)$$

$$\hat{\mathbf{v}} \cdot \hat{\mathbf{k}}_s = \cos \theta \sin \theta_s \cos(\phi_s - \phi) + \sin \theta \cos \theta_s \quad (8.37)$$

$$\hat{\mathbf{h}}_s \cdot \hat{\mathbf{k}}_i = -\sin \theta \sin(\phi_s - \phi) \quad (8.38)$$

$$\hat{\mathbf{h}} \cdot \hat{\mathbf{k}}_s = \sin \theta_s \sin(\phi_s - \phi) \quad (8.39)$$

where θ and θ_s are the incident and scattered angle, while ϕ and ϕ_s are the azimuthal incidence and scattered angles respectively.

Because GNSS signals are transmitted at circular polarizations, a change of polarization base is required. The fields in Eqs. 8.30–8.33 must be introduced in

$$E_{cross-pol}^s = \frac{1}{2} [(E_{vv}^s - E_{hh}^s) + i(E_{vh}^s + E_{hv}^s)] \quad (8.40)$$

$$E_{co-pol}^s = \frac{1}{2} [(E_{vv}^s + E_{hh}^s) + i(E_{vh}^s - E_{hv}^s)] \quad (8.41)$$

8.6.1.2 KA in Physical Optics Approximation (KPO)

Unlike the Geometrical Optics solution, the Physical Optics Approximation of Eq. 8.25 accounts for contributions of the scattered field over the entire rough surface, not only *well-oriented facets*. However, this analysis is limited to surfaces with small slopes. As given in Ulaby et al. (1982, Sect. 12–4.5), the scattered fields are

$$E_{pq}^s = \frac{-ik_s e^{-ik_s R_0}}{4\pi R_0} E_0 \int \bar{U}_{pq} e^{i(\mathbf{k}_s - \mathbf{k}_i) \cdot \mathbf{r}'} d^2 \mathbf{r}' \quad (8.42)$$

where \bar{U}_{pq} , for linear polarizations, are detailed in Ulaby et al. (1982, Appendix 12C). In order to transform into circular polarization basis, Eqs. 8.40 and 8.41 need to be applied.

8.6.1.3 Alternative Formulations of KA

An alternative formulation for the vector (polarimetric) response of electromagnetic scattering using the Kirchhoff tangent-plane approximation, here depending only on the surface topography and its local Fresnel reflection coefficients is developed in Treuhhaft et al. (2011, Eq. 16)

$$\mathbf{E}(\mathbf{r}) \cdot \hat{\mathbf{p}}_s = \mathbf{E}_0 \cdot \hat{\mathbf{p}}_s \frac{e^{ik|\mathbf{r}-\mathbf{r}_T|}}{|\mathbf{r}-\mathbf{r}_T|} + \frac{i}{4\pi} \int_S \frac{A_i(\mathbf{r}') e^{ik|\mathbf{r}-\mathbf{r}'|}}{|\mathbf{r}-\mathbf{r}'|} (\mathbf{R}\hat{\mathbf{p}}_{ref} \hat{\mathbf{p}}_s)(\mathbf{k}_i(\mathbf{r}') - \mathbf{k}_s(\mathbf{r}')) \cdot \hat{\mathbf{n}}(\mathbf{r}') d^2\mathbf{r}' \quad (8.43)$$

where $\hat{\mathbf{p}}$ are the polarimetric base vectors, \mathbf{E}_0 and A_i relate to the incident field as $\mathbf{E}_i(\mathbf{r}') = \mathbf{E}_0 e^{ik|\mathbf{r}'-\mathbf{r}_T|} / |\mathbf{r}'-\mathbf{r}_T| = A_i(\mathbf{r}') \hat{\mathbf{p}}_i$; \mathbf{r} , \mathbf{r}_T , and \mathbf{r}' are the receiver, transmitter and surface integration point positions respectively; $\mathbf{R}\hat{\mathbf{p}}_{ref}$ is the vector field at the surface due to local specular reflection by a facet (see Treuhhaft et al. 2011, Eq. 14); and subscripts s , and i refer to scattering (or received), and incidence respectively. Note that the first term in the right-hand side of the equation corresponds to the signal reaching the receiver directly from the transmitter (no scattering). This term should be removed when interested in the reflected component solely. This formulation can be useful to evaluate the polarimetric response of GNSS signals through realistic realizations of the surface (Montecarlo-like simulations). Note that in such numerical evaluation of the integrals, the surface sampling length must be shorter than the electromagnetic wavelength. Similarly, Clarizia et al. (2012) presents a facet-like approach to the KA, consistent with full KA, but less computationally expensive.

8.6.1.4 Validity Limits of Kirchhoff Approximations

The Kirchhoff Approximation (Eq. 8.25) can be applied when both the correlation length of the surface, l , and its average radius of curvature are greater than the electromagnetic wavelength. For the radius of curvature to be large enough, the surface vertical-scale roughness (standard deviation of the surface heights, σ) must be small compared to l^2/λ . Note that this latter condition limits the surface's vertical-scale roughness σ with respect to its horizontal-scale one, l , but it still permits large σ (provided that l is long enough).

Its Geometric Optics limit (Eqs. 8.30–8.33, or Eqs. 8.40 and 8.41) has validity when the standard deviation of the surface height is large compared to the electromagnetic wavelength, that is, the incident radiation has small wavelength compared to the surface structure (also called high-frequency limit).

Finally, the Physical Optics limit (Eq. 8.42) is also called low-frequency regime, and it requires both small vertical-scale roughness and small slopes statistics. Table 8.3 shows the validity of each limit of the Kirchhoff Approximation.

Note that in all the formulations above, the frequency term of the electromagnetic wave has been removed for simplicity. The factor $e^{i2\pi f t}$ should be added back in all of them, where f is the resulting carrier frequency after taking into account

Table 8.3 Validity ranges of the Kirchhoff approximation and its different regimes (From [Zhurbenko 2011](#))

Method	Equations	Validity limit
KA	8.25	$kl > 6$ and $l^2 > 2.7 \sigma\lambda$ and $R_0 \gg XY/\lambda$ (far-field)
KGO	8.30–8.33 (lin.pol.) 8.40 and 8.41 (circ.pol.)	$k\sigma > 2$ and $R_0 \gg XY/\lambda$
KPO	8.42 and Ulaby et al. (1982, Appendix 12C)	$k\sigma < 1$ and $\sigma_{slopes} < 0.25$ and $R_0 \gg XY/\lambda$

the Doppler effects. The Doppler effects due to the surface scattering geometry (projections of the different velocities along the propagation path) were described in Sect. 8.4 and Eq. 8.6.

8.6.2 Summary of Other Methods

As listed in [Elfouhaily and Guérin \(2004\)](#), more than 30 different approaches and methods have been reported to deal with electromagnetic scattering off rough surfaces. That reference performs an exhaustive review of several aspects of them all. This section will compile brief summaries of the most popular ones.

Small Perturbation Method (SPM): This method tries to find a solution to the partial differential boundary equation by expanding the field in a perturbation series of the slopes of the surface ([Rice 1951, 1963](#)). The SPM is a good model for small slopes statistics (both standard deviation of the sea surface height and correlation length below the electromagnetic wavelength), it is the most appropriate for Bragg scattering issues, and to assess polarimetric performances.

Two-Scale Composite Model (2SCM): This approach sums the contribution of the large scale roughness and the small scale effect to the scattered field. While the large scale contribution is modeled through the KGO, the small roughness contribution is the SPM solution averaged over the statistics of the tilt of the large scale sea surface characterization ([Bass and Fuks 1979; Valenzuela 1978](#)). Besides the non-coherent received power scattered from smooth and large slopes oriented in the appropriate direction (KGO), it is also possible to receive additional power from other non-specular mechanisms, such as diffraction and Bragg resonance. These mechanisms are produced in the sea surface roughness small scale and when the radius of curvature is smaller than the electromagnetic wavelength. Given that most of the Earth reflecting surfaces present a continuous roughness spectra, the main problem of the 2SCM is to define the limit between large and small scales in which to apply KGO and SPM respectively.

Integral Equation Method (IEM): This is a unifying theory suggested in late 1980s to bridge the gap between KA and SPM, and thus it covers all roughness scales (Fung and Pan 1986; Fung et al. 1992; Fung 1994). The integral equations of the electromagnetic fields are solved iteratively from the charges and electric currents on the sea surface. In the first iteration only the induced currents are used (Kirchhoff approximation). The second iteration in the small slope statistics leads to the SPM. The IEM is computationally expensive, but quite accurate, reason why it is specially useful to serve as reference to compare with the previous models.

Small Slope Approximation (SSA) This method was also suggested in mid 1980s to unify KA and SPM (Voronovich 1985, 1994a,b). The SSA is applicable irrespective of the wavelength of radiation, provided that the slopes of the roughness are small compared to the angles of incidence and scattering.

8.6.3 Received GNSS Scattered Fields

The GNSS scattered fields correspond to circular polarization, as in Eqs. 8.40 and 8.41, where the linear fields could be either Eqs. 8.30–8.33 (KGO); or Eqs. 8.42 and 8.43; or any other solution of the scattered fields in the rest of possible approximations (e.g. Sect. 8.6.2). However, the scattered fields as given by these formulations do not take into account the GNSS signal structure. The structure, given by a set of phase-shifts or jumps in the transmitted signals, will emerge after the correlation process taking place in the GNSS receiver. Therefore, the *received* fields are the result of cross-correlating the scattered fields s and the well-known replicas r of the code modulations c , for different delays τ and frequencies f . For simplicity we here assume that the modulation corresponds to a BKPS code (such as GPS' C/A, L2C, or P), trains of chips, each chip being τ_c long. The autocorrelation function is then the *triangle* function, $\Lambda(\delta\tau)$

$$\begin{aligned}\Lambda(\delta\tau) &= \frac{1}{\tau_i} \int_0^{\tau_i} c(t)c(t + \delta\tau)dt = \\ &= \begin{cases} 1 - \delta\tau/\tau_c, & |\delta\tau| \leq \tau_c \\ -\tau_c/\tau_i, & |\delta\tau| > \tau_c \end{cases} \quad (8.44)\end{aligned}$$

and τ_i is the integration time.

The GNSS receiver cross-correlates the scattered signal s (which was transmitted with modulation c) with a replica of the code r . Such replica is mounted on a carrier or intermediate frequency phasor: $r(t, f_c) = c(t)e^{i2\pi f_c t}$, where f_c is the central correlation frequency, or frequency at which the scattered signal is assumed to reach the receiver. This procedure is also called match-filter signal processing.

If the scattered fields were reflected off the Earth surface in a purely specular way, the scattered signal s would come from a small area around the specular point (Fresnel zone), where the Doppler frequency factor could be assumed constant. Therefore, s could reduce to $s = \tilde{E}_{pq}(\mathbf{r}_R; \mathbf{r}_{\text{spec}}) e^{i2\pi f_D(\mathbf{r}_{\text{spec}})t}$, being $f_D(\mathbf{r}_{\text{spec}})$ the Doppler frequency of the ray-path reflected at the specular point, and $\tilde{E}_{pq}(\mathbf{r}_R; \mathbf{r}_{\text{spec}})$ the field from the ray-path reflected at the specular point, reaching the receiver coordinates, as modelled in the previous sections around the specular point, but with the phase-shifts introduced by the GNSS modulation (we use \tilde{E} for fields with phase-shift modulations, and E for fields as modelled in the previous sections). Then, the result of the cross-correlation

$$Y(\tau, f_c) = \int_0^{\tau_i} s(t) r(t + \tau, f_c) dt \quad (8.45)$$

could be simplified

$$\begin{aligned} Y(\tau, f_c) &= \int_0^{\tau_i} \tilde{E}_{pq}(\mathbf{r}_R, t; \mathbf{r}_{\text{spec}}) e^{-i2\pi f_D(\mathbf{r}_{\text{spec}})t} c(t + \tau) e^{i2\pi f_c t} dt \\ &\sim \tau_i E_{pq}(\mathbf{r}_R; \mathbf{r}_{\text{spec}}) \Lambda(\tau) S(f_c - f_D) \end{aligned} \quad (8.46)$$

note that the field \tilde{E} has become E , and S is the *sinc-exponential* function introduced in Eq. 8.7.

$$S(\delta f) = \frac{1}{\tau_i} \int_0^{\tau_i} e^{-i2\pi \delta f t} dt = \frac{\sin(\pi \delta f \tau_i)}{\pi \delta f \tau_i} e^{-i\pi \delta f \tau_i} \quad (8.47)$$

If the correlation modelled frequency f_c were close enough to the real Doppler frequency of the signal, f_D , then $|S| \rightarrow 1$. If no instrumental noise is considered, then the waveform reduces to the triangle function centered at the signal receiving time, with maximum amplitude given by the scattered field $|E_{pq}(\mathbf{r}_R; \mathbf{r}_{\text{spec}})|$ and an overall phase driven by propagation, scattering phase shifts, and correlation process.

It is important to highlight that Eq. 8.46 assumes purely specular reflections only. For diffuse scattering, $E_{pq}(\mathbf{r}_R; \mathbf{r}_{\text{spec}})$ must be replaced by any of its integral forms. If we re-shape the integral forms given in the previous sections and add the frequency factor: $\tilde{E}_{pq}(\mathbf{r}_R) \equiv \int_S \tilde{E}_{pq}(\mathbf{r}_R; \mathbf{r}') e^{-i2\pi f_D(\mathbf{r}')t} d^2 \mathbf{r}'$, then:

$$\begin{aligned} Y(\tau, f_c) &= \int_0^{\tau_i} dt \int_S \tilde{E}_{pq}(\mathbf{r}_R; \mathbf{r}') e^{-i2\pi f_D(\mathbf{r}')t} d^2 \mathbf{r}' c(t + \tau) e^{i2\pi f_c t} \\ &\sim \tau_i \int_S E_{pq}(\mathbf{r}_R; \mathbf{r}') \Lambda(\tau(\mathbf{r}')) S(\delta f(\mathbf{r}')) d^2 \mathbf{r}' \end{aligned} \quad (8.48)$$

Note that both local delay $\tau(\mathbf{r}')$ and local frequency shift $\delta f = f_c - f_D(\mathbf{r}')$ are functions of the surface point under integration \mathbf{r}' , as explained in Sect. 8.4. $Y(\tau, f_c)$ corresponds to the complex waveform as coherently correlated during τ_i , and central

correlation frequency f_c . This approach to the GNSS-R modelling is appropriate to study any issue for which the complex nature of the field is relevant (for instance, coherence of the signals). However, it involves the implementation of realistic Earth surface topography realizations at high resolution grids (Δx and $\Delta y < \lambda$), for proper integration of $\int_S d^2\mathbf{r}'$. It is computationally expensive, and studies based on this approach need to implement large sets of surface realizations for each surface conditions for the conclusions to be statistically meaningful.

8.6.4 The Bi-static Radar Equation for GNSS Modulated Signals

In most of the GNSS-R observational scenarios the time during which the signals can be coherently integrated is relatively small because the carrier phase of individual reflection points sum together in unpredictable ways at the receiver, changing along the dynamic conditions, and thus introducing random phase behavior. As it will be explained in Sect. 8.7, this phase behavior is a limiting factor for the coherent integration time. Moreover, this random-like behavior provokes speckle: fluctuations in the total received power level due to constructive and destructive interferences between individual reflections. Speckle (also called fading) is a major source of noise. For these reasons, the integration strategy tends to chose a short coherent integration time (\leq than signal coherence time) and relatively long non-coherent averaging (to reduce the effects of the speckle noise). The phase information of the signal is lost during the non-coherent integration process, resulting in amplitude $\langle |Y| \rangle$ or power $\langle |Y|^2 \rangle$ waveforms.

Power waveforms are typically modelled using the radar equation, bi-static for the GNSS-R case. The main reference for GNSS-R bi-static radar equation was given in [Zavorotny and Voronovich \(2000\)](#), publication where it was comprehensively deduced from expressions similar to Eq. 8.48. That derivation considered Gaussian surface statistics and assumed KGO scattering. The formulation below follows [\(Cardellach 2002\)](#):

$$\begin{aligned} & \langle |Y_{pq}(\tau, f_c)|^2 \rangle \\ &= \frac{P_T}{(4\pi)^2} \frac{\lambda^2}{4\pi} \tau_i^2 \int_S \frac{G_T(\mathbf{r}') G_R(\mathbf{r}') \sigma_{pq}^0(\mathbf{r}') \Lambda^2(\tau - \tau(\mathbf{r}')) |S(f_c - f_D(\mathbf{r}'))|^2}{R^2(\mathbf{T}, \mathbf{r}') R^2(\mathbf{r}', \mathbf{R})} d^2\mathbf{r}' \end{aligned} \quad (8.49)$$

where

- P_T , G_T , and G_R are the transmitted power, transmitter's antenna gain, and receiver's antenna gain respectively;
- λ is the electromagnetic wavelength;

- τ_i the integration time; \mathbf{r}' any point on the surface where to integrate the functions; τ the delay at which the correlation function is being evaluated; and f_c the central correlation frequency;
- $R(\mathbf{a}, \mathbf{b})$ the distance between points \mathbf{a} and \mathbf{b} ;
- $\tau(\mathbf{r}')$ is the delay of the ray-path from the transmitter to the surface point \mathbf{r}' and from there to the receiver; and $f_D(\mathbf{r}')$ its Doppler frequency;
- σ^0 is the bi-static scattering coefficient, defined as the fraction of incident power that can be scattered into certain direction and polarization state $_{pq}$, normalized by the incident power density and area.
- Note that other sources of power attenuation or loss might also be introduced, such as atmospheric attenuation; cabling/instrumental loss; quantification (number of bit sampling) loss.... All these factors would simply multiply the right-hand side of Eq. 8.49

The bi-static scattering coefficient for KGO is (e.g. [Ulaby et al. 1982](#); [Zavorotny and Voronovich 2000](#); [Cardellach 2002](#))

$$\sigma_{pq}^0 = \pi k^2 |R_{pq}|^2 \frac{q^2}{q_z^4} PDF(Z_x, Z_y) \quad (8.50)$$

where k is the electromagnetic wavenumber; R_{pq} the scattering coefficients; and $PDF(Z_x, Z_y)$ is the 2-D Probability Density Function of the surface slopes Z (along the x-direction Z_x , and y-direction Z_y). In order to extend the bi-static radar equation to other electromagnetic scattering models, σ^0 must be replaced by its corresponding expression.

This bi-static radar equation can also be seen as the 2D-convolution between the Woodward Ambiguity Function (WAF) $\chi^2(\tau, f_c)$ (impulse response from a single delay-Doppler cell) and a function $\Sigma(\tau, f_c)$ to weight each delay-Doppler cell based on the scattering coefficient, geometry, antenna patterns... ([Marchan-Hernandez et al. 2008](#))

$$\langle |Y_{pq}(\tau, f_c)|^2 \rangle = \chi^2(\tau, f_c) * * \Sigma(\tau, f_c) \quad (8.51)$$

with

$$\chi^2(\tau, f_c) = \Lambda^2(\tau) |S(f_c)|^2 \quad (8.52)$$

and

$$\Sigma(\tau, f_c) = \frac{P_T}{(4\pi)^2} \frac{\lambda^2}{4\pi} \tau_i^2 \int_S \frac{G_T(\mathbf{r}') G_R(\mathbf{r}') \sigma_{pq}^0(\mathbf{r}')}{R^2(\mathbf{T}, \mathbf{r}') R^2(\mathbf{r}', \mathbf{R})} \delta(\tau - \tau(\mathbf{r}')) \delta(f_c - f_D(\mathbf{r}')) d^2 \mathbf{r}' \quad (8.53)$$

being $\delta(x - x_0)$ Dirac delta functions.

8.7 Noise and Coherence Issues

The thermal noise of the correlation measurement depends on the temperature of the system, T , the integration bandwidth B_i , as well as the coherent integration time τ_i (e.g. [Cardellach 2002](#)):

$$\langle |Y_n|^2 \rangle = \tau_i^2 k T B_i \quad (8.54)$$

where k is the Boltzmann's constant. The power signal-to-thermal noise ratio (SNR) is thus the result of dividing Eq. 8.49 by the power of the noise above. The resulting expression cancels out the explicit dependency on the coherent integration time τ_i , but it keeps implicit dependency through the factor $1/B_i = \tau_i$, as well as the factor $|S^2|$. Therefore, the signal-to-noise level seems to increase linearly when the integration is coherently performed during a longer period of time τ_i , as far as the signal itself is coherent during this integration interval. However, the Doppler stripe which defines the delay-Doppler cell narrows with longer τ_i (effect implicit in $|S^2|$). As a result, increasing the integration time has the combined effect of $1/B_i$ (increasing SNR) and the reduction of the area from where the scattered signal is contributing to the power (decreasing the SNR).

Besides the thermal noise, the reflected signal also might suffer fading or speckle under diffuse scattering conditions. The received reflected signal at every instant of time comes from a certain surface area which consists of many scattering points, each generating an elementary contribution to the total received field, and all of them summed up vectorially (amplitude and phase, Eq. 8.2). As seen in Eq. 8.2 and Sect. 8.6, the phase of each individual contribution has a significant geometric term, related to the distance between the scatter and the receiver. As a consequence, if the receiver moves a little amount, all these individual phases will change, and the total vectorial sum of the fields might lead to different values of the total amplitude. The sum might become constructive as well as destructive, leading to the effect called fading: as the receiver moves over a rough surface, the time series of the measured amplitudes result in a series of different values, even if the statistical conditions of the surface have not changed. When imaging sensors are used, this same effect happens within each resolution element (pixel), resulting in different total amplitudes in different pixels, even if their statistical characteristics are the same. It is then called speckle, and it corresponds to the same phenomena as fading, but on the space domain. [Elachi \(1987\)](#) shows that the total amplitude have an oscillation spectrum with frequencies from zero to an upper bound frequency f_M . This higher frequency is given by the size of the illuminated area from where the contributions are being vectorially summed, D , the electromagnetic wavelength λ , the altitude and speed of the receiver h and v respectively:

$$f_M = \frac{Dv}{\lambda h} \quad (8.55)$$

Fading events driven by this spectral component of the oscillation are the most common, determining the shortest interval of time without a fading event: $1/f_M$. Coherent integration times longer than $1/f_M$ result in significantly diminished power levels.

This is equivalent to the Cittert-Zernike theorem, for quasi-monochromatic spatially incoherent source, [Thompson et al. \(1986\)](#). According to this theorem, the illuminated areas act as uniformly illuminated radiating apertures, of diameter D . Such apertures thus have a radiation pattern, the first lobe of which becomes:

$$\theta \sim \frac{\lambda}{D} \quad (8.56)$$

The signal is coherent within the lobe, so the longest time during which the receiver can coherently integrate the signal is the time needed to cross the lobe. If L is the width of the lobe at the receiver altitude h , this crossing time is $\tau_{coh} = L/v \sim (h\theta)/v$, which is equivalent to the coherence time obtained from Eq. 8.55.

Applying this formula separately in the along- and the across-track directions of the GNSS-R receiver movement, the pattern appears as a set of extremely narrow lobes across the Doppler stripe direction, determined by the distance between the delay-Doppler cells (apertures). Along the craft's trajectory, the beam is limited by the size of the Doppler stripe width, which in turn depends on the coherent integration time τ_i . Since the Doppler strip is much narrower than the distance between spots, the angular size of the lobule in the along-track direction is much larger. The time it takes the craft to cross the lobule is the time that the signal can be coherently integrated. Beyond that interval the signal becomes incoherent and the correlation with the replica drops off. An illustration of these ideas is presented in Fig. 8.16.

A more refined estimation of the coherence time for different delays τ along the waveform, and taking into account the possibility of observations at any elevation angle e , is presented in [Zuffada et al. \(2003\)](#):

$$\tau_{coh} = \frac{\lambda}{2v} \sqrt{\frac{h}{2c\tau \sin e}} \quad (8.57)$$

where c is the speed of light.

[Elachi \(1987\)](#) justifies that for a large number of individual scatterers within the illuminated area, the total amplitude has a Rayleigh distribution, the total power an exponential distribution, and the total phase a uniform distribution. The exponential distribution of the total power indicates that its standard deviation depends on the mean power itself ($\sigma_{speckle} = \langle P \rangle_N / \sqrt{N}$). This is the typical noise behavior detected in GNSS-R observations. Fading/speckle has been identified as the major source of random variability in the GNSS-R data. The most effective way to reduce the speckle is by averaging in a non-coherent way the largest possible set of observations, while increasing the signal-to-thermal noise of the sensor does not reduce the relative standard deviation of the signal efficiently.

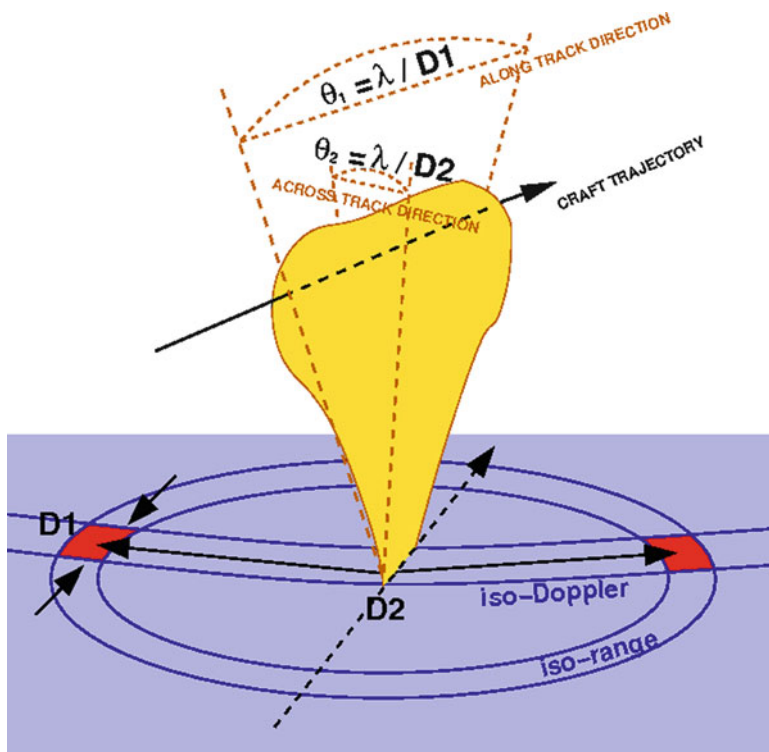


Fig. 8.16 Sketch of the lobule of coherent signal, produced by the two cells that compound a delay-Doppler power bin. The maximum distance between cells depends on the annulus size, and it determines the coherence angle in the across-track direction. The along-track coherent aperture is determined by the width of the Doppler strip, which in turn depends on the integration time

8.8 Systematic Errors

Most of the GNSS-R applications are based on either delay-observations (e.g. altimetry), or power measurement (e.g. surface roughness characterization). The systematic errors found in GNSS-R delay measurements are of the same nature and order of magnitude than the systematic errors identified in GNSS positioning and navigation: clock errors, atmospheric propagation effects, instrumental delays (cabling and radio-frequency chains; antenna phase patterns), and multi-path (see Chaps. 1 and 2). In particular, atmospheric and sea roughness induced delay-bias in GNSS-R are also tackled in Chap. 9.

The systematic effects affecting power measurements are due to the lack of accurate information on the transmitted signals (power, purity of the transmitted polarization, precise antenna phase patterns). Similarly, uncertainties in the receiving antennas and instrumental losses (cabling and radio-frequency chains) can also introduce systematic errors in the power measurements.

8.9 PARIS Interferometric Technique (PIT)

A high-gain high-directivity antenna pointing directly to a given individual GNSS transmitter can provide a clean sampling of the real transmitted signal by this particular transmitter. Therefore, an alternative way to detect reflected GNSS signals emitted by the same transmitter is to cross-correlate these reflected signals against the field received by the high-gain direct-looking antenna. This approach is illustrated in the bottom panel of Fig. 8.17, and it is the candidate technique to be implemented in a potential future European Space Agency (ESA) GNSS-R

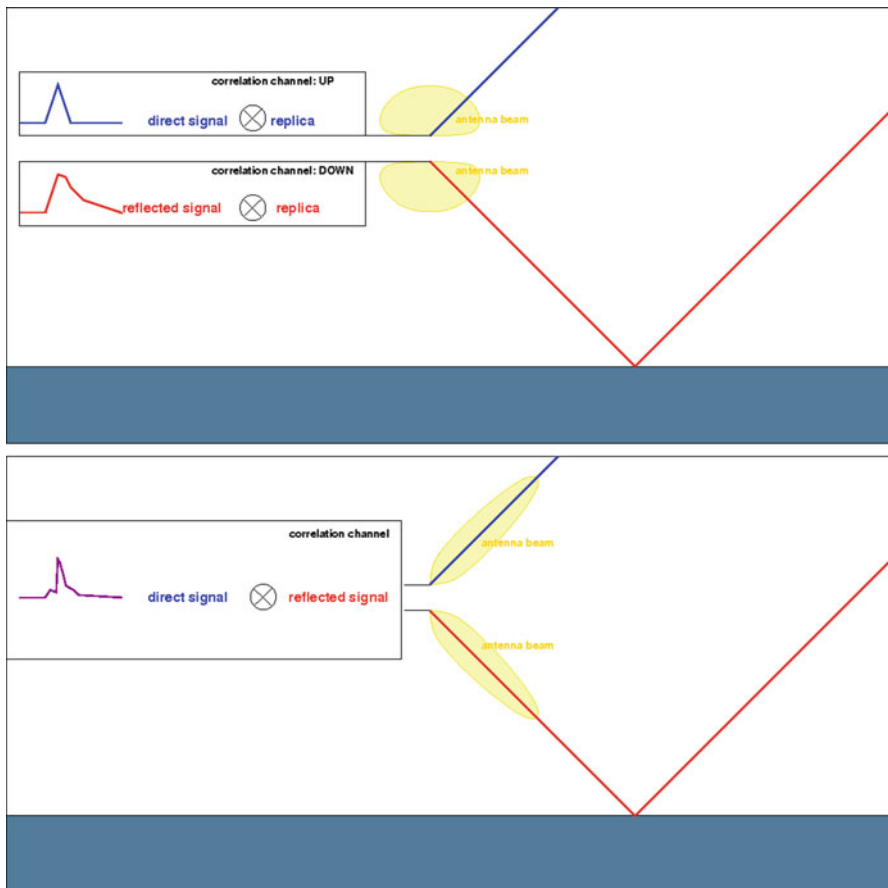


Fig. 8.17 Sketch of the traditional, code-replica approach to the GNSS signal detection (*top*) and the PIT one (*bottom*). The standard GNSS-R receiver needs to know the modulation codes in both direct and reflected signals, to cross-correlate against each of them (*top*), whereas the GNSS-R receiver in PIT approach (*bottom*) directly cross-correlates both signals, with no need to generate the replicas. However, higher and more directive antennas are required, to compensate the higher noise levels and to isolate individual GNSS transmitters

Table 8.4 Summary of the main differences between the code-replica approach and the PARIS interferometric technique

Code-correlation	PIT
Correlation of the signals (either direct or reflected) against well-known, publicly available, modulation codes (C/A, L2C in GPS)	Correlation of the total field received by an up-looking antenna against the total field received by a down-looking antenna
Two waveforms, direct and reflected, can be generated separately	Direct and reflected signals generate the only waveform
Only publicly available narrow bandwidth modulations are used	The full power spectral density of the transmitted GNSS signals is exploited: all modulations (both public/encrypted, narrow and wide bandwidth) contribute to the waveform
Group-delay precision is limited by publicly available narrow-bandwidth modulation codes	Group-delay precision is not limited by publicly available codes
The waveform presents noise introduced by either the direct or the reflected signal	Noise from both direct and reflected radio-links is present in the waveform
Relatively low-gain low-directivity antennas are needed	High-gain highly-directive antennas are required
The correlation process permits to separate and identify the different visible GNSS transmitters	The correlation process cannot separate and/or identify the different GNSS transmitters, unless they are distant along the delay-Doppler space, or a high-gain, narrow-beam antenna points to a single GNSS
Parallel multi-static performance easily implementable	Parallel multi-static performance requires parallel beam-forming capabilities of the receiving antennas

altimetric mission ([Martín-Neira et al. 2011](#)). Sometimes it is called PARIS-approach (PAssive Reflectometric Interferometric System), although in some other publications the PARIS concept might also be fully equivalent to GNSS-R. We will use the term PARIS Interferometric Technique (PIT). Note that, unlike the replica-correlation approach, in the PIT there is no need of knowing the code modulations, meaning that also the encrypted wide bandwidth codes are being captured. In fact, the PIT approach allows exploiting the full power spectral density of the transmitted GNSS signals. Because of this, higher group-delay precision can be obtained, making it attractive for altimetric applications. Other differences between both approaches are summarized in Table 8.4.

The PIT waveform is slightly different from the BPSK-codes' waveforms. It contains the contributions from all the simultaneously transmitted codes from the observed GNSS satellite. Figure 8.18 shows a real PIT waveform obtained from an aircraft at 200 m altitude, from a reflection off estuary calm waters. The data was acquired during the experimental campaign described in [Rius et al. \(2012\)](#). The resulting PIT waveform almost corresponds to the theoretical one for specular reflection ([Martín-Neira et al. 2011](#), Fig. 6). The contribution of the C/A code within the PIT waveform is shown (dashed Λ^2 function). M-code (B.O.C.) features are

Fig. 8.18 Real PIT waveform obtained during the experimental campaign described in Rius et al. (2012), from an aircraft at 200 m altitude flying over estuary calm waters. The PIT waveform has contribution from all the transmitted codes, which for that particular GPS satellite were C/A, P(Y), and M codes. Compare with the theoretical PIT waveform in Martín-Neira et al. (2011, Fig. 6)

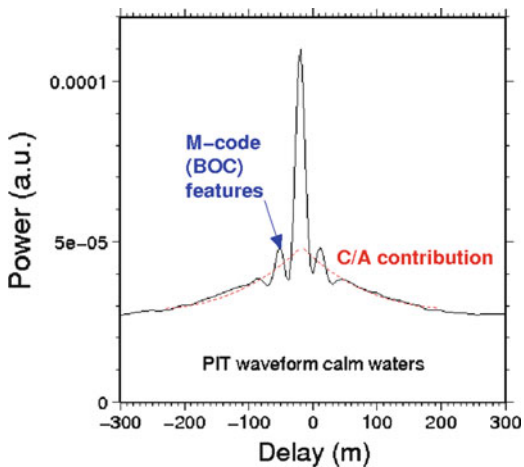
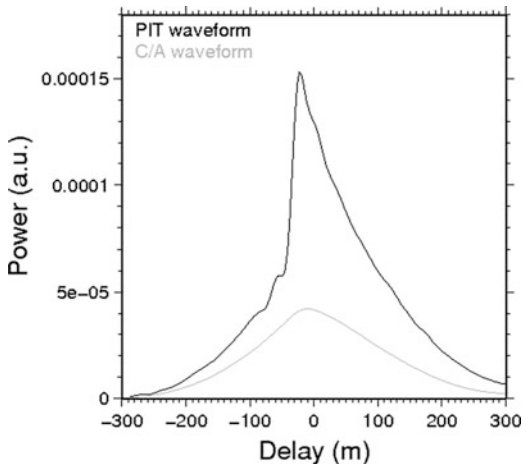


Fig. 8.19 Real PIT waveform and C/A reflected waveforms obtained during the experimental campaign described in Rius et al. (2012), using two different receivers (Rius et al. 2011; Nogués-Correg et al. 2007) from an aircraft at 3 km altitude flying over Ocean waters. The floor-noise levels have been subtracted for better comparison. Coherence integration time: 1 ms; non-coherent averaging: 20 s



also seen. Another example of a PIT waveform under rougher surface conditions is displayed in Fig. 8.19. The plot shows both real PIT and C/A-code waveforms taken simultaneously with two different receivers (PIR-A Rius et al. 2011 and GOLD-RTR Nogués-Correg et al. 2007) from an aircraft flying at 3 km altitude over the Ocean surface. Both suffer distortion due to the diffuse scattering, but the PIT waveform still presents a steeper leading edge.

8.10 Observables

In the frame of these GNSS-R Chapters, we will define the *observables* as measurable objects (scalar values, arrays, ...) from which geo-physical information can be derived. Different receiving instruments produce different types of observables,

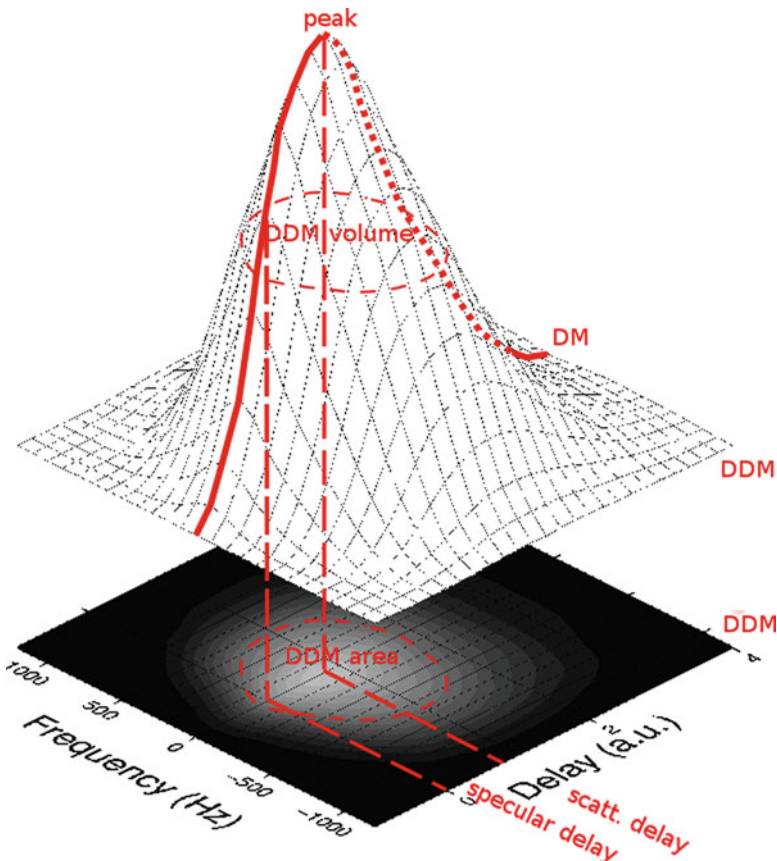


Fig. 8.20 Sketch of a delay and delay-Doppler map and some of the observables that can be defined: delay of the peak (scatterometric delay); specular delay; DDM area and volume above a given threshold

but most of the dedicated GNSS-R receivers are able to provide delay and/or delay-Doppler waveforms. Sometimes they yield power waveforms, and some others their in-phase and quadrature (I/Q) components (thus providing phase information of the received field). We consider here the delay and delay-Doppler waveforms as the primary observables, from where the rest of them can be defined. A complementary list of observables and their inversion techniques are compiled in [Cardellach et al. \(2011\)](#) (Fig. 8.20):

Delay waveform or Delay-Map (DM) Output of the signal correlation process, when conducted along a set of delay-bins or lags, τ_i : $W(\tau)$. The inter-lag interval is the delay between subsequent correlation samples. It can be given as power waveforms or with phase information (amplitude and phase, or I/Q). Fitting

models against DM observables has been widely used to estimate some reflecting surface parameters (mostly roughness) (e.g. [Garrison et al. 2002](#); [Cardellach et al. 2003](#); [Komjathy et al. 2004](#)).

Delay-Doppler waveform or Delay-Doppler Map (DDM) Output of the signal correlation process, when conducted along a set of delay-bins and also a set of central correlation frequencies, δf : $W(\tau, \delta f)$. It can be given in amplitude/power units or as complex values (phase/amplitude or I/Q). Examples of different uses of DDM for surface roughness characterization can be found in [Germain et al. \(2004\)](#), [Cardellach and Rius \(2008\)](#), and [Marchan-Hernandez et al. \(2008\)](#).

Integrated spectrum and delay [Elfouhaily et al. \(2002\)](#) shown that the frequency-integrated delay spread ($IDM(\tau) = \int_{Dopplers} DDM(\tau, f)df$) and delay-integrated Doppler spread ($IDS(f) = \int_{Delays} DDM(\tau, f)d\tau$) relate to the roughness conditions of the scattering surface.

Specular group delay Observable obtained from the delay-derivative of the delay-waveform, $W'(\tau) = \partial W(\tau)/\partial\tau$. The delay of the radio-link reflected off the specular point, ρ_{spec} , is given by the delay-location of the peak of the derivative:

$$\frac{\partial^2 W}{\partial\tau^2}|_{\rho_{spec}} = 0 \quad (8.58)$$

This observable was suggested in [Hajj and Zuffada \(2003\)](#) and proved in [Rius et al. \(2010\)](#), where derivation and application details are given.

Scatterometric delay Delay of the peak of the delay waveform, with respect to the specular delay, $\rho_{scatt} = \rho_{peak} - \rho_{spec}$. The derivative of the waveform can be used to estimate the peak's delay:

$$\frac{\partial W}{\partial\tau}|_{\rho_{peak}} = 0 \quad (8.59)$$

It is called *scatterometric* because it contains information about the roughness of the reflecting surface. Note that when the surface is smooth and the reflection purely specular, the waveform is shaped as the modulation auto-correlation function, and its peak location corresponds to the delay of the specular radio-link. Then, $\rho_{scatt} = 0$. It has been widely use, starting in [Nogués-Correig et al. \(2007\)](#).

Phase-delay Delay of the specular radio-link estimated using phase-information out of the complex waveform. Note that only specular-like reflections (little diffuse contribution) provide meaningful phase information. The main challenges of phase-delay observations are the potential cycle slips present in the data, together with the unwrapping of measured $[-\pi, \pi]$ phases to obtain the dynamic delay. Examples of different ways to extract and process phase-delay observables can be found in e.g. [Treuhhaft et al. \(2001\)](#), [Martín-Neira et al. \(2002\)](#), [Semmling et al. \(2011\)](#), and [Fabra et al. \(2011\)](#).

Volume/Area of the DDM The spreading of the DDM relates to the roughness of the surface. The spreading can be also characterized by the area or the volume of the DDM above certain power threshold. These observables were suggested in [Marchan-Hernandez et al. \(2008\)](#), yielding reasonable correlation with the roughness correction of collocated L-band radiometric measurements.

Lag-hologram Spectral content of the complex (I/Q) delay waveform, independently measured at each correlation-lag. This observable has been used to characterize the sub-structure of Antarctic dry-snow, down to 200–300 m depth. More details can be checked at [Cardellach et al. \(2012\)](#) and Chap. 11.

Polarimetric ratio This observable is generated by comparing the peak-power received simultaneously by the LHCP and RHCP ports of a surface-looking dual-polarization antenna (or similarly, from two close-by antennas at complementary circular polarizations). As shown in Fig. 8.13, the relative power between both circular co- and cross-polar contributions is sensitive to dielectric properties of the reflecting surface, especially around the Brewster angle (elevation angles of observation below 40° for soil moisture observations; below 10° for sea-water reflections). [Fabra \(2013\)](#) shows the dynamic range of the Brewster angle of sea-ice (changing brine, temperature) between ~61° and 73°. It could also be defined in linear polarizations, with slightly different interpretation.

Interferometric phase When two or more radio-links reach the receiving antenna with no diffuse effects (coherent reflection/s and/or direct link), the geometric differences between them makes them have different Doppler frequencies. The result is an interferometric pattern from which the geometric information can be derived. Examples of applications of this interference pattern can be found in [Cardellach et al. \(2004\)](#) and [Helm et al. \(2004\)](#).

Interferometric amplitude Similarly, the interferences between direct and reflected branches of the signal are captured by the amplitude or SNR of the received fields. The analysis of these patterns (frequencies, location of their notches, ...) provides information about the receiver's altitude, useful to extract snow depth ([Larson et al. 2009](#)), coastal tides ([Larson et al. 2013](#)), and surface dielectric properties, linked to soil moisture and vegetation ([Larson et al. 2008](#); [Small et al. 2010](#); [Rodriguez-Alvarez et al. 2012](#)). Based on this principle, the American geodetic GNSS networks are being re-analyzed to extract historical time series of snow coverage and vegetation information ([PBO H2O 2012](#)).

References

- Bass FG, Fuks IM (1979) Wave scattering from statistically rough surfaces. International series in natural philosophy, vol 93. Pergamon, Oxford, p 537
- Beckmann P, Spizzichino A (1987) The scattering of electromagnetic waves from rough surfaces. Artech House, Inc., Norwood, p 511
- Blanch S, Aguasca A (2004) Seawater dielectric permittivity model from measurements at L band. In: Proceedings of 2004 IEEE international geoscience and remote sens-

- ing symposium, IGARSS'04, Anchorage, vol 2. IEEE, Piscataway, pp 1362–1365. doi:10.1109/IGARSS.2004.1368671
- Cardellach E (2002) Sea surface determination using GNSS reflected signals. Ph.D. Dissertation, Polytechnical University of Catalonia (UPC), Barcelona
- Cardellach E, Rius A (2008) A new technique to sense non-Gaussian features of the sea surface from L-band bi-static GNSS reflections. *Remote Sens Environ* 112:2927–2937. doi:10.1016/j.rse.2008.02.003
- Cardellach E, Ruffini G, Pino D, Rius A, Komjathy A, Garrison JL (2003) Mediterranean balloon experiment: Ocean wind speed sensing from the stratosphere using GPS reflections. *Remote Sens Environ* 88:351–362
- Cardellach E, Ao CO, de la Torre-Juárez M, Hajj GA (2004) Carrier phase delay altimetry with GPS-reflection/occultation interferometry from Low Earth Orbiters. *Geophys Res Lett* 31(10):L10402
- Cardellach E, Fabra F, Nogués-Correig O, Oliveras S, Ribó S, Rius A (2011) GNSS-R ground-based and airborne campaigns for ocean, land, ice, and snow techniques: application to the GOLD-RTR data sets. *Radio Sci* 46:RS0C04. doi:10.1029/2011RS004683
- Cardellach E, Fabra F, Rius A, Pettinato S, D'Addio S (2012) Characterization of dry-snow sub-structure using GNSS reflected signals. *Remote Sens Environ* 124:122–134. doi:10.1016/j.rse.2012.05.012
- Clarizia MP, Gommenginger C, Di Bisceglie M, Galdi C, Srokosz MA (2012) Simulation of L-band bistatic returns from the Ocean surface: a facet approach with application to Ocean GNSS reflectometry. *IEEE Trans Geosci Remote Sens* 50(3). doi:10.1109/TGRS.2011.2162245
- Elachi C (1987) Spaceborne radar remote sensing: applications and techniques. IEEE, New York. ISBN:0-87942-241-6
- Elfouhaily TM, Guérin C-A (2004) A critical survey of approximate scattering wave theories from random rough surfaces. *Waves Random Media* 14:R1–R40. doi:10.1088/0959-7174/14/4/R01
- Elfouhaily T, Thompson DR, Linstrom L (2002) Delay-Doppler analysis of bistatically reflected signals from the Ocean surface: theory and application. *IEEE Trans Geosci Remote Sens* 40:560–573. doi:10.1109/TGRS.2002.1000316
- Fabra F (2013) GNSS-R as a source of opportunity for sea ice and dry snow remote sensing. Ph.D. Dissertation, Polytechnical University of Catalonia (UPC), Barcelona
- Fabra F, Cardellach E, Rius A, Oliveras S, Nogués-Correig O, Belmonte-Rivas M, Semmling M, D'Addio S (2011) Phase altimetry with dual polarization GNSS-R over sea-ice. *IEEE Trans Geosci Remote Sens* 50(6):10. doi:10.1109/TGRS.2011.2172797
- Fung AK (1994) Microwave scattering and emission models and their applications. Artech House, Norwood
- Fung AK, Pan GW (1986) An integral equation model for rough surface scattering. In: Proceedings of the international symposium on multiple scattering of waves in random media and random rough surface, 29 July–2 August 1985, University Park, PA. Pennsylvania State University Press, pp 701–714
- Fung AK, Li Z, Chen KS (1992) Backscattering from a randomly rough dielectric surface. *IEEE Trans Geosci Remote Sens* 30(2):356–369
- Garrison JL, Komjathy A, Zavorotny VU, Katzberg SJ (2002) Wind speed measurement using forward scattered GPS signals. *IEEE Trans Geosci Remote Sens* 40:50–65
- Germain O, Ruffini G, Soulard F, Caparrini M, Chapron B, Silvestrin P (2004) The eddy experiment: GNSS-R speculometry for directional sea-roughness retrieval from low-altitude aircraft. *Geophys Res Lett* 31:L21307. doi:10.1029/2004GL020991
- Hajj G, Zuffada C (2003) Theoretical description of a bistatic system for Ocean altimetry using the GPS signal. *Radio Sci* 38(5):1089. doi:10.1029/2002RS002787
- Helm A, Beyerle G, Nitschke M (2004) Detection of coherent reflections with GPS bipath interferometry. <http://arxiv.org/pdf/physics/0407091v1.pdf>
- Ishimaru A (1978) Wave propagation and scattering in random media, vol 2. Academic, New York, p 572

- Komjathy A, Armatys M, Masters D, Axelrad P (2004) Retrieval of Ocean surface wind speed and wind direction using reflected GPS signals. *J Atmos Ocean Technol* 21:515–526
- Krotikov VD (1962) Dielectric properties of dry soils. *Izvest Vuz Radiophys* 5:1057
- Larson KM, Small EE, Gutmann E, Bilich A, Braun J, Zavorotny V (2008) Use of GPS receivers as a soil moisture network for water cycle studies. *Geophys Res Lett* 35:L24405. doi:10.1029/2008GL036013
- Larson KM, Gutmann E, Zavorotny V, Braun J, Williams M, Nievinski F (2009) Can we measure snow depth with GPS receivers? *Geophys Res Lett* 36:L17502. doi:10.1029/2009GL039430
- Larson KM, Ray R, Nievinski F, Freymueller J (2013) The accidental tide gauge: a case study of GPS reflections from Kachemak Bay, Alaska. *IEEE Geosci Remote Sens Lett* 10(5):1200–1204. doi:10.1109/LGRS.2012.2236075
- Marchan-Hernandez J, Rodriguez-Alvarez N, Camps A, Bosch-Lluis X, Ramos-Perez I, Valencia E (2008) Correction of the sea state impact in the L-band brightness temperature by means of delay-Doppler maps of global navigation satellite signals reflected over the sea surface. *IEEE Trans Geosci Remote Sens* 46:2914–2923
- Martín-Neira M (1993) A passive reflectometry and interferometry system (PARIS): application to Ocean altimetry. *ESA J* 17:331–355
- Martín-Neira M, Colmenarejo P, Ruffini G, Serra C (2002) Altimetry precision of 1 cm over a pond using the wide-lane carrier phase of GPS reflected signals. *Can J Remote Sens* 28(3):394–403
- Martín-Neira M, D'Addio S, Buck C, Flouri N, Prieto-Cerdeira R (2011) The PARIS Ocean altimeter in-orbit demonstrator. *IEEE Trans Geosci Remote Sens* 49(6, part 2):2209–2237. doi:10.1109/TGRS.2010.2092431
- Nogués-Correig O, Cardellach Galí E, Sanz Campderròs J, Rius A (2007) A GPS-reflections receiver that computes Doppler/delay maps in real time. *IEEE Trans Geosci Remote Sens* 45:156–174
- PBO H2O Server (2012) <http://xenon.colorado.edu/portal/>
- Rice SO (1951) Reflection of electromagnetic waves from slightly rough surfaces. *Commun Pure Appl Math* 4:351–378
- Rice SO (1963) Reflection of EM from slightly rough surfaces. Interscience, New York
- Rius A, Cardellach E, Martín-Neira M (2010) Altimetric analysis of the sea surface GPS reflected signals. *IEEE Trans Geosci Remote Sens* 48(4):2119–2127. doi:10.1109/TGRS.2009.2036721
- Rius A, Cardellach E, Oliveras S, Valencia E, Park H, Camps A, van der Marel H, van Bree R, Altena B, Nogués-Correig O, Ribó S, Tarongí J, Martín-Neira M (2011) Altimetry with GNSS-R interferometry: first proof of concept experiment. *GPS Solut* 1–11. doi:10.1007/s10291-011-0225-9
- Rius A, Fabra F, Ribó S, Arco Fernandez JC, Oliveras S, Cardellach E, Camps A, Nogués-Correig O, Kainulainen J, Rohue E, Martín-Neira M (2012) PARIS interferometric technique proof of concept: sea surface altimetry measurements. In: Proceedings of IEEE international geoscience and remote sensing symposium (IGARSS) 2012, Munich, pp 7067–7070. doi:10.1109/IGARSS.2012.6352035
- Rodriguez-Alvarez N, Bosch-Lluis X, Camps A, Ramos-Perez I, Valencia E, Park H, Vall-Llossera M (2012) Vegetation water content estimation using GNSS measurements. *IEEE Geosci Remote Sens Lett* 9(2):282–286
- Semmling M, Beyerle G, Stosius R, Dick G, Wickert J, Fabra F, Cardellach E, Ribó S, Rius A, Helm A (2011) Detection of Arctic Ocean tides using interferometric GNSS-R signals. *Geophys Res Lett* doi:10.1029/2010GL046005
- Small EE, Larson KM, Braun JJ (2010) Sensing vegetation growth using reflected GPS signals. *Geophys Res Lett* 37:L12401. doi:10.1029/2010GL042951
- Stratton JA (1941) Electromagnetic theory. McGraw-Hill, New York, p 615
- Thompson AR, Moran JM, Swenson GW (1986) Interferometry and synthesis in radio astronomy. A Wiley-Interscience publication, Wiley, New York. ISBN:0-471-80614-5
- Treuhaft RN, Lowe ST, Zuffada C, Chao Y (2001) Two-cm GPS altimetry over Crater Lake. *Geophys Res Lett* 28(23):4343–4346

- Treuhhaft RN, Lowe ST, Cardellach E (2011) Formulating a vector wave expression for polarimetric GNSS surface scattering. *Prog Electromagn Res B* 33:257–276
- Ulaby FT, Moore RK, Fung AK (1982) Microwave remote sensing: active and passive, vol 2. Artech House, Inc., Norwood, p 1064
- Ulaby FT, Moore RK, Fung AK (1986) Microwave remote sensing: active and passive, vol 3. Artech House, Inc., Norwood, p 2162
- Valenzuela G (1978) Theories for the interaction of electromagnetic and oceanic waves – a review. *Bound Layer Meteorol* 13:61–85
- Voronovich AG (1985) Small-slope approximation in wave scattering from rough surfaces. *Sov Phys JETP* 62(1):65–70
- Voronovich AG (1994a) Small-slope approximation for electromagnetic wave scattering at a rough interface of two dielectric half-spaces. *Waves Random Media*, Springer Berlin Heidelberg 4:337–367
- Voronovich AG (1994b) Wave scattering from rough surfaces. Springer series on wave phenomena. Springer, Berlin/Heidelberg
- Zavorotny VU, Voronovich AG (2000) Scattering of GPS signals from the Ocean with wind remote sensing application. *IEEE Trans Geosci Remote Sens* 38:951–964
- Zhurbenko V (ed) (2011) Electromagnetic waves. InTech, Vienna. ISBN:978-953-307-304-0, Chapter 10 by: Ticconi F, Pulvirenti L, Pierdicca N
- Zuffada C, Elfouhaily T, Lowe S (2003) Sensitivity analysis of wind vector measurements from Ocean reflected GPS signals. *Remote Sens Environ* 88(3):341–350

Chapter 9

Ocean Remote Sensing Using GNSS-R

This chapter is organized in two main sections, to tackle the essential Oceanic application of the GNSS reflectometry: sea surface altimetry and surface roughness.

Other potential areas of interest for oceanography and marine applications are the retrievals of dielectric properties of the surface (related to temperature and salinity); and ship detection. Although the ratio between the co-polar and the cross-polar components of the Fresnel reflection coefficients for sea water presents up to 10 % sensitivity to salinity conditions ([Cardellach et al. 2011](#), Fig. 7), the effects of the roughness are not well modelled yet. These applications are still immature and no further details are given in this Chapter.

9.1 Altimetry

The concept GNSS-R was proposed in 1993 by ESA ([Martín-Neira 1993](#)) to provide additional measurements of the sea surface to increase the spatial and temporal resolution of the Radar Altimeters (RA), which typically only measure the ocean height at the sub-satellite point (mono-static nadir-looking systems). As it will be shown in Sect. 9.1.3, the single-measurement precision-level of the LEO-based GNSS-R is expected to be lower than standard space-based microwave RA. However, and as seen in Chap. 8, the potential temporal and spatial coverage/resolution of the concept suggests its complementarity with mono-static RA. This passive wide-swath altimeter concept lends itself to new applications, such as the detection of tsunamis, Ocean eddies or other meso-scale features in ocean height. Significant impact of GNSS-R data into ocean circulation models was demonstrated in [Le Traon et al. \(2002\)](#) through assimilation of simulated data from a single GNSS-R satellite mission. In order to achieve user required precision levels, the altimetric application is more demanding than other GNSS-R applications, in terms of required SNR,

bandwidth, directivity of the antennas, etc. GNSS altimetry, with its higher spatial and temporal sampling, could make contributions to the following research topics:

Eddies and fronts are essential to understand Ocean circulation on all space and time scales, but a large fraction of their kinetic energy is associated with spatial scales that cannot be resolved with a single radar altimeter. Mesoscale variability is key to understand large-scale circulation and climate variability through eddy transport of momentum in interactions with the mean flow and meridional heat transport. GNSS altimetry, with its relatively large number of simultaneous measurements, can provide greater spatial and temporal resolution, and these can be traded against each other for a particular application.

Tsunamis at open waters have a relatively small vertical signal (typically a few decimeters) but very large horizontal pattern, corresponding to ocean waves of long periods (5–60 min) and long wavelengths (up to 800 km). Its detection and warning must be as quick as possible, preferably 15–25 min after its origin. The synoptic-view capabilities of the GNSS-R system might help detecting them timely. [Stosius et al. \(2010\)](#) shown that strong tsunamis with magnitudes ≥ 8.5 can be detected with certainty from any orbit altitude within 15–25 min by a 48/8 or 81/9 Walker constellation of GNSS-R satellites if tsunami waves of 20 cm or higher can be detected by the technique.

Geostrophic Velocities and Gravity Anomalies are estimated based on measurements of the surface slope. Radar altimeters can measure surface slopes in only one direction—along track, except at widely time-spaced track crossover points. With GNSS altimetry, the slope measurements could be done along the paths of the multiple simultaneous specular points on the surface. Over time, a single resolution cell would be crossed by several such paths, in different orientations. This potentially allows 2-D surface slopes to be estimated for larger set of resolution cells.

Tides, in particular higher-order tidal components, might be better identified than in standard RA because of the non-repeating nature of the GNSS concept. Another possible advantage of the GNSS-R altimetry could be better sampling of internal tides, of wavelengths below about 100 km. These tides play an important role in large-scale circulation and vertical mixing in the deep ocean.

Physical-Chemical-Biological Interactions mostly occur at scales not resolved with radar altimeters. One of the more important of these interactions is the oceans connection to the carbon cycle, which is crucial to understanding long-term climate variations.

The GNSS-R can measure the electromagnetic slant delay between the transmitter and the receiver, after the signal rebounds off the sea surface, ρ . This electromagnetic delay contains a geometric component ρ_{geo} due to the total distance travelled by the signal; it also includes atmospheric induced delays ρ_{atm} (ionospheric and tropospheric effects); instrumental components ρ_{ins} (clock errors, sub-system delays, antenna offsets); and noise n :

$$\rho = \rho_{geo} + \rho_{atm} + \rho_{ins} + n \quad (9.1)$$

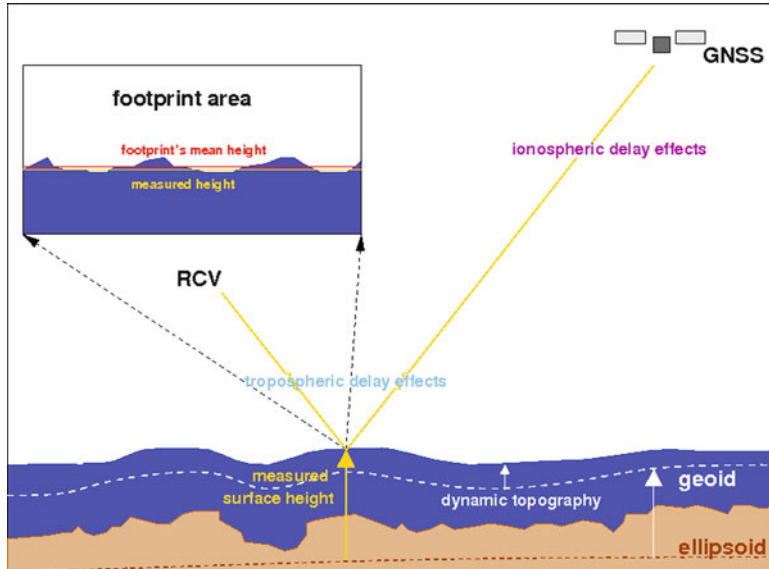


Fig. 9.1 Sketch of the different sea level heights concepts: the measured instantaneous sea level height is affected by dynamical components and small scale roughness effects, in comparison with the geoid, the height of the Ocean surface if the Oceans and atmosphere were in equilibrium and at rest relative to the rotating Earth. These quantities are usually given with respect to a reference ellipsoid. The delay-measure is also affected by atmospheric effects

The delays are usually given in the time domain, but they can be also given as ranges, in the space domain, multiplying by the speed of light. From here on we will call them range or delay indistinctly.

Assuming it is possible to separate, correct and/or reduce the non-geometric components of the slant delay, a measure of the vertical location of the reflecting surface can then be extracted from its geometric contribution. This vertical location, usually known as the altimetric solution, corresponds to an average or statistical central tendency of the instantaneous surface height across the footprint. It needs to be distinguished from the Mean Sea Level (MSL) at that same location, which is the measure of the average height after a long time series. The instantaneous measured height is thus affected by local tides, atmospheric pressure, changing currents, eddies and wind (e.g. Gill 1982) – that is, the dynamic component of the ocean height; as well as short-scale roughness effects within the measurement footprint. This latter, known as the Sea State Bias, also includes the electromagnetic bias, for which signals tend to be more reflected from the Ocean waves' troughs than crests, resulting in a biased statistical estimator (e.g. Chapron et al. 2001). Figure 9.1 sketches these different concepts.

As just mentioned, the measured delay also contains non-geometric terms. The delays induced by the atmosphere are a significant source of error if not well corrected. They include ionospheric as well as tropospheric effects. These will be tackled in Sect. 9.1.2.

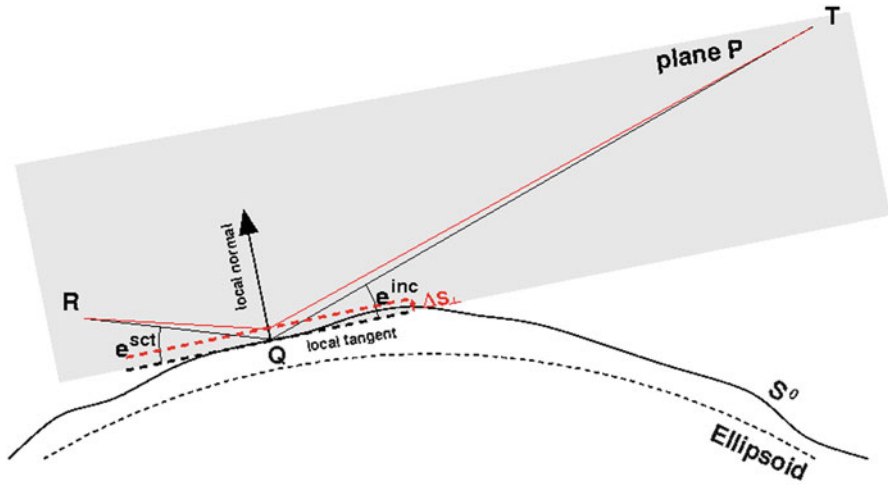


Fig. 9.2 Not scaled sketch of the general altimetric inversion: an operator must find the specular point \mathbf{Q} on an a-priori surface S^0 , fulfilling three conditions ($\mathbf{Q} \in P$, and $\mathbf{Q} \in S^0$, and $e^{inc} = e^{sct}$, Fresnel reflection). The operator then computes the geometric delay between the transmitter \mathbf{T} , the specular point \mathbf{Q} , and the receiver \mathbf{R} . Straight lines are used for simplicity, but certain operators could also take into account the atmospheric-induced bending of the ray propagation (e.g. ray-tracing operators)

In order to solve the altimetric problem, an accurate knowledge of the position of both transmitter's \mathbf{T} and receiver's \mathbf{R} antennas' phase centers are required, expressed as their 3D vector with respect to the center of the Earth. We assume that both can be obtained (Precise Orbit Determination of the GNSS transmitters, and GNSS-based plus Inertial Navigation Systems—or others—for the receiver). In some cases it might also be interesting to extract the receiver's altitude with respect to a reference Earth ellipsoid H_{rcv}^{ref} .

The general bi-static altimetric problem is slightly more complex than the mono-static nadir-looking radar one. The inversion procedure requires a forward operator F such that given the transmitter and receiver coordinates \mathbf{T} and \mathbf{R} , and given an a-priori surface topography S^0 finds the specular point \mathbf{Q} that fulfills three conditions (see Fig. 9.2): (1) vectors \mathbf{TQ} , \mathbf{QR} , and the normal at \mathbf{Q} are coplanar (horizontal gradients in the atmosphere would break this assumption); (2) $\mathbf{Q} \in S^0$; and (3) $e^{inc} = e^{sct}$ (Fresnel reflection). The operator then computes the geometric range between \mathbf{T} -to- \mathbf{Q} -to- \mathbf{R} :

$$\rho_{geo}^{mod} = F(\mathbf{T}, \mathbf{R}, S^0) \quad (9.2)$$

It is possible to correct for vertical displacements of the a-priori surface around \mathbf{Q} , $S(\mathbf{Q}) = S^0(\mathbf{Q}) + \Delta S_\perp(\mathbf{Q})\hat{\mathbf{n}}(\mathbf{Q})$ by linearizing around this a-priori solution, so that the modelled range fits the measured one:

$$\rho_{geo}^{obs} - \rho_{geo}^{mod} = \frac{\partial F}{\partial S_{\perp}} \Delta S_{\perp} \quad (9.3)$$

and finally it should be inverted following a least-squares scheme.

Some comments about the procedure described above:

- Local vertical displacements could also force horizontal shifts of the specular location, if condition 3 does not further apply (in fact this is what happened—not made on purpose—on Fig. 9.2). This is a small effect, affecting only those situations in which a very low altitude receivers is used and the vertical component of the a-priori surface is wrong by meters. Simpler models can be used in these cases as it will be explained below.
- The operator F can just be a straight propagator through an homogeneous medium (straight rays), or a more sophisticated operator to account for atmospheric gradients, such as ray-tracers (Jones and Stephenson 1975). Horizontal atmospheric gradients could bend the ray out of the plane P . The atmospheric vertical gradients can also displace the horizontal location of the specular point. This could still be solved by applying the same procedure iteratively, using each i-solution as i + 1 a-priori where to find again the new i + 1 specular point.
- The operators could also take into account and try to solve for non-geometric contributions to the reflected delay (Eq. 9.1). In that case, the operator in Eq. 9.2 should output a more general delay ρ (rather than ρ_{geo}), and ancillary parameters would enter as operator's input to help separating the different components of ρ .
- Similarly, this inversion approach could be applied to differential delays, that is, delays with respect to the direct radio-link (from **T** to **R** through the medium, with no reflection off the Earth surface): $\Delta\rho = \rho_{geo} - \rho_{dir}$. In the equations above ρ_{geo} should be replaced by $\Delta\rho$ and the operator implemented accordingly.

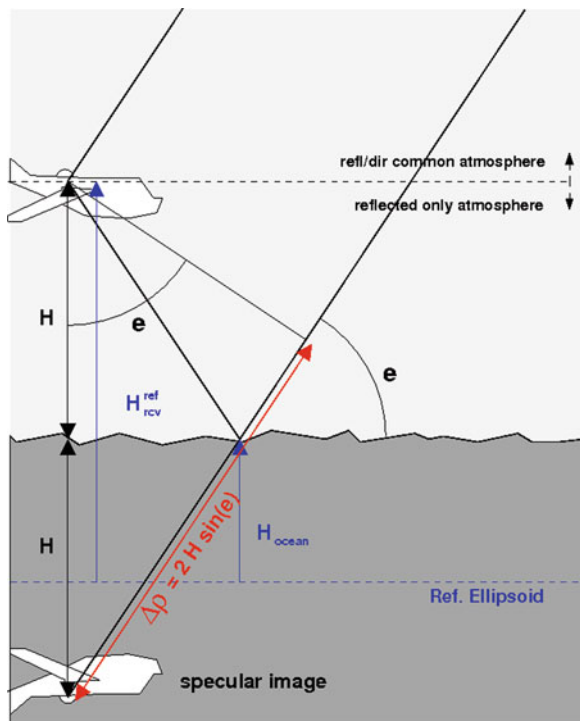
For low altitude receivers (aircrafts, or ground-based campaigns), simpler altimetric models can be applied. In these scenarios it is especially advantageous to work with the differential delay $\Delta\rho$, so that some of the instrumental and atmospheric errors might cancel out. Moreover, the differential delay $\Delta\rho = \rho_{geo} - \rho_{dir}$ is a simple function of the elevation angle of observation e , and the (low) altitude of the receiver above the Ocean surface H :

$$\Delta\rho = 2H \sin e \quad (9.4)$$

Note that H here is not the Ocean height, but the vertical distance between the surface and the receiver (see Fig. 9.3). This model applies when the incidence angle over the region can be assumed as a constant value (parallel incidence), and the mean surface locally horizontal (the altitude H is thus defined along the surface's local normal direction). The Ocean instantaneous height can then be obtained subtracting H from the receiver's altitude with respect to the reference ellipsoid: $H_{ocean} = H_{ref}^{ref} - H$.

The following subsection details how to obtain ρ and/or $\Delta\rho$ from the GNSS-R waveforms when the range is measured through the delay of the code (delay of the

Fig. 9.3 Sketch of the low receiver altitude altimetric model, assuming parallel incidence, and planar horizontal reflecting surface



correlation function), called group-delay or pseudo-range. When the carrier phase can be tracked, variations in the range can be monitored with much better precision, since an entire cycle corresponds to $\lambda \sim 20$ cm change (~ 0.5 mm/cARRIER phase degree). This latter approach is called carrier phase altimetry, but it is usually not applicable to Oceanic observations. The reason is the roughness, which introduces random phase behavior and thus impedes long coherence times of the reflected signals. A recent method has been presented to perform carrier-based altimetry over rough Ocean conditions from low altitude receivers. Under such conditions, the spectral analysis of the Doppler residual still carries altimetric information content, despite roughness conditions. The method is explained in [Semmling et al. \(2012\)](#), where a precision of the order of 10 cm in 20 min arch is reported from a coastal experiment on top of a ~ 700 m high cliff. The phase-delay altimetry will not be detailed in this Chapter, but it has also been successfully applied over continental-ice ([Cardellach et al. 2004](#), spaceborne) and sea-ice ([Semmling et al. 2011](#); [Fabra et al. 2011](#)).

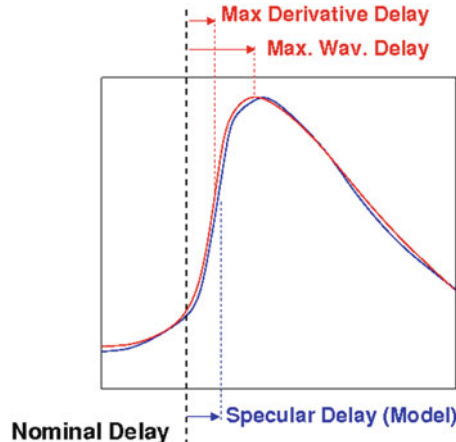


Fig. 9.4 Altimetric group delay as defined in three different approaches: Peak-Delay; Model-Fitting; and Peak-Derivative. The GNSS-R receiver assumes certain value for the reflected delay (Nominal Delay, $\rho_{nominal}$), however the real data (in red) might be displaced from this a-priori assumption. This displacement will be noticed in the location of the waveform's peak (Max. Wav. Delay, ρ_{peak}); and the location of the peak of the first derivative (Max. Derivative Delay, $\rho_{derivative-peak}$). The former is only related to the time-arrival of the reflected signal when the reflecting surface is smooth; otherwise the derivative's peak indicates the specular ray-path delay. An alternative way to identify the specular delay is to fit a model (in blue) to the data, $\rho_{model-spec}$

9.1.1 Group Delay Altimetry

A reflection off a very smooth surface would produce amplitude waveforms looking like their codes' autocorrelation functions (e.g. triangular for GPS C/A), and the path-ray distance traveled by the reflected signal would simply correspond to the range given by the peak of the reflected correlation function. Nevertheless, and since most Oceanic reflections occur off rough surfaces, this approach cannot generally be used: Rius et al. (2002) shown that variations in the delay of the reflected waveform's peak mostly account for changes in the surface roughness rather than surface elevation: the peak is not a good indicator of the specular path range. Dedicated techniques are then required to identify the specular point delay within the waveform.

Unlike GNSS geodetic and positioning receivers, GNSS-R receivers tend to operate in open-loop, a technique that does not require to track the phase of the carrier and thus the signal's coherence can be short. Instead, the open-loop approach assumes/guess a certain delay and Doppler, to build the replicas of the code. The delay-shift shown by the real waveform with respect to this a-priori modelled delay informs about the correctness of the first guess (Nominal Delay in Fig. 9.4). Then,

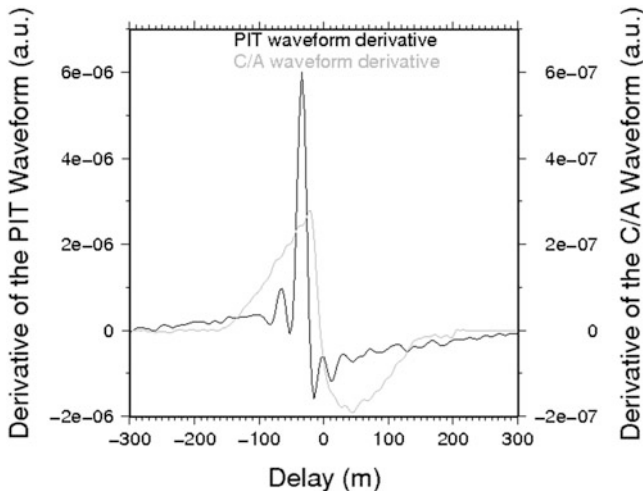


Fig. 9.5 Derivative of the P/T and C/A waveforms shown in Fig. 8.19, with respect to the delay. The delay of the derivative's peak correspond to the delay of the specular ray-path, which is not the delay of the waveform's peak (compare with Fig. 8.19). The PIT technique has better group-delay resolution than the C/A code

the receiver nominal reflected delay $\rho_{nominal}$ needs to be corrected by a delay-shift $\delta\rho$ to obtain the reflected delay ρ : $\rho = \rho_{nominal} + \delta\rho$. The correction is defined as follows, according to different techniques shown in Fig. 9.4:

Peak-Delay: the altimetric range is obtained from the delay of the peak: $\delta\rho = \rho_{peak} - \rho_{nominal}$. This only applies for reflections off smooth surfaces (little diffuse component), such as in Martín-Neira et al. (2001) or Rius et al. (2011);

Model-Fitting: which consists on fitting a theoretical model to the data. The best-fit model implicitly indicates the delay-location where the specular point lies: $\delta\rho = \rho_{model-spec} - \rho_{nominal}$. Examples can be found in e.g. Lowe et al. (2002);

Peak-Derivative: Hajj and Zuffada (2003) suggested and Rius et al. (2010) shown that the maximum of the derivative of the waveform's leading edge corresponds to the specular ray-path delay: $\delta\rho = \rho_{derivative-peak} - \rho_{nominal}$. Two examples of waveforms' derivative made with real data are displayed in Fig. 9.5. They correspond to the derivatives of the waveforms shown in Fig. 8.19, that is, two waveforms taken simultaneously using two different receivers (Rius et al. 2012; Nogués-Correig et al. 2007) from an aircraft flying at 3 km altitude over the Ocean (experimental campaign described in Rius et al. 2012). The peak of these derivatives correspond to the delay of the specular ray-path. Note the different group-delay resolution for C/A and PIT techniques.

The determination of the specular range should be done on a sufficiently integrated waveform, to minimize the effects of the speckle (see Sect. 8.7). In highly

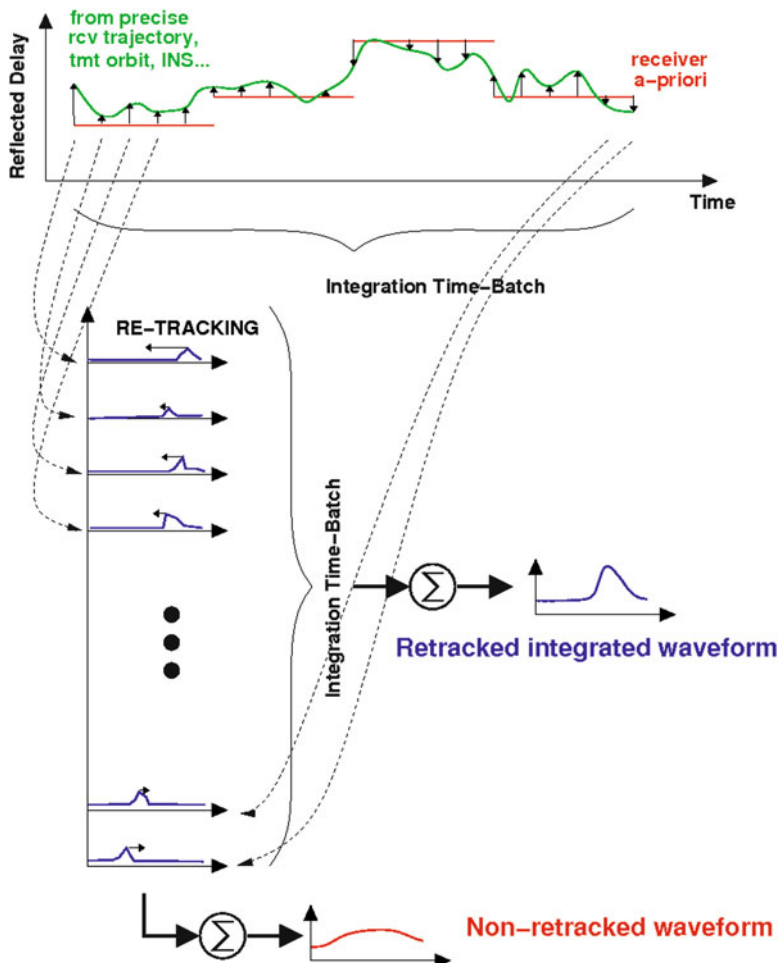


Fig. 9.6 Sketch of the re-tracking concept, to align the individual waveforms before integration, and thus avoid the defocusing introduced by coarse time-batched a-priori delay model used by the receiver

dynamic scenarios (space- and air-based receivers), and whenever the a-priori estimation of the nominal delay by the receiver, or some of its parameters, are not updated as fast as the dynamic changes of the geometric conditions, a re-alignment of the waveforms must be conducted before its integration. This re-alignment uses refined a-posteriori estimates of the involved parameters. This process is called re-tracking, and consists in delay-shifts of each individual waveform with respect to the rest, using the a-posteriori interpolated geometric information (receiver trajectory and attitude, transmitter precise orbits, clock errors information). The concept is illustrated in Fig. 9.6.

9.1.2 Atmospheric Corrections

As described in Chap. 2, the total delay suffered by microwave GNSS signals is affected by the atmosphere: its neutral or dry-component, and the moist or water vapor content of the troposphere, as well as the charged particles confined in the ionosphere.

For altimetric applications of the GNSS-R, as it is for navigation and positioning GNSS applications, these effects need to be corrected. General speaking, the strategy to solve the atmosphere-induced delays in GNSS-R is the same as in standard GNSS positioning. The list below highlights the main differences:

- The GNSS-R ray-path through the atmosphere is two-fold: from the transmitter down to the surface; and from the surface up back to the receiver. For receivers installed at space-based platforms, this means that the signals cross most of the atmosphere twice, including the ionosphere if the LEO is high enough.
- For space-based receivers above or on top of the ionosphere, the ionospheric effect comes from two different regions of the ionospheric layers: the regions are at large distances, of the order of $\sim 2H_{orb} \cos e$ (H_{orb} being the orbital height of the receiver; e the elevation angle of observation).
- For low-altitude receivers, the ionosphere is crossed only once, and the troposphere is partially crossed twice (fully crossed on the way down, partially crossed on the way up). This requires some degree of vertical resolution in the atmospheric information to be used for corrections. Alternatively, a combination of tropospheric mapping functions (Niell 1996) and exponential vertical structure of the troposphere might be a suitable approximation (e.g. Fabra et al. 2011; Cardellach et al. 2011): then, the comp component of the troposphere (dry/wet) can be estimated as $\rho_{atm}^{comp} = \rho_{TS}^{comp} + \rho_{SR}^{comp}$ where subindex TS and SR stand for the atmospheric propagation effects between the transmitter and the surface and between the surface and the receiver, respectively. These depend on the delay produced by that same component of the atmosphere in a zenith-like ray-path through the mapping functions M^{comp} . In order to estimate the correction of the first branch (transmitter-surface), information on atmospheric surface conditions are required to compute its zenith delay from the surface level ($ZD(0)$):

$$\rho_{TS}^{comp} = M^{comp} ZD^{comp}(0) \quad (9.5)$$

See (e.g. Davis et al. 1985) and Chap. 2 for ZD models. The second branch should only account for the atmospheric layer between the surface and the receiver's altitude h :

$$\rho_{SR}^{comp} = M^{comp} ZD^{comp}(0) [1 - e^{-\frac{h}{H_{atm}}}], \quad (9.6)$$

being $H_{atm} \sim 8$ km the typical altitude of the troposphere at the experimental location. This results in the total reflected atmospheric delay due to a given component modelled as

$$\rho_{atm}^{comp} = M^{comp} ZD^{comp}(0) [2 - e^{-\frac{h}{H_{atm}}}] \quad (9.7)$$

If differential delays $\Delta\rho$ are being used instead of total reflected delays ρ , then the theoretical atmospheric delay of the direct radio-link should also be subtracted. The direct atmospheric delay can be estimated from the receiver in static conditions (ground-based experiment): $\rho_{atm-dir}^{comp} = M^{comp} ZD^{comp}(H_{rv})$. Otherwise, when the experimental conditions do not permit to separate the ZD, the exponential model reads

$$\rho_{atm-dir}^{comp} = M^{comp} ZD^{comp}(0) e^{-\frac{h}{H_{atm}}} \quad (9.8)$$

resulting in

$$\Delta rho_{atm}^{comp} = 2M^{comp} ZD^{comp}(0) [1 - e^{-\frac{h}{H_{atm}}}] = 2\rho_{SR}^{comp} \quad (9.9)$$

Comparing with Eq. 9.6, it is clear that this is twice the delay between the surface and the receiver (the effect of the upper part of the atmosphere cancels out when subtracting the direct signal as indicated in Fig. 9.3).

- The ionospheric effects are typically corrected using a particular combination of two-frequency GNSS observations, because of their dispersive nature (see Chaps. 2, 4 and 7) (e.g. Blewitt 1990). No detailed studies have been done to investigate the degree of correctness of applying this same approach to GNSS-R observations. In particular, possible frequency-dependent effects induced by the surface roughness should be studied (for example, it would be worth checking how different frequencies have different sensitivity to slightly different roughness scales, and how this could induce slightly different sampling of the surface facets, resulting in systematically different statistical footprint-averaged delays).
- GNSS-R observations at very slant angles of observations might require the use of ray-tracers to solve for both altimetry and atmospheric corrections simultaneously (e.g. Semmling et al. 2011). An example of ray-tracer operator is given in Jones and Stephenson (1975).

9.1.3 GNSS-R Ocean Altimetric Performance

This section compiles some of the experimental altimetric GNSS-R work conducted. It presents the achieved altimetric performance as claimed by their authors. The performance is given in terms of the measurement precision level, preferably over Ocean waters. Technical aspects such as the type of observable (from group-delay or phase-delay); the code (C/A, P, PIT); and the integration time used for the retrievals are also reported. Other important aspects to scale the performance are the altitude of the receiver during the experiment, as well as the static or dynamic conditions of the experiment. This information is given in Table 9.1.

Table 9.1 Some GNSS-R altimetric experiments and the achieved performance as claimed by their authors. Some of them give the performance for a single satellite observation (S), whereas others indicate the performance of a combined multi-satellite measurement—using several footprints simultaneously (M). The use of code (C/A, P) observation or Interferometric technique (PIT) is also indicated

H_{rcv} (km)	Platf.	Surf.	Code	S/M	σ_H (m)	τ_{int} (s)	Comments
Phase-delay altimetry							
0.480	Static	Lake	C/A	S	0.02	1	Treuhart et al. (2001)
0.008	Static	Pond	C/A	S	0.003	1.0	Wide-lane freq. combination and P Martín-Neira et al. (2002)
400	LEO	Ice	C/A	S	0.7	0.2	Cardellach et al. (2004)
1.025	Static	Lake	C/A	S	0.02	1	Helm et al. (2004)
0.825							
0.7	Static	Ocean	C/A	M	0.5	1,200	Spectral retrievals (Semmling et al. 2012)
Group-delay altimetry							
0.02	Static	Estuary	C/A	M	3.3	5.0	Martín-Neira et al. (2001)
1.5/3	Aircraft	Ocean	P(Y)	M	0.05	2.0	Lowe et al. (2002)
1	Aircraft	Ocean	C/A	S	3/(2sin e)	1	Ruffini et al. (2004)
				M	0.1	400	
3	Aircraft	Ocean	C/A	S	1.4	1	Rius et al. (2010)
0.018	Static	Estuary	PIT	S	0.075	1	Rius et al. (2011)
3	Aircraft	Ocean	PIT	S	0.13	20	Rius et al. (2012)
			C/A	S	0.27	20	

The precision obtained when the surface roughness and dynamical conditions permit to acquire phase-delay observation is of the order of 2 cm, in integration times of 1 s. These results have been reported from different experimental sites, using different processing techniques, and receiver altitudes from a few meter to LEO altitudes. However, these conditions do not always apply. Ocean waters tend to be rough. Novel techniques have been found to permit altimetric observations from phase observables under rougher conditions (up to significant wave heights ≤ 1.2 m Semmling et al. 2012), but even those degrade with respect to calm water scenarios.

Group-delay observables have to be used in most of the Ocean GNSS-R altimetric measurements. Different experiments, using different instrumental set-ups, processing techniques, and even receiver altitudes (up to 3 km), resulted in 1-s, 1 GNSS satellite, C/A group delay altimetric precision of the order of 1 m. Most of these experiments have been conducted with avionic antennas, that is antennas with low-gain hemispherical patterns. Multiple-satellite approaches, higher integration time strategies, and considerations about systematic errors that could be corrected improve significantly the precision.

The use of wide bandwidth codes, such as P(Y), or the PARIS interferometric technique (PIT), which makes use of the whole bandwidth with no need to model the codes, also improve the performance: ~ 7 cm precision in P(Y) airborne

multi-satellite altimetry; 7.5 cm precision for static PIT in 1-s and 1-GNSS satellite; and ~ 0.6 m for 1-s 1-GNSS satellite airborne PIT. Note that the processing of air-borne altimetric campaigns have in general the drawback of trajectories with highly and non-predictable dynamics. Those are sometimes difficult to solve at a few centimeter precision level.

The theoretical expected performance of the PIT technique from space-based, LEO, platforms has been detailed in [Martín-Neira et al. \(2011\)](#). This study assumes much higher antenna gains, and it predicts 13–17 cm precision in 100-km along-track averaging for an in-orbit demonstration mission (23 dBi gain antennas, 800 km orbital height), and 5–7.5 cm from an operational one (30 dBi antennas, 1,500 km orbital height).

9.2 Ocean Surface Roughness

The GNSS, L-band signals, have electromagnetic carrier wavelengths longer than the fine surface ripples generated by instantaneous winds. In principle, only surface features of typical length longer than the electromagnetic carrier wavelength can be sensed, meaning that L-band signals are not in an optimal frequency for wind monitoring. However, as the wind blows, it transfers energy to the Ocean, increasing the waves' height and length. One of the discussions among the GNSS-R community is the strength of the link between GNSS-R observations and wind speed. Some studies adjusted or calibrated the apparent Ocean surface slopes at L-band, in the form of a modified relationship between the variance of the slopes and the wind ([Katzberg et al. 2006](#), Eq. 3), and valid for a wide range of wind speeds. Some others present L-band roughness parameters as a product by itself (e.g. [Cardellach et al. 2003](#); [Germain et al. 2004](#)). Based on [Elfouhaily et al. \(1997\)](#) spectrum, Fig. 9.7 displays different relationships between the variance of the slopes and wind at different stages of development of the sea. It shows that the variance for a given wind speed depends on the stage of development of the sea. On the other hand, the drag coefficient is a relevant parameter to model momentum exchanges between the sea waves and the atmosphere. It can be a function of both the wind speed and the wave age (e.g. [Nordeng 1991](#); [Makin et al. 1995](#)). This opens potential inversion schemes, closer to data assimilation approaches, in which independent wind information could be combined with GNSS-R observations of the L-band roughness to infer information about wave age or dragging-related parameters.

The L-band roughness parameters might also be suitable sea surface descriptors to provide roughness corrections to L-band radiometric missions for improving their sea surface salinity measurements. The L-band radiometric measurements of the surface salinity have a major systematic effect induced by the surface roughness, in particular, to the portion of the spectrum to which L-band signals are sensitive. There are a set of promising studies along these lines, such as [Marchan-Hernandez et al. \(2008\)](#), [Valencia et al. \(2009\)](#), and [Camps et al. \(2011\)](#).

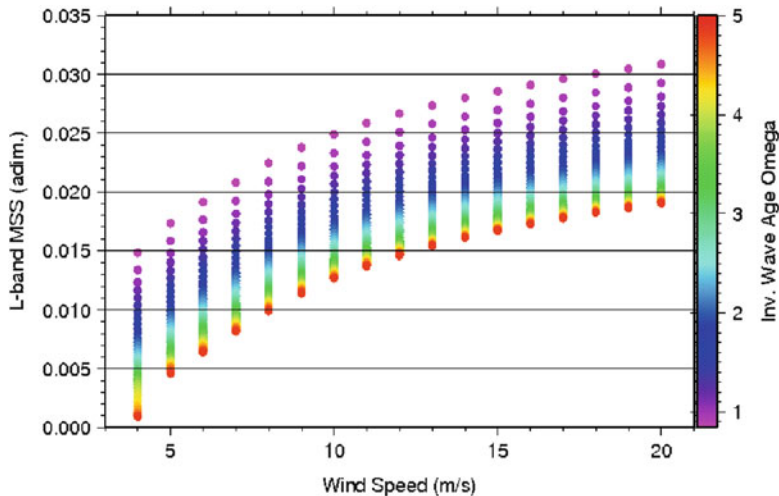


Fig. 9.7 MSS of the Ocean surface (related to slopes' variances, $MSS = 2\sigma_{\text{slopes}}^2$) as sensed using L-band signals, as a function of the wind speed and the inverse wave age (stage of development: fully developed sea for $\Omega \sim 0.84$). The spectrum by Elfouhaily et al. (1997) was used, together with the $3k_{EM}$ criterion to split roughness scales to which L-band should be insensitive

A constellation of 8 GNSS-R small satellites at 35° orbit inclination will monitor Tropicalseas to capture tropical storms and hurricanes as part of the NASA Earth System Science Path-finder program. The mission is called CYClon GNSS (CYGNSS) and it will try to get synoptic information of their wind fields. Most of the inner core Ocean surface of the cyclones is not properly observed by conventional remote sensing instruments because of the intense precipitation in the eye wall and inner rain bands. L-band signals can propagate through heavy rain, reason why CYGNSS observations can contribute understanding the processes that drive the intensity of such storms, and thus help improving the intensity forecasts (which have not improved much in the last 20+ years). The mission is expected to be launch in 2016, and it continues the work of Katzberg et al. (2001), Katzberg et al. (2006), and Katzberg and Dunion (2009).

9.2.1 Surface Modelling

Modelling and inverting GNSS scattering processes requires information about the reflecting surface. It can be given as statistical properties of its slopes (slopes' probability density function in Eq. 8.50), or as actual numerical realizations of the elevation of the surface, z , at a fine grid on the XY plane (integration

points in Eqs. 8.30–8.33, 8.42, or 8.43). In Ocean applications, both statistical characterization and numerical surface realizations can be obtained from the Ocean waves' spectrum.

This section reports about a few popular spectra; then it describes how to use them to model the statistics of the slopes; and finally a brief summary on how to generate numerical realizations of surfaces making use of the spectra.

9.2.1.1 Ocean Wave Spectra

Ocean wave spectra inform about the distribution of the Ocean wave energy density with respect to the waves' temporal or spatial frequencies, as well as their directions. The waves' spatial frequency (wavenumber $k = 2\pi/\lambda$) and the time-frequency spectra can be converted into each other making use of a particular dispersion relation between k and ω . For deep waters (depth larger than half wave's wavelength) the dispersion reads: $\omega = \sqrt{gk}$, so

$$S(k) = S(\omega) \frac{\partial \omega}{\partial k} = S(\omega) \frac{g}{2\omega} \quad (9.10)$$

g being the acceleration due to gravity.

Spectra can be measured for a particular site and epoch, or it can also be modelled as functions of a given set of parameters. Typical parameters that relate to the sea state conditions are the wind and the significant wave height (SWH). Other parameters that can affect the spectrum are the fetch (length of water over which the wind has blown), and stage of development of the sea. The waves grow higher in altitude and longer in period as the wind blows longer or over larger areas. As the wind keeps blowing and the waves keep growing the sea is under developing stage, the so called *developing sea*. However, after some time of steady wind conditions the phase velocity of the waves' crests matches the wind speed, waves and wind reach a point of equilibrium. From this point on, the waves neither grow higher nor increase their period, regardless of the wind duration. The sea is then *fully developed*. When the wind drops it will enter in the *decaying phase*. Many spectra consider fully developed seas solely, but some of them account for the stage of development.

$\Psi(\mathbf{k})$ represents the distribution of the waves' energy as a function of their 2-dimensional wavenumber $\mathbf{k} = 2\pi/\lambda \hat{\mathbf{u}}$. In particular, it is the Fourier transform of the auto-covariance function of the surface displacements

$$\Psi(\mathbf{k}) = FT \{ \langle z(\mathbf{r}_0) z(\mathbf{r}_0 + \mathbf{r}) \rangle \} \quad (9.11)$$

where $z(\mathbf{r})$ is the elevation of the sea surface at coordinates $\mathbf{r} = (x, y)$. The spectrum is normalized so that

$$\sigma_z^2 = \langle z^2 \rangle = \int_{-\infty}^{\infty} \int_{-\infty}^{\infty} \Psi(k_x, k_y) dk_x dk_y = \int_0^{\infty} S(k) dk \quad (9.12)$$

being $S(k)$ the omni-directional spectrum

$$S(k) = \int_{-\pi}^{\pi} \Psi(k, \phi) k d\phi \quad (9.13)$$

The SWH is defined as $SWH = 4\sqrt{\sigma_z^2}$.

The following spectra are a few popular ones. Those given as frequency spectrum can be transformed into wavenumber spectrum using Eq. 9.10.

Pierson-Moskowitz: A simple wave spectrum is the Pierson-Moskowitz spectrum (Pierson and Moskowitz 1964), empirically obtained from measurements in North Atlantic (1964)

$$S_{PM}(\omega) = \frac{\alpha g^2}{\omega^5} e^{-\beta(\frac{g}{\omega U_{19.4}})^4} \quad (9.14)$$

where α and β are constant values $\alpha = 0.0081$, $\beta = 0.74$, and $U_{19.4}$ represents the speed of the wind at 19.4 m altitude. It was revised in Henrique et al. (2003).

JONSWAP: A well-accepted long-wave spectrum after experimental campaigns in the North Sea (Hasselmann et al. 1973), and formulated as a modification of the Pierson-Moskowitz spectrum, and it include limited fetch conditions. It is expected to be a reasonable model for seas with peak period T_p and SWH in the range $3.6\sqrt{SWH} < T_p < 5\sqrt{SWH}$

$$S_J(\omega) = \frac{\alpha g^2}{\omega^5} e^{-\beta(\frac{\omega_p}{\omega})^4} \gamma^r \quad (9.15)$$

where $r = \exp\{-(\omega - \omega_p)^2/(2\sigma^2\omega_p^2)\}$ and ω_p is the peak wave-frequency. The empirical values are: $\omega_p = 22(g^2/(U_{10}F))^{1/3}$; $\gamma = 3.3$; $\sigma = 0.07$ ($\omega \leq \omega_p$) or $\sigma = 0.09$ ($\omega > \omega_p$). U_{10} is the wind speed at 10 m altitude, and F is the fetch length.

Elfouhaily et al.: The directional spectrum suggested in Elfouhaily et al. (1997) is widely used in the GNSS-R community. It is a full wavenumber spectrum to properly describe long and short waves. Both fetch and wave age (stage of development of the sea) are included as input parameters.

$$\Psi(k, \phi) = \frac{1}{2\pi} k^{-4} [B_l + B_h] [1 + \Delta(k) \cos(2\phi)] \quad (9.16)$$

where B_l , B_h , and $\Delta(k)$ are given in (Elfouhaily et al. 1997, Eqs. 31, 40, 57) respectively.

Besides waves generated by the blowing wind, the surface might present waves from distant or past storms, what is called the *swell*. They typically present regular waves of relatively long wavelength. The reason is that long waves travel faster than the short ones, *escaping* from the storm. Typical swell wavelength are of the order of

a few hundreds of meters, with SWH of a few meters (mostly between half and 2 m high, higher values possible). There are no general rules to link swell wavelength and SWH, as illustrated in [Suresh et al. \(2010, Fig. 4\)](#). A possible way to obtain a spectra of given peak wavelength λ_p and given SWH is to play with a simple spectral model (such as Pierson-Moskowitz), setting $k_p = 2\pi/\lambda_p$ and re-normalizing the spectra to obtain the desired SWH. From Eq. 9.12, the re-normalization reads:

$$\frac{\Psi(\mathbf{k})}{4\sqrt{\int_{-\infty}^{\infty} \int_{-\infty}^{\infty} \Psi(k_x, k_y) dk_x dk_y}} SWH \quad (9.17)$$

Note that in this way the steepness of the swell (SWH/λ_p) can be tuned. Steepness seems to be one of the key factors of the dissipation of the swell ([Ardhuin et al. 2009](#)).

Linearity is assumed, and the wind-driven spectrum can be added to the swell-spectrum to obtain the total surface spectrum

$$\Psi^{surface}(\mathbf{k}) = \Psi^{wind}(\mathbf{k}) + \Psi^{swell}(\mathbf{k}) \quad (9.18)$$

9.2.1.2 Surface Slopes Probability

The bi-static scattering coefficient in Eq. 8.50, depends on the slopes' probability density function $PDF(Z_x, Z_y)$. As it is shown below, such probability is usually a function of the mean of the square slopes (MSS). The MSS can be extracted from the slopes' spectrum. The omni-directional slope spectrum is given by

$$k^2 S(k) \quad (9.19)$$

whereas the spectra of the slope along the X and Y directions are

$$k_x^2 \Psi(\mathbf{k}) \quad (9.20)$$

$$k_y^2 \Psi(\mathbf{k}) \quad (9.21)$$

respectively. Therefore, the mean of the square slope along the X-direction, $MSS_x = \sigma_{Z_x}^2$ is

$$MSS_x = \int_{-\infty}^{\infty} \int_{-\infty}^{\infty} k_x^2 \Psi(\mathbf{k}) dk_x dk_y \quad (9.22)$$

Similarly for the slopes along the Y-direction, $MSS_y = \sigma_{Z_y}^2$:

$$MSS_y = \int_{-\infty}^{\infty} \int_{-\infty}^{\infty} k_y^2 \Psi(\mathbf{k}) dk_x dk_y \quad (9.23)$$

The total MSS or omni-directional slope is

$$MSS = \int_{-\infty}^{\infty} \int_{-\infty}^{\infty} (k_x^2 + k_y^2) \Psi(\mathbf{k}) dk_x dk_y = MSS_x + MSS_y \quad (9.24)$$

This last equation reduces to $MSS = 2\sigma_{slopes}^2$ in isotropic cases.

It is important to highlight that Eqs. 9.22–9.24 give the statistics of the slopes accounting for all the waves' scales. However, GNSS L-band signals have electro-magnetic wavelengths of the order of ~ 0.2 m and they are in principle insensitive to roughness scales smaller than the electromagnetic wavelength. The heuristic criterion proposed by Brown (1978) to set the upper bound of the integral, based on satellite-based measurements of microwave back-scattering cross-sections, is $k \leq 3k_{EM}$ (being k_{EM} the electrognanetic carrier wavenumber). Optimized expressions of this bound, for airborne GPS signals, were given in Thompson et al. (2005). Figure 9.7 shows the L-band MSS as a function of the wind speed and inverse wave age (stage of development), using the spectrum in Elfouhaily et al. (1997), and applying the $3k_{EM}$ criterion.

The most used distributions are the Gaussian in isotropic cases; 2D bivariate normal distribution for anisotropic scenarios; or 2D Gram-Charlier distribution for higher order effects.

Bivariate normal distribution: This distribution is suitable for anisotropic seas, but it does not account for up/down-wind asymmetries. Being M the slopes' covariance matrix

$$M = \begin{pmatrix} \kappa_{20} & \kappa_{11} \\ \kappa_{11} & \kappa_{02} \end{pmatrix} = Rot(\phi_w) \begin{pmatrix} \kappa_w & 0 \\ 0 & \kappa_c \end{pmatrix} Rot(\phi_w)^{-1} \quad (9.25)$$

where κ_w and κ_c are variances in the up/down wind direction and cross-wind direction respectively; $Rot(\phi_w)$ is the rotation matrix by the angle ϕ_w defined between the up-wind direction and the X-axis; the slopes distribution reads

$$PDF^{normal}(Z_x, Z_y) = \frac{1}{2\pi \sqrt{Det(M)}} e^{-\frac{1}{2}(Z_x, Z_y) M^{-1} \begin{pmatrix} Z_x \\ Z_y \end{pmatrix}} \quad (9.26)$$

It reduces to a Gaussian distribution under isotropic cases, when $\kappa_{20} = \kappa_{02}$ and $\kappa_{11} = 0$.

Gram-Charlier distribution: It was suggested in Cox and Munk (1954) after the analysis of photographic observations of the Sun glitter, where deviations from a normal two-dimensional Gaussian distribution were detected. The distribution accounts for skewness and peakedness in the statistics of the slopes. The skewness terms are sensitive to asymmetries induced by up/down-wind features.

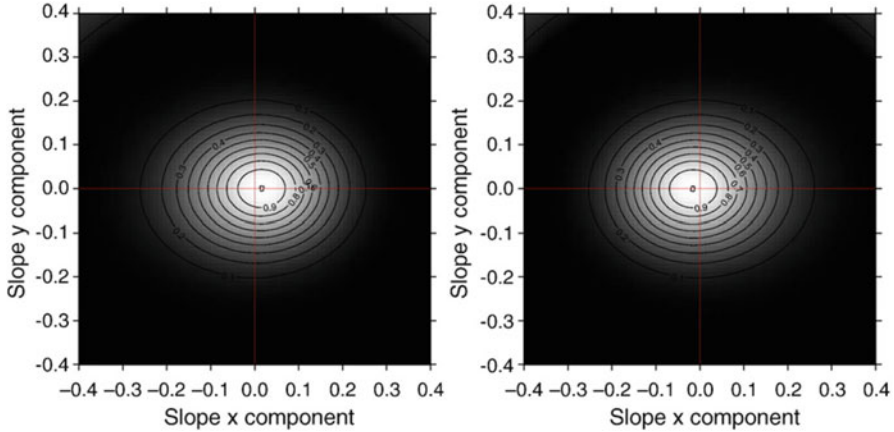


Fig. 9.8 Gram-Charlier distribution for two identical cases (wind set to 8 m/s, along the X-axis), but 180° shift in the wind direction. On the *left panel* the down-wind direction points towards positive X, while it points towards negative X on the *right panel*. Bivariate normal distributions do not present these asymmetries along the wind direction

$$PDF^{GC}(Z_x, Z_y) = PDF^{normal}(Z_x, Z_y) \left[1 - \frac{1}{2} C_{21} \left(\frac{Z_x^2}{\sigma_{Z_x}^2} - 1 \right) \frac{Z_y}{\sigma_{Z_y}} - \right] \quad (9.27)$$

$$- \frac{1}{6} C_{03} \left(\frac{Z_y^3}{\sigma_{Z_y}^3} - 3 \frac{Z_y}{\sigma_{Z_y}} \right) + \frac{1}{24} C_{40} \left(\frac{Z_x^4}{\sigma_{Z_x}^4} - 6 \frac{Z_x^2}{\sigma_{Z_x}^2} + 3 \right) + \quad (9.28)$$

$$+ \frac{1}{4} C_{22} \left(\frac{Z_x^2}{\sigma_{Z_x}^2} - 1 \right) \left(\frac{Z_y^2}{\sigma_{Z_y}^2} - 1 \right) + \frac{1}{24} C_{04} \left(\frac{Z_y^4}{\sigma_{Z_y}^4} - 6 \frac{Z_y^2}{\sigma_{Z_y}^2} + 3 \right) + \dots \quad (9.29)$$

Figure 9.8 shows the up/down-wind features captured by a 2D Gram-Charlier distribution.

9.2.1.3 Surface Generation

For studies of phase-related behavior of the scattering, it might be interesting to model the surface as realistic numerical realizations of its fine topography (elevation z as function of the horizontal coordinates $z(x, y)$). Some polarization issues, not well-solved by the KGO approach, might also require Montecarlo-like simulations based on scattering integrals (e.g. Eqs. 8.42, or 8.43) off realistic surfaces.

Realizations of the surface elevation can be obtained from Inverse Fourier Transforms of the squared root of the wavenumber spectra:

$$z(\mathbf{r}) = \mathbb{R} \left\{ IFT \left\{ \sqrt{2\Psi(\mathbf{k})} e^{i \phi(\mathbf{k})} \right\} \right\} \quad (9.30)$$

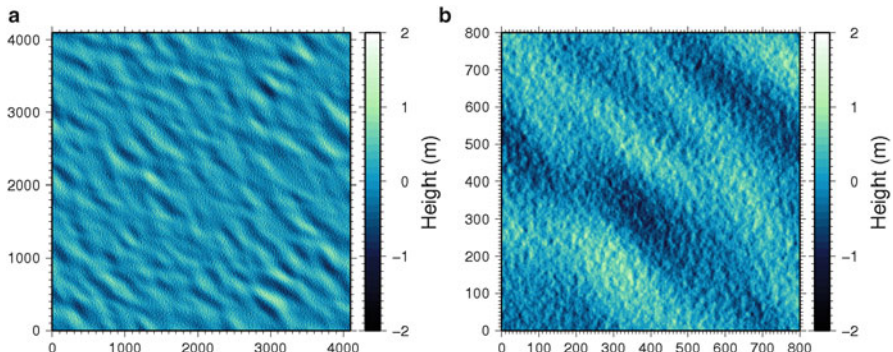


Fig. 9.9 Example of a particular numerical realization of the surface topography. It has been made with the wind-driven waves' spectrum in Elfouhaily et al. (1997), fully developed, 6 m/s along the X-direction. A swell of $\lambda_p = 400$ m and $SWH = 1$ and 50° direction has been added using Pierson-Moskowitz spectrum. A close-up is displayed on the right panel. X- and Y-axis annotations are given in meter

where a random arbitrary phase is added to each wavenumber, $\phi(\mathbf{k})$, and the real part \Re is taken. It is worth checking the normalization (see Eq. 9.17) as well as the MSS to detect any possible problem in the definition of the used wavenumber spectra. Figure 9.9 presents a numerical realization of a surface topography with both wind-driven waves and swell obtained from Eq. 9.30, using (Elfouhaily et al. 1997) spectrum for wind-driven waves, and Pierson-Moskowitz for long peak wavelength to model the swell.

Because of the speckle, which induces noise proportional to the power (Sect. 8.7), the scattering off one single realization is not significant, but large ensembles are required.

9.2.2 Retrieval Approaches

This section compiles some of the GNSS-R Ocean surface roughness inversion techniques applied so far, mostly to extract surface winds and MSS. In particular, some approaches extract the wind speed, some others wind vector; isotropic MSS; 2D-MSS; and discrete and non-parameterized slopes' PDF. Other studies do not seek the inversion into an Oceanographic parameter, but a direct link to another remote sensing technique: roughness corrections required in L-band radiometry in order to properly extract surface salinity.

The techniques are briefly described below, and terminology for GNSS-R observables follows the one given in Sect. 8.10:

DM-fit: After re-normalizing and re-aligning the delay-waveform, the best fit against a theoretical model gives the best estimate for the geophysical and

instrumental-correction parameters. Depending on the model used for the fit, the geophysical parameters can be 10-m altitude wind speed, or sea surface slopes' variance (mean square slopes–MSS). Some of the works done with this methodology are: (e.g. [Katzberg et al. 2001](#); [Garrison et al. 2002](#); [Cardellach et al. 2003](#); [Komjathy et al. 2004](#))

Multiple-satellite DM-fit: extends the DM-fit inversion to several simultaneous satellite reflection observations, which resolves the anisotropy (wind direction or directional roughness ([Armatys 2001](#); [Komjathy et al. 2004](#))).

DDM-fit: The fit is performed on a delay-Doppler waveform ([Germain et al. 2004](#)). In this way, anisotropic information can be obtained from a single satellite observation.

Trailing-edge: As suggested from theoretical models in [Zavorotny and Voronovich \(2000\)](#) and [Garrison et al. \(2002\)](#) implements in real data a technique in which the fit is performed on the slope of the trailing edge, given in dB.

Delay and Doppler spread: [Elfouhaily et al. \(2002\)](#) developed a stochastic theory that results in two algorithms to relate the sea roughness conditions with the Doppler spread (IDS in Sect. 8.10) and the delay spread (IDM in Sect. 8.10) of the reflected signals. The technique was applied to LEO-based GNSS-R observations taken from one of the UK-DMC satellites ([Gleason 2006](#)), where 5 GNSS-R measured IDS correlated with the MSS records taken by nearby Buoys.

Scatterometric-delay: For a given geometry, the delay between the range of the specular point and the range of the peak of the reflected delay-waveform is nearly linear with MSS. This fact is used to retrieve MSS ([Nogués-Correig et al. 2007](#); [Rius et al. 2010](#)).

DDM Area/Volume: Simulation work in [Marchan-Hernandez et al. \(2008\)](#) indicates that the volume and the area of the delay-Doppler maps are related to the changes in the brightness temperature of the ocean induced by the roughness. The hypothesis has been experimentally confirmed in [Valencia et al. \(2009\)](#). This approach might be valuable for potential use of GNSS-R observations in support to Oceanic L-band radiometric missions.

Discrete-PDF: When the bi-static radar equation for GNSS signals is re-organized in a series of terms, each depending on the surface's slope Z' , the system is linear with respect to the Probability Density Function (PDF) of the slopes. Discrete values of the PDF(Z') are therefore obtained. This retrieval does not require an analytical model for the PDF (no particular statistics assumed). When the technique is applied on delay-Doppler-maps, is it possible to obtain the directional roughness, together with other non-Gaussian features of the PDF (such as up/down-wind separation [Cardellach and Rius \(2008\)](#)). An example is given in Fig. 9.10.

Coherence-time: Finally, when the specular component of the scattering is significant (very low altitude observations, very slant geometries, or relatively calm waters), the coherence-time of the interferometric complex field depends on the sea state. It is then possible to develop the algorithms to retrieve significant wave height ([Soulat et al. 2004](#); [Valencia et al. 2010](#)).

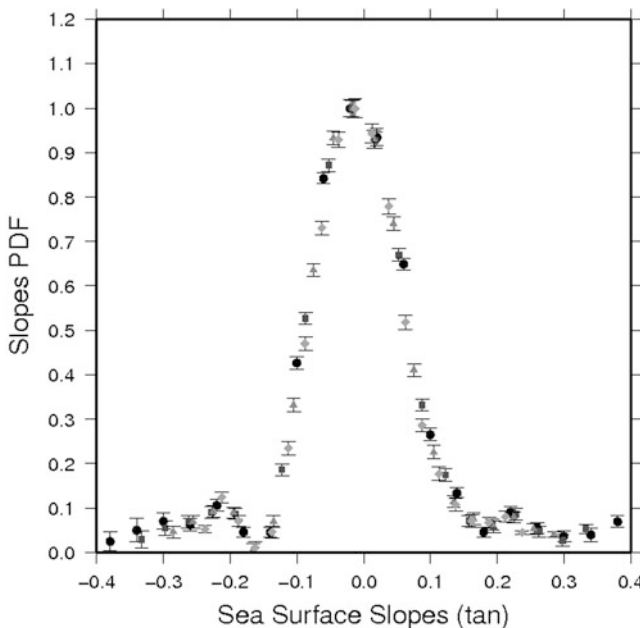


Fig. 9.10 Example of a slopes' PDF retrieved without parameterization, but as a set of discrete unknowns, from real air-borne GNSS-R data. Non-Gaussian features can be seen, most importantly the $+/-$ asymmetry, linked to *up/down-wind* surface imprints (Image from [Cardellach and Rius \(2008\)](#), where the concrete meaning of negative slopes and further details can be obtained)

References

- Ardhuin F, Chapron B, Collard F (2009) Observation of swell dissipation across Oceans. *Geophys Res Lett* 36:L06607. doi:10.1029/2008GL037030
- Armatys M (2001) Estimation of sea surface winds using reflected GPS signals. Ph.D. thesis, University of Colorado
- Blewitt G (1990) An automatic editing algorithm for GPS data. *Geophys Res Lett* 17(3):199–202
- Brown GS (1978) Backscattering from a Gaussian-distributed, perfectly conducting rough surface. *IEEE Trans Antennas Propag AP-26*:472–482
- Camps A, Marchan JF, Valencia E, Ramos I, Bosch-Lluis X, Rodriguez N, Park H, Alcayde A, Mollfulleda A, Galindo J, Martinez P, Chavero S, Angulo M, Rius A (2011) PAU instrument aboard INTA MicroSat-1: a GNSS-R demonstration mission for sea state correction in L-band radiometry. In: Proceedings of IEEE geoscience remote sensing symposium (IGARSS), Vancouver, pp 4126–4129. doi:10.1109/IGARSS.2011.6050141
- Cardellach E, Rius A (2008) A new technique to sense non-Gaussian features of the sea surface from L-band bi-static GNSS reflections. *Remote Sens Environ* 112:2927–2937. doi:10.1016/j.rse.2008.02.003
- Cardellach E, Ruffini G, Pino D, Rius A, Komjathy A, Garrison JL (2003) Mediterranean balloon experiment: Ocean wind speed sensing from the stratosphere using GPS reflections. *Remote Sens Environ* 88(3):351–362

- Cardellach E, Ao CO, de la Torre-Juárez M, Hajj GA (2004) Carrier phase delay altimetry with GPS-reflection/occultation interferometry from low Earth orbiters. *Geophys Res Lett* 31(10):L10402
- Cardellach E, Fabra F, Nogués-Correig O, Oliveras S, Ribó S, Rius A (2011) GNSS-R ground-based and airborne campaigns for Ocean, land, ice, and snow techniques: application to the GOLD-RTR data sets. *Radio Sci* 46:RS0C04. doi:10.1029/2011RS004683
- Chapron B, Vandemark D, Elfouhaily T, Thompson DR, Gaspar P, LaBroue S (2001) Altimeter sea state bias': a new look at global range error estimates. *Geophys Res Lett* 28(20):3947–3950
- Cox C, Munk W (1954) Measurements of the roughness of the sea surface from photographs of the Sun's glitter. *J Opt Soc Am* 44(11):838–850
- Davis JL, Herring TA, Shapiro II, Rogers AEE, Elgered G (1985) Geodesy by radio interferometry: effects of atmospheric modeling errors on estimates of baseline length. *Radio Sci* 20(6):1593–1607
- Elfouhaily T, Chapron B, Katsaros K, Vandemark D (1997) A unified directional spectrum for long and short wind-driven waves. *J Geophys Res* 102(C7):15781–15796
- Elfouhaily T, Thompson DR, Linstrom L (2002) Delay-Doppler analysis of bistatically reflected signals from the Ocean surface: theory and application. *IEEE Trans Geosci Remote Sens* 40:560–573. doi:10.1109/TGRS.2002.1000316
- Fabra F, Cardellach E, Rius A, Oliveras S, Nogués-Correig O, Belmonte-Rivas M, Semmling M, D'Addio S (2011) Phase altimetry with dual polarization GNSS-R over sea-ice. *IEEE Trans Geosci Remote Sens* 50(6):10. November, doi:10.1109/TGRS.2011.2172797
- Garrison JL, Komjathy A, Zavorotny VU, Katzberg SJ (2002) Wind speed measurement using forward scattered GPS signals. *IEEE Trans Geosci Remote Sens* 40(1):50–65
- Germain O, Ruffini G, Soulard F, Caparrini M, Chapron B, Silvestrin P (2004) The eddy experiment: GNSS-R speculometry for directional sea-roughness retrieval from low-altitude aircraft. *Geophys Res Lett* 31:L21307. doi:10.1029/2004GL020991
- Gill AE (1982) Atmosphere-Ocean dynamics. International geophysics series, vol 30. Academic Press, San Diego
- Gleason S (2006) Remote sensing of Ocean, ice, and land surfaces using bistatically scattered GNSS signals from low Earth orbit. Ph.D. thesis, University of Surrey
- Hajj G, Zuffada C (2003) Theoretical description of a bistatic system for Ocean altimetry using the GPS signal. *Radio Sci* 38(5):1089
- Hasselmann K, Barnett TP, Bouws E, Carlson H, Cartwright DE, Enke K, Ewing JA, Gienapp H, Hasselmann DE, Kruseman P, Meerburg A, Miller P, Olbers DJ, Richter K, Sell W, Walden H (1973) Measurements of wind-wave growth and swell decay during the joint North Sea wave project (JONSWAP). *Dtsch Hydrogr Z* 12:95
- Helm A, Beyerle G, Nitschke M (2004) Detection of coherent reflections with GPS bipath interferometry. <http://arxiv.org/pdf/physics/0407091v1.pdf>
- Henrique J, Alves GM, Banner ML, Young IR (2003) Revisiting the Pierson-Moskowitz asymptotic limits for fully developed wind waves. *J Phys Oceanogr* 33:1301–1323
- Jones R, Stephenson J (1975) A versatile three-dimensional ray tracing computer program for radio waves in the ionosphere. OT report 75–76. National Geophysical Data Center, Boulder
- Katzberg SJ, Dunion J (2009) Comparison of reflected GPS wind speed retrievals with dropsondes in tropical cyclones. *Geophys Res Lett* 36:L17602. doi:10.1029/2009GL039512
- Katzberg SJ, Walker RA, Roles JH, Lynch T, Black PG (2001) First GPS signals reflected from the interior of a tropical storm: preliminary results from Hurricane Michael. *Geophys Res Lett* 28(10):1981–1984
- Katzberg SJ, Torres O, Ganoe G (2006) Calibration of reflected GPS for tropical storm wind speed retrievals. *Geophys Res Lett* 33:L18602. doi:10.1029/2006GL026825
- Komjathy A, Armatys M, Masters D, Axelrad P (2004) Retrieval of Ocean surface wind speed and wind direction using reflected GPS signals. *J Atmos Ocean Technol* 21:515–526
- Le Traon PY, Dibarbouré G, Ruffini G, Cardellach E (2002) Mesoscale Ocean altimetry requirements and impact of GPS-R measurements for Ocean mesoscale circulation mapping. eprint arXiv:physics/0212068

- Lowe ST, Zuffada C, Chao Y, Kroger P, Young LE, LaBrecque JL (2002) 5-cm-precision aircraft Ocean altimetry using GPS reflections. *Geophys Res Lett* 29(10):1375. doi:10.1029/2002GL014759
- Makin VK, Kudryavtsev VN, Mastenbroek C (1995) Drag of the sea surface. *Bound Layer Meteorol* 73:159–182
- Marchan-Hernandez J, Rodriguez-Alvarez N, Camps A, Bosch-Lluis X, Ramos-Perez I, Valencia E (2008) Correction of the sea state impact in the L-band brightness temperature by means of delay-doppler maps of global navigation satellite signals reflected over the sea surface. *IEEE Trans Geosci Remote Sens* 46:2914–2923
- Martín-Neira M (1993) A passive reflectometry and interferometry system (PARIS): application to Ocean altimetry. *ESA J* 17:331–355
- Martín-Neira M, Caparrini M, Font-Rosselló J, Lannelongue S, Vallmitjana CS (2001) The PARIS concept: an experimental demonstration of sea surface altimetry using GPS reflected signals. *IEEE Trans Geosci Remote Sens* 39:142–149
- Martín-Neira M, Colmenarejo P, Ruffini G, Serra C (2002) Altimetry precision of 1 cm over a pond using the wide-lane carrier phase of GPS reflected signals. *Can J Remote Sens* 28(3):394–403
- Martín-Neira M, D'Addio S, Buck C, Flouri N, Prieto-Cerdeira R (2011) The PARIS Ocean altimeter in-orbit demonstrator. *IEEE Trans Geosci Remote Sens* 49(6, part 2):2209–2237. doi:10.1109/TGRS.2010.2092431
- Niell A (1996) Global mapping functions for the atmospheric delay at radio wavelengths. *J Geophys Res* 101:3227–3246. doi:10.1029/95JB03048
- Nogués-Correig O, Galí EC, Campderròs JS, Rius A (2007) A GPS-reflections receiver that computes Doppler/delay maps in real time. *IEEE Trans Geosci Remote Sens* 45:156–174
- Nordeng TE (1991) On the wave age dependent drag coefficient and roughness length at sea. *J Geophys Res* 96(C4):7167–7174
- Pierson WJ, Moskowitz L (1964) A proposed spectral form for fully developed wind seas based on the similarity theory of A.A. Kitagorodskii. *J Geophys Res* 69:5181–5190
- Rius A, Aparicio JM, Cardellach E, Martín-Neira M, Chapron B (2002) Sea surface state measured using GPS reflected signals. *Geophys Res Lett* 29:37
- Rius A, Cardellach E, Martín-Neira M (2010) Altimetric analysis of the sea surface GPS reflected signals. *IEEE Trans Geosci Remote Sens* 48(4):2119–2127. doi:10.1109/TGRS.2009.2036721
- Rius A, Cardellach E, Oliveras S, Valencia E, Park H, Camps A, van der Marel H, van Bree R, Altena B, Nogués-Correig O, Ribó S, Tarongí J, Martín-Neira M (2011) Altimetry with GNSS-R interferometry: first proof of concept experiment. *GPS Solut* 1–11. doi:10.1007/s10291-011-0225-9
- Rius A, Fabra F, Ribó S, Arco Fernandez JC, Oliveras S, Cardellach E, Camps A, Nogués-Correig O, Kainulainen J, Rohue E, Martín-Neira M (2012) PARIS interferometric technique proof of concept: sea surface altimetry measurements. In: Proceedings of IEEE international geoscience and remote sensing symposium (IGARSS) 2012, Munich, pp 7067–7070. doi:10.1109/IGARSS.2012.6352035
- Ruffini G, Soulat F, Caparrini M, Germain O, Martín-Neira M (2004) The eddy experiment: accurate GNSS-R Ocean altimetry from low altitude aircraft. *Geophys Res Lett* 31:L12306. doi:10.1029/2004GL019994
- Semmling M, Beyerle G, Stosius R, Dick G, Wickert J, Fabra F, Cardellach E, Ribó S, Rius A, Helm A (2011) Detection of arctic Ocean tides using interferometric GNSS-R signals. *Geophys Res Lett.* doi:10.1029/2010GL046005
- Semmling M, Schmidt T, Wickert J, Schön S, Fabra F, Cardellach E, Rius A (2012) On the retrieval of the specular reflection in GNSS carrier observations for Ocean altimetry. *Radio Sci* 47:RS6007. doi:10.1029/2012RS005007
- Soulat F, Caparrini M, Germain O, Lopez-Dekker P, Taani M, Ruffini G (2004) Sea state monitoring using coastal GNSS-R. *Geophys Res Lett* 31:L21303
- Stosius R, Beyerle G, Helm A, Hoechner A, Wickert J (2010) Simulation of space-borne tsunami detection using GNSS-Reflectometry applied to tsunamis in the Indian Ocean. *Nat Hazards Earth Syst Sci* 10:1359–1372. doi:10.5194/nhess-10-1359-2010

- Suresh RRV, Annapurnaiah K, Reddy KG, Lakshmi TN, Balakrishnan Nair TM (2010) Wind sea and swell characteristics off East Coast of India during Southwest Monsoon. *Int J Oceans Oceanogr* 4(1):35–44
- Thompson DR, Elfouhaily TM, Garrison JL (2005) An improved geometrical optics model for bistatic GPS scattering from the Ocean surface. *IEEE Trans Geosci Remote Sens* 40(1):2810–2821
- Treuhhaft RN, Lowe ST, Zuffada C, Chao Y (2001) Two-cm GPS altimetry over Crater Lake. *Geophys Res Lett* 28(23):4343–4346
- Valencia E, Marchan-Hernandez JF, Camps A, Rodriguez-Alvarez N, Tarongi JM, Piles M, Ramos-Perez I, Bosch-Lluis X, Vall-llossera M, Ferre P (2009) Experimental relationship between the sea brightness temperature changes and the GNSS-R delay-Doppler maps: preliminary results of the albatross field experiments. *IEEE Proc IGARSS III*:741–744. doi:10.1109/IGARSS.2009.5417871
- Valencia E, Camps A, Marchan-Hernandez JF, Rodriguez-Alvarez N, Ramos-Perez I, Bosch-Lluis X (2010) Experimental determination of the Sea correlation time using GNSS-R coherent data. *IEEE Geosci Remote Sens Lett* 7(4):675–679. doi:10.1109/LGRS.2010.2046135
- Zavorotny VU, Voronovich AG (2000) Scattering of GPS signals from the Ocean with wind remote sensing application. *IEEE Trans Geosci Remote Sens* 38:951–964

Chapter 10

Hydrology and Vegetation Remote Sensing

10.1 Introduction

Soil moisture content is one of important land parameters in hydrology, climatology, agriculture vegetation, which provides useful information for energy balance and crop yield expectation and plays an important role in the interaction between continental surfaces and atmosphere (Njoku and Entekhabi 1996). Microwave remote sensing has advantages with all weather detection, day-night ability and penetration through a medium. The wavelength of microwave electromagnetic wave is between 1 and 100 cm. The commonly used bands are: X (~ 0.8 cm), K (~ 3 cm), C (~ 5 cm), S (~ 10 cm), L (~ 20 cm) and P (~ 50 cm). Microwave remote sensing is good for soil moisture observations, especially at P-band (0.775 GHz, ~ 50 cm) and L-band (1.4GHz, ~ 20 cm), where the atmospheric attenuation is reduced and vegetation penetration is better at L-band (Njoku and Entekhabi 1996; Jackson et al. 1996).

The real part of dielectric constant of water is about 80, while dry soil is almost 3.5. When the soil is wetter, it is the increase of dielectric constant and the decrease of emissivity or increase of reflectivity. The basic reason for microwave soil moisture detection is the larger dielectric constant differences between water and dry soil (Njoku and Entekhabi 1996).

The dielectric constant is the permittivity ratio of a substance to free space (Njoku and Entekhabi 1996; Ulaby et al. 1981). It is also called dielectric permittivity (ϵ^*), which is a complex function with real and imaginary components. The real part can also be expressed as the relative permittivity, which is a function of frequency and the ratio of the electric-field storage capacity to that of free space. The imaginary part is usually expressed in terms of dielectric losses. The real part decreases with increasing frequency and dispersive losses, free water relaxation and bound water relaxation losses are all included in dispersive losses. In theory, dielectric constant is subject to the following factors:

1. The incident wave frequency, temperature, salinity.
2. volumetric moisture constant of soil

3. fraction between free water and bound water
4. buck density
5. shape of soil grain;
6. The shape of the impurities in the water

In fact, dielectric constant is mostly affected by soil moisture, and soil texture has little effects. GNSS satellites orbiting at 20,000 km altitude transmit low signal-to-noise (SNR) L band frequencies. After reflecting from the Earth's surface, the signals' polarization is mostly swapped and the correlation function is distorted (Cardellach et al. 2011). Therefore, GNSS-R is essentially a kind of microwave remote sensing working at L-band, which could remotely sense the hydrology and vegetation.

10.2 Hydrology GNSS-Reflectometry

Nowadays, airborne and space borne radiometers (passive) and radars (active) are commonly used for soil moisture remotes sensing. However, they have their own advantages and disadvantages. Radiometers measure the apparent temperature of surface, and soil moisture is retrieved from its emissivity. Radiometric measurements are less sensitive to surface roughness, but are influenced by background temperature and increasing susceptible to man-made radio frequency interference (RFI). The temporal resolution is high and the data processing is simple, but its spatial resolution is low (Jackson et al. 1996; Masters 2004). Compared with radiometers, monostatic radars are less sensitive to soil moisture, and backscattering coefficient is affected mainly by the surface characteristic, such as surface roughness, dielectric constant of soil, and vegetation construction. Furthermore, data processing is complex and time resolution is low (Jackson et al. 1996; Masters 2004). However, combining radiometer and monostatic radar is another applicable method for surface soil moisture retrieval (Shi et al. 2012).

In order to retrieve global soil moisture, ESA and NASA have launched and will launch L-band space-borne Soil moisture and ocean salinity (SMOS) mission (Kerr et al. 2001) and Soil Moisture Active and Passive mission (SMAP) (Entekhabi et al. 2010), respectively. Their spatial resolutions are in kilometer scale. But these space borne missions require a global network of stations, which can provide in situ measurements of soil moisture with better temporal and spatial resolutions. Of course, there are some limitations for the current available ground-based experiments. As for large scale (about 300 m in diameters), cosmos neutron can provide soil moisture estimation at several centimeter depth. As for small scale (about 50 cm in diameter), GNSS-R technique can provide soil moisture measurement at the 0 ~ 5 cm depth, which is much similar with SMOS and SMAP data sets (Larson et al. 2008a).

GNSS-R can provide an efficient method to calibrate and validate the space borne missions and measure the intermediate soil moisture as a new remote sensing tool. As it is well known, the fundamental basis for GNSS-R soil moisture sensing is

similar with other microwave remote sensing technique. However, it has unique advantages below (Zavorotny and Voronovich 2000a):

1. GNSS can provide longtime, stable and free signals and GNSS-R receiver is passive, small size, light weight and low power consumption;
2. GNSS working at L-band (1.57542 GHz and 1.22760 GHz) is suitable for soil moisture retrieval;
3. Compared with microwave radiometry, thermal variation of background does not contaminate GNSS reflected signals;
4. GNSS-R receiver can simultaneously receiving multiple satellite signals in the field of view, and greatly improve the spatial and temporal resolution;
5. GNSS-R receiver has self-positioning and self-timing capabilities with easily accessing geographic information network, and therefore it is easy to set up a wide range of soil moisture observation network.

Therefore, GNSS-R remote sensing is able to create a low-cost global soil moisture network monitoring system, validate and calibrate the space borne remote sensing data sets.

In addition, vegetation cover is one of the difficult problems that should be considered in soil moisture estimation. Meanwhile, GNSS-R with low-cost, small power consumption, high spatial and temporal resolution and some other advantages make it possible for vegetation parameters monitoring, such as vegetation biomass and vegetation growth condition monitoring.

10.3 Hydrology Sensing from GNSS-R

GNSS-R for hydrology sensing is a new and promising tool. For example, Zavorotny and Voronovich (2000a) established the quantitative relationship between soil moisture and the received waveforms. Rodriguez-Alvarez et al. (2011) have developed a ground-based SMIGOL reflectometry. Interference pattern technique (IPT) was used to retrieve land geophysical parameters, such as surface topography, soil moisture and vegetation height, et al. In addition, the GPS receivers commonly used in geodesy and geophysics is also used for soil and vegetation studies from GPS multipath information (Larson et al. 2010). Meanwhile, the microwave scattering models are used to do theoretical analysis of vegetation biomass or study GNSS-R reflected signals' polarization properties. In the following, the commonly used methods for land geophysical parameters are introduced.

10.3.1 Waveform Correlation

Scattering model, Z-V model, was previously used for calculations of GPS ocean reflections in order to obtain the correlation function and the correlation power of

the sea surface waveforms (Zavorotny and Voronovich 2000b). It is the integral form of bistatic radar equation as.

$$P = \iint_A \frac{G^2 \Lambda^2 |S|^2}{4\pi R_{ts}^2 R_{rs}^2} \delta^\circ d\rho \quad (10.1)$$

where A is the integral area, Λ is the correlation function used to define Fresnel Zone, S is the Doppler filter function and Doppler zone is inferred, and G is the antenna's effective coverage zone. As for ocean part, δ° is calculated from ocean surface scattering using GO model (Zavorotny and Voronovich 2000b). In 2000, Zavorotny and Voronovich (2000a) extended the method toward remote sensing of soil moisture and pointed out that GPS scattering signals would provide good opportunities for soil moisture remote sensing from aircrafts and satellites. The peak of reflection signals is correlated with soil moisture and its tail is affected by the surface roughness. Zavorotny and Voronovich (2000a) assume that direct signals are RHCP and the down-looking antenna is omnidirectional LHCP. Elevation angle of 40° is considered. Theoretical simulations show good sensitivity to soil moisture, but directly retrieving soil moisture from waveforms would be difficult due to the surface roughness effect. The polarimetric ratios (HR/VR and LR/RR) were introduced to overcome surface roughness effect. Theoretical simulations HR/VR had demonstrated better performance than LR/RR ratio especially at low to moderate values of the moisture content (Zavorotny and Voronovich 2000a).

10.3.2 Interference Pattern Technique (IPT)

Spanish researchers of UPC have been doing land geophysical parameters retrieval using the interference pattern technique (IPT) (Rodriguez-Alvarez et al. 2011). IPT measures the interference of the direct and the reflected signals, which has been successfully retrieved the surface topography, vegetation height and soil moisture in vegetation-covered soils. Ground-based instrument Soil Moisture Interference-pattern GNSS Observations at L-band (SMIGOL) reflectometry was developed during 2008 and had been used in the experimental campaigns to test the theoretical results. Different from the previous works using LHCP antennas, when a LHCP was used, soil moisture information could not be fully detected and the vertical polarization antenna pointing to the horizon was used. The direct and reflected signals performed interference automatically at the antenna (Rodriguez-Alvarez et al. 2011). The received signals were a function of elevation and azimuth angles of GPS satellite positions. These angles vary in time as GPS satellites move. Surface's topography was the first time retrieved as a function of elevation and azimuth angles of satellite. To revisit the same surface scenarios, 3 h were used. SMIGOL can be located at different heights over the surface. But the maximum height should make sure that the direct and reflected signals must be added coherently at the antenna, which means that the direct and reflected signals must arrive within the same GPS chip interval.

The IPT has been successfully used to implement three kinds of retrievals: surface topography (Rodriguez-Alvarez et al. 2009a), vegetation height (Rodriguez-Alvarez et al. 2009b), and bare or vegetation-covered soil moisture (Rodriguez-Alvarez et al. 2010a). However, coarse resolution digital elevation model estimation was used for surface's topography correction. Vegetation height was a function of notch number and notch position and could be retrieved independently from the soil moisture and surface roughness (Rodriguez-Alvarez et al. 2010b).

Two field experiments were also done. The first one is Palau Field Experiment (wheat) operated from February 2008 to October 2008. The second one is GRAJO (the GPS and Radiometric Joint Observations) field experiment (Rodriguez-Alvarez et al. 2011; Monerris et al. 2009). Three plots were include: bare soil, perennial grass and barley. For Palau Field Experiment, soil moisture retrieval was about $2.5 \sim 4.7\%$, but for GRAJO field experiment, the soil moisture retrieval error was about $2.0 \sim 3.2\%$. For barley and wheat, vegetation height retrieval was quite satisfactory: RMSE = $3 \sim 5$ cm. Maize height results were quite satisfactory: RMSE = 6.3 cm. Therefore, the IPT was demonstrated to a useful tool for retrievals of land geophysical parameters (Rodriguez-Alvarez et al. 2011).

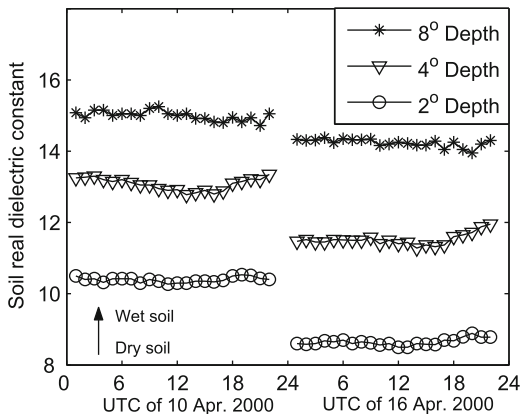
10.3.3 *Hydrology Sensing from GNSS*

In order to receive weak GNSS reflected signals, Special receiver should be designed. There are two commonly used receiver antenna: one is RHCP pointing to the zenith to receive direct signal, and the other one is LHCP pointing to nadir to receive reflected signals. Larson et al. (2008a, b) showed the conventional GPS receivers used in geophysics and geodesy network can be used to monitor global soil moisture. Although the purpose of this kind of receivers is to maximize the direct signals and suppress the reflected ones, it is well known that they cannot be completely rejected. The kind of receiver is generally at lower height to about 2 m, so that the delay time between direct signal and reflected signal is short and coherence will be produced at the antenna.

Soil moisture can also be measured by using existing networks of standard GPS receivers. Its fundamental is to use the multipath reflection amplitudes at GPS sites to estimate soil moisture. The GPS antenna receives not only the direct signal but also the reflected signal, which is not along a direct path. Masters et al. (2000, 2004) obtained soil moisture at a USDA/SCAN (United States Department of Agriculture/Soil Climate Analysis Network) site, located on the Central Plains Experimental Range of Colombia, with the peak power of the GPS reflections (Fig. 10.1). Katzberg et al. (2006) has also successfully estimated soil reflectivity and dielectric constant with GPS reflected signals.

Multipath also impacts the SNR (signal-to-noise ratio), and provides an alternative method for quantifying multipath effects. GPS signals are mostly influenced by the near-surface ($0 \sim 5$ cm) soil moisture and its spatial resolution is much higher, about 50-m radius, very similar to SMOS and SMAP datasets. The GPS multipath

Fig. 10.1 Soil moisture dielectric constant at the USDA/SCAN (United States Department of Agriculture/Soil Climate Analysis Network) site on the Central Plains Experimental Range of Colombia from peak power of the GPS reflections (Modified from Masters et al. 2000)



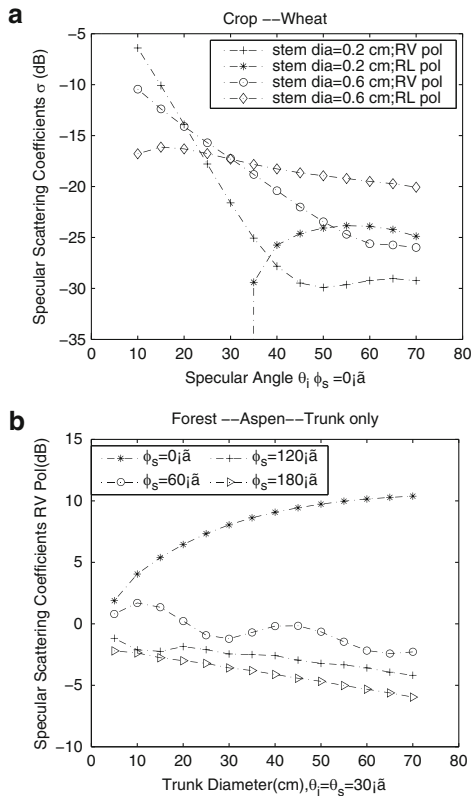
amplitudes were compared with the Noach land surface model. Although, GPS multipath amplitudes and the land surface model were not calibrated, the multipath amplitudes showed good correlation relationship with nearby precipitation records. Experimental data conducted at Marshall, CO, showed that good correlation of 0.91 was shown with the shallow water content reflectometry over a period of 83 days. Subsequently, Marshall Experiment was extended to span 210 days (Larson et al. 2010). Reflector depth and its variation through time were assessed. The penetration depth of GPS signals should be used appropriately and a retrieval algorithm should be developed to convert GNSS SNR data to soil moisture in the future.

10.3.4 GNSS-R Scattering Properties

The microwave scattering models have been developed to better understand the interaction of microwave signals with targets (such as soil or vegetation). They are either based on the distorted born approximation (DBA) or radiative transfer (RT) theory. As for the latter, two processes (extinction and emission) are utilized to describe the change of microwave intensity propagating through the medium.

Wu et al. (2012) used the Bi-mimics model for GNSS-R soil or vegetation study, only the specular scattering coefficients at the first Fresnel zone should be considered. So the model was modified to the specular direction. As it is well known, the existing models are developed for linear radar cross section or scattering coefficient. However, in order to overcome ionospheric effects, the transmitted signals by GNSS constellations are RHCP. Therefore circular polarization should be used for GNSS-R remote sensing, including co-polarization and cross-polarization. Wu et al. (2012) used the modified model to do initial research on GNSS-R vegetation biomass, including crop (wheat) and forest (Aspen in Mimics's Handbook). Specular scattering simulations were carried out at RV and RL polarization, where the incident angles were between 10° to 70° . Figure 10.2 showed the theoretical simulations of vegetation diameters versus specular scattering coefficients.

Fig. 10.2 Specular scattering coefficients vs. specular angles (upper) and trunk diameters (bottom)



From Fig. 10.2, we can see that when the stem diameters are fixed, scattering coefficients sigma is different for RV and RL pol, but when the polarization RV or RL is fixed, different diameters have different δ° . In Fig. 10.2, scattering azimuth angles are considered at RV pol, as the trunk diameter increases, the specular scattering coefficients change in different forms. Therefore, GNSS-R vegetation biomass response is a complex process, which is influenced by observation geometry (azimuth and zenith angles), polarization and vegetation structure, among others.

10.3.5 GNSS-R Polarization

When GNSS signals reflected from the Earth surface, its waveform was distorted and polarization flipped. To reduce polarization loss and receive reflected signals efficiently, different antennas were used for different receivers: such as the modified DMR receiver used in SMEX 02, it used the LHCP to receive reflected signals. As mentioned above, the one used in ground-based instrument SMIGOL reflectometry was vertical polarization. Also, linear and circular polarizations were all used in BAO tower experiment.

Wu and Li (2012) investigated the reflected signals' polarization properties in microwave radiative transfer model. Assume that the transmitted signals are RHCP, polarizations of RR, RL, RH, RV and $R \pm 45^\circ$ were simulated. From their simulations, it can be seen that the as for RL polarization, scattering values only exist at larger incident angles. Dynamic ranges of linear polarization (both horizontal and vertical) were larger and their scattering respond existed at the whole incident angles (from 10° to 70°). V polarization dynamic ranges were larger than H polarization. Linear polarization is suitable for receivers which were able to track signals from the whole scattering angles range. But LHCP polarization response only exists at the larger incident angles. In addition to the scattering zenith angles, scattering azimuth angles are also influenced the polarization scattering properties.

10.4 GNSS-R Forest Biomass Monitoring

As for GNSS-R scattering, there are two scattering zones: one is the first Fresnel Zone and the other is glistening area. As for the former, it is usually defined as the locus of points, surrounding the specular reflection point, and compared with the one reflected by the specular point itself, the phase shifts of reflected waves are less than or equal to π ; as for the latter, it is defined as the area for which the scattered power has dropped down by a factor $1/e$ (-4.3 dB) (Ferrazzoli et al. 2010). The coherent scattering comes from the first Fresnel zone, and the incoherent scattering comes from the glistening zone.

In the case of ocean surfaces, the coherent scattering is much larger than the incoherent one and coherent component is consequently neglected. However, as for the land conditions, the land surfaces roughness scales are always less than the GNSS wavelength, unless topographic effects are considered. Therefore, land surface does not own a glistening area and diffuse scattering is usually much lower than the coherent component.

Ferrazzoli et al. (2010) presented some theoretical simulations of the specular scattering coefficients of a forested area to demonstrate the potentiality of GNSS-R in forest biomass monitoring. The model developed at Tor Vergata University was used in the study. It is a discrete model. Intrinsically, the Tor Vergata model is bistatic. However, it is well known that the GNSS signal is significantly high in the specular direction only due to the low power flux density at the earth surface. Therefore, only specular direction simulations were presented at their paper and the forest specular scattering coefficient was modeled like the following:

$$\sigma_{pq}^0(\theta_s, \theta_s = \theta_i, \varphi_s - \varphi_i = 0) = \sigma_{pq}^{0coh}(\theta_i, \theta_i, 0) + \sigma_{pq}^{0inc}(\theta_i, \theta_i, 0) \quad (10.2)$$

where θ_i and φ_i are the incident zenith and azimuth angles, θ_s and φ_s are the scattering zenith and azimuth angles, p and q stand for polarizations, σ_{pq}^{0coh} is the coherent scattering component and σ_{pq}^{0inc} is the incoherent part. The simplified

model is able to take GNSS circular polarization into account. Compared with the monostatic radar saturation for vegetation biomass monitoring, specular scattering coefficients of GNSS-R is increasing with the forest biomass increasing. Theoretical study showed that forests do not mask the RL coherent specular reflection from soil, and it is larger than incoherent scattering of vegetation and soil (Ferrazzoli et al. 2010). It is concluded that the specular measurements at low incidence angels and RL polarization were more suitable for forest biomass monitoring.

10.5 Summary

Soil moisture is one of the most important geophysical parameters for hydrology study. GNSS-R works at L-band, which is similar with SMOS and SMAP. With many simultaneous transmitted signals of GNSS constellations, the time and spatial resolutions increase. Meanwhile it has unique advantages of low cost, light weight and small power, which makes it a promising and robust remote sensing technique for hydrology study. Nowadays, GNSS-R reflected or multipath signals are found to be correlated with soil moisture and vegetation growth. Meanwhile, theoretical study in electromagnetic wave scattering and propagation are carried out to present GNSS-R vegetation biomass and reflected signals polarization study.

References

- Cardellach E, Fabra F, Nogues-Correig O, Oliveras S, Ribo S, Rius A (2011) GNSSR ground-based and airborne campaigns for ocean, land, ice, and snow techniques: application to the GOLDTRR data sets. *Radio Sci* 46:RS0C04. doi:[10.1029/2011RS004683](https://doi.org/10.1029/2011RS004683)
- Entekhabi D et al (2010) The soil moisture active passive (SMAP) mission. *Proc IEEE* 98(5):704–716
- Ferrazzoli P, Guerriero L, Pierdicca N, Rahmoune R (2010) Forest biomass monitoring with GNSS-R: theoretical simulations. *Adv Space Res*. doi:[10.1016/j.asr.2010.04.025](https://doi.org/10.1016/j.asr.2010.04.025)
- Jackson TJ, Schmugge J, Engman ET (1996) Remote sensing applications to hydrology: soil moisture. *Hydrol Sci J* 41(4):517–530
- Katzberg S, Torres O, Grant MS, Masters D (2006) Utilizing calibrated GPS reflected signals to estimate soil reflectivity and dielectric constant: Results from SMEX02. *Remote Sens Environ* 100(1):17–28
- Kerr YH et al (2001) Soil moisture retrieval from space: The Soil Moisture and Ocean Salinity (SMOS) mission. *IEEE Trans Geosci Remote Sens* 39(8):1729–1735
- Larson KM, Small EE, Gutmann ED, Bilich AL, Braun JJ, Zavorotny VU (2008a) Use of GPS receivers as a soil moisture network for water cycle studies. *Geophys Res Lett* 35:L24405. doi:[10.1029/2008GL036013](https://doi.org/10.1029/2008GL036013)
- Larson KM, Small EE, Gutmann E, Bilich A, Axelrad P, Braun J (2008b) Using GPS multipath to measure soil moisture fluctuations: initial results. *GPS Solut* 12(3):173–177
- Larson KM, Braun JJ, Small EE, Zavorotny VU, Gutmann ED, Bilich AL (2010) GPS multipath and its relation to near-surface soil moisture content. *IEEE J Sel Topics Appl Earth Obs Remote Sens* 3(1):91–99

- Masters D (2004) Surface remote sensing applications of GNSS Bistatic Radar: soil moisture and aircraft altimetry. Ph.D. dissertation, University of Colorado at Boulder
- Masters D, Zavorotny V, Katzberg S, Emery W (2000) GPS signal scattering from land for moisture content determination. In: Proceeding of the IEEE international geosciences and remote sensing symposium, Honolulu, HI, 24–28 July, pp 3090–3092
- Masters D, Axelrad A, Katzberg SJ (2004) Initial results of landreflected GPS bistatic radar measurements in SMEX02. *Remote Sens Environ* 92:507–520
- Monerris A, Rodriguez-Alvarez N, Vall-llossera M et al (2009) The GPS and RAdiometric Joint Observations experiment at the REMEDHUS site (Zamora-Salamanca region, Spain). In: Proceedings of 2009 IEEE international on geoscience and remote sensing symposium (IGARSS 2009) 3:286–289
- Njoku EG, Entekhabi D (1996) Passive microwave remote sensing of soil moisture. *J Hydrol* 184(1–2):101–129
- Rodriguez-Alvarez N, Marchan-Hernandez JF, Camps A et al (2009a) Topographic profile retrieval using the Interference Pattern GNSS-R technique. In: Proceeding of 2009 IEEE international symposium geoscience and remote sensing (IGARSS 2009) 3:420–423
- Rodriguez-Alvarez N, Monerris A, Bosch-Lluis X et al (2009b) Soil moisture and vegetation height retrieval using GNSS-R techniques. In: Proceeding of 2009 IEEE international symposium geoscience and remote sensing (IGARSS 2009) 3:869–872
- Rodriguez-Alvarez N, Monerris A, Bosch-Lluis X et al (2010a) Soil moisture and vegetation height retrieval using GNSS-R techniques. *Proc IGARSS 2010*(3):869–872
- Rodriguez-Alvarez N et al (2010b) Land geophysical parameters retrieval using the Interference Pattern GNSS-R Technique. *IEEE Trans Geosci Remote Sens*:1–14. doi:[10.1109/TGRS.2010.2049023](https://doi.org/10.1109/TGRS.2010.2049023)
- Rodriguez-Alvarez N, Bosch-Lluis X, Camps A, Aguasca A, Vall-llossera M, Valencia E, Ramos-Perez I, Park H (2011) Review of crop growth and soil moisture monitoring from a ground-based instrument implementing the Interference Pattern GNSS-R Technique, *Radio Sci* 46:RS0C03. doi:[10.1029/2011RS004680](https://doi.org/10.1029/2011RS004680)
- Shi JC et al (2012) Progresses on microwave remote sensing of land surface parameters. *Sci China Earth Sci* 55(7):1052–1078
- Ulaby FT, Moore RK, Fung AK (1981) Microwave remote sensing: active and passive, vol I, *Microwave remote sensing fundamentals and radiometry*. Addison-Wesley, Advanced Book Program, Reading, p 456
- Wu X, Li Y (2012) GNSS-R reflected signals polarization characteristics: theoretical study on vegetation remote sensing. In: Geoscience and remote sensing symposium (IGARSS), 2012 IEEE International. 2012: IEEE
- Wu X, Li Y, Xu J (2012) Theoretical study on GNSS-R vegetation biomass. In: Geoscience and remote sensing symposium (IGARSS), 2012 IEEE International. 2012: IEEE
- Zavorotny VU, Voronovich AG (2000a) Bistatic GPS signal reflections at various polarizations from rough land surface with moisture content. In: Proceedings of IGARSS00, Honolulu, HI
- Zavorotny VU, Voronovich AG (2000b) Scattering of GPS signals from the ocean with wind remote sensing application. *IEEE Trans Geosci Remote Sens* 38:951964

Chapter 11

Cryospheric Sensing Using GNSS-R

11.1 Dry Snow Monitoring

When ice entirely retains sub-freezing temperatures and no melting occurs it is called dry snow. Its density is very low, and L-band signals can penetrate a few hundreds of meters of snow depth. Dry snow zones occur within the interior regions of the Greenland and Antarctica ice sheets, where total ice depth can be of a few kilometers. The deeper the layer of snow, the older its age. The snow layers, down to where L-band signals can penetrate, correspond to the snow accumulated in the last a few thousands of years (e.g. [Spikes et al. 2004](#); [Arthern et al. 2006](#); [Fujita et al. 2011](#)) (it depends on the actual time series of accumulation rates and snow vertical profile of density). Understanding the climatology of these regions is important to understand how these ice sheets might respond to climate change. In particular, better maps of snow accumulation are needed to understand and predict ongoing changes in the size of the Antarctic ice sheet (e.g. [Wingham et al. 1998](#)), important in driving global sea level (e.g. [Church et al. 2001](#)). These regions would be densely sampled by a potential future GNSS-R space-based mission in a polar orbit ([Fabra 2013](#)).

A GNSS-R experiment was conducted at Dome Concordia, Antarctica, taking data during 12 days in December 2009. Two GNSS antennas were deployed: a zenith-looking Right-Hand Circular Polarized (RHCP) antenna for geodetic positioning, and a dual-polarized (RHCP + LHCP) horizon-looking antenna to collect the signals reflected off the snow. The system was mounted on top of the ~45 m high American Tower, and connected to a dedicated GNSS-R receiver (GOLD-RTR ([Nogués-Correig et al. 2007](#))), and pointing over a pristine snow area of flat and smooth surface. Details of the set-up can be found in [Cardellach et al. \(2012\)](#) and [Fabra \(2013\)](#).

The experimental work concluded that

- L-band GNSS signals penetrate into dry snow down to 200–300 m depth;
- The signals reflected off these smooth surfaces have long coherence times;

- The signals present interferometric fringes, produced by the interference between reflections off different internal snow layers;
- A technique was developed to estimate the depth of the reflecting layers, based on a geometric optics multiple-ray model and the lag-hologram, a radio-holographic observable defined over the entire delay waveform (not only the peak).

As suggested by Hawley et al. (2006), a potential application of this technique is to calculate snow accumulation rates combining the so-obtained geometry of internal layers with density profiles at given spots.

11.1.1 Dry Snow Reflection Model: Multiple-Ray Single-Reflection

Rays are reflected off both the external snow surface and internal snow boundaries. Given the clear multiple interference patterns observed in the experimental data, the volumetric scattering (Wiehl et al. 2003) is neglected. The model is based on a geometrical optics approach, where the different contributions to the total received field are modeled as rays bouncing in different layers. Figure 11.1 sketches the course of the multiple rays. We assume locally horizontal layers, parallel incidence, and propagation/reflection through the snow layers following the Snell's law. Only circular co-polar transmissions and circular cross-polar reflections are included. The model considers a set of rays contributing to the total received signal, where each ray might suffer single-reflections solely, so it is called Multiple-Rays Single-Reflection (MRSR) model.

The snow sub-structure is given by the vertical profile of the snow density, which can be transformed into vertical profile of the snow permittivity (Ulaby et al. 1986). The real part of the relative permittivity, ϵ' , is obtained by solving Eq. 11.1; Then, its imaginary part, ϵ'' , can be calculated as in Eq. 11.2:

$$\frac{\epsilon' - 1}{3\epsilon'_i} = v_i \frac{\epsilon'_i - 1}{\epsilon'_i + 2\epsilon'} \quad (11.1)$$

$$\epsilon'' = 3v_i \epsilon'_i \frac{(\epsilon')^2(2\epsilon' + 1)}{(\epsilon'_i + 2\epsilon')(2(\epsilon')^2)} \quad (11.2)$$

where ϵ'_i and ϵ''_i are the real and imaginary parts of the permittivity of the ice. These values can be set to 2.93 and 0.001 respectively (Ulaby et al. 1986). And v_i is the volume fraction of ice in the snow, which depends on the snow density, ρ , as:

$$v_i = \frac{\rho}{0.916} \quad (11.3)$$

The following equations describe the equations of the amplitude U_i and the delay ρ_i with which a ray that incises into the snow, propagates down to the i -layer, rebounds, and propagates back to the snow-air interface, finally reaches the receiver. Their derivations can be found in [Cardellach et al. \(2012\)](#).

$$U_i = R_{i,i+1} \prod_{k=1}^{k=i} T_{k-1k} T_{kk-1} e^{-2\alpha_k d_k} \quad (11.4)$$

being

$$d_k = \frac{H_k}{\cos(\theta_k)}$$

And the phase

$$\rho_i = \rho_0 + \sum_{k=1}^{k=i} 2n_k \frac{H_k}{\cos(\theta_k)} - \left(\sum_{k=1}^{k=i} D_k \right) \sin(\theta_0) \quad (11.5)$$

being

$$D_k = 2H_k \tan(\theta_k) \quad (11.6)$$

where (see Fig. 11.1 for some definitions):

- R_{ij} and T_{ij} stand for Fresnel cross-polar reflection and co-polar transmission coefficients in the interface between the i -th and j -th layers;
- α_k is the attenuation coefficient in the k -th layer: $\alpha_k = \frac{2\pi}{\lambda} |Ima\{\sqrt{\epsilon_k}\}|$;
- H_k and θ_k are the layer's thickness and incidence angle (sketched in Fig. 11.1), and θ_k follow Snell's refraction law: $\sqrt{\epsilon_{k-1}} \sin \theta_{k-1} = \sqrt{\epsilon_k} \sin \theta_k$;
- ρ_0 is the differential delay between the snow-air specular reflection and the direct radio-link: $\rho_0 = 2H_0 \cos \theta_0$;
- And n_k is the refractive index of the k -th layer: $n_k = \sqrt{\epsilon_k}$.

The Fresnel coefficients, in circular basis are

$$T = T_{co} = \frac{1}{2}(T_{\parallel} + T_{\perp}) \quad (11.7)$$

$$R = R_{cross} = \frac{1}{2}(R_{\parallel} - R_{\perp}) \quad (11.8)$$

with

$$T_{\perp} = \frac{2 \cos \theta_{k-1}}{\cos \theta_{k-1} + \sqrt{\frac{\epsilon_k}{\epsilon_{k-1}} - \sin^2 \theta_{k-1}}} \quad (11.9)$$

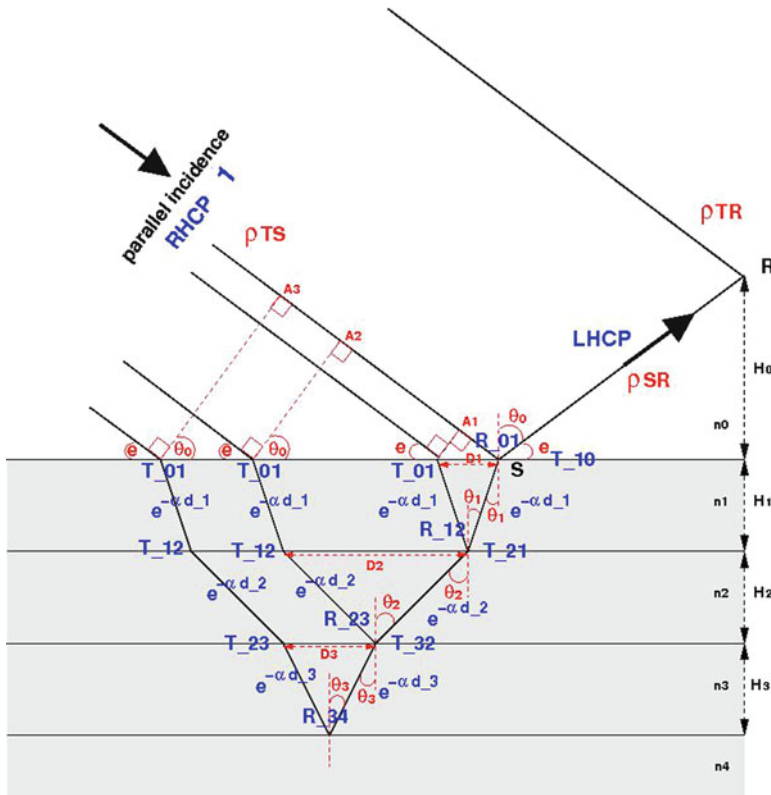


Fig. 11.1 Sketch of the multiple-ray single-reflection approach implemented to model the dry snow internal reflections. The amplitude factors affecting each segment are plotted in blue, red for the rest of parameters used in the computations. R is the location of the receiving antenna, S is the specular point of a reflection off the snow-air interface. T is not included in the figure, it represents the GNSS transmitter position, very far away, so it illuminates the area with parallel incidence. The incident RHCP power at the surface level is set to 1 (Figure from [Cardellach et al. \(2012\)](#))

$$T_{\parallel} = \frac{2 \cos \theta_{k-1}}{\cos \theta_{k-1} + \sqrt{\frac{\epsilon_{k-1}}{\epsilon_k} - (\frac{\epsilon_{k-1}}{\epsilon_k} \sin \theta_{k-1})^2}} \quad (11.10)$$

$$R_{\perp} = \frac{\epsilon_{k-1} \cos \theta_{k-1} - \sqrt{\epsilon_{k-1} \epsilon_k - (\epsilon_{k-1} \sin \theta_{k-1})^2}}{\epsilon_{k-1} \cos \theta_{k-1} + \sqrt{\epsilon_{k-1} \epsilon_k - (\epsilon_{k-1} \sin \theta_{k-1})^2}} \quad (11.11)$$

$$R_{\parallel} = \frac{\epsilon_k \cos \theta_{k-1} - \sqrt{\epsilon_{k-1} \epsilon_k - (\epsilon_{k-1} \sin \theta_{k-1})^2}}{\epsilon_k \cos \theta_{k-1} + \sqrt{\epsilon_{k-1} \epsilon_k - (\epsilon_{k-1} \sin \theta_{k-1})^2}} \quad (11.12)$$

The received complex waveform is not simply the complex sum of all these i -fields, but the modulation of the GNSS signals must also be taken into account. The i -layer contribution can be obtained as the GPS C/A auto-correlation function (triangle function) shifted by the delay at which the i -layer reflected signal arrives (with respect to the direct signal), ρ_i (Eq. 11.5), and multiplied by the amplitude corresponding to the i -layer, U_i (Eq. 11.4). Moreover, the i -layer contribution, once at the receiver coordinates, has a different phase than the phase of the direct ray contribution, that is: there is a rotation in complex space between the two contributions. The phase is given by

$$\phi_i = 2\pi \frac{\rho_i}{\lambda} \quad (11.13)$$

The total received waveform will thus be:

$$Y(\tau) = Y^{dir}(\tau) + \sum_{i=0}^{N_{layers}} \left[(1.0 - \frac{|\rho_i - \tau|}{L_{C/A}}) U_i e^{j\phi_i} \right] \quad (11.14)$$

where τ is the delay-variable along the waveform; Y^{dir} is the GPS C/A auto-correlation function (triangle function) centered at the nominal zero-delay, and it represents the contamination by the direct signal being captured by the horizon-looking antenna. It should not be a big contribution, since this antenna is cross-polar (LHCP) whereas direct signals are essentially co-polar (RHCP); $L_{C/A}$ is the length of the GPS C/A triangle function, and j is the complex unity, $j = \sqrt{-1}$.

Equation 11.14 is thus the MRSR model, where U_i and ρ_i are given by Eqs. 11.4 and 11.5 respectively.

From the model it is also possible to obtain the theoretical value of the interference frequency between the ray reflected in the i -th layer and the direct radio-link:

$$f_i[Hz] = \frac{-1}{\lambda} \frac{d\rho_i}{dt} \quad (11.15)$$

In particular, the interferences between the direct signal and the external layer specular reflection is

$$f_{surf}[Hz] = \frac{-2H_0}{\lambda} \cos e \frac{de}{dt} \quad (11.16)$$

(e for elevation angle). Interferences between the direct radio-link and rays reflected off layers beneath the surface have frequencies more negative than Eq. 11.16.

11.1.2 Dry Snow Observable: Lag-Hologram

With radio-holographic techniques it is possible to obtain the maximum spatial compression of the main ray separately from that of the other rays' trajectories. This makes it possible to evaluate the intensity of radio waves at each ray trajectory

and to determine the corresponding frequency displacement from a reference ray. A reference wave field (reference ray) is used to reveal the spectra from the total received field.

Using the direct signal (with no reflection) as a reference field, the technique tries to see the rest of possible contributing rays present in the data (atmospheric multi-path, surface, sub-surface reflections ...). Once the reference field has been used to counter-rotate the phase of the reflected signal, a spectral analysis is performed. In radio-occultation applications, the holography is applied at the peak of the received waveform solely (because this is the only data provided by standard and radio-occultation receivers). We here present a new holographic observable which uses each of the lags of the received waveform. The generation of the lag-hologram follows the steps below:

- Time series of N complex (I/Q) waveforms from the horizon-looking antenna are taken: $Y(\tau_i, t_j)$;
- The phases of each τ_i lag of these waveforms are then counter-rotated by the phase of the direct signal. The direct signal is here defined as the peak of the waveform captured with the zenith-looking antenna: $Y(\tau_i, t_j) e^{-i \phi_{dir}(\tau_{peak}, t_j)}$;
- For each lag τ_i , a Fourier analysis is conducted independently on its time series: $LH(\tau_i, f) = FT\{Y(\tau_i, t_j) e^{-i \phi_{dir}(\tau_{peak}, t_j)}\}$;
- Since the geometric parameter that changes with time (and thus forces the potential interference to change) is the elevation angle, it is more practical to express the frequency in terms of elevation rate (oscillation cycles/degree-elevation) rather than Hz (oscillation cycles/second). The conversion between them is given by

$$f[\frac{\text{cycle}}{\text{deg} - el}] = \frac{f[\text{Hz}]}{\frac{de}{dt}[\text{deg} - el/\text{s}]} = \frac{f[\text{Hz}]}{\frac{de}{dt}[\text{rad}/\text{s}]} \frac{2\pi}{360} \quad (11.17)$$

- finally, each lag (τ_i) of the lag-hologram is normalized (independently to the other lags):

$$LH^{norm}(\tau_i, f_j) = \frac{1}{\sum_k \|LH(\tau_i, f_k)\|} LH(\tau_i, f_j) \quad (11.18)$$

Examples of lag-holograms from both real data and MRSR model are given in Fig. 11.2. They show that besides the direct signal (frequency zero), the next contribution is from reflections off the snow-air interface, and the sub-surface reflecting elements. The lag-holograms also show that different lags of the waveform can capture different sub-surface reflections. This is due to the filtering effect of the delay correlation with the code. That is, rays delayed more than one C/A code chip (~ 300 m) from the k -th lag cannot contribute to its power. Then, in order to capture reflections from deep layers it is necessary to observe the spectral content of lags away from the specular one.

Once the lag-holograms from real data are obtained, the MRSR model permits to convert the frequency axis into snow depth axis. This is done (1) modelling ρ_i s as in

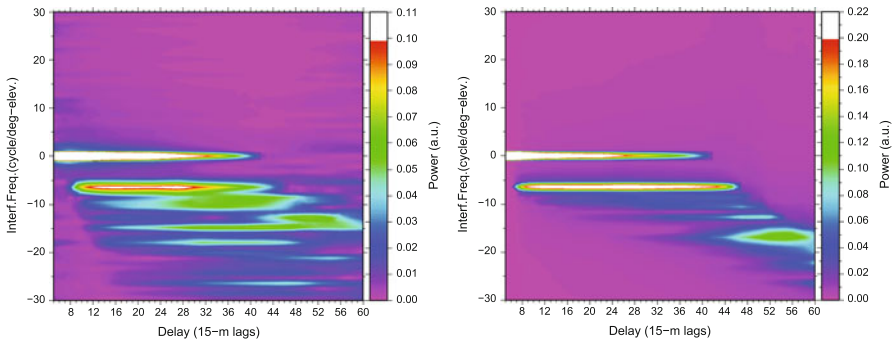


Fig. 11.2 (Left:) Example of lag-hologram for a time series of $N = 128$ 1-s complex waveforms in a GNSS-R Dry Snow experiment at Concordia Station (Antarctica). It corresponds to PRN 13, December 16, 2009, between 44.5° and 45.5° elevation. Here the frequency is given as interferometric cycles per degree-elevation (conversion from Hz as in Eq. 11.17). The zero-frequency corresponds to the reference field: the direct ray. According to Eq. 11.16, frequencies more negatives than -5.8 cycle/deg-el correspond to scattering off reflecting-elements below the snow-air interface. Note different spectral content for different delay along the waveform. (Right:) Lag-hologram of a series of 128 synthesized complex waveforms the geometry of each of them follow the geometry of the 128 real waveforms in the left panel (From Cardellach et al. (2012))

Eq. 11.5 for the range of elevations embedded in the time series of observations used to produce the lag-hologram; and (2) taking its (numerical) derivative with respect to the elevation angle. The study in Cardellach et al. (2012) used this approach to identify a set of sub-surface reflecting layers at the experimental set, located at 10, 70, 130 and 240 m depth, with vertical resolution between 5 and 10 m. The vertical resolution of the identified layers is mainly given by the length of the time series used to generate the spectral analysis. Other secondary factors are the geometry (it is function of the elevation angle).

11.2 Wet Snow Monitoring

11.2.1 Observations from Space-Borne GNSS-R

Snow and ice on the land are important components of climate systems and a critical storage component in the hydrologic cycle as well. However, in situ observations of snow distribution are sparse, and remotely sensed products are imprecise and only available at a coarse spatial scale, e.g., the U.S. Snowpack Telemetry (SNOWTELE) network (Serreze et al. 1999). As the ice thickness is related to the amplitude of the reflected signal as a function of the incidence angle or relative amplitudes between different polarizations (Lowe et al. 2002), the snow/ice thickness can be retrieved from the GPS reflected signals. Komjathy et al. (2000) has derived the condition of sea and fresh-water ice as well as the freeze/thaw state of frozen ground from aircraft experiments with GPS reflections over the Arctic sea ice and ice

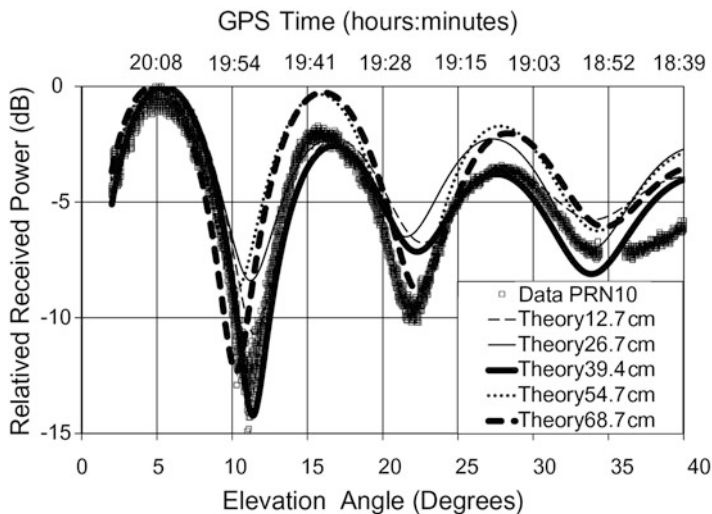


Fig. 11.3 Theoretical (*lines*) and measured (*squares*) elevation plots for a reservoir covered by a 0.3 cm thick snow layer on top of 12.7-, 26.7-, 39.4-, 54.7-, and 68.7-cm-thick ice layers with $h=50.5$ cm for the GPS satellite PRN 10 ([Jacobson 2010](#))

pack near Barrow, Alaska, USA. The correlation was quite consistent for forward-scattered GPS returns and RADARSAT backscattered measurements. This behavior of the reflected signal showed clearly the sensitivity to ice condition, indicating that the GPS reflected signals can well determine the ice status and features. The potential of sensing sea ice from low Earth orbit was explored using two signals from two different ice concentrations by [Gleason \(2010\)](#). This result showed some agreement between GPS measurements and estimates of ice concentration from the Advanced Microwave Scanning Radiometer for Earth Observing System (AMSR-E) instrument, but due to the small amount of data no conclusions could be made.

11.2.2 *Observations from Ground GNSS-R*

The change in snow depth is also monitored using the corresponding multi-path modulation of the ground GPS signal. The tested results for two spring 2009 snowstorms in Colorado showed strong agreement between GPS snow depth estimates, field measurements, and nearby ultrasonic snow depth sensors ([Larson et al. 2009](#)). In addition, Fig. 11.3 shows the measurement and theoretical results for a 0.3 cm thick snow layer on top of 12.7-, 26.7-, 39.4-, 54.7-, and 68.7-cm-thick ice layer from the GPS satellite PRN 10 ([Jacobson 2010](#)). It has shown that a theoretical ice thickness of 39.4 cm agrees best with the measurements with regards to the first deep fade shape.

11.3 Sounding the Sea Ice Conditions

Due to complex and varying conditions of sea ice, e.g. an inaccessible environment and persistent cloud covering, it is very difficult to monitor sea ice conditions with conventional instruments. Thus, measuring sea ice conditions mainly relies on satellite radar techniques. However, no single sensor is capable of providing the essential range of observations ([Livingstone et al. 1987](#); [Rubashkin et al. 2000](#)). For example, Synthetic-aperture radar (SAR) images have sufficient spatial resolution to resolve detailed ice features, but repeat times of existing satellites are relatively long when compared to the change rate of open water fraction in the ice pack, although this aspect may be improved with more satellites in the future. Furthermore, SAR data carry a substantial penalty in cost for image acquisition and processing. In addition, space-borne passive microwave sensors may provide more frequent coverage at several wavelengths, but they have substantially lower spatial resolution. While optical and thermal sensors provide a middle ground in resolution and temporal sampling between SAR and passive microwave satellites, they are limited by cloud cover and visibility conditions.

The GPS reflectometry can measure the sea ice conditions as a new technique. [Komjathy et al. \(2000\)](#) analyzed the aircraft experiment of GPS reflections from Arctic sea ice and over the ice pack near Barrow, Alaska, USA. Correlations from comparisons between RADARSAT backscatter and GPS forward scattered data indicate that the GPS reflected signals could provide useful information on sea ice conditions. The reflected signal shape was quite consistent for the moderate altitudes of the airborne GPS receiver and the peak power changed significantly along the flight track. This behavior of the reflected signal showed clearly the sensitivity to ice condition, indicating that the GPS reflected signals can be used to determine the ice features. In addition, as the effective dielectric constant of ice depends on various factors, such as the ice composition, density, age, origin, salinity, temperature, morphology ([Shohr 1998](#)), the internal ice states can be determined with the reflection coefficient over a frozen sea surface by the effective dielectric constant of ice and the dielectric constant of the underlying water under some conditions ([Melling 1998](#)). In the future, GPS reflected signals might provide more detailed information and internal states of sea ice, including the floe ridges, frost flowers, broken ice, and fine-scale roughness at the snow-ice interface. Therefore, the reflected GPS signals have a high potential and applications in sensing and investigating the sea ice state, particularly for inaccessible and atrocious sea ice cover.

References

- Arthern RJ, Winebrenner DP, Vaughan DG (2006) Antarctic snow accumulation mapped using polarization of 4.3-cm wavelength microwave emission. *J Geophys Res* 111:D06107. doi:10.1029/2004JD005667
- Cardellach E, Fabra F, Rius A, Pettinato S, D'Addio S (2012) Characterization of dry-snow sub-structure using GNSS reflected signals. *Remote Sens Environ* 124:122–134. doi:10.1016/j.rse.2012.05.012

- Church JA et al (2001) Sea level change. In: Houghton J et al (eds) Climate change: the scientific basis. Cambridge University Press, New York
- Fabra F (2013) GNSS-R as a source of opportunity for sea ice and dry snow remote sensing. PhD Dissertation, Polytechnical University of Catalonia (UPC), Barcelona
- Fujita S, Holmlund P, Andersson I, Brown I, Enomoto H, Fujii Y, Fujita K, Fukui K, Furukawa T, Hansson M, Hara K, Hoshina Y, Igarashi M, Iizuka Y, Imura S, Ingvander S, Karlin T, Motoyama H, Nakazawa F, Oerter H, Sjoberg LE, Sugiyama S, Surdyk S, Strom J, Uemura R, Wilhelms F (2011) Spatial and temporal variability of snow accumulation rate on the East Antarctic ice divide between Dome Fuji and EPICA DML. *Cryosphere* 5:1057–1081. doi:10.5194/tc-5-1057-2011
- Gleason S (2010) Towards sea ice remote sensing with space detected GPS signals: demonstration of technical feasibility and initial consistency check with low resolution sea ice information. *Remote Sens* 2:2017–2039
- Hawley RL, Morris EM, Cullen R, Nixdorf U, Shepherd AP, Wingham DJ (2006) ASIRAS airborne radar resolves internal annual layers in the dry-snow zone of Greenland. *Geophys Res Lett* 33:L04502
- Jacobson MD (2010) Snow-covered lake ice in GPS multipath reception – theory and measurement. *Adv Space Res* 46(2):221–227. doi:10.1016/j.asr.2009.10.013
- Komjathy A, Maslanik JA, Zavorotny VU, Axelrad P, Katzberg SJ (2000) Sea ice remote sensing using surface reflected GPS signals. In: Proceedings of the IEEE international geosciences and remote sensing symposium (IGARSS 2000), Honolulu, Hawaii, 24–28 July, pp 2855–2857
- Larson KM, Gutmann ED, Zavorotny U, Braun J, Williams M, Nievinski F (2009) Can we measure snow depth with GPS receivers? *Geophys Res Lett* 36, L17502. doi:10.1029/2009GL039430
- Livingstone CE, Onstott RG, Arsenault LD, Gray AL, Singh KP (1987) Microwave sea-ice signatures near the onset of melt. *IEEE Trans Geosci Remote Sens* GE-25(2):174–187
- Lowe ST, Kroger P, Franklin G, LaBerecque JL, Lerma J, Lough M, Marcin MR, Muellerschoen RJ, Spitzmesser D, Young LE (2002) A delay/doppler-mapping receiver system for GPS-reflection remote sensing. *IEEE Trans Geosci Remote Sens* 40(5):1150–1163
- Melling H (1998) Detection of features in first-year pack ice by synthetic aperture radar (SAR). *Int J Remote Sens* 19(6):1223–1249
- Nogués-Correig O, Galí EC, Campderròs JS, Rius A (2007) A GPS-reflections receiver that computes Doppler/delay maps in real time. *IEEE Trans Geosci Remote Sens* 45:156–174
- Rubashkin SG, Pavel'ev AG, Yakovlev OI et al (1993) Reflection of radar waves by the ocean surface for bistatic radar using two satellites. *J Commun Technol Electron* 38(9):64–70
- Shogr ME (1998) Field observations and model calculations of dielectric properties of Arctic sea ice in the microwave C-band. *IEEE Trans Geosci Remote Sens* 36(2):463–478
- Serreze MC, Clark MP, Armstrong RL, McGinnis DA, Pulwarty RS (1999) Characteristics of the western United States snowpack from snowpack telemetry (SNOWTELE) data. *Water Resour Res* 35(7):2145–2160. doi:10.1029/1999WR900090
- Spikes VB, Hamilton GS, Arcone SA, Kaspari S, Mayewski PA (2004) Variability in accumulation rates from GPR profiling on the West Antarctic Plateau. *Ann Glaciol* 39:238–244
- Ulaby FT, Moore RK, Fung AK (1986) Microwave remote sensing: active and passive, vol III, Volume scattering and emission theory, advanced systems and applications. Artech House, Inc, Dedham, p 1100
- Wiehl M, Legrésy B, Dietrich R (2003) Potential of reflected GNSS signals for ice sheet remote sensing. *Prog Electromagn Res* 40:177–205
- Wingham DJ, Ridout AL, Scharroo R, Arthern RJ, Schum CK (1998) Antarctic elevation change from 1992 to 1996. *Science* 282:456

Chapter 12

Summary and Future Chances

12.1 Status of GNSS Remote Sensing

12.1.1 Atmospheric Sensing

Ground-based together with space borne GPS radio occultation observations (Ao 2009) have been widely used in atmospheric and ionospheric sounding, including sensing tropospheric precipitable water vapor (PWV), ionospheric total electron content (TEC) and atmospheric profile information (e.g., pressure, temperature, humidity, tropopause and ionospheric electron density), gravity waves and sporadic E-layers as well as their variation characteristics,. For example, the dual frequency ground GPS array could detect ionospheric response and its processes during large geomagnetic storms (Jin et al. 2008). Schmidt et al. (2010) observed upper tropospheric warming and lower stratospheric cooling using GPS RO data (2001–2009). Meanwhile, ground GPS also observed the plasma bubbles and retrieved reliable propagation characteristics of the depletions without assumptions about the mapping of the depletion along magnetic field lines to large latitudinal distances, comparable with airglow data (Haase et al. 2011). These observations have facilitated greater advancements in meteorology, climatology, numerical weather model, atmospheric science and space weather (e.g., Jin et al. 2007; Jin and Luo 2009; Schmidt et al. 2010). Although a number of progresses in atmospheric and ionospheric sensing have been made using ground and space-borne GNSS observations in the past few years, they still do not satisfy actual requirements for short-time scales and higher temporal-spatial resolution monitoring together due to the lack of observations (Jin et al. 2006, 2008; Nesterov and Kunitsyn 2011).

12.1.2 Ocean Sensing

In the last few years, several experiments were carried out and numerous advancements have been made. For example, the National Oceanic and Atmospheric Administration (NOAA) Hurricane Hunter research aircraft carrying a GPS reflectometry instrument flew into Hurricane Michael off the South Carolina coast in October 2000 (Katzberg et al. 2001). The first GPS signals reflected from the sea surface inside tropical cyclones were analyzed and the wind speed results were obtained (Katzberg et al. 2001). UK-DMC carried a GPS reflectometry experiment as a secondary payload, from which geophysical parameters of the Earth surface were successfully inferred, e.g., sea surface roughness (Gleason et al. 2005). Good altimetry accuracy results have been obtained in very calm sea states with GPS reflected signals (Gleason et al. 2010). Currently, the GPS reflected signals from the ocean surface can be used to make altimetric sea surface height measurements with the achievable accuracy an active topic of research (Martin-Neira et al. 2001; Katzberg and Dunion 2009). Good examples of ocean roughness and wind sensing using GPS signals have been retrieved by Armatys et al. (2000) and Cardellach and Ruis (2007). However, further research is needed in detailed analysis of the electromagnetic field scattering theory, power and Delay-Doppler parameter retrieval methods (Lowe et al. 2002) and characterizing the L-band surface slopes' probability density function.

12.1.3 Hydrology Sensing

The power level of the GPS reflected signal from the land contains information about the soil moisture, dielectric constant, surface roughness, and possible vegetative cover of the reflecting surface (Masters 2004). Some experiments using GPS reflected signals have made estimates of the soil moisture. For example, Katzberg et al. (2006) obtained the soil reflectivity and dielectric constant using a GPS reflectometer installed on an HC130 aircraft during the Soil Moisture Experiment 2002 (SMEX02) near Ames, Iowa, which were consistent with results found for other microwave techniques operating at L-band. Simulations have been performed by Ferrazzoli et al. (2010), which have opened up the possibility of sensing forest biomass using GNSS reflections. In addition, the multi-path from ground GPS networks is possibly related to the near-surface soil moisture. Larson et al. (2008a, b) found nearly consistent fluctuations in near-surface soil moisture from the ground GPS multi-path, comparable with soil moisture fluctuations in the top 5 cm of soil measured from conventional sensors. However, GPS multipath signals are very complex due to various factors, e.g., vegetable, foliage, and glass debris. To infer the soil moisture parameters from ground GPS multipath, it is necessary to further remove the other factors' effects.

12.1.4 Cryosphere Mapping

Komjathy et al. (2000) has derived the condition of sea and fresh-water ice as well as the freeze/thaw state of frozen ground from aircraft experiments with GPS reflections over the Arctic sea ice and ice pack near Barrow, Alaska, USA. The correlation was quite consistent for forward-scattered GPS returns and RADARSAT backscattered measurements. This behavior of the reflected signal showed clearly the sensitivity to ice condition, indicating that the GPS reflected signals can well determine the ice status and features.

12.2 Future Developments and Chances

12.2.1 More GNSS Networks and Constellations

More and more permanent GNSS stations are being established around the globe, including more than 300 permanent worldwide IGS stations and thousands of regional continuous GNSS network stations, e.g., \sim 1,000 continuous GPS stations of the GPS Earth observation network in Japan and more than 300 continuous GPS stations in China. Moreover, the new navigation systems, including Russia's modernized GLONASS, European Union's GALILEO system, and China's Beidou/COMPASS, are being developed, particularly with multi-frequencies (Wu et al. 2010). Along with Space Based Augmentation Systems (e.g., QZSS and IRNSS), the ground-based GNSS network can receive more line-of-sight (LOS) signals from future multi-frequency GNSS satellite constellations (over 30) through the atmosphere and ionosphere. These new signals will mean great improvements in the temporal-spatial resolution coverage of the atmosphere. Furthermore, multi-path from ground GPS networks could provide useful estimates of the near surface soil moisture. In the future, the continuously increasing International GNSS Service (IGS) networks together with regional GPS network around the world may provide a new tool to estimate global land soil moisture in near real-time for hydrology and climate studies.

12.2.2 Advanced GNSS Receivers

The Blackjack GPS receiver developed by the Jet Propulsion Laboratory (JPL) has been widely used in most current space-borne GNSS missions for precise orbit determination and radio occultation (Montenbruck and Kroes 2003), e.g., Satellite de Aplicaciones Cientificas-C (SAC-C, 2000), CHAllenging Minisatellite Payload for gravity, magnetic and radio occultation (CHAMP, 2000), JASON-1

(2000), ICESat (2001), and Gravity Recovery and Climate Experiment (GRACE, 2002). In order to satisfy new mission requirements and quasi real-time data processing capabilities in the near future, additional GNSS receivers are needed for emerging applications and tracking signals from not only GPS, but also, GALILEO, GLONASS and other new GNSS systems, like China Beidou/COMPASS. Now JPL is developing the next generation multi-antenna GNSS receiver called the TriG (Tri-GNSS, GPS+Galileo+GLONASS) receiver for precision orbit determination and radio occultation observations. The TriG receiver has a modular design to obtain multi-GNSS refraction and reflection measurements with tracking L1 C/A, L2 Codeless, and the new L2C and L5 signals from GPS as well as new GNSS signals from Galileo and GLONASS (Tien et al. 2010).

For fully deriving scientifically relevant geophysical parameters such as ocean altimetry, sea state or soil moisture using GPS reflected signals, the Departament de Teoria del Senyal i Comunicacions (TSC) of the Universitat Politècnica de Catalunya (UPC) has developed the GNSS Reflectometer Instrument for the Passive Advanced Unit (griPAU). The griPAU instrument is a real-time and high resolution Delay-Doppler Map (DDM) reflectometer operating at the GPS L1 frequency with the C/A codes, which computes 24×32 complex points DDM with configurable resolution and selectable coherent as well as incoherent integration times. The high sensitivity of griPAU instrument will improve the quality of the retrieved geophysical parameters (Jin et al. 2011). For the coming higher number of satellite constellations, new signals, and frequencies of GNSS systems, e.g., the modernized multi-frequency GPS and the future Galileo system, the ICE (IEEC-CSIC, Spain) is also actively engaged in GNSS-R instrument development and scientific understanding of the GNSS scattering and reflected signals applications.

Additionally, the Surrey Satellite Technology Limited (SSTL), together with partners from the National Oceanography Centre (NOC), the University of Bath and the Surrey Space Centre (SSC) of the University of Surrey, is developing a next generation Space GPS Receiver-Remote Sensing Instrument (SGR-ReSI) to further exploit GNSS potential for remote sensing in the fields of land, ocean, cryosphere and atmospheric science (Unwin et al. 2010). The SGR-ReSI is a highly versatile and multi-frequency GNSS navigation receiver for both Reflectometry and Radio Occultation applications.

Lastly, a simple alternative that will provide data publicly to the entire scientific community for use in application validation is the software receiver based approach being pursued by several Universities in Canada (Gleason 2010). Although this strategy would not provide the high performance of some of the other instruments, it will be capable of capturing both RO and reflections data for both ground-based and on-board processing. Notably, the reflection data and the instrument design will be released in the public domain under an open source license. This type of small, inexpensive, low power instrument is expected to be capable of flying on University built nanosatellites. It is expected one or more of these new instruments will be flown on a satellite mission in the next few years.

12.2.3 *New Missions and Systems*

Space-borne GPS reflectometry and refractometry experiments have been successful in providing estimates of a number of the Earth's surface characteristics and atmospheric and ionospheric information, e.g., the Taiwan/US FORMOSAT-3/COSMIC mission with six satellites. However, these missions still have some restrictions due to low temporal-spatial resolutions and are approaching their end of operations. In order to fully utilize these new GNSS remote sensing tools, more and more new missions and systems are being developed. For example, the FORMOSAT-3/COSMIC mission will reach the end of its design life in about 2011, and the National Oceanic and Atmospheric Administration (NOAA) and National Space Organization (NSPO) intend to launch the next generation follow-on FORMOSAT-7/COSMIC-2 mission between 2014 and 2017 (Yen 2010). This follow-on mission has a new constellation of 12 satellites with GNSS RO receiver to receive GPS, GLONASS and GALILEO satellite signals. It will collect a large amount of occultation point data primarily for weather forecasting including typhoons and hurricane and space weather monitoring as well as meteorological, climate, ionospheric, and geodetic research.

CICERO (Climate Community Initiative for Continuing Earth Radio Occultation) is a follow-on mission to the COSMIC as a self-supporting enterprise for the greater GNSS-RO science and wider user communities who will share in its design, evolution, and success (www.geooptics.com). The CICERO project changes the way to collect and disseminate Earth observational data with 100 micro-satellites in Low-Earth Orbit (LEO) performing GNSS atmospheric radio occultation (GNSS-RO) and GNSS Surface Reflection (GNSS-SR) measurements (see Fig. 12.1). The CICERO constellation is designed with lower cost of acquiring data essential to understanding our planet and expands the possibilities for obtaining new types of data from space. The plan is to initially launch 20 satellites with follow-on launches to reach a sustained array of 100 spacecrafts. The full CICERO constellations are expected to deliver nearly 100,000 atmospheric profiles per a day (Yunck et al. 2007). Meanwhile, since CICERO has GNSS Surface Reflection (GNSS-SR), it is expected to detect more detailed Earth's surface characteristics and time-varying evolutions.

The past UK-DMC GPS Reflectometry experiment launched in 2003 has successfully showed that GNSS signals can be used from space in a bi-static radar configuration to analyze reflections off the ocean, ice and land. In order to further test and implement GNSS-R, a new UK satellite with a GNSS-R instrument onboard, TechDemoSat-1, is planned for launch in the near future (Unwin et al. 2010). It will be designed to estimate several Earth observables, including Directional Mean Square Slope (DMSS), ice edge detection, ice freeboard measurement, and ionospheric delay (e.g., total electron content), in a format that allows proper verification of inversion models by relevant scientists. The DMSS of the ocean is an important parameter that has interest from both operational users (shipping,

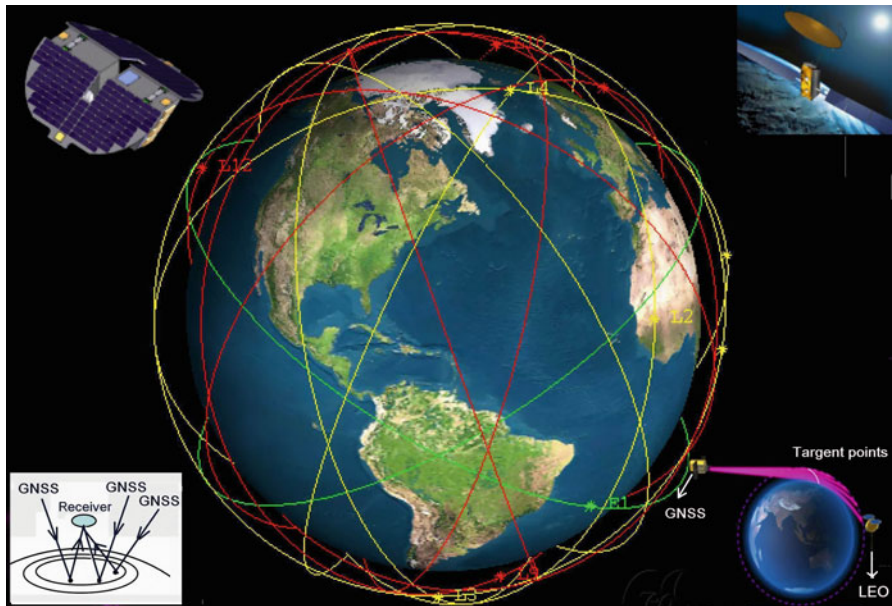


Fig. 12.1 CICERO (Climate Community Initiative for Continuing Earth Radio Occultation) with about 100 satellites (Yunck et al. 2007). The *left lower corner* shows the GNSS-Reflectometry and the *right lower corner* represents GNSS Radio Occultation

off-shore energy) and scientific users (wave, weather and climate modelling). Other parameters that potentially can be measured using GNSS-R include ocean states, ice edge, ice concentration, ionospheric mapping and soil moisture.

12.2.4 New and Emerging Applications

Various methods have been proposed for determining the ocean roughness and cryosphere, but there are insufficient spaceborne data to validate the methods or monitor more details. Moreover, the traditional instruments have a long delay with low spatial resolutions. In next few years, more space-borne GPS reflectometry and refractometry experiments will be launched with the next generation GNSS Receiver-Remote Sensing Instrument (e.g. Shuttle measurements). Some new scientific applications of the utilization of the GNSS-R are expected in various environment remote sensing fields with high spatial-temporal resolution and near real time in the near future, particularly some notable emerging applications include monitoring sea ice, sea states, ocean eddy, ocean surface oil, geohazards and space aircraft. These near-real-time GNS reflection data are expected to be open in the public domain. The analysis of these real-time data may play a key role in predicting

high winds, dangerous sea states, risk of flooding, ocean eddy and storm surges. Furthermore, high-sampling ocean surface roughness will be estimated from future denser GNSS reflected signals, which may improve our understanding of the air-sea exchanges, the floe ridges, frost flowers, broken ice, and fine-scale roughness at the snow-ice interface, particularly for inaccessible and atrocious sea ice cover.

Also the GNSS reflectometry together with ground observation networks of seismology and geodesy are expected to be applied in a geohazard warning system. The German Indonesian tsunami early warning system for the Indian Ocean was established after the Sumatra earthquake of December 2004 (www.gitews.de). It will later be extended to the Mediterranean and the Atlantic Ocean using new space-based GNSS reflectometry and scatterometry with all available signal sources, including the modernized GPS, the restored GLONASS, the establishing Galileo and the upcoming Compass GNSS. Moreover, future GNSS reflected signals may be used to monitor crustal deformation, like Synthetic Aperture Radar (SAR), and GNSS reflectometry is expected to observe the global-scale geodynamic processes together with other sensors.

12.3 Summary

The refracted, reflected and scattered GNSS signals have been used as a remote sensing tool in the atmosphere, ocean, land, hydrology and cryosphere. With continuously increasing global permanent IGS stations and regional continuous GNSS stations and more satellite constellations of the future multi-frequency GNSS and Space Based Augmentation Systems, such as GPS, GLONASS, Galileo, Beidou/COMPASS, QZSS and IRNSS, the denser ground GNSS stations can receive more multi-path signals and line of sight signals of GNSS satellites through the atmosphere and ionosphere. It can monitor more detailed ground surface characteristics and processes and evolutions of the atmospheric and ionospheric profiles at global and regional scales.

With more and more space-borne GPS reflectometry and refractometry missions in the near future (e.g., follow-on FORMOSAT-7/COSMIC-2 mission, CICERO and TechDemoSat-1), these missions will monitor more detailed Earth's surface characteristics and atmospheric and ionospheric information with high temporal-spatial resolutions (Jin et al. 2011). Furthermore, some advanced GNSS receivers are being developed with improved algorithms for the various possible applications and quasi real-time data processing capabilities to satisfy the future space-based high-performance missions (e.g., next generation TriG (Tri-GNSS) receiver with the ability to generate multi-GNSS refraction and reflection). It is also possible in the next few years a low cost instrument will be made public capable of operating on limited resource satellites, such as those being developed by Universities. New remote sensing applications using GNSS signals are expected to continue expanding over a global scale in the coming years.

References

- Ao CO (2009) Atmospheric sensing using GNSS radio occultations. In: Gleason S, Gebre-Egziabher D (eds) GNSS applications and methods. Springer, Norwood. ISBN 978-1-59693-329-3
- Armatys M, Komjathy A, Axelrad P, Katzberg SJ (2000) A comparison of GPS and scatterometry sensing of ocean wind speed and direction. In: Proceedings of the IEEE international geoscience and remote sensing symposium, Honolulu, HI, USA, pp 2861–2863
- Cardellach E, Ruis A (2007) Sea surface slopes' PDF from GNSS reflected signals. In: Proceedings of the IEEE international geoscience and remote sensing symposium, Barcelona, Spain, pp 1342–1345
- Ferrazzoli P, Guerriero L, Pierdicca N, Rahmoune R (2010) Forest biomass monitoring with GNSS-R: theoretical simulations. *Adv Space Res.* doi:[10.1101/j.asr.2010.04.025](https://doi.org/10.1101/j.asr.2010.04.025)
- Gleason S (2010) Towards sea ice remote sensing with space detected GPS signals: demonstration of technical feasibility and initial consistency check with low resolution sea ice information. *Remote Sens* 2:2017–2039
- Gleason S, Hodgart S, Sun Y, Gommenginger C, Mackin S, Adjrad M, Unwin M (2005) Detection and processing of bistatically reflected GPS signals from low Earth orbit for the purpose of ocean remote sensing. *IEEE Trans Geosci Remote Sens* 43(6):1229–1241
- Gleason S, Gommenginger C, Cromwell D (2010) Fading statistics and sensing accuracy of ocean scattered GNSS and altimetry signals. *Adv Space Res* 46(2):208–220
- Haase JS, Dautermann T, Taylor MJ, Chapagain N, Calais E, Pautet D (2011) Propagation of plasma bubbles observed in Brazil from GPS and airglow data. *Adv Space Res.* doi:[10.1101/j.asr.2010.09.025](https://doi.org/10.1101/j.asr.2010.09.025)
- Jin SG, Luo OF (2009) Variability and climatology of PWV from global 13-year GPS observations. *IEEE Trans Geosci Remote Sens* 47(7):1918–1924. doi:[10.1101/TGRS.2008.2010401](https://doi.org/10.1101/TGRS.2008.2010401)
- Jin SG, Park J, Wang J, Choi B, Park P (2006) Electron density profiles derived from ground-based GPS observations. *J Navig* 59(3):395–401. doi:[10.1017/S0373463306003821](https://doi.org/10.1017/S0373463306003821)
- Jin SG, Park J, Cho J, Park P (2007) Seasonal variability of GPS-derived Zenith Tropospheric Delay (1994–2006) and climate implications. *J Geophys Res* 112:D09110. doi:[10.1029/2006JD007772](https://doi.org/10.1029/2006JD007772)
- Jin SG, Luo OF, Park P (2008) GPS observations of the ionospheric F2-layer behavior during the 20th November 2003 geomagnetic storm over South Korea. *J Geod* 82(12):883–892. doi:[10.1007/s00190-008-0217-x](https://doi.org/10.1007/s00190-008-0217-x)
- Jin SG, Feng GP, Gleason S (2011) Remote sensing using GNSS signals: current status and future directions. *Adv Space Res* 47(10):1645–1653. doi:[10.1101/j.asr.2011.01.036](https://doi.org/10.1101/j.asr.2011.01.036)
- Katzberg SJ, Dunion J (2009) Comparison of reflected GPS wind speed retrievals with dropsondes in tropical cyclones. *Geophys Res Lett* 36:L17602. doi:[10.1029/2009GL039512](https://doi.org/10.1029/2009GL039512)
- Katzberg SJ, Walker RA, Roles JH, Lynch T, Black PG (2001) First GPS signals reflected from the interior of a tropical storm: preliminary results from Hurricane Michael. *Geophys Res Lett* 28(10):1981–1984
- Katzberg S, Torres O, Grant MS, Masters D (2006) Utilizing calibrated GPS reflected signals to estimate soil reflectivity and dielectric constant: results from SMEX02. *Remote Sens Environ* 100(1):17–28
- Komjathy A, Maslanik JA, Zavorotny VU, Axelrad P, Katzberg SJ (2000) Sea ice remote sensing using surface reflected GPS signals. In: Proceedings of the IEEE international geosciences and remote sensing symposium (IGARSS 2000), Honolulu, Hawaii, 24–28 July, pp. 2855–2857
- Larson KM, Small EE, Gutmann ED, Bilich AL, Braun JJ, Zavorotny VU (2008a) Use of GPS receivers as a soil moisture network for water cycle studies. *Geophys Res Lett* 35:L24405. doi:[10.1029/2008GL036013](https://doi.org/10.1029/2008GL036013)
- Larson KM, Small EE, Gutmann E, Bilich A, Axelrad P, Braun J (2008b) Using GPS multipath to measure soil moisture fluctuations: initial results. *GPS Solut* 12(3):173–177

- Lowe ST, Kroger P, Franklin G, LaBerecque JL, Lerma J, Lough M, Marcin MR, Muellerschoen RJ, Spitzmesser D, Young LE (2002) A delay/Doppler- mapping receiver system for GPS-reflection remote sensing. *IEEE Trans Geosci Remote Sens* 40(5):1150–1163
- Martin-Neira M, Caparrini M, Font-Rosello J et al (2001) The PARIS concept: an experimental demonstration of sea surface altimetry using GPS reflected signals. *IEEE Trans Geosci Remote Sens* 39:142–149
- Masters D (2004) Surface remote sensing applications of GNSS Bistatic Radar: soil moisture and aircraft altimetry. Ph.D. dissertation, University of Colorado, Boulder
- Montenbruck O, Kroes R (2003) In-flight performance analysis of the CHAMP BlackJack GPS Receiver. *GPS Solut* 7(2):74–86. doi:[10.1007/s10291-003-0055-5](https://doi.org/10.1007/s10291-003-0055-5)
- Nesterov IA, Kunitsyn VE (2011) GNSS radio tomography of the ionosphere: the problem with essentially incomplete data. *Adv Space Res*. doi:[10.1016/j.asr.2010.11.034](https://doi.org/10.1016/j.asr.2010.11.034)
- Schmidt T, Wickert J, Haser A (2010) Variability of the upper troposphere and lower stratosphere observed with GPS radio occultation bending angles and temperatures. *Adv Space Res* 46:150–161. doi:[10.1016/j.asr.2010.01.021](https://doi.org/10.1016/j.asr.2010.01.021)
- Tien JY, Young L, Meehan T, Franklin G, Hurst KJ, Esterhuizen S, Trig Gnss Receiver Team (2010) Next generation of spaceborne GNSS receiver for radio occultation science and precision orbit determination. AGU Fall meeting, San Francisco, CA, USA, 13–17 Dec 2010, Abstract G51A-0661
- Unwin M, de Vos van Steenwijk R, Gommenginger C, Mitchell C, Gao S (2010) The SGR-ReSI – a new generation of space GNSS receiver for remote sensing. In: Proceedings of ION, Portland, Oregon, USA, 21–24 Sept 2010
- Wu Y, Jin SG, Wang Z, Liu J (2010) Cycle slip detection using multi-frequency GPS carrier phase observations: a simulation study. *Adv Space Res* 46(2):144–149. doi:[10.1016/j.asr.2009.11.007](https://doi.org/10.1016/j.asr.2009.11.007)
- Yen N (2010) FORMOSAT-7/COSMIC-2 joint plan and current progress. Joint OPAC-4 & GRAS-SAF climate & IROWG-1 workshop, Graz, Austria, 6–11 Sept 2010
- Yunck TP, McCormick CC, Lenz C (2007) The CICERO project: a community initiative for continuing Earth Radio Occultation, Second FORMOSAT-3/COSMIC data users workshop, Boulder, CO, USA, 22–24 Oct 2007

Index

A

- Afraimovich, E., 79
Aguasca, A., 190
Antenna phase centre, 12
Anti-spoofing (AS), 166
A priori
 constraint, 37
 information, 124, 135, 141, 142
Armatys, M., 262
Atmospheric
 boundary layer, 128, 132, 133, 140–141
 correction, 224–225
 delay, 5, 11, 17–29, 58, 78, 105, 106,
 224, 225
 pressure, 19, 34, 39–42, 44, 50, 51, 105,
 121, 122, 217
 refraction, 5, 14, 17–18, 33, 99–100,
 121, 134
 refractive index, 49, 99
Augmentation segment, 9–10
Austen, J.R., 62, 80
Azimuth, 176, 178, 181, 196, 244, 247, 248

B

- Bassiri, S., 61
Beidou, 9, 10
Bending angle, 102–106, 110–117, 124–126,
 128–134, 140–142, 145, 147, 148,
 162, 163
Beyerle, G., 108, 129
Bi-static radar, 175, 192, 201–202, 235, 265
Bivariate normal distribution, 232, 233
Blanch, S., 190
Bouguer's rule, 102, 103, 111

Broadcast, 4, 6–10, 15, 63

Brown, G.S., 232

C

- Calais, E., 62
Camps, A., 227
Cardellach, E., 209–211, 226, 251, 253,
 257, 262
Carrier phase, 12, 26, 63, 64, 66, 70, 161, 163,
 166, 201, 220
Chen, S.-Y., 140
Circular polarizations, 189, 196, 199, 211,
 246–248
Civil applications, 8, 13
Clarizia, M.P., 197
Clock
 bias, 63, 205
 drift, 37
 error, 12, 34, 105, 106, 108–110, 113, 114,
 127, 129, 166, 205, 216, 223
 frequency, 11, 12, 34, 110, 113, 114, 205
 offset, 63, 107–109
 parameter, 9, 37, 223
Code
 delay, 22
 phase combination, 11, 22, 26, 35, 63, 70,
 221, 225
 pseudorange, 64
 smoothing, 64, 66, 115
Combining algorithms, 103, 111, 123
Compass, 3, 267
Coordinate transformation, 112
Covariance propagation, 124, 229
Cox, C., 232

Cross-correlation, 183, 200, 206
 Cycle slip detection, 64, 210

D

Data assimilation, 134, 140–143, 149, 227
 Delay-Doppler map (DDM), 188, 209–211, 235, 264
 Dielectric constant, 189–191, 241, 242, 245, 246, 259, 262
 Differential
 code biases, 64
 Doppler, 105
 equation, 101, 198
 GPS, 9, 10, 109
 group delay, 11
 phases, 110
 positioning, 108
 Doppler
 delay, 113, 175, 184–188, 202–205, 208–210, 221, 231, 262, 264
 effect, 198
 frequency shift, 186, 187, 200, 201, 211
 integration, 204, 205
 Double difference, 26, 34–35, 109, 129
 Dual-frequency, 21, 26, 62–66, 70, 97, 113, 114, 149, 163, 168, 261
 Dunion, J., 228

E

Earth observation, 58, 175, 263, 265
 rotation, 14
 Eccentricity, 7
 EGNOS. *See* European Geostationary Navigation Overlay Service (EGNOS)
 Elachi, C., 203, 204
 Electromagnetic wave
 field, 112, 175, 176, 189, 192, 193, 199, 202, 262
 scattering, 178, 197, 198, 249
 Electron density, 5, 15, 18, 21, 22, 24, 62, 63, 70, 79–90, 105, 113, 130, 162, 164–169, 261
 content, 164
 Elevation, 26–29, 35, 36, 39, 48, 50, 53, 54, 65, 68, 81, 106, 147, 148, 176, 178, 179, 181, 184, 187, 191, 204, 211, 219, 221, 224, 228, 229, 233, 244, 245, 255–258
 Elfouhaily, T.M., 193, 198, 210, 227, 228, 230, 232, 234, 235
 Ephemerides, 12, 66
 European Geostationary Navigation Overlay Service (EGNOS), 8, 10

F

Fabra, F., 210, 211, 251
 Ferrazzoli, P., 248, 262
 Foelsche, U., 136
 Forest biomass, 248, 262
 Frequency
 effect, 21, 26, 63, 110, 144, 149, 205, 211, 225, 242
 offset, 188
 Fresnel zone, 111, 126, 181, 187, 189, 200, 244, 246, 248

G

Galilei, G., 6
 Galileo
 application, 264
 signal, 264, 265
 system, 5, 6, 10, 264
 Garrison, J.L., 235
 Geocentric latitude, 66
 Geodetic network, 211
 analysis, 211
 Geodynamics, 14, 95, 267
 Geometric
 conditions, 81, 182
 mapping function, 33
 optics, 100–101, 110–111, 126, 130, 132, 142, 148, 178, 182, 194, 196, 197, 252
 range, 105, 106
 Geometry-free combination, 252
 Geophysical source, 50, 86, 88, 104, 115, 121, 124, 184, 235, 243–245, 249, 262, 264
 parameters, 104, 115, 121, 124, 235, 243–245, 249, 262, 264
 Germain, O., 210
 Gleason, S., 258
 Glistening zones, 176–178, 182–184, 248
 Global Navigation Satellite System
 (GLONASS), 3, 5–6, 8, 10, 68, 96, 98, 146, 177–179, 263–265, 267
 Global Positioning System (GPS)
 altimetry, 264
 analysis center, 245, 262
 antenna, 42, 106, 107, 127, 245
 clock, 108–110, 127
 constellation, 4, 63
 control segment, 4, 5
 error, 11, 34, 50, 61, 108–110
 meteorology, 5
 navigation, 25
 network, 43, 58, 62, 82, 263
 observation equation, 23

radio occultation, 58, 96, 100, 104, 136, 261
reflectometry, 259, 262, 265, 267
GLONASS. *See* Global Navigation Satellite System (GLONASS)
Gobiet, A., 136
Gorbunov, M.E., 126
GPS. *See* Global Positioning System (GPS)
GRACE. *See* Gravity Recovery and Climate Experiment (GRACE)
Gram-Charlier distribution, 232, 233
Gravity Recovery and Climate Experiment (GRACE), 108, 128, 160, 264
Ground segment, 5, 7
 stations, 5
Group delay, 11, 206, 210, 220–222, 225, 226
Guérin, C.-A., 193, 198

H

Hajj, G.A., 61, 136, 210, 222
Hardy, K.R., 72
Hawley, R.L., 252
Healy, S.B., 131
Helm, A., 211, 226
Henrique, J., 230
Herring, T.A., 36
He, W., 136
Hopfield, H.S., 19
Hopfield model, 19–20
Ho, S.-P., 136
Huang, C.-Y., 140
Humphreys, T.E., 50
Huygens-Fresnel principles, 181, 182
Hydrology, 3, 15, 241–249, 262, 263, 267

I

IGS. *See* International GNSS service (IGS)
Indirection signal, 25
Instrumental bias, 74, 164
Integer ambiguity, 23
Integrity, 5, 8
Interferometric phase
 amplitude, 211
 fringes, 252
International Earth Rotation Service (IERS), 50
International GNSS service (IGS), 13, 35,
 37–40, 42–44, 48, 50–55, 58, 62, 67–70,
 74, 107, 109, 263, 267
International Terrestrial Reference Frame, 14
International Union of Radio Science (URSI),
 24, 83, 167
Interpolation, 37, 51, 71, 107, 109
Ionosphere-free combination, 34, 115

Ionospheric
 anomalies, 169–170
 correction, 115, 116, 168
 delay, 11, 12, 18, 20–26, 37, 61, 74, 78,
 106, 113, 168, 265
 disturbance, 170
 effect, 62, 63, 115, 216, 224, 225, 246
 electron density, 24, 63, 80, 81, 83, 84, 86,
 88, 164, 261
 mapping, 62, 71–74, 79–90, 266
 model, 24–25, 62, 72, 83, 168
 noise, 109
 profile, 24, 82, 88, 114, 168, 170, 267
 residual, 64, 130, 150
 scintillation, 115, 130, 170
 sounding, 24, 63–65, 159–170, 261
 tomography, 63, 79–82, 168–169

J

Jensen, A.S., 112
Jet Propulsion Laboratory (JPL), 62, 68, 69,
 73, 93, 97–99, 108, 129, 135, 139, 146,
 263, 264
Jones, R., 225

K

KA in Physical Optics Approximation (KPO),
 196, 198
Katzberg, S.J., 228, 245, 262
KGO. *See* Kirchhoff geometrical optics (KGO)
Kirchengast, G., 137
Kirchhoff approximation (KA), 193, 194,
 197–199
Kirchhoff geometrical optics (KGO), 192,
 194–196, 198, 199, 201, 202, 233
Klobuchar, J.A., 24
Komjathy, A., 257, 259, 263
KPO. *See* KA in Physical Optics
 Approximation (KPO)
Krasilnikova, T.G., 115
Kuo, Y.-H., 136, 138
Kursinski, E.R., 126, 131, 136

L

Larson, K.M., 245, 262
Least squares adjustment, 73
LEO. *See* Low earth orbit (LEO)
Leroux, C., 29
Le Traon, P.Y., 215
Limb sounding, 5, 62, 124–126, 149

Linear, 29, 37, 40–43, 57, 80, 81, 116, 131, 134, 196, 199, 211, 235, 246, 247, 248
combination, 26, 35, 106, 113, 115, 130
Line-of-sight (LOS), 25, 96, 150, 263, 267
Liu, A.S., 95
Liu, H., 140
Li, Y., 247
Loading tide, 50
Low earth orbit (LEO), 62, 96, 98, 105–110, 112–114, 127, 129, 140, 146–150, 159–161, 163–167, 178, 179, 187–189, 215, 224, 226, 227, 235, 258, 265
Lowe, S.T., 222, 226

M

Mapping function, 33, 35–37, 50, 71, 224
Marchan-Hernandez, J., 210, 211, 227, 235
Marini, J.W., 36
Martin-Neira, M., 208, 210, 222, 226, 227
Masters, D., 245
Mean anomaly, 85
Mean of the square slopes (MSS), 228, 231, 232, 234, 235
Microwave radiometry, 243
Minster, J.B., 62
Modulation code, 63, 116, 183, 199, 206, 207
MSS. *See* Mean of the square slopes (MSS)
Multi-frequency, 5, 263, 264, 267
Multipath, 12, 17–29, 105, 109–112, 127–129, 132, 140, 148, 165, 166, 243, 245, 246, 249, 262
Multi-system, 5, 8
Munk, W., 232

N

Navigation
message, 9, 10, 12, 108
signal, 7, 11, 98, 108
Near-real-time, 3, 14, 58, 62, 114, 141, 263, 266
Neiman, P.J., 139
Neutral atmosphere, 18–19, 33, 35, 96, 99, 100, 104–106, 110, 113, 115–117, 121, 125, 130, 167, 224
Niell, A.E., 36, 50, 52
Nogués-Correig, O., 210

O

Observational model, 123
Ocean altimetry
circulation, 215, 216

loading tide displacement, 50
remote sensing, 3, 215–236
surface, 27, 208, 218, 226–228, 234, 248, 262, 266, 267
tide, 50
wave spectra, 216, 217, 219, 229–231
Oceanography, 13, 215, 234, 264
Operational control system (OCX), 5
Orbit, 4, 7, 9, 10, 12, 13, 14, 35, 62, 63, 95, 96, 98, 106–109, 112–114, 128, 129, 131, 136, 138, 163, 166, 167, 173, 177–179, 216, 223, 224, 227, 228, 251, 258, 263, 264
determination, 9, 14, 107, 163, 166, 167, 227, 263, 264

P

Parameters, 3, 9, 15, 17, 18, 24, 25, 27, 34–37, 41–43, 53, 62, 63, 66, 67, 74, 80–82, 84, 86, 88–90, 102–104, 112, 115, 116, 121, 123–125, 131, 147, 148, 159, 161, 162, 167, 168, 186, 189, 210, 219, 223, 227, 229, 230, 234–236, 241, 243–245, 249, 254, 256, 262, 264–266
PARIS interferometric technique (PIT), 206–208, 222, 225–227
Path
delay, 17–29, 62, 202
range effect, 161
P-code, 10, 11, 116, 183
Phase
centre, 105, 107, 218
combination, 105
delay, 105, 106, 108, 110, 113, 126, 141, 143, 220, 225, 226
difference, 104, 114, 255
measurement, 11, 26, 37, 105, 106, 109, 110, 115, 127, 129, 141, 165
model, 105, 107
Phase-locked-loop (PLL), 128
Physical optics approximation, 196
Pierson-Moskowitz spectrum, 230, 231, 234
PIT. *See* PARIS interferometric technique (PIT)
Planetary science, 93–94
Plate motion, 14
PLL. *See* Phase-locked-loop (PLL)
POD. *See* Precise orbit determination (POD)
Point positioning, 35
PPP. *See* Precise point positioning (PPP)
Precipitable water vapor (PWV), 34, 42, 51–58, 261

- Precise ephemerides, 66
 point positioning, 35
- Precise orbit determination (POD), 14,
 106–109, 129, 218
- Precise point positioning (PPP), 35
- Pre-processing, 66
- PRN. *See* Pseudo-random noise (PRN)
- Pseudo-random noise (PRN), 10, 11, 183
- Pseudorange, 12, 26, 35, 63, 64, 163
- PWV. *See* Precipitable water vapor (PWV)
- Q**
- Quasi-Zenith Satellite System (QZSS), 5, 7,
 177, 263, 267
- R**
- Radar, 21, 64, 74, 75, 86, 167, 175, 192,
 201–203, 215, 216, 218, 235, 242, 244,
 246, 248, 259, 265
 altimetry, 74, 215, 216
 Radiative transfer, 246, 247
- Radio occultation, 3, 5, 15, 58, 62, 93–117,
 136, 146–150, 159, 162, 163, 167, 256,
 261, 263–266
- Radiosonde, 36, 52, 53, 57, 96, 133, 135–138,
 140, 141, 143, 144, 146, 148
- Randel, W.J., 137
- Receiver Independent Exchange Format
 (RINEX), 66, 67
- Reference frame, 14
- Reflected signals, 3, 15, 25, 29, 175, 177,
 181, 188, 203, 206, 207, 220, 221, 235,
 243–245, 247, 249, 256–259, 262–264,
 267
- Refractive index, 5, 17, 22–24, 49, 62, 98–106,
 111, 113, 116, 131, 148, 162, 170, 253
- Regional systems, 7–8
- Relativistic effect, 12, 107, 110
- RINEX. *See* Receiver Independent Exchange
 Format (RINEX)
- Rius, A., 207, 208, 210, 221, 222, 226, 262
- Rodriguez-Alvarez, N., 243
- Root-mean-square (RMS), 26, 52, 53, 68–70,
 82, 129, 131, 136
- Ruffini, G., 226
- S**
- SA. *See* Selective availability (SA)
- Saastamoinen, J., 19
- Saastamoinen model, 19, 37
- Satellite
- antenna, 25, 27, 28, 32, 137, 251
 elevation angle, 65, 244
 geodesy, 95, 146
 geometry, 9, 12, 57, 108
 navigation, 4, 6, 11
 orbit, 4, 6, 9, 10, 12, 62, 108, 109, 112, 128,
 129, 136, 167, 242
 positioning, 6, 244
- Scattering coefficients, 202, 231, 246–248
 theories, 192–202, 262
- Schmidt, T., 137, 261
- Schreiner, W., 136
- Sea level, 19, 36, 38, 40, 41, 116, 217, 251
- Seasonal variation, 42–46, 55–56, 82, 86, 87
- Selective availability (SA), 4, 11, 12, 108,
 109, 129
- Semmling, M., 210, 220
- Signal transmission
- coherence, 183, 201, 221
 - reflection, 25, 175, 244, 252–255
 - refraction, 253
- Single, 67–70, 72, 98, 108, 110, 112, 113, 125,
 130, 132, 163, 164, 166, 175, 178, 202,
 215, 216, 226, 234, 252–255, 259
 difference, 70
- Small perturbation method (SPM), 198, 199
- Small slope approximation (SSA), 199
- Smith, E.K., 121
- Snajdrova, K., 52
- Snell's law, 101, 102, 252, 253
- Soil moisture, 3, 191, 211, 241–246, 249,
 262–264, 268
- Solar radiation, 12, 18, 20, 50, 61, 74
- Space segment, 4, 6, 8, 9
- Spatial resolution, 76, 126, 242, 245, 249, 259,
 261, 263, 265–267
- Specular angles
- point, 178, 179, 181, 186–188, 200, 218,
 219, 222, 235, 248, 254
 - ray path, 219, 221, 222
 - reflection, 178, 181, 183, 185, 187, 195,
 197, 200, 248, 253, 255
- Spherical
- harmonics, 62, 65, 66, 68, 69, 71, 73
 - symmetry, 101–103, 114, 116, 126,
 130–132, 142, 147, 149, 162, 163, 167
- SPM. *See* Small perturbation method (SPM)
- SSA. *See* Small slope approximation (SSA)
- Standard deviation, 74, 135, 136, 144, 197,
 198, 204
- Steiner, A.K., 137
- Stephenson, J., 225
- Stosius, R., 216
- Suresh, R.R.V., 231

T

- TEC. *See* Total electron content (TEC)
 Thermal noise, 105, 109, 116, 127, 166, 203, 204
 Thompson, A.R., 204
 Thompson, D.R., 232
 Tidal loading, 138
 Tomographic reconstruction, 62, 80–82
 Total electron content (TEC), 3, 15, 18, 23, 62, 63, 65, 68, 70, 71, 74, 85, 113, 163, 167, 168, 261, 265
 Transition matrix, 191
 Treuhhaft, R.N., 197, 210, 226
 TriG, Tri-GNSS (GPS+Galileo+GLONASS), 264
 Tropical tidal waves, 138
 cyclones, 136, 139–140, 143, 146, 262
 Tropopause, 3, 15, 96, 125, 132, 136–138, 261
 Tropospheric
 delay, 12, 19, 20, 26, 33, 35, 37, 78
 effect, 216, 217
 model, 19–20, 33
 water vapor, 3, 15, 18
 Tsuda, T., 137

U

- Ulaby, F.T., 190, 191, 194, 196, 198
 Undifferenced algorithm, 35
 Universal Time (UT), 13, 76, 82, 88–90
 URSI. *See* International Union of Radio Science (URSI)
 US Air Force (USAF), 5, 96, 97
 User segment, 8, 9, 12

V

- Valencia, E., 227, 235
 Very long baseline interferometry (VLBI), 52, 53
 Vienna mapping functions (VMF), 36, 37

VLBI. *See* Very long baseline interferometry (VLBI)

VMF. *See* Vienna mapping functions (VMF)
 Vorobev, V.V., 115
 Voronovich, A.G., 201, 235, 243, 244

W

- WAF.** *See* Woodward ambiguity function (WAF)
 Ware, R., 5, 62
 Water vapor radiometry (WVR), 52
 Waveform correlation, 188, 243–244
 Weintraub, S., 121
 Woodward ambiguity function (WAF), 202
 Wu, X., 246, 247
 WVR. *See* Water vapor radiometry (WVR)

X

- Xie, F., 134, 140, 149

Y

- Yakovlev, O.I., 95
 Yunck, T.P., 126

Z

- Zavorotny, V.U., 201, 235, 243, 244
 Zeng, Z., 138
 Zenith hydrostatic delay (ZHD), 34, 35, 40–42, 49, 51
 Zenith tropospheric delay (ZTD), 33–35, 37–52, 58
 Zenith wet delay (ZWD), 34, 35, 41, 42, 51
 ZHD. *See* Zenith hydrostatic delay (ZHD)
 ZTD. *See* Zenith tropospheric delay (ZTD)
 Zuffada, C., 147, 204, 210, 222
 Z-V model, 243
 ZWD. *See* Zenith wet delay (ZWD)